Univerza
v Ljubljani
Fakulteta
za gradbeništvo
in geodezijo

LIZA STANČIČ

UGOTAVLJANJE SPREMEMB REČNIH PRODIŠČ Z DALJINSKIM ZAZNAVANJEM

DOKTORSKA DISERTACIJA

MONITORING CHANGES OF FLUVIAL GRAVEL BARS WITH REMOTE SENSING

DOCTORAL DISSERTATION

INTERDISCIPLINARNI DOKTORSKI ŠTUDIJSKI PROGRAM

VARSTVO OKOLJA

Ljubljana, 2022

_____

Hrbtna stran: **STANČIČ LIZA** 2022

Univerza
v Ljubljani
Fakulteta
za gradbeništvo
in geodezijo

Doktorandka

LIZA STANČIČ

UGOTAVLJANJE SPREMEMB REČNIH PRODIŠČ Z DALJINSKIM ZAZNAVANJEM

Doktorska disertacija

MONITORING CHANGES OF FLUVIAL GRAVEL BARS WITH REMOTE SENSING

Doctoral dissertation

Ljubljana, oktober 2022

Mentor: prof. dr. Krištof Oštir, Univerza v Ljubljani, Fakulteta za gradbeništvo in geodezijo.

Somentor: izr. prof. dr. Žiga Kokalj, Znanstvenoraziskovalni center Slovenske akademije znanosti

in umetnosti.

Komisija za spremljanje doktorske študentke:

doc. dr. Simon Rusjan, Univerza v Ljubljani, Fakulteta za gradbeništvo in geodezijo,

prof. dr. Mitja Kaligarič, Univerza v Mariboru, Fakulteta za naravoslovje in matematiko,

prof. dr. Mathias Schardt, Graz University of Technology in Joanneum Research.

ERRATA

Page   Line   Error   Correction

»This page is intentionally blank.«

ZAHVALA

IV

Stančič, L. 2022. Monitoring Changes of Fluvial Gravel Bars with Remote Sensing.
PhD Th. Ljubljana, UL FGG, Interdisciplinary doctoral study programme Environmental Protection.

»This page is intentionally blank.«

Stančič, L. 2022. Monitoring Changes of Fluvial Gravel Bars with Remote Sensing.
PhD Th. Ljubljana, UL FGG, Interdisciplinary doctoral study programme Environmental Protection.

V

BIBLIOGRAFSKO-DOKUMENTACIJSKA STRAN IN IZVLEČEK

Izvleček

Prodišča so dinamična območja odlaganja plavin v rekah. Opravljajo pomembne ekološke funkcije in veljajo za pokazatelje sprememb hidroloških značilnosti rek. Satelitski posnetki s kratkim časom ponovnega obiska in velikim območjem hkratne pokritosti so idealen vir podatkov za spremljanje številnih naravnih značilnosti, vključno s prodišči. Prosto dostopni podatki daljinskega zaznavanja sistemov Sentinel-2 in Landsat imajo prostorsko ločljivost, ki je lahko preveč groba za natančno odkrivanje prodišč, zlasti na gorskih območjih, kjer so reke in z njimi povezane značilnosti ozke. Zato smo razvili podpikselsko metodo kartiranja, ki temelji na analizi vsebnosti spektralnega signala. Za referenco smo uporabili letalske ortofote, satelitske posnetke zelo visoke ločljivosti in terensko kartiranje. Poleg spektralnih pasov Sentinel-2 in Landsat smo za boljše ločevanje med izbranimi razredi pokrovnosti uporabili spektralne indekse. Samodejno izbrani končni piksli so omogočili kartiranje s podobno natančnostjo kot ročno izbrani končni piksli. Končne piksle, izbrane na enem posnetku študijskega območja med sezono olistanja, lahko uspešno uporabimo za SMA drugih posnetkov istega območja, pridobljene z istim sistemom daljinskega zaznavanja na drugi točki sezone olistanosti. Karte deležev pokrovnosti so natančnejše od kart, izdelanih s trdo klasifikacijo s Spectral Angle Mapper z uporabo istih vhodnih podatkov. Ob upoštevanju teh ugotovitev smo izdelali karte deležev proda, vegetacije in vode za Sočo, Savo in Vjoso (Albanija) za obdobje več kot 30 let. Tematska natančnost kart je znotraj 90%. Preizkusili smo tudi sposobnost kart deležev pokrovnosti za zaznavanje sprememb in ugotovili, da je mogoče natančno zaznati spremembe v obsegu vsaj 400 m^2. Časovne vrste lahko uporabimo tudi za zaznavanje odstranjevanja proda, kot je vidno na znanih območjih odvzema proda pri naselju Dolje na Soči in pri Kranju na Savi. Disertacija prispeva k znanosti z novimi spoznanji o uporabi podpikselskega kartiranja za spremljanje naravnih procesov. Razvito metodo lahko uporabimo za proučevanje območij, kjer je na voljo manj terenskih podatkov. Na podlagi novo pridobljenega znanja je mogoče sprejemati boljše odločitve o upravljanju z vodami in varstvu habitatov.

VI   Stančič, L. 2022. Monitoring Changes of Fluvial Gravel Bars with Remote Sensing.

PhD Th. Ljubljana, UL FGG, Interdisciplinary doctoral study programme Environmental Protection.

»This page is intentionally blank.«

BIBLIOGRAPHIC-DOCUMENTALISTIC INFORMATION AND ABSTRACT

Abstract

Gravel bars are dynamic areas of bedload deposition in rivers. They perform important ecological functions and are considered indicators of changes in the hydrological characteristics of rivers. Satellite images with a frequent revisit period and a large area of simultaneous coverage are an ideal data source for monitoring many natural features including gravel bars. Openly and freely available remote sensing data from the Sentinel-2 and Landsat systems have a spatial resolution that may be too coarse for accurate detection of gravel bars, especially in mountainous areas where rivers and related features are narrow. We therefore developed a sub-pixel mapping method based on spectral mixture analysis. Very high resolution aerial orthophotos and satellite images, as well as field mapping, were used as reference. Sentinel-2 and Landsat spectral bands were supplemented with spectral indices to increase the separability between land cover classes of interest. Automatically selected endmembers led to results with similar accuracy as when manually selected endmembers were used. Endmembers selected on one image of the study area during the leaf-on season could be used to analyse another image of the same study area acquired with the same remote sensing system at a different time. The fraction maps were found to be more accurate than maps produced by hard classification with Spectral Angle Mapper using the same input data. Considering these findings, we produced fraction maps of gravel, vegetation, and water presence for the Soča and Sava rivers in Slovenia, and the Vjosa river in Albania for a period of over 30 years. The thematic accuracy of the maps was within 90%. We also tested the ability of fraction maps for change detection and found that changes of at least 400 m^2 could be accurately detected. The time series plots can also be used to detect gravel removal as demonstrated at known excavation sites near the Dolje settlement on Soča and near Kranj on Sava. The dissertation contributes to science with new insights about the application of sub-pixel mapping for monitoring natural processes. The developed method can be applied to study areas where less in situ data are available. More informed management decisions can be made based on newly acquired knowledge.

VIII

Stančič, L. 2022. Monitoring Changes of Fluvial Gravel Bars with Remote Sensing.
PhD Th. Ljubljana, UL FGG, Interdisciplinary doctoral study programme Environmental Protection.

»This page is intentionally blank.«

KAZALO / TABLE OF CONTENT

»This page is intentionally blank.«

LIST OF FIGURES

»This page is intentionally blank.«

KAZALO SLIK

XXII

Stančič, L. 2022. Monitoring Changes of Fluvial Gravel Bars with Remote Sensing.
PhD Th. Ljubljana, UL FGG, Interdisciplinary doctoral study programme Environmental Protection.

XXIV

Stančič, L. 2022. Monitoring Changes of Fluvial Gravel Bars with Remote Sensing.
PhD Th. Ljubljana, UL FGG, Interdisciplinary doctoral study programme Environmental Protection.

»This page is intentionally blank.«

Stančič, L. 2022. Monitoring Changes of Fluvial Gravel Bars with Remote Sensing.
PhD Th. Ljubljana, UL FGG, Interdisciplinary doctoral study programme Environmental Protection.

XXV

LIST OF TABLES

XXVI

Stančič, L. 2022. Monitoring Changes of Fluvial Gravel Bars with Remote Sensing.
PhD Th. Ljubljana, UL FGG, Interdisciplinary doctoral study programme Environmental Protection.

KAZALO PREGLEDNIC

XXVIII
Stančič, L. 2022. Monitoring Changes of Fluvial Gravel Bars with Remote Sensing.
PhD Th. Ljubljana, UL FGG, Interdisciplinary doctoral study programme Environmental Protection.

OKRAJŠAVE / ABBREVIATIONS

ALS	Aerial Laser Scanning
ARI1	Anthocyanin Reflectance Index
BAI	Burn Area Index
BRBA	Band Ratio for Built-up Areas
CAS	Cyclical Aerial Photography of Slovenia
EM	Endmember
EO	Earth Observation
ETM+	Enhanced Thematic Mapper Plus
EVI	Enhanced Vegetation Index
HPP	Hydroelectric Power Plant
IFOV	Instantaneous Field of View
MAE	Mean Absolute Error
ML	Machine Learning
MNDWI	Modified Normalised Difference Water Index
MSAVI2	Modified Soil Adjusted Vegetation Index 2
MSI	Multi-Spectral Imager
NDII	Normalised Difference Infrared Index
NDVI	Normalised Difference Vegetation Index
NDVI-GREEN	Normalised Difference Vegetation Index multiplied by green band
NDWI	Normalised Difference Water Index
NPCRI	Normalised Pigment Chlorophyll Ratio Index
OLI	Operational Land Imager
PLC	Path Length Correction
PSRI	Plant Senescence Reflectance Index
RF	Random Forest
RMSE	Root-Mean-Square Error
SAM	Spectral Angle Mapper
SAR	Synthetic Aperture Radar
SCS+C	Modified Sun-Canopy-Sensor correction
SMA	Spectral Mixture Analysis
SVM	Support Vector Machine
TIRS	Thermal Infrared Sensor
TM	Thematic Mapper
VECA	Variable Empirical Coefficient Algorithm
VHR	Very High Resolution

»This page is intentionally blank.«

SLOVAR / GLOSSARY

Endmember, pure pixel – sl. Končni piksel: Pixel representing the spectral properties of a single land cover class. Endmembers may be measured with a spectro-radiometer, found on an actual satellite image, or estimated based on image data.

Endmember selection, endmember extraction – sl. Izbor končnih pikslov: Determination of pixels representing land cover classes of interest on a satellite image. The selection can be done manually with the help of reference data with a higher spatial resolution, or automatically, for example with a region growing algorithm to find the extremities of the image feature space.

Fully constrained spectral mixture analysis – sl. Polno omejena analiza vsebnosti spektralnega signala: Method for calculating land cover presence where the fraction values within each pixel need to sum up to one and must be non-negative.

Hard classification – sl. Trda klasifikacija: Method for recognising features on a satellite image where the whole area of each pixel is assigned to a single class.

Image endmember – sl. Končni piksel, izbran na posnetku: Pixel on a satellite image chosen to represent the spectral properties of a particular land cover class. Reference data with a higher spatial resolution is usually necessary to ensure pixel purity.

Land cover fraction, land cover abundance – sl. Delež pokrovnosti: Share of a pixel covered by a particular land cover class. The share is determined based on the degree of similarity of the pixel's spectral signature to the spectral signature of the particular land cover class.

Non-linear spectral unmixing – sl. Nelinearna analiza vsebnosti spektralnega signala: Method for calculating the presence of selected land cover classes in a setting where the classes are very closely mixed. Each incoming photon therefore interacts with more than one class. Non-linear spectral unmixing is necessary, for example, when analysing the materials present in sand or soil.

Non-pixel endmember – sl. Končni piksel, ki ni izbran na posnetku: Spectral properties of a selected land cover class that are not derived from a single pixel on a satellite image, but estimated based on the image data. Non-pixel endmember need to be used when images are highly mixed and no pure pixels are present.

Soft classification – sl. Mehka klasifikacija: Method for recognising features on a satellite image where the cover of each pixel is defined as a mix of different land cover classes. The mix is represented by land cover fractions.

Spectral angle mapper – sl. Klasifikacija na podlagi kota med spektri: Method for assigning selected land cover classes to pixels based on a comparison of angles between vectors of reference spectra and pixels spectra. The smallest calculated angle means the biggest similarity between the two spectra under consideration.

Spectral mixture analysis – sl. Analiza vsebnosti spektralnega signala: Method for determining the presence of selected land cover classes in a pixel based on the pixel's spectral properties.

Transferred endmember – sl. Prenesen končni piksel: Pixel chosen to represent the spectral properties of a land cover class selected on one satellite image and used to determine land cover fractions on another satellite image.

1   INTRODUCTION

Successful nature conservation, sustainable development, and integrated resource management rely on accurate monitoring which in turn depends on reliable data. This is underlined by the UN Statistical Commission, which defined a comprehensive set of 231 indicators to track progress towards the Sustainable Development Goals (SDGs) (UN, 2017). Data used to obtain information on the indicators must be collected in a comparable manner worldwide, must be responsive to change, and must provide repeatable observations. It is also beneficial if data collection is not very expensive and lengthy. Remote sensing can play an important role in seeking global universality of goals, greater objectivity of monitoring methods, and reproducibility of the approach (Scott and Rajabifard, 2017). In Earth observation (EO), data are collected with sensors that are not in contact with the surface; the data are then transmitted to ground stations and processed accordingly. Subsequently, the processed images are interpreted and analysed, and the acquired information is used for selected applications (Oštir, 2006). A key factor in using satellite images to obtain information about the Earth's surface is resolution (Campbell and Wynne, 2011).

Features such as good spatial, radiometric, and spectral resolution, the possibility of multi-level assessment (local, regional, global), increasing frequency of imaging, and free access have led to satellite images becoming an important source of various environmental data (de Sherbinin et al., 2014). International associations and organisations, such as the UN and the Group on Earth Observations (GEO) recommend EO data as a primary source of information or as a support for other statistical data in monitoring the progress in sustainable development (GEO, 2017). However, there is much room for new developments. In hydrology, for example, obtaining data from alternative sources (e.g. remote sensing) is considered one of the main challenges (Blöschl et al., 2019). In this doctoral dissertation, we investigate the possibility of using satellite images to obtain the data needed to monitor gravel bars in rivers. This is related to the SDG indicator of change in the extent of water-related ecosystems over time (UN, 2017).

The introductory chapter defines the research problem that motivated the dissertation, describes the hypotheses and objectives that guided the workflow, and concludes with an overview of the dissertation structure.

1.1   Definition of the Research Problem

The main research problem addressed by the proposed dissertation is the mapping of river ecosystems. Several remote sensing products show the presence of surface water worldwide (Huang et al., 2018). Different applications are available to view the extent of water over time (Donchyts et al., 2016; Pekel et al., 2016). Other lines of research have focused on detecting and monitoring specific water-related

features, for example, creating global inventories of rivers (Allen and Pavelsky, 2018), lakes (Verpoorter et al., 2014), and wetlands (Prigent et al., 2001). These products are based on freely and openly available remote sensing data with a spatial resolution of 10 m or less. This resolution is more than sufficient to obtain a global overview. However, when focusing on changes that are smaller in size, a spatial resolution of 10 m means that some important features may not be detected. This is especially true for areas with a high spatial heterogeneity of different land cover classes. Slovenia is generally characterised by such spatial fragmentation (Foški, 2017; Hladnik, 2005). When analysing rivers specifically, areas close to the river's source are problematic because rivers are narrow and therefore difficult to detect on images with a coarser spatial resolution. To address the spatial resolution problem, we focused on sub-pixel mapping. Instead of assigning the entire pixel to a single class, the fraction maps created by sub-pixel mapping indicate the share of each pixel occupied by a particular land cover class. In this way, even features smaller than the spatial resolution of a given sensor can be detected and mapped.

There are already applications of sub-pixel mapping in hydrology. Many of them focus on delineating smaller features such as wetlands (Kamal and Phinn, 2011; Reschke and Hüttich, 2014) or sharp transitions such as coastline mapping (Bishop-Taylor et al., 2019; Liu et al., 2016). However, we applied the approach to mapping gravel bars in rivers. We focused on gravel bars that form above the water surface and are not overgrown with vegetation. Gravel bars are important features in the fluvial environment that provide many crucial ecosystem functions. They are dynamic features that change rapidly following changes in hydrological characteristics. Changes in water level lead to changes in gravel bar extent. When monitoring gravel bar changes it is therefore crucial to examine dates with similar hydrological conditions. Gravel bars in Slovenia are mapped through fieldwork or digitisation of aerial photographs (Ranfl, 2010). Field mapping is time-consuming and therefore allows harmonised observation only in a small area. Mapping based on aerial photographs provides high spatial resolution, but is limited by the execution of aerial surveys. In Slovenia, each location is systematically imaged by an aerial survey once every three to four years (Surveying and Mapping Authority of the Republic of Slovenia, 2015). Intermittent surveys are rare due to high financial costs. On the other hand, satellite images provide a simultaneous overview of a large area, a new image is available every few days, and the data can be freely available. Remote sensing data with frequently repeated observations are therefore well suited for monitoring gravel bars. However, gravel bars often occur as narrow forms and may be missed in whole or in part when mapped using satellite images with a coarser spatial resolution. Sub-pixel mapping can therefore make an important contribution to more accurate monitoring of gravel bars. Existing methods for gravel bar detection using EO are based on manual delineation of aerial orthophotos (Geodetic Institute of Slovenia, 2021) or satellite images (Serlet et al., 2018). However, our aim was to develop a method that is automated as much as possible.

Spectral mixture analysis (SMA) can be used to determine the degree of presence of different selected land cover classes within each pixel. This is done by comparing the spectral response of each pixel to the spectral responses of the endmembers representing pure pixels that contain only a single land cover class of interest. The spectral responses of the pixels can be augmented with spectral indices that increase the separability of the different land cover classes. The results of SMA are land cover fractions that provide sub-pixel mapping information.

We developed the method for monitoring gravel bars in a study area on the Soča river in Slovenia, for which many ancillary remote sensing and in situ data are available. These data were used as a reference for validating our results. The availability of reference data allowed us to observe and compare the influence of different variables on the final result. In this way, we were able to derive the main characteristics of the proposed method that can be transferred for the analysis of other areas. We also demonstrated the possibility and accuracy of such transfer with case studies on the Sava river in Slovenia and the Vjosa river in Albania. There are several similarities between the Soča, which was used for developing the method, and Sava and Vjosa, which were used to further extend and test the method. All of the examined rivers spring in young mountains of alpine orogeny. Due to steep slopes they have large potential energy. There is also a lot of material available for the rivers to erode. Therefore, all of the rivers carry extensive amounts of gravel with Vjosa being particularly well-known for its gravel deposits. Soča and Sava have similar average annual discharges of 80 m^3/s while that of Vjosa is slightly higher at 150 m^3/s. The rivers all have nivo-pluvial flow regimes with peaks in spring and autumn and lows in summer and winter.

Most existing applications of sub-pixel mapping focus on the analysis of a smaller number of timestamps with up to ten different satellite images. Gravel bars are features that are constantly changing, and therefore we monitored them using a time series approach. Additionally, satellite images are now available openly and freely, with a return period of less than a week and a commitment to maintain operational data provision (Berger et al., 2012; Masek et al., 2020; Woodcock et al., 2008). In relation to the time series approach, our analysis included several tests regarding the temporal component of monitoring, such as the transferability of endmembers, modelling vegetation at different phenological stages, and optimal smoothing of time series data to eliminate outliers but maintain meaningful discontinuities.

Several constraints must be considered when monitoring natural phenomena using EO. A key limitation for optical data is the obstruction of the Earth's surface by clouds and their shadows. This is particularly pressing when trying to determine changes immediately after heavy rain, as it is always necessary to wait for clear skies. A second limitation arises from the study's focus on narrow river valleys framed by steep, high slopes. These can be particularly problematic when the Sun incidence angles are low and

4

Stančič, L. 2022. Monitoring Changes of Fluvial Gravel Bars with Remote Sensing.
PhD Th. Ljubljana, UL FGG, Interdisciplinary doctoral study programme Environmental Protection.

topographic shadow obscures much of the area under observation. Another important point to consider relates to spectral signal analysis. The spectral properties of different land cover classes change seasonally, for example in the case of deciduous vegetation, and may also be the result of various physical factors, such as water, whose reflectance is affected by depth, turbidity, Sun glint, and other factors. Our study addresses many of these considerations using a variety of methods. Nevertheless, some of these issues remain as challenges for further research.

1.2   Research Hypotheses and Objectives

The aim of the study is to develop a method for monitoring gravel bars in rivers using EO data. Freely and openly available data are used, with selected very high resolution (VHR) data used for validation. We use sub-pixel mapping to obtain the highest level of mapping detail from the input satellite image. Three land cover classes are considered in the analysis: gravel, vegetation, and water. These have sufficiently different spectral properties to make the use of a SMA possible and meaningful. We test different configurations to produce the most accurate fraction maps possible. These maps are then used to monitor gravel bars and detect changes.

The doctoral dissertation examines the following two hypotheses.

Hypothesis 1: Using spectral mixture analysis, it is possible to distinguish gravel bars, surface water, and vegetation in fluvial ecosystems.
Sub-hypothesis 1.1: The land cover of fluvial ecosystems can be determined with a thematic accuracy of 90% by analysing the spectral signal composition of freely available satellite images with a spatial resolution of up to 10 m.

We test the assumption that SMA can be used to accurately map the land cover classes of interest. Different configurations are tested to determine those that lead to the highest accuracy of the resulting fraction maps. We examine the influence of the input images applied for the SMA, including the type of remote sensing system used for acquisition, geometric and radiometric accuracy, spatial resolution, and use of spectral indices. The tests also focus on the characteristics of the endmembers used for SMA – the possibility to automatically select accurate and appropriate endmembers, the optimal number of endmembers considered, the addition of shade as an endmember, and the transferability of endmembers between different images.

The accuracy of the resulting fraction maps is verified both at the pixel level and at the level of the entire study area to account for geometric shifts of the input images. Visual interpretation of aerial orthophotos and field mapping are used as reference data for pixel-level validation. In the study area-level validation, we compare the results based on manual delineation and different land cover classifications based on

machine learning. Aerial orthophotos and VHR satellite images are used as input data to produce reference classifications. Finally, we compare the fraction maps resulting from the soft classification with maps obtained by a hard classification based on the spectral angle mapping approach to investigate the contribution of sub-pixel mapping for monitoring gravel bars.

If we can confirm the proposed Hypothesis 1 and Sub-hypothesis 1.1, we may conclude that SMA can be used for sub-pixel mapping of fluvial gravel bars. Therefore, the confirmation would allow us to proceed with the use of the proposed method for monitoring and change detection.

Hypothesis 2: Time series analysis of sub-pixel land cover maps allows the detection of seasonal changes in the extent and location of gravel bars.
Sub-hypothesis 2.1: In addition to seasonal dynamics, changes in the extent of gravel bars due to exceptional anthropogenic and natural events larger than 500 m^2 can also be detected.

After successfully developing a sub-pixel mapping method, we test its application on a time series of satellite images to monitor changes. The variability of the extent and location of gravel bars can be a result of anthropogenic interventions such as in-channel mining and building infrastructure in the riparian area. Changes can also be due to natural hydromorphological processes in the river channel. Additionally, there are seasonal variations in the extent of gravel bars due to seasonal changes in discharge. An increased discharge can lead to gravel bar flooding and thus also a change in the location of above-water areas of bedload deposits. These seasonal changes are not the prime focus of our study as they do not represent real displacement of gravel bars. Nevertheless, we monitored the seasonality of the variability of gravel bar presence to enable the detection of real changes caused by exceptional events.

We analyse the annual seasonality of gravel bar presence by examining all available Sentinel-2 images within the period 2019-2020. Different aspects of time series development are considered, including endmember selection, vegetation modelling at different phenological stages, and temporal smoothing of the resulting land cover presences. The validity of the resulting time series data is verified by comparison with hydrological data measured in situ at a gauging station. Next, we demonstrate the ability to make comparisons between different years and satellite sensors by producing fraction maps of gravel presence for three different rivers with a total combined length of over 250 km and observing a time span of over 30 years using Sentinel-2 and Landsat images. Finally, we test the ability of the proposed method to detect changes in gravel bars. Both the precision and sensitivity of change detection based on fraction maps are verified using VHR reference data. We also studied the possibility of monitoring gravel bars using time series data by observing how known changes manifest themselves on land cover presence plots.

6

Stančič, L. 2022. Monitoring Changes of Fluvial Gravel Bars with Remote Sensing.
PhD Th. Ljubljana, UL FGG, Interdisciplinary doctoral study programme Environmental Protection.

The confirmation of Hypothesis 2 and Sub-hypothesis 2.1 would allow the proposed sub-pixel mapping method to be recommended for monitoring changes in fluvial gravel bars.

We set the following research objectives to reach the aim of the study and verify the proposed hypotheses:
- study and summarise the characteristics of the processes driving gravel bar formation and changes,
- define the reference data and the validation method for an accuracy assessment of the gravel bar maps produced,
- analyse the characteristics of openly and freely available input satellite images that affect the accuracy of fraction maps and select the optimal settings that result in the best products,
- test and validate different strategies for selecting endmembers required for the SMA,
- produce fraction maps of the fluvial environment based on the SMA and compare them to the results of a hard classification performed with the same input data,
- develop a time series of land cover presence in the fluvial environment based on the created fraction maps,
- produce fraction maps of gravel presence for several hundreds of kilometres of rivers and over a time period of several decades, and
- assess the ability of fraction maps to detect changes in gravel bars, both by comparing two timestamps and by observing a time series of presence data.

The expected results of different tests combined with validation will provide new insights into the potential of using EO data to monitor the natural environment. The use of EO data that covers large areas at the same time allows the method to be deployed over a larger area simultaneously. This can overcome technical and logistical limitations often associated with field monitoring methods. In addition, EO data enables a faster detection of changes. The focus of the dissertation is on gravel bars, but the findings could also apply to other small and dynamic features with a distinct spectral response. We develop a pioneering process of sub-pixel mapping for change detection in gravel bars by adapting, augmenting, and improving existing SMA approaches. The developed method enables more accurate monitoring of the ecologically and socially important ecosystem. The results of the process and new insights into algorithm development will be useful to apply the method to other land cover classes in different ecosystems for various purposes in the future. The expected results enable more accurate mapping and conservation of areas characterised by high spatial fragmentation, such as mountainous areas, as the developed method allows the detection of changes that would not be noticeable with input EO data due to their spatial resolution. By testing the method in a study area where many reference data are available, we aim to develop a workflow that can be applied to other locations with a lower

abundance of data. In this way, we hope to contribute to a wider use of EO data for better monitoring and understanding of the processes on the Earth's surface.

In addition to technical and applied considerations, the dissertation includes findings from a variety of disciplines, including geodesy, geography, and hydrology, with the goal to strive towards interdisciplinarity, and wide dissemination of findings about the benefits of remote sensing. With the geographical approach of a holistic view of space, we work to bridge the gap between technical sciences, natural sciences, and humanities.

1.3   Dissertation Structure

The dissertation has five chapters.

The first (this) chapter is introductory and contains the definition of the research problem, the statement of the aim of the dissertation, the hypotheses, the objectives, and the expected results, and concludes with an overview of the structure of the dissertation.

The second chapter summarises the existing literature that forms the basis for the dissertation. The first part focuses on gravel bars, the geomorphological processes that form them, the different types and shapes of gravel bars, and their role in the wider fluvial system. The second part concerns the selected method for mapping gravel bars – the SMA. The development of the method is presented, followed by a description of the processes, assumptions, and formulations associated with the method. The characteristics of endmember selection and spectral unmixing, which are the main steps of SMA, are outlined.

The third chapter is central to the dissertation as it describes the tests that were performed to develop the workflow that results in the most accurate gravel bar maps. The tests are conducted by mapping a selected study area on the Soča river in Slovenia, where the river is narrow and there are many gravel bars. First, the data and materials used to produce gravel bar maps are described. Second, the validation method applied to compare the different fraction maps is defined. Third, the optimal characteristics necessary for the input satellite images are determined. Next, we test the different methods and settings for selecting endmembers. Then, land cover fraction maps are developed and compared with the results of hard land cover classification using the same inputs. Finally, we produce a time series of land cover presence based on the proposed fraction mapping method.

In the fourth chapter, the potential of applying the proposed method for monitoring gravel bars is evaluated. Gravel bar maps are produced for more extensive river sections that span several hundred kilometres. We test the ability of the proposed gravel bar monitoring method to detect changes in various

aspects, including its sensitivity and precision. We also evaluate the detection of change using a comparison of selected fraction maps as well as time series plots of gravel presence. The results from the fraction maps are also compared with in situ measurements from gauging stations.

The fifth and final chapter discusses the results and verifies the proposed research hypotheses. The dissertation is evaluated in terms of its wider context and contribution to science. Identified limitations of the proposed method and possible solutions are described. In conclusion, opportunities for further research and applications are outlined.

Stančič, L. 2022. Monitoring Changes of Fluvial Gravel Bars with Remote Sensing.
PhD Th. Ljubljana, UL FGG, Interdisciplinary doctoral study programme Environmental Protection.

9

2 THEORETICAL BACKGROUND

This chapter presents the main concepts related to the motivation for the thematic application, as well as the background of the method chosen to achieve fluvial gravel bars monitoring. In terms of thematic consideration, fluvial gravel bars are described, including the geomorphological processes that form them, the patterns of their formation, and their role in the larger river system. The second part of the chapter describes the method proposed for mapping and monitoring gravel bars in narrow rivers – spectral mixture analysis (SMA). The theoretical framework of the main method components and the associated terminology are outlined.

2.1 Characteristics of Fluvial Gravel Bars

Gravel bars are areas of temporary sediment deposition in riverbeds (Robert, 2003). They are interesting from both a hydromorphological and ecological perspective. Fluvial gravel bars are classified as habitat types that should be maintained in a favourable condition as a matter of priority according to the European Habitats Directive (EC DG ENVIRONMENT, 2013; OJ L 206, 1992). In Slovenia, their importance for environmental conservation was adopted by the Decree on Habitat Types (Official Gazette of the Republic of Slovenia, No. 112/03, 2003). Gravel bars are dynamic and unstable habitats that are sensitive to hydrological changes and as such are good indicators of disturbances in the fluvial environment (Kiss and Andrasi, 2014). They play a role in water filtration, groundwater infiltration, mitigation of river bank erosion, and in increasing the river's attractiveness for recreation (Robert, 2003). Moreover, as contact areas between water and land, they represent an important habitat type with high species diversity and the occurrence of rare species (Langhans and Tockner, 2014; Zeng et al., 2015). In Slovenia, several animal species, such as the birds little ringed plover (*Charadrius dubius*) and common tern (*Sterna hirundo*), and plant species, such as *Chondrilla chondrilloides*, are closely associated with gravel bars (Richards, 1990; Snow and Perrins, 1998; Geršič, 2010). Vegetation sampling on gravel bars in Slovenia demonstrated the high diversity of species and communities that develop in such habitats (Škornik et al., 2016). The notably high vegetation complexity is caused by variable flood disturbance and changing soil properties. These findings highlighted the importance of preserving gravel bars as an integral part of functioning fluvial ecosystems (Škornik et al., 2017). Almost 2,300 ha of gravel bars in Slovenia have been identified as potential habitat areas of European importance (Jogan et al., 2004).

The existence of gravel bars is threatened due to in-channel mining (Jogan et al., 2004; Klaneček et al., 2005). In addition to material extraction, the extent of gravel bars is also influenced by other human activities, such as the construction of hydropower plants, gravel retention systems, and flood control measures (Geršič, 2010). Major interventions in the river environment, such as the construction of dams, disturb the balance between inflow and outflow of sediments. Planned removal, excavation, and

emptying of sediments from the river channel is necessary in some places due to deposition (Nistor et al., 2021; Ranfl, 2010). Decades of studies on impounded rivers have shown that hydropower operations result in numerous morphological changes downstream from the dam, including widening of the riverbed, reduction in the number of rapids and pools, increase in gravel bars and islands, and increase in bedrock outcrops in the riverbed. Daily water discharges result in the removal of finer particles. Fewer meanders and sequences of rapids and pools reduce the riverbed roughness and increase the carrying capacity of the river, i.e. its ability to transport sediments (Assani and Petit, 2004).

2.1.1 Geomorphological Processes of Fluvial Sedimentation

River channels consist of the riverbed, which is permanently or temporally covered with water at normal discharge, and river banks, which are the sloping land on the edges of the river channel (Mikoš et al., 2002a; Szoszkiewicz et al., 2020). Rivers are constantly reshaping their channels. High waters have the largest influence on river channel changes. During high water periods, geomorphological processes (erosion, transport, and sedimentation) occur with the highest intensity. Erosion actively transforms the riverbed, sediments are then transported, and subsequent sedimentation transforms the riverbed passively (Ranfl, 2010). Erosion can occur by downcutting when the river deepens its own bed, or laterally by wearing away of the outer river banks in bends. Sediment transport in the river occurs in solution, in suspension, or by traction or saltation along the riverbed. Minerals, dissolved in water as it percolates through the soil, are transported in solution. Particles of clay, silt, and sand are transported in suspension as suspended load. The largest proportion of sediment is usually transported in suspension. The deposition of suspended load forms sand bars in the lower river courses (Strahler and Strahler, 2005). Larger, more rounded, and heavier sediments are transported along the bottom of the riverbed by bouncing, sliding, and rolling. These are known as bedload and are key for the development of gravel bars (Geršič et al., 2014). The amount of transported sediment depends on river discharge and flow velocity. The carrying capacity of the river increases with the square of its flow velocity (Tarbuck and Lutgens, 2005). Thus, a higher carrying capacity can be achieved by a faster flow velocity, a higher discharge, a steeper gradient, finer material, a narrower riverbed, and a steeper river bank slope (Robert, 2003).

The geomorphological processes that occur in a given river section depend on the relationship between the carrying capacity of the river and the amount of sediment present. When the carrying capacity is larger than the sediment amount, the riverbed is deepening. When the two quantities are balanced, an equilibrium river section is formed. When the sediment amount is larger than the carrying capacity, deposition occurs (Ranfl, 2010).
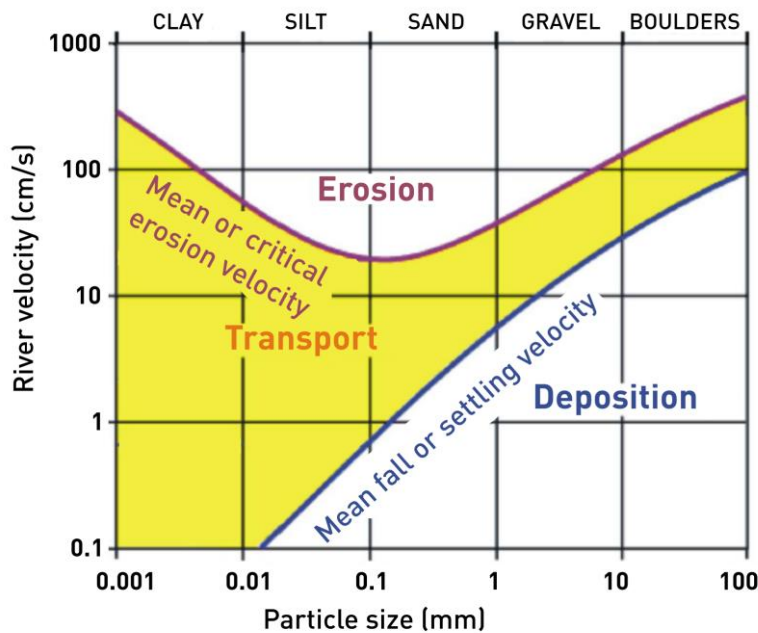
Figure 1: Hjulström's diagram of fluvial geomorphological processes (source: Geršič, 2010; Nichols, 2009).
Slika 1: Hjulströmov diagram rečnih geomorfoloških procesov (vir: Geršič, 2010; Nichols, 2009).

The relationships between particle erosion, transport, and deposition are shown in the Hjulström diagram (Figure 1). Depending on the relationship between water flow velocity and particle size, the diagram shows the critical erosion velocity curve and the average fall or settling velocity curve. The areas between the curves represent different geomorphological processes (Nichols, 2009).

The carrying capacity of a river can be calculated from average annual discharge duration, slope at the riverbed bottom, width of the riverbed bottom, slope of the bank cross-sections, and mean sediment grain size (Mikoš et al., 2002b). The average annual discharge duration curve is obtained by arranging the chronologically sorted hydrological data on discharges from the hydrogram by size. Data on mean sediment grain size are obtained by analysing the grain size of sediments from samples collected in situ (Ranfl, 2010).

2.1.2   Gravel Bar Formation

To develop a method for gravel bar mapping it is necessary to understand the processes of gravel bar formation in order to know where in the river bed gravel bars can be expected. Even more importantly, the dynamics help to explain the patterns of their disintegration and re-establishment. This is key for successful monitoring and accurate interpretation of results. Robert (2003) distinguishes between different gravel bar types based on the processes that formed them. Accordingly, gravel bar types are divided into two main categories – unit and complex bars. Complex bars are formed in successive

periods of erosion and deposition. Unit bars are formed only by deposition and have a stable morphology. Longitudinal, transverse, point, and diagonal bars are different types of unit bars. In complex settings, it is difficult to make a clear classification because the bars are formed by different combinations of processes. In the case of complex gravel bars, we can distinguish all the above forms as well as the medial and lateral bars (Figure 2). In addition to the classification according to the formation processes, it is also common to classify gravel bars according to their position in the riverbed. In this respect, there are two main types of fluvial gravel bars. The first type includes bars that form in the middle of the riverbed. The second type consists of bars along the river bank. Despite different specific classifications, it should be noted that one bar type can be transformed into another over time (Robert, 2003).
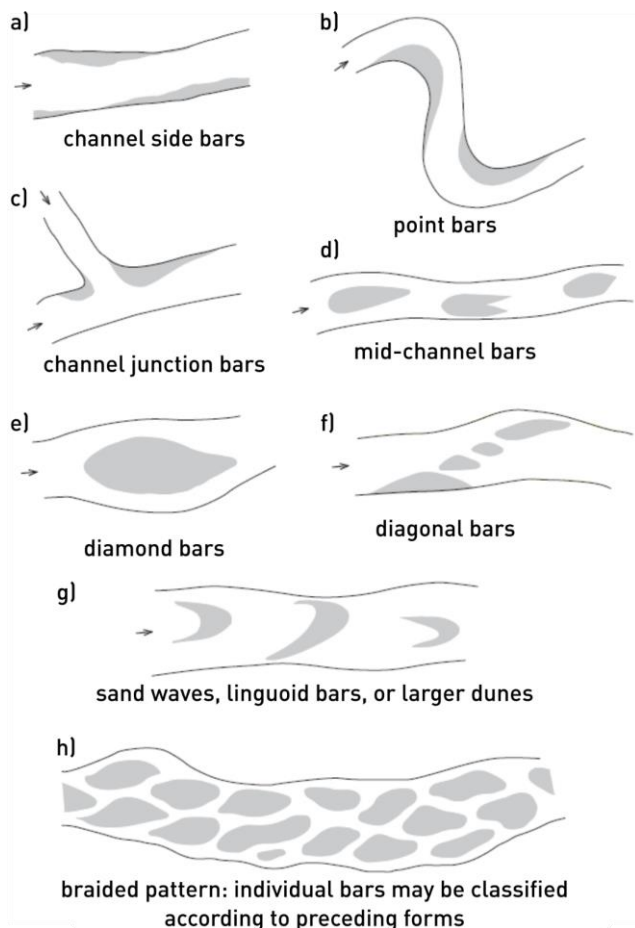
Figure 2: Fluvial gravel bar types (source: Robert, 2003).

Slika 2: Tipi rečnih prodišč (vir: Robert, 2003).

The main reason for gravel bar formation is a local reduction in the carrying capacity of a river. This often occurs in the inner part of river bends, where friction losses lead to a reduction in flow velocity and thus to a smaller carrying capacity. As a result of the reduced carrying capacity, sediment deposition

occurs. The deposited sediments cause further friction, and so the sedimentation process continues (Tarbuck and Lutgens, 2005).

Gravel bars can also form in the middle of the river channel. Where the shear force is close to the critical force for particle displacement, patches of bedload sediment pushed along the bottom of the riverbed may begin to deposit. In the first stage of gravel bar formation, coarser bedload material is deposited in the area between individual river flows with higher carrying capacities. Later, finer material is deposited behind larger particles in these areas of lower carrying capacity. Other sediments that are being pushed along the riverbed bottom continue to accumulate on these areas of deposition, causing the gravel bar to grow in width and length (Robert, 2003). Due to the resulting hydro-morphological feature, the river flow is divided into two parts (Kiss and Balogh, 2015).

The described deposition in the form of a mid-channel gravel bar is one of the formation mechanisms of branched or braided streams. A second characteristic mechanism is the transition of a transverse gravel bar to a mid-channel bar, also under the influence of sediment patches pushed along the riverbed. Additionally, braided streams may develop through processes of erosion. When a gravel bar is dissected, a new river channel is formed by erosion of a side bar. Another erosional process in river braiding is the disintegration of bars into a network of channels with intermediate bars due to deposition in the form of characteristic sedimentary tongues (Figure 3). There are two other important braiding processes. The first is the formation of successive straight and narrow chutes and downstream deposits in the form of lobes. The last important branching process is the relatively sudden switching of river flow from one channel to another (Robert, 2003).
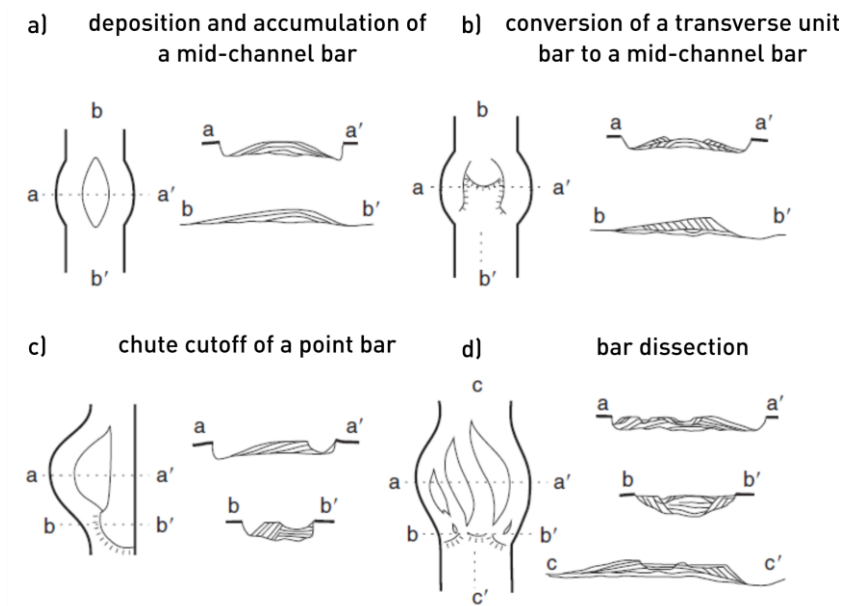
Figure 3: Braiding processes and depositional morphology (source: Robert, 2003).

Slika 3: Procesi razvejanja in morfologija odlaganja delcev (vir: Robert, 2003).

Gravel bars are normally part of the riverbed. The height of gravel bars is usually lower than the height of the top of the river channel. As the height of gravel bars increases and they are covered by permanent vegetation, gravel bars can develop into fluvial islands. These represent more stable features as they are not removed by regular floods (Kiss and Andrasi, 2014). Despite the different names, gravel bars and fluvial islands are features with similar origins and morphological characteristics (Robert, 2003).

2.1.3   The Role of Gravel Bars in the Fluvial Gravel Regime

The shape of gravel bars and the size of deposited particles depend on the average slope of the riverbed and the river discharge. Sediments at the bottom of the riverbed can be divided in two layers – an upper and a subsurface layer. The upper layer has a coarser particle composition because river flow washes out the finer particles, while the coarser particles remain in place because of their weight. Generally, particles of similar size to those already present at the riverbed bottom remain in place. Thus, the largest particles are deposited in erosion pools, coarser material in gravel bar heads, and finer material at bar edges. The reason for the removal of particles that have a different size structure than those already present is the turbulence of the river flow. Turbulence is low in the pools, then increases until the head of the bar and remains high until the next pool. Large deposited particles on the bar head increase turbulence, reducing the likelihood of smaller particles being deposited near them (Robert, 2003). The diversity of sediment sizes decreases in lower river reaches (Ranfl, 2010).
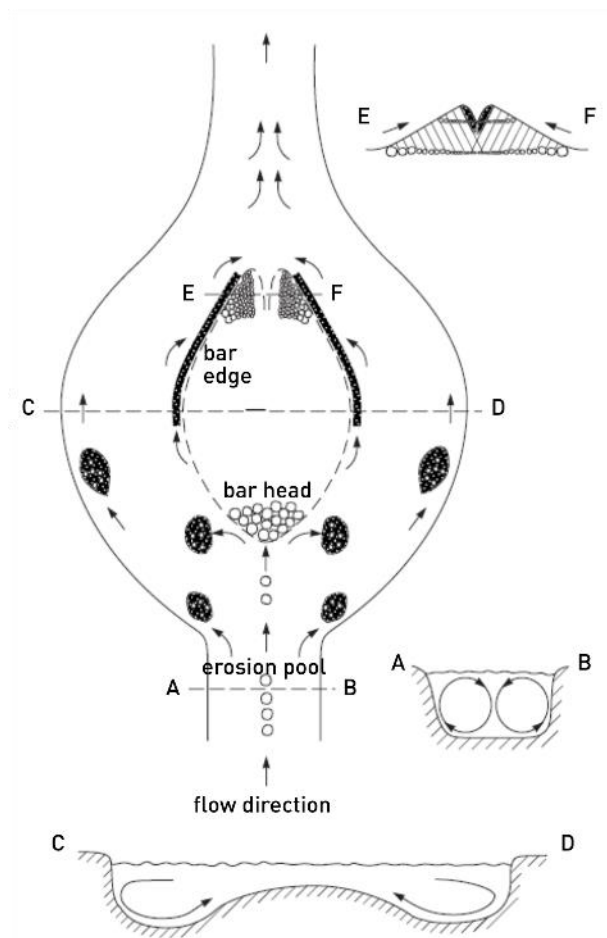
Figure 4: Model of secondary flows, sediment sorting, and downstream deposition of finer particles in a gravel bar. The arrows on the image of the gravel bar indicate the direction of bedload transport. The arrows on the cross-sections indicate the flow direction and secondary circulation (source: Robert, 2003).

Slika 4: Model sekundarnega toka, sortiranja sedimentov in dolvodnega odlaganja drobnejših delcev na prodišču. Puščice na sliki prodišča prikazujejo smer rinjenih plavin. Puščice na prečnih prerezih prikazujejo smer toka in sekundarni tok (vir: Robert, 2003).

Based on several sources, Robert (2003) notes that the patterns of flow and deposition of particles in channels along the central bars are similar to those in individual meandering riverbeds. In bends, the water flow is moved towards the outer bank under the influence of centrifugal force. This leads to an increase in water level in the outer part of the riverbed, especially in fast flows and sharp bends. Due to the locally unbalanced forces of gradient and gravity, a secondary flow is formed. At the water surface, the secondary flow runs towards the outer bank, while at the bottom of the riverbed it flows towards the inner bank. Gravel bars form and grow on the inner part of the bend (Figure 4).

The highest carrying capacity of a river is at peak discharge. As discharge increases, material is removed from upstream parts of gravel bars, and as discharge decreases, material begins to be deposited. At the topographically highest parts of gravel bars, reverse processes occur – deposition when discharge is high

and erosion when discharge is low. Although the particular material that makes up gravel bars is changed at higher discharges, the location of bars in the riverbed usually does not change (Robert, 2003).

Gravel bars are typical features of braided rivers. Gravel bar head consists of shallow rapids which have a higher gradient and roughness in a general area of lower gradient. Rapids form across the riverbed as water flows over larger rocks. In an area of rapids, the river flow is shallow and fast. The basic unit of braided rivers is the pool, which is located upstream of the gravel bar. The pool is a larger depression in the riverbed bottom where the river flow slows down (Ranfl, 2010). Some authors also consider the combination of a pool and gravel bar as the basic unit of a riverbed. In braided rivers, pool and bar units line up next to each other in parallel rows. The sequence of pools and bars forms the third basic unit of braided streams, namely a series of river confluences and bifurcations (Robert, 2003).

The number, location, shape, composition, and size of gravel bars indicate the geomorphological processes occurring in the river channel. Gravel bars are also very dynamic features that can be easily and rapidly changed. They are therefore good indicators of alterations in the fluvial environment. Gravel bars that form above the river flow surface can be observed with optical remote sensing. The wide availability of free and open satellite images allows rapid detection of changes in gravel bars and monitoring of associated processes.

2.2   Spectral Mixture Analysis

To enable the use of free and open data for monitoring narrow rivers in mountainous environments, a land cover fraction mapping method, based on the spectral mixture analysis (SMA) is proposed. The origins, main concepts, and existing applications of SMA are presented in the next chapters.

The SMA can mitigate mapping limitations associated with the spatial resolution of satellite images (Atkinson, 2005; Foody et al., 2005). With SMA, it is possible to perform thematic mapping at sub-pixel level by determining the proportion of selected land cover classes in each pixel (e.g., Ling et al., 2016; Mylona et al., 2018). This is done by comparing the spectral signature of each pixel with those of the selected land cover classes of interest. The spectral signatures of the target land cover classes are therefore key information for the SMA. Pure pixels that contain only one land cover class and represent the extreme points in spectral space are referred to as endmembers (Keshava, 2003; Somers et al., 2011; Veganzones and Graña, 2008).

The original purpose for developing SMA was to observe rock surface and mineral composition on Mars (Adams et al., 1986). The method has since been used for various objectives, including land cover mapping (Ling et al., 2016), forest disturbance detection (Hirschmugl et al., 2014), determining land cover fractions in urban areas (Kärdi, 2007; Priem et al., 2019), monitoring urban expansion (Aina et

al., 2019), soil degradation monitoring (Dubovyk et al., 2015), grassland monitoring (Shao et al., 2018), river bank mapping (Niroumand-Jadidi and Vitti, 2017), and coastline mapping (Foody et al., 2005; Muslim et al., 2007). Both hyperspectral (Keshava, 2003; Somers et al., 2011) and multispectral images have been analysed with SMA, including images acquired by Landsat (Wu, 2004) and Sentinel-2 (Mylona et al., 2018) that were used in this study.

2.2.1   Endmember Selection

Several methods for selecting (also known as extracting) endmembers have been proposed. Both the number and the spectral properties of endmembers have to be selected. Determining the sufficient number of endmembers to correctly describe the variability in a scene usually involves testing different configurations and selecting the one that yields the smallest error (Somers et al., 2011). Endmember spectral signatures can be obtained from available spectral libraries, created using laboratory or field measurements with spectro-radiometers (Schmidt and Scarth, 2009). Alternatively, endmembers can be selected from image pixels themselves. However, this is only possible if the land cover types in the analysed image occur in such a formation that pure pixels are present. If all pixels are mixed, non-pixel endmembers can be estimated based on the image data (Du, 2018).

We used the N-FINDR algorithm for automatic selection of image endmembers. It is an established method that has been shown to be effective in finding distinctive pixels (Du, 2018). The algorithm determines the endmembers by searching for the user-defined number of pixels which form the extremities of a geometric body with the largest volume in the multidimensional space defined by the number of input image bands.
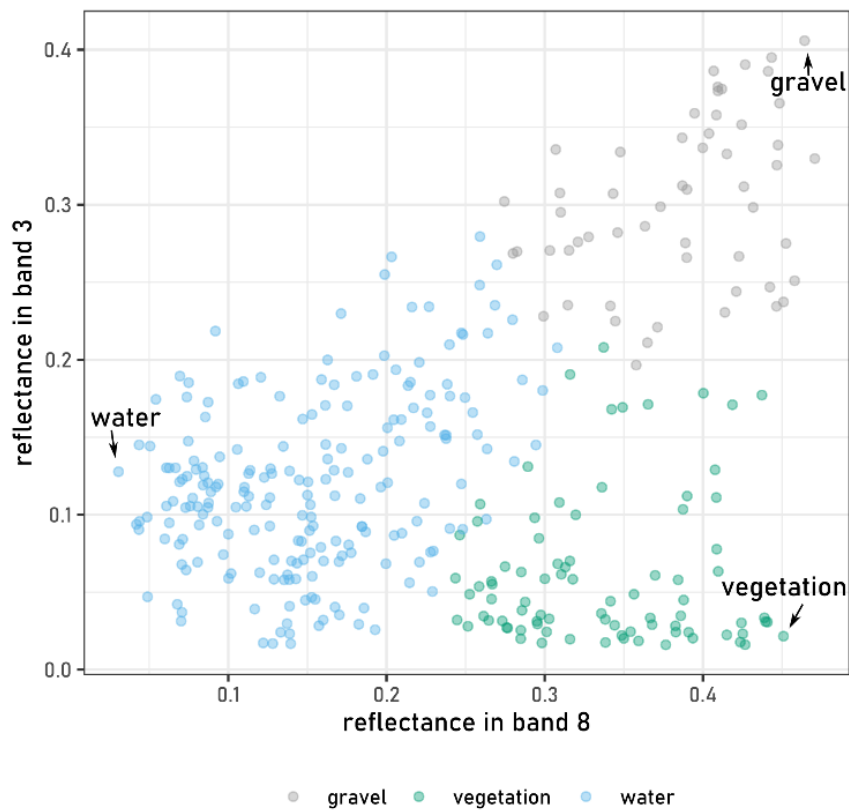
Figure 5: An example of endmembers selected as extreme points in a three-dimensional spectral space.

Slika 5: Primer končnih pikslov, izbranih kot skrajne točke v trodimenzijskem spektralnem prostoru.

To begin with, a random set of pixels is selected and the volume of the geometric body that they outline is calculated (Figure 5). Then, one of the pixels is swapped with a different new pixel and the volume of the newly formed geometric body is calculated. If the new volume is larger than the previous volume, the first pixel is replaced by the second pixel as a potential endmember. This process continues until no more pixels can be exchanged (Winter, 1999).

2.2.2   Spectral Unmixing

The SMA works by modelling the reflectances of mixed pixels. The method converts the reflectance in a satellite image to fractions (also known as abundances) of the selected land cover classes using information about the spectral characteristics of endmembers, i.e., the spectral representations of pure land cover classes. The methods of modelling can be divided into linear and nonlinear. The choice of the model reflects the expected mechanism of spectral signal mixing in the analysed image. Linear mixing occurs when different land cover classes exist in a spatially bounded formation. The key physical assumption of linear SMA is that each incoming photon reacts with only one land cover type. Conversely, nonlinear mixing occurs where different materials are closely intertwined. In such cases, spectral signal mixing is more complex because each single incoming photon reacts with numerous

different land cover types resulting in multiple scattering effect (Keshava, 2003; Keshava and Mustard, 2002).

Nonlinear mixing often occurs in analysis of sand or soil when many different materials appear very close together. Simplifications and assumptions are often necessary to enable nonlinear mixture modelling. The bilinear model is commonly used with the assumption that the product of two or more endmembers represent the multiple scattering effect. If we consider p endmembers and only take into account scattering between two endmembers a signature matrix M_{NL} can be defined as [m_1, m_2, ..., m_p, $m_1 m_2$, ..., $m_{p-1} m_p$]. A pixel vector r can then be expressed as (Du, 2018):

$$r = M_{NL} \propto_{NL} + \varepsilon \tag{1}$$

with $\propto_{NL}$ representing an abundance vector combining linear and nonlinear abundances. Subsequently, an ordinary least squares solver can be applied to estimate $\propto_{NL}$ (Dobigeon et al., 2014; Heylen et al., 2014).

However, in modelling land cover, linear spectral mixing is considered more often as the different land cover classes are not as intermixed as for example different materials in soil. In line with the assumptions of linear spectral mixing, the mixed pixel signal (r) can be described as a combination of endmember spectral signals, weighted by sub-pixel land cover presence. The model is therefore described as follows (Adams et al., 1986; Somers et al., 2011):

$$r = Mf + \varepsilon \tag{2}$$

where M is an array with columns representing the spectral signatures of selected endmembers, f is a vector of land cover presence fractions, and ε is noise or signal fraction that cannot be modelled with the selected endmembers.

The described equation can be solved if the spectral signals of endmembers are known and the number of endmembers is less than the number of spectral bands in the analysed image. Commonly used equation solvers are quadratic programming, maximum likelihood method, and least squares method. The SMA can be applied without constraints, but to obtain physically meaningful results, the coefficient values in Equation (2 are often restricted to positive numbers. An additional condition that can be implemented is that the sum of the coefficients must equal one. When the outlined conditions are applied, the resulting SMA can be described as fully constrained (Somers et al., 2011).

After establishing the theoretical background related to the geomorphological features under observation – fluvial gravel bars – this chapter provided an overview of the method proposed for monitoring. The method development, the key steps, and examples of existing applications were presented. The next chapter describes the main tests and decisions made in relation to the development of an SMA-based method for gravel bar monitoring.

3   METHODS

The chapter describes the process of selecting the most appropriate method for mapping gravel bars with SMA. Characteristics of input satellite images and reference data are presented first. Next, the validation process for comparing different methods is explained. Then, the most optimal characteristics of input satellite images are chosen, followed by an overview of the endmember selection process. The resulting soft classification using SMA is then compared to the results of a hard classification. The chapter concludes with a description of tests associated with the development of a land cover time series.

```
┌─────────────────────────────────┐
│           METHODS               │
└─────────────────────────────────┘
  │
  ├──▶ ┌─────────────────────────────────────────────┐
  │    │ 1. description of input data                │
  │    └─────────────────────────────────────────────┘
  │
  ├──▶ ┌─────────────────────────────────────────────┐
  │    │ 2. definition of validation method          │
  │    └─────────────────────────────────────────────┘
  │
  ├──▶ ┌─────────────────────────────────────────────┐
  │    │ 3. determination of input satellite image characteristics │
  │    └─────────────────────────────────────────────┘
  │
  ├──▶ ┌─────────────────────────────────────────────┐
  │    │ 4. definition of endmember selection method  │
  │    └─────────────────────────────────────────────┘
  │
  ├──▶ ┌─────────────────────────────────────────────┐
  │    │ 5. production of land cover fraction maps     │
  │    └─────────────────────────────────────────────┘
  │
  └──▶ ┌─────────────────────────────────────────────┐
       │ 6. development of time series of land cover presence │
       └─────────────────────────────────────────────┘
```
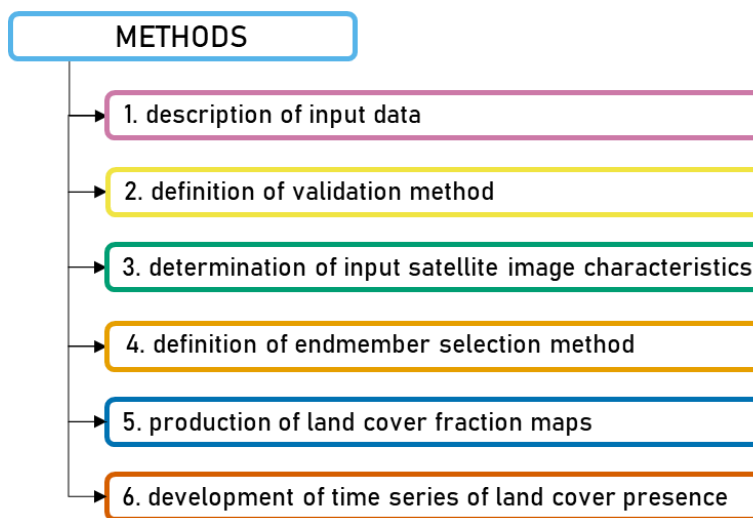
3.1   Data and Materials

Fluvial gravel bar mapping was performed using Landsat and Sentinel-2 optical satellite images. Additionally, a vector layer of water lands was used to delineate the area of analysis. Finally, WorldView-2 and Pléiades very high resolution images along with areal orthophotos were used for validation. A detailed description of the data used is given below.

3.1.1   Input Satellite Images

Passive Landsat and Sentinel-2 optical satellite images were used as input data. Landsat is a system of the United States Geological Survey (USGS) that has been in operation since 1972 (Barsi et al., 2014; Wulder et al., 2019). Gravel bars can be mapped with images acquired by the Thematic Mapper (TM)[1],

---

[1] The TM sensor was carried on board Landsat 4, which was operating from 1982 until 2001, and Landsat 5, which was operating from 1984 until 2013.

the Enhanced Thematic Mapper Plus (ETM +)[2], and the Operational Land Imager (OLI)[3] sensors. Since 1982, Landsat has been providing images with a spatial resolution of 30 m and a temporal resolution of 16 days. The images consisted of seven bands until the launch of Landsat 7 with the ETM+ which introduced the additional panchromatic band. From 2013 onwards, OLI and the Thermal Infrared Sensor (TIRS) enable sensing in three additional bands (coastal aerosol, cirrus, and additional thermal band), bringing the total number of bands in Landsat images to eleven.

The Sentinel-2 system is operated by the European Space Agency (ESA) for the European Commission. Sentinel-2 images acquired with the Multi-Spectral Instrument (MSI) sensor have spectral characteristics that are similar to Landsat; Sentinel-2 acquires images in 13 comparable spectral bands (Table 1, Figure 6). The images have spatial resolutions of 10 m, 20 m, or 60 m, depending on the spectral band. The first satellite – Sentinel-2A – was launched in June 2015 and the second – Sentinel-2B – in March 2017, increasing the temporal resolution of the system at the equator from ten to five days (Drusch et al., 2012; Gatti and Galoppo, 2018).

Table 1: Characteristics of the sensors acquiring images used in the analysis (source: Drusch et al., 2012, Barsi et al., 2014, Gatti and Galoppo, 2018).

Preglednica 1: Značilnosti senzorjev, ki so zajeli posnetke, uporabljene v analizi (vir: Drusch in sod., 2012, Barsi in sod., 2014, Gatti in Galoppo, 2018).

sensor	Sentinel-2 MSI			Landsat 7 ETM+			Landsat 8 OLI		
name	band	central wavelength (nm)	spatial resolution (m)	band	central wavelength (nm)	spatial resolution (m)	band	central wavelength (nm)	spatial resolution (m)
coastal aerosol	B1	443	60				B1	443	30
blue	B2	490	10	B1	483	30	B2	483	30
green	B3	560	10	B2	565	30	B3	563	30
red	B4	665	10	B3	660	30	B4	655	30
pan				B8	710	15	B8	590	15
red edge 1	B5	705	20						
red edge 2	B6	740	20						
red edge 3	B7	783	20						
NIR 1	B8	842	10	B4	838	30	B5	865	30
NIR 2	B8A	865	20						
water vapour	B9	945	60						
cirrus	B10	1 375	60				B9	1 375	30
SWIR 1	B11	1 610	20	B5	1 650	30	B6	1 650	30
SWIR 2	B12	2 190	20	B7	2 220	30	B7	2 200	30

---

[2] The ETM+ sensor is carried on board Landsat 7, which has been operating since 1999 until present. The scan line corrector of the sensor failed in 2003 resulting in approximately 25% data loss for any given scene.

[3] The OLI sensor is carried on board Landsat 8, which has been operating since 2013 until present.
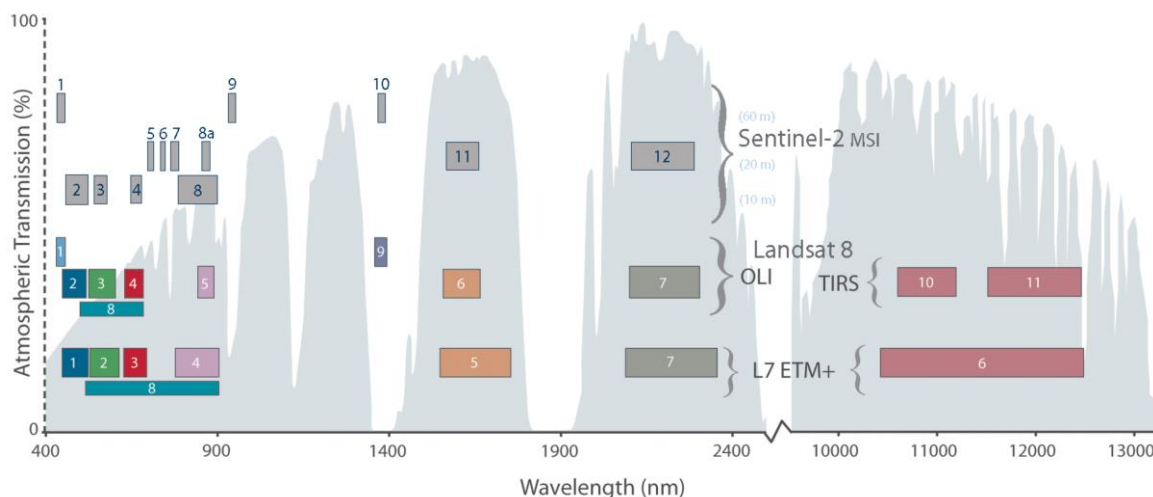
Figure 6: Spectral bands of Landsat 7, Landsat 8, and Sentinel-2 (source: NASA, 2015).

Slika 6: Spektralni kanali Landsat 7, Landsat 8 in Sentinel-2 (vir: NASA, 2015).

3.1.2   Water Cadastre

The Water Lands dataset from the Water Cadastre maintained by the Slovenian Water Agency was selected to focus our observation area on riparian zones (Slovenian Water Agency, 2021a). Water lands of inland running waters comprise the riverbed up to the first significant geomorphological transition. River banks and active gravel bars are therefore included in the analysis. The dataset was developed in accordance with the Water Act (Official Gazette of the Republic of Slovenia, No. 67/02, 2002) and is based on the map of surface waters. During a pilot study in 2011, surface waters were mapped on 10% of the area of Slovenia that included the larger river valleys. The approach was based on stereorestitution from cyclic aerial photography of Slovenia (CAS). The main challenge in the pilot approach was the detection of water surfaces under canopy, especially because CAS is conducted during the leaves-on period due to the requirements of agriculture monitoring. Aerial laser scanning (ALS) data acquired during a pilot campaign in 2011 provided a new source for mapping surface water, so the mapping method was updated in 2012. The final method used stereo pairs of the latest CAS images as the basis for data collection, with ALS acquired in 2014 and 2015 and derived products supporting interpretation and mapping in forested areas. In 2015 and 2016, surface waters on the remaining 90% of Slovenia were mapped using this method (Geodetic Institute of Slovenia, 2021). The minimum width of the mapped running surface water is 1 m. The positional and vertical accuracies of the acquisition are ± 1 m.

3.1.3   Definition of Land Cover Classes of Interest

In line with our research question we considered three land cover classes that are most widely present in riparian environments – gravel, vegetation, and water. The characteristics of SMA as described above require that we consider land cover classes with very different spectral signatures. If we examined

classes with similar spectral signatures, it would be very difficult to determine their individual contributions to the spectral signal from a particular signal. Thus, we had to make some simplifications when selecting the land cover classes to be considered. The gravel class included gravel bars, rocks and boulders, sand, and built-up areas. We minimised the intrusion of built-up areas and focused our analysis on gravel bars by restricting the area of observation to the extent of water lands with the data set described above. The vegetation class included trees, shrubs, and grassland. The water class included rivers, streams, and standing water. Shade can sometimes erroneously be mapped as water, therefore we tested the possibility of mapping it as a separate class, as described below.

3.2   Validation of Fraction Maps

Three different approaches were tested for the validation of land cover fraction maps. First, a pixel-based approach using aerial orthophotos as reference was implemented. In the second approach, the maps were also validated on a per-pixel basis, but using in situ land cover mapping as reference. The pixel-based approach can be seen as providing site-specific accuracy (Campbell and Wynne, 2011). We also implemented an area-based validation approach which provides non-site-specific accuracy to account for possible misalignment of pixels due to errors in satellite image geometry.
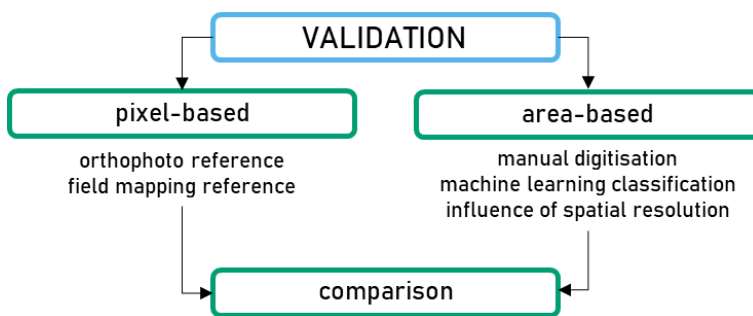
3.2.1   Case Study Area

A section of the Soča river in north-western Slovenia, Central Europe, was selected to test different methods for mapping and monitoring gravel bars. The selected river section is approximately 15 km long and is centred on 46.2° N, 13.6° E. The section is located between the settlements of Kobarid and Tolmin (Figure 7).
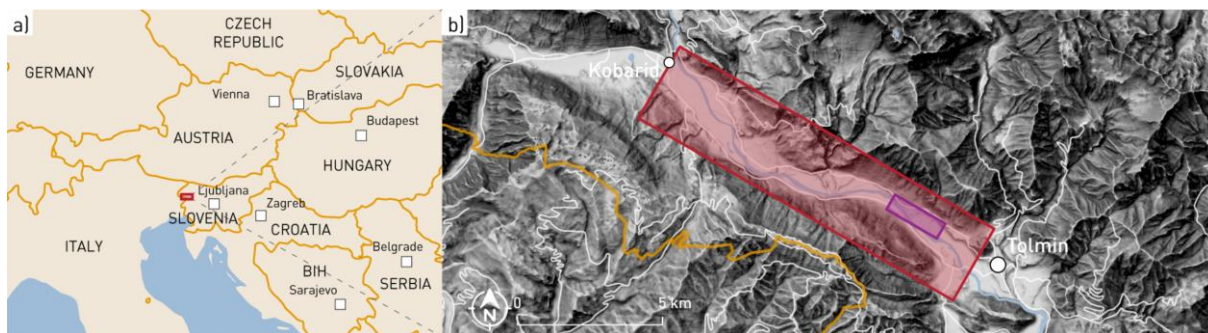
Figure 7: Overview of the study area. a) Location of the study area (red rectangle) in the upper Soča river basin, north-western Slovenia, Central Europe, centred on 46.2° N, 13.6° E (data source: Natural Earth, 2020). b) A closer view of the study area. The red rectangle indicates the entire study area, while the purple rectangle marks the location of the enlarged view in Figure 22 (data source: Surveying and Mapping Authority of the Republic of Slovenia, 2016, 2021a, 2021b).

Slika 7: Pregled študijskega območja. a) Lokacija študijskega območja (rdeč pravokotnik) v porečju zgornje Soče, v severozahodni Sloveniji, s sredinskimi koordinati 46.2° severno in 13.6° vzhodno (vir podatkov: Natural Earth, 2020). b) Bližnji pogled študijskega območja. Rdeč pravokotnik označuje celotno območje, vijolični pravokotnik pa lokacijo bližnjega pogleda na Slika 22 (vir podatkov: GURS, 2016, 2021a, 2021b).

The bedrock in the area consists of limestone and dolomite (Geological Survey of Slovenia, 2019). The climate is mountainous to temperate Mediterranean with most of the area belonging to the temperate climate with no dry season and a warm summer – Cfb – according to the Köppen-Geiger classification (Ogrin, 1996; Ogrin and Plut, 2009). The flow regime of the river is nivo-pluvial with the main discharge peak in April or May due to snowmelt. There is a secondary discharge peak in November due to heavy autumn rainfall. The main low discharge period is in January or February as precipitation is temporally stored in the form of snow. The secondary low discharge period is in August when evapotranspiration is highest (Ogrin and Plut, 2009). Precipitation is very high in this area, averaging over 2500 mm annually for the last 50 years (Slovenian Environment Agency, 2021a).

The terrain in the Soča basin in Slovenia is varied, ranging from 153 to 2864 m above sea level. The combined effect of topography and precipitation results in high erosion rates and consequently large amounts of river bedload in the Soča. The selected river section contains several gravel bars and is therefore very suitable as a test area. In addition, the river is often not wider than 20 m, making the

section interesting for the application of SMA. The wider study area was narrowed down to the extent of the water lands (Slovenian Water Agency, 2021). Most of the study area is covered by water, followed by gravel bars and deciduous forest (Figure 8).
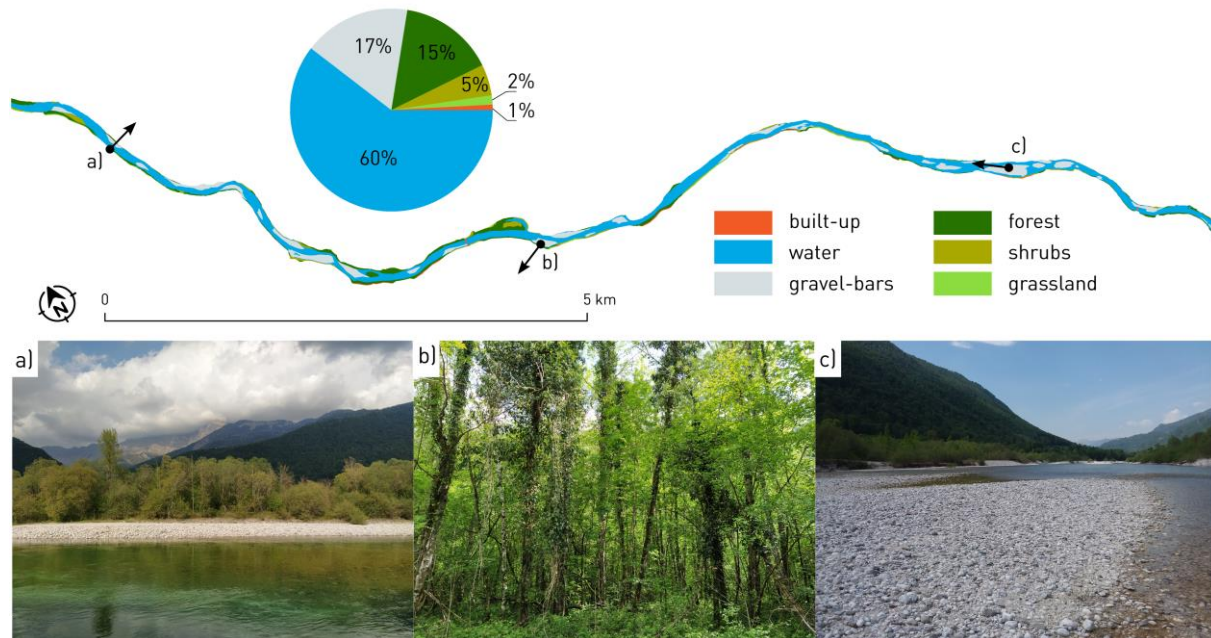
Figure 8: Land cover of the study area. The arrows show the viewing direction of photographs (data source: Ministry of Agriculture, Forestry and Food of the Republic of Slovenia, 2020; Slovenian Water Agency, 2021a); photographs: Liza Stančič).

Slika 8: Pokrovnost študijskega območja. Puščice kažejo smer fotografiranja (vir podatkov: Ministrstvo za kmetijstvo, gozdarstvo in prehrano RS, 2020; Direkcija RS za vode, 2021; fotografije: Liza Stančič).

3.2.2 Pixel-Based Validation

The pixel-based validation method compared land cover fractions obtained by SMA with those observed on reference data on a pixel level (Schug et al., 2018). The results of pixel-based validation can be considered as site-specific accuracy as they provide the agreement between the fraction maps and reference data at specific locations (Campbell and Wynne, 2011). We used aerial orthophotos, very high resolution satellite images (WorldView-2, Pléiades), or own field mapping as reference data sources. Independent of the reference data, 50 random plots were selected in the study area. Their size corresponded to the spatial resolution of satellite images and covered the extent of one pixel. Within each plot, a regular grid of 100 points was created and the land cover class at each point was determined. Reference land cover fraction values were calculated and compared to fractions obtained from the SMA. The comparison was then made by computing the mean absolute error (MAE):

$$\text{MAE} = \frac{1}{n}\sum_{i=1}^{n}|x_i - x| \qquad (3)$$

as the absolute difference between the land cover fractions on the reference data (x) and the land cover fractions derived from the SMA (x_i) (Demarchi et al., 2012; Okujeni et al., 2018; Li, 2021). The value of MAE was calculated for all 50 plots ($n = 50$).

3.2.2.1 Aerial Orthophotos

In the programme of the CAS, aerial orthophotos are acquired each year for about one-third of Slovenia. Thus, the same area is imaged once every 2 to 4 years. The timing of the imaging varies depending on weather conditions. For the study area, the three most recent orthophotos were acquired on 26 June 2015, 14 October 2017, and 5 September 2020. Visible spectral bands are available with a spatial resolution of 0.25 m and 0.5 m, and a near infrared band is available with a spatial resolution of 0.5 m. All of the available products are acquired simultaneously and later pan-sharpened and resampled as needed (Surveying and Mapping Authority of the Republic of Slovenia, 2021c). The positional accuracy of aerial orthophotos is 0.2 m (Surveying and Mapping Authority of the Republic of Slovenia, 2021c).

3.2.2.2 Field Mapping

A field mapping campaign was conducted in the study area from 25 April 2020 to 3 May 2020. We randomly selected 50 plots with an extent of 60 m × 60 m. Plots were sized to fit at least one whole pixel of each of the analysed satellite images into each mapped plot. The selection of plots to be mapped was done by first plotting a grid of 60 m × 60 m over the entire study area. Subsequently, we used the Random selection function in the QGIS software (version 3.10) to select 50 plots in the whole study

area (QGIS Development Team, 2020). The most recent aerial orthophotos at the time, acquired on 14 October 2017, were used as background on which changes were recorded. The positional accuracy of the field mapping can therefore be considered identical as that of aerial orthophotos (0.2 m). We mapped the three land cover classes of interest – gravel, vegetation, and water – at a scale of 1 : 1000. The plots selected for field mapping were mostly covered by vegetation (Figure 9).
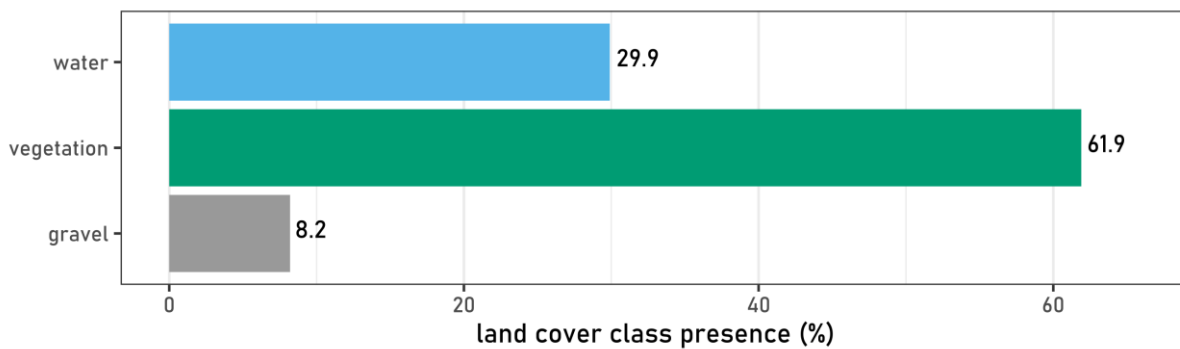
Figure 9: Land cover presence as determined with field mapping on 50 randomly selected plots.

Slika 9: Prisotnost razredov pokrovnosti, določena s terenskim kartiranjem na 50 naključno izbranih območjih.

3.2.3   Area-Based Validation

The geolocation accuracy of Sentinel-2 images is known to be within 11 m for 95% of the images (Clerc and MPC Team, 2021). However, even small shifts can lead to considerable inaccuracies when analyses are performed at the level of single pixels. To account for such potential errors, we also carried out a validation of the fraction maps at the scale of the entire study area (Li et al., 2020). This constituted the area-based validation. The result of area-based validation is non-site-specific accuracy as it reports the agreement between fraction map and reference data in terms of the overall figures and not at specific locations (Campbell and Wynne, 2011). The extent of each land cover class of interest was calculated using the fraction maps and compared with the extents based on reference data. Different sources for obtaining reference data were tested, namely manual digitisation and supervised classification based on machine learning (ML). For both methods of obtaining reference data, aerial orthophotos were used as input images. Additionally, very high resolution (VHR) satellite images were used for machine learning-based classification.

3.2.3.1   Manual Digitisation

Based on aerial orthophotos acquired on 26 June 2015, we manually digitised three land cover classes – gravel, vegetation, water –, and shade. We digitised ten non-contiguous areas along the study river section, totalling 0.8 km^2. The scale of digitisation was 1 : 1500. The digitisation required approximately eight operator hours in total.

3.2.3.2   Machine Learning-Based Classification

Supervised ML-based classification was also used to provide the reference data. Training samples were selected from areas with uniform land cover based on either aerial orthophotos or VHR satellite images. We compared the Random Forest (RF) and Support Vector Machine (SVM) classification algorithms. For classification based on RF, 2000 training samples in the form of random pixels were selected from the predefined areas with uniform land cover. Classification models with 500 decision trees and with 1000 decision trees were built for comparison, one. For the SVM, a kernel with radial basis function was chosen. Again, two different models were tested, one based on 1000 training samples and a second based on 2000 training samples. Model training and image classification were performed in the R programming language (R Core Team, 2021) using the packages randomForest (Liaw and Wiener, 2002) and e1071 (Meyer et al., 2021). Based on the four classification models described above, we produced land cover maps of the water lands in the study area from aerial orthophotos and VHR satellite images.
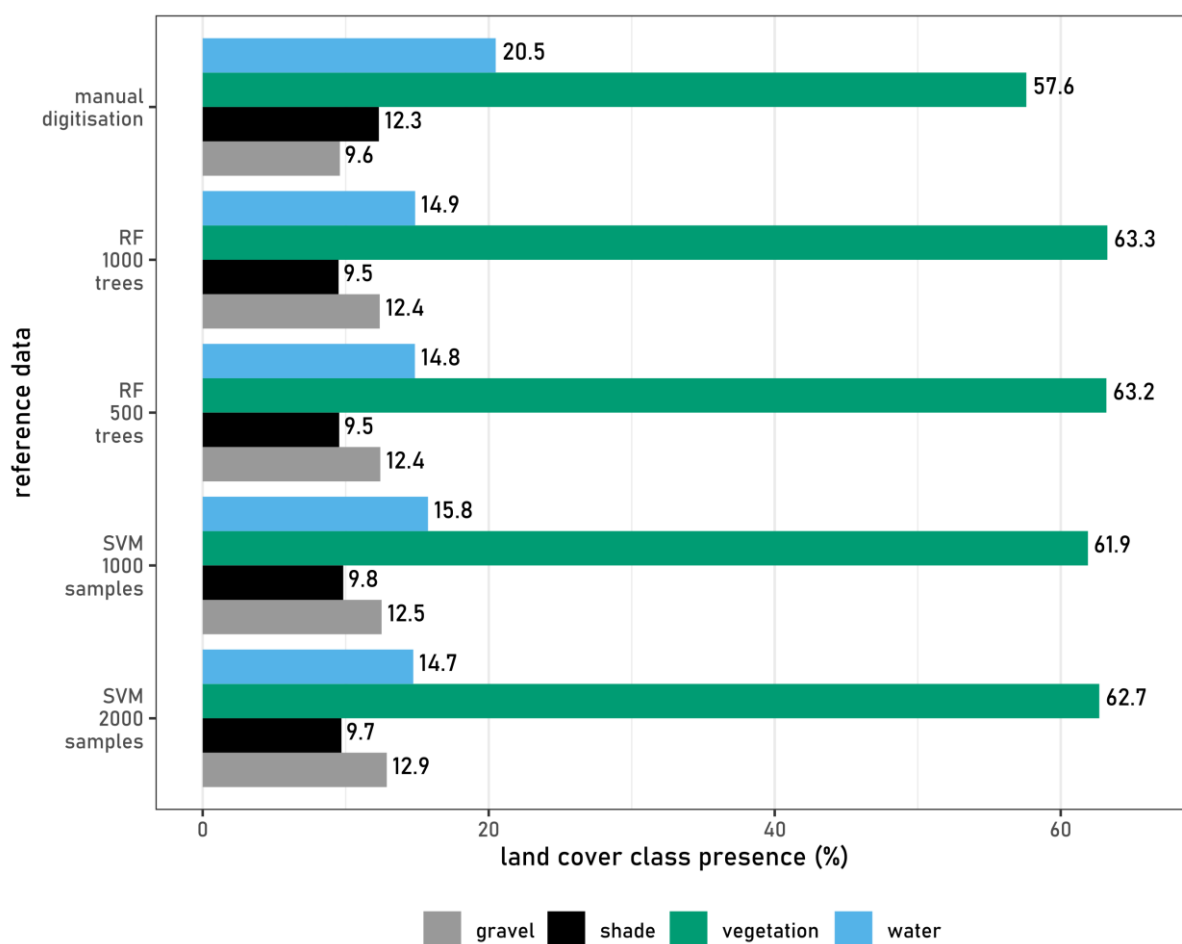
Figure 10: Presence of the different land cover classes of interest in the reference datasets considered.

Slika 10:   Prisotnost izbranih razredov pokrovnosti na različnih referenčnih podatkih.

We compared the different area-wise reference datasets based on the detected presence of the land cover classes of interest (Figure 10). The area classified by ML was cropped to the extent covered by manual digitisation so that exactly the same area was considered. The classification methods based on ML performed very similarly, with differences between the various results within 1.5%. The largest difference was recorded for the vegetation class, which was also the most widely represented in the analysed area. Compared to manual digitisation, ML-based classification performed worst in classifying water, which was under-detected. Shade was also under-detected with the ML-based method, while gravel and vegetation were over-detected. Oversizing of river bar areas is also in line with existing literature (Kryniecka and Magnuszewski, 2021). One possible reason for the misclassifications of gravel is that shallow water areas have a very similar spectral signal to gravel because the spectral signal of gravel from the riverbed can pass through clear water and be recorded by the sensor. Manual classification did not classify single pixels, but took into account connected land cover areas and was therefore not influenced by the reflectances of single pixels in shallow water. As for shade, its under-detection with ML-based methods may be explained by the fact that shade can also be found within vegetated areas in small extents and so it could be falsely included within the vegetation class by the ML algorithms. Nevertheless, the manual and the ML-based classifications give comparable results. The ML-based classification will be used for validation in other areas on the Soča, Sava, and Vjosa rivers, because it is faster (Schwarz et al., 2003; Ilsever and Unsalan, 2013; Rastiveis et al., 2013; Hölbling et al., 2017) and produces more consistent results (Tarko et al., 2018; Kraff et al., 2020).

As all of the ML-based classifications gave very similar results, the main decision point for selecting one of them for further work was speed (computing time). We measured the times required for model training and image classification of all tested configurations (Table 2). Classification of an area of 109.7 km^2 with a spatial resolution of 0.5 m took over three hours. The fastest method was the one using a RF algorithm with 500 trees, therefore this configuration was selected for further reference classifications.

Table 2: Computing time for training different machine learning-based classification models and classification of an orthophoto with a spatial resolution of 0.5 m and an area of 109.7 km^2.

Preglednica 2: Trajanje učenja različnih klasifikacijskih modelov na podlagi strojnega učenja in klasifikacije ortofota s prostorsko ločljivostjo 0.5 m in površino 109.7 km^2.

model	RF 500 trees	RF 1000 trees	SVM 1000 samples	SVM 2000 samples
train time (h:min:s)	0:00:56	0:01:35	0:11:33	0:38:31
classification time (h:min:s)	3:06:05	3:12:18	3:01:05	5:48:08
total time (h:min:s)	**3:07:01**	**3:13:53**	**3:12:38**	**6:26:39**

3.2.3.3 Spatial Resolution of Reference Data

Aerial orthophotos are available with a spatial resolution of 0.25 m. They need to be classified to be used as reference data and this classification is a computationally intensive process. However, orthophotos are also available at a 0.5 m resolution. We were interested in whether the different spatial resolutions give comparable results in the validation of the fraction maps. We therefore used identical training samples and classification algorithms, but applied them to reference data with different resolutions.
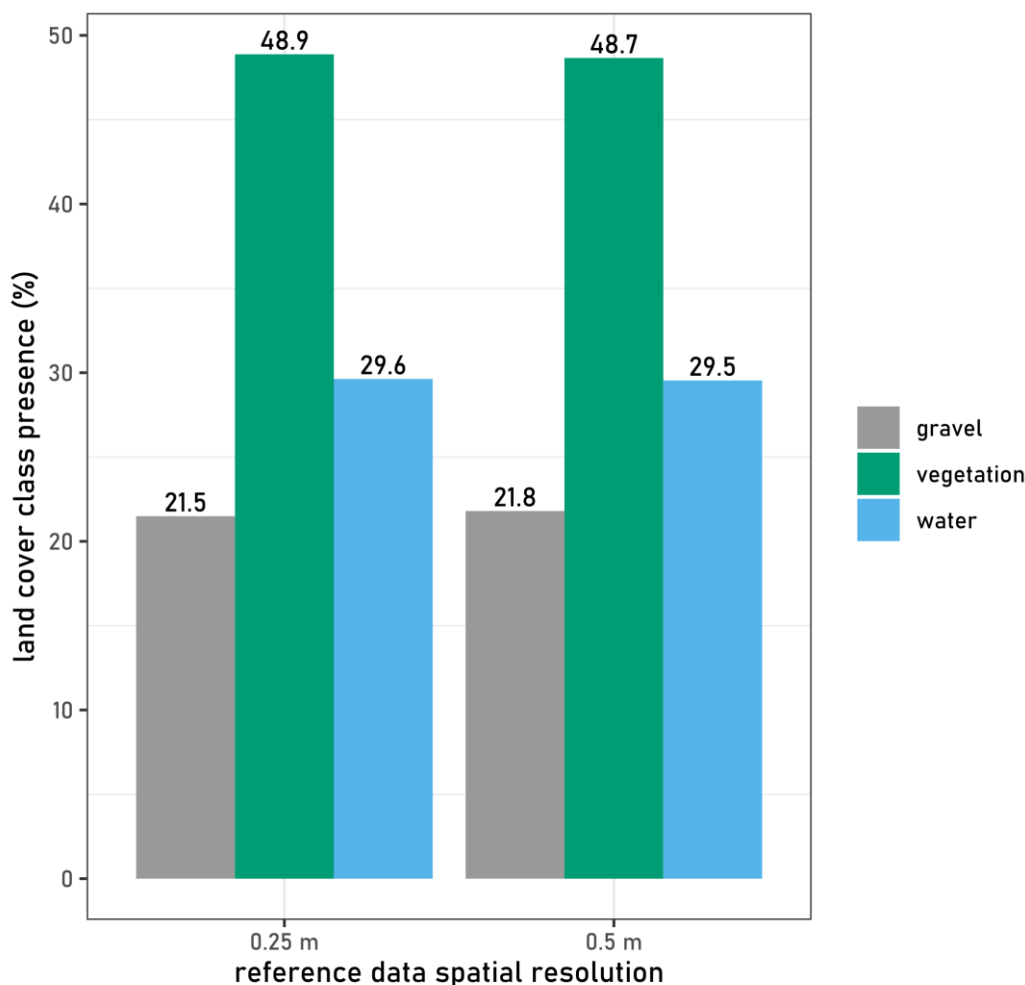
Figure 11: Presence of the land cover classes of interest on reference datasets with different spatial resolutions.

Slika 11:   Prisotnost izbranih razredov pokrovnosti na referenčnih podatkih z različno prostorsko ločljivostjo.

We then calculated the presence of each land cover class of interest in the reference datasets with different spatial resolutions (Figure 11). Classification of 0.5 m images was twice as fast as that of 0.25 m images. We found that the differences in the presence of land cover classes between the two maps were within 0.32% and thus can be considered negligible. Based on these findings, 0.5 m reference data can be recommended for validation.

It is important to note that data used for ground truth cannot be considered error-free (Carlotto, 2009). An accuracy assessment of the reference data for the year 2015 showed an overall accuracy of 98%. This is reasonable, since we are only considering three land cover classes very different spectral characteristics. The accuracy of reference data is thus sufficient for further analysis. Nevertheless, we must keep in mind that ground truth contains errors and can be a source of uncertainty when benchmarking different results (Chehdi and Cariou, 2019). Indeed, claims have been made that the term "ground truth" is inappropriate in itself and should be replaced by terms such as "surface observations" or "field measurement" (Woodhouse, 2021). We use another of terms proposed in the literature – "reference data".

3.2.4   Comparison of Pixel-Based and Area-Based Validation

We compared the results of pixel-based and area-based validation in terms of which fraction map achieved the highest accuracy for each of the land cover classes considered (Table 3). Five different land cover fraction maps were considered, each based on different input data:

- a Sentinel-2 image with endmembers selected on the same image,
- a Sentinel-2 image with endmembers transferred from a different image,
- a Landsat 7 image with endmembers selected on the same image,
- a Landsat 8 image with endmembers selected on the same image, and
- a Landsat 8 image with endmembers transferred from a different image.

Table 3: Comparison of pixel-based and area-based validation results. The most accurate fraction maps for each land cover class are given.

Preglednica 3: Primerjava rezultatov validacije na podlagi posameznih pikslov in celotne proučevane površine. Navedene so najbolj natančne karta deležev pokrovnosti za vsak razred pokrovnosti.

land cover class	most accurate fraction map	
	pixel-based*	area-based**
gravel	Sentinel-2 – same image endmembers	Sentinel-2 – transferred endmembers
vegetation	Sentinel-2 – transferred endmembers	Sentinel-2 – same image endmembers
water	Sentinel-2 – same image endmembers	Sentinel-2 – transferred endmembers
total	Sentinel-2 – transferred endmembers	Sentinel-2 – transferred endmembers

* automatic endmember selection

** shade areas excluded from samples

Both validation methods show that the most accurate map overall is the one based on the Sentinel-2 image with transferred endmembers. The transferred endmembers consist of two endmembers describing water reflectance, resulting in better separation between gravel and water and consequently more accurate fraction maps. Because both validation methods give similar results, they are used interchangeably in subsequent tests.

3.2.5   Conclusions on Validation Method

The test area on the Soča between the settlements of Kobarid and Tolmin is a suitable study area for the development of gravel mapping methods. Sufficient reference and auxiliary data are available to allow validation of the method and interpretation of the results. Two different validation methods were developed, one based on comparing pixel-wise land cover fractions and the other evaluating the presence of different land cover classes in the study area as a whole. The pixel-based validation method was used first and the area-based method was developed later due to concerns related with the geometric accuracy of satellite images. The two validation methods produced similar results in selecting the most accurate fraction maps. Therefore, the different methods and configurations in the next chapters are validated using both proposed methods interchangeably. We followed a pragmatic approach where the tests done at the beginning of the study were validated using the pixel-based method while tests conducted later were validated using the area-based method.

The next chapter focuses on the investigation of satellite image properties that affect the accuracy of the SMA.

3.3   Characteristics of Satellite Images Used

Together with endmember spectral signatures, satellite images are the main input to the SMA. Providing images with suitable properties is therefore key for accurate results. We first examined the differences between Sentinel-2 and Landsat, two of the most commonly used optical EO systems. We then tested the influence of different pre-processing corrections. The contribution of different spatial resolutions of the input satellite images was also studied. Finally, we explored the influence of complementing the spectral bands of the satellite images with different spectral indices.
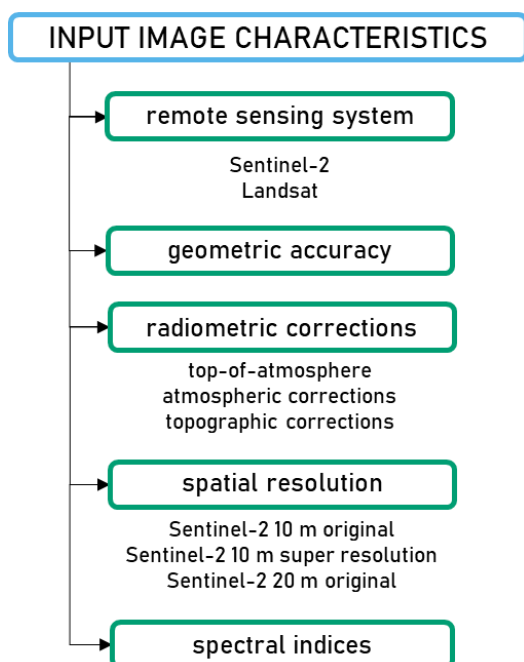
3.3.1   Remote Sensing Systems Used as Sources of Satellite Images

Sentinel-2 and Landsat have comparable spectral characteristics. However, an important difference between the two systems is their temporal resolution as outlined in chapter 3.1.1 above; Landsat provides longer time series starting in 1982 with a revisit time of 16 days, while Sentinel-2 has denser time series with a revisit time of 5 days but only since 2017. In gravel bar monitoring, long time series enable insights into the impacts of many different flood, rockslide, infrastructure interventions, and other events in the past which can inform about the possible impacts of similar events in the future. On the other hand, denser time series make it possible to observe the process dynamics in greater details and closer to the real time. We investigated whether data from the two remote sensing systems produce comparable results and if the outputs can be used interchangeably to take advantage of the most favourable characteristic of each system.

Two Sentinel-2 images, a Landsat 7, and a Landsat 8 image were used for the comparison. The Sentinel-2 images were acquired on 11 July 2015 and on 23 April 2020, the Landsat 7 was acquired on 9 July 2015, and the Landsat 8 image was acquired on 25 April 2020 (Figure 12).
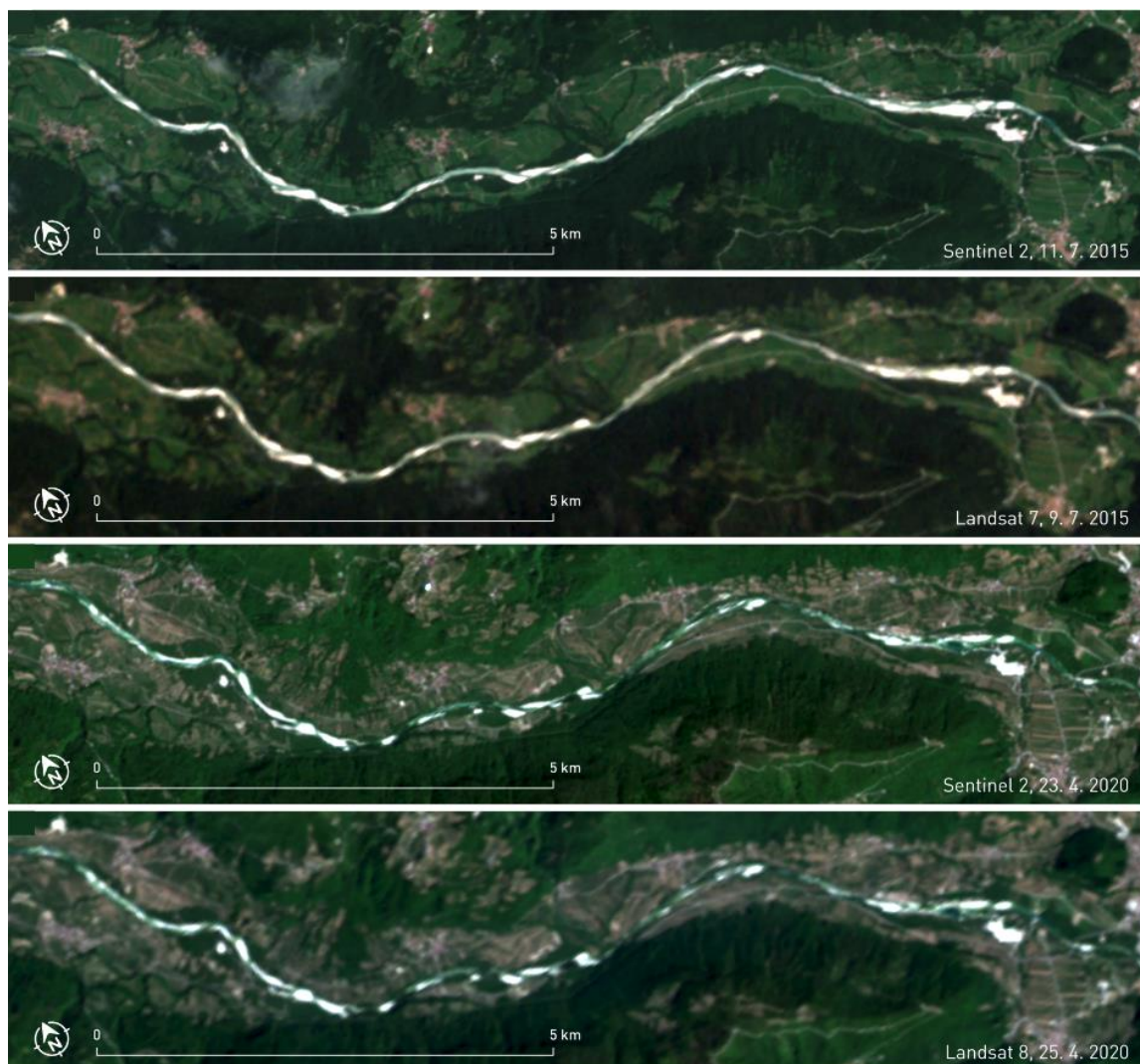
Figure 12: Overview of the satellite images used in the analysis; true colour composites (data source: ESA, 2021; U. S. Geological Survey, 2021a, 2021b).

Slika 12: Pregled satelitskih posnetkov, uporabljenih v analizi; naravno barvni kompoziti (vir podatkov: ESA, 2021, U. S. Geological Survey, 2021a, 2021b).

The endmembers used for SMA of the different images were calculated based on the average reflectance values of pure pixels. Pixel selection was done manually, using reference data to ensure pixel purity. Four pixels were used to calculate the gravel endmember, nine for surface water, and 20 for vegetation. The number of pixels used was identical for the different images and was limited by the number of pure pixels that could be detected on the Landsat images. The Landsat images have a lower spatial resolution than the Sentinel-2 images and therefore fewer pure pixels.

The resulting land cover fraction maps were validated with the pixel-wise method. Aerial orthophotos, acquired on 26 June 2015, were used to validate the 2015 maps, while field mapping was used as reference for the 2020 maps.

Table 4: Pixel-wise mean absolute error of land cover fraction maps per land cover class for different analysed satellite images using manually selected endmembers. The best results per land cover class in bold.

Preglednica 4: Povprečna absolutna napaka po pikslih za karte deležev pokrovnosti na podlagi različnih satelitskih posnetkov z ročno izbranimi končnimi piksli za izbrane razrede pokrovnosti. Najboljši rezultati za vsak razred pokrovnosti v krepki pisavi.

land cover class	Landsat 7, 9. 7. 2015	Sentinel-2, 11. 7. 2015	Landsat 8, 25. 4. 2020	Sentinel-2, 23. 4. 2020
gravel	0.087	0.078	**0.069**	0.095
vegetation	0.114	0.111	**0.108**	**0.108**
water	0.124	0.082	**0.074**	0.080
total	0.108	0.090	**0.084**	0.094

The results indicate that comparable fraction map accuracies can be achieved using Sentinel-2, Landsat 7, and Landsat 8 images (Table 4). We report the MAE as the selected accuracy measure for land cover fraction maps (Schug et al., 2018; Suess et al., 2018). The MAE is less than 0.1 for most of the land cover classes of interest on the majority of images which means that the land cover fractions are correct within ± 10%. Vegetation is the most problematic, with MAE of 0.11 on all maps. Vegetation in the study area occurs in many different forms. We attempted to account for this variability by selecting a large number of different pixels from which the vegetation endmember was computed. However, certain vegetation types are still spectrally more similar to water or gravel and are therefore misclassified. Furthermore, it is apparent that the fraction maps based on Landsat 7 achieve the lowest accuracies. Landsat 7 is the oldest of the three remote sensing systems considered, imaging since April 1999. Compared to Landsat 8, it has a lower radiometric resolution and wider spectral bands (Irons et al., 2012; Roy et al., 2016), leading to larger errors in spectral analysis. Nevertheless, in all cases gravel fractions are mapped very successfully (Table 4), which means that all tested remote sensing systems can be used for monitoring gravel bars.

3.3.2   Geometric Accuracy of the Input Satellite Images

The geometric quality of images is important information in time series analysis. Poor geometric quality and misalignment of images may cause the detection of false changes which are not a results of actual changes on the Earth's surface, but appear because of a shift in location. It is therefore crucial to ensure we are always observing the same location when monitoring processes with EO data. Sentinel-2 Data Product Quality Reports state that the absolute geolocation performance is below 11 m for 95% of images and the multi-temporal geometric performance is around 12 m (Clerc and MPC Team, 2021). This is expected to improve by applying geometric refinement with the use of tie points from the Global Reference Image (Clerc and MPC Team, 2021; Dechoz et al., 2015). The additional refinement step has not yet been deployed operationally, but preliminary test show that the absolute geolocation of images will be better than 8 m and that multi-temporal co-registration accuracy from different orbits will surpass 5 m (Clerc and MPC Team, 2021). However, these values refer to a global estimate and not many

Stančič, L. 2022. Monitoring Changes of Fluvial Gravel Bars with Remote Sensing.
PhD Th. Ljubljana, UL FGG, Interdisciplinary doctoral study programme Environmental Protection.

37

investigations examine the actual geometric performance of the utilised images. We therefore performed several tests to study the geometric performance of Sentinel-2 images and investigated if there are any factors that have an important influence on the geometric accuracy.
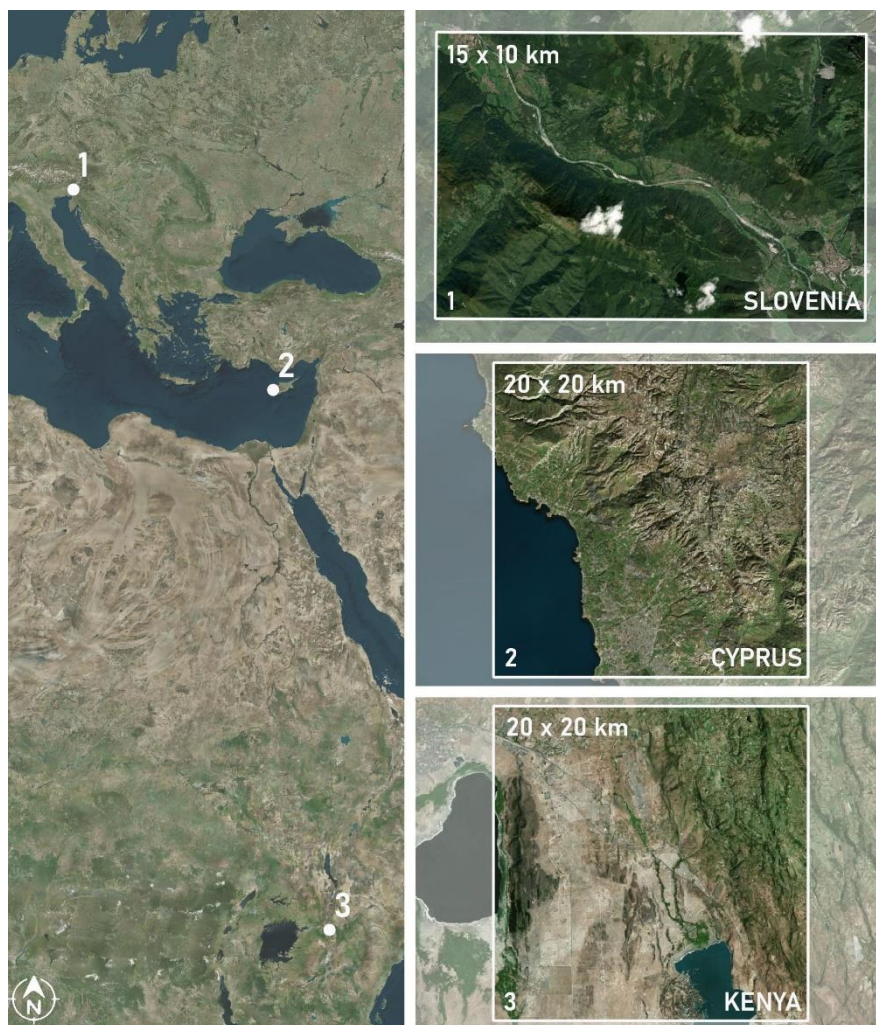
Figure 13: Study areas selected for the analyses of the geometric accuracy of Sentinel-2 images (basemap: Bing, 2021).

Slika 13: Študijska območja, izbrana za analize geometrijske točnosti posnetkov Sentinel-2 (podlaga: Bing, 2021).

We conducted the analysis using images processed to Level-1C. Three study areas were selected in Kenya, Cyprus, and Slovenia (Figure 13). In each study area, between 10 and 20 reference points were selected which could be clearly seen and were assumed to remain stable during the observation period. Reference points were mostly crossroads and were verified using VHR data (Bing, 2021; OpenStreetMap contributors, 2021; Surveying and Mapping Authority of the Republic of Slovenia, 2021e). All Sentinel-2 images of the study areas with at most 10% cloud cover acquired between 1

38   Stančič, L. 2022. Monitoring Changes of Fluvial Gravel Bars with Remote Sensing.

PhD Th. Ljubljana, UL FGG, Interdisciplinary doctoral study programme Environmental Protection.

January 2017 and 31 December 2020 were analysed. In total, 395 images were analysed in Kenya, 444 in Cyprus, and 264 in Slovenia.

Geometric shifts in images were analysed by registering all images to a selected reference image. An image acquired in April 2020 was selected as reference in all study areas. The visible spectral bands were combined in a single image which was then used in the analyses. The registration of different images was done using unnormalised cross-correlation (Guizar-Sicairos et al., 2008) as implemented in the Python package scikit-image (version 0.18.3) (van der Walt et al., 2014). The resulting shifts in the x- and y-directions were plotted for each study area and the resulting average shifts were calculated (Figure 14).
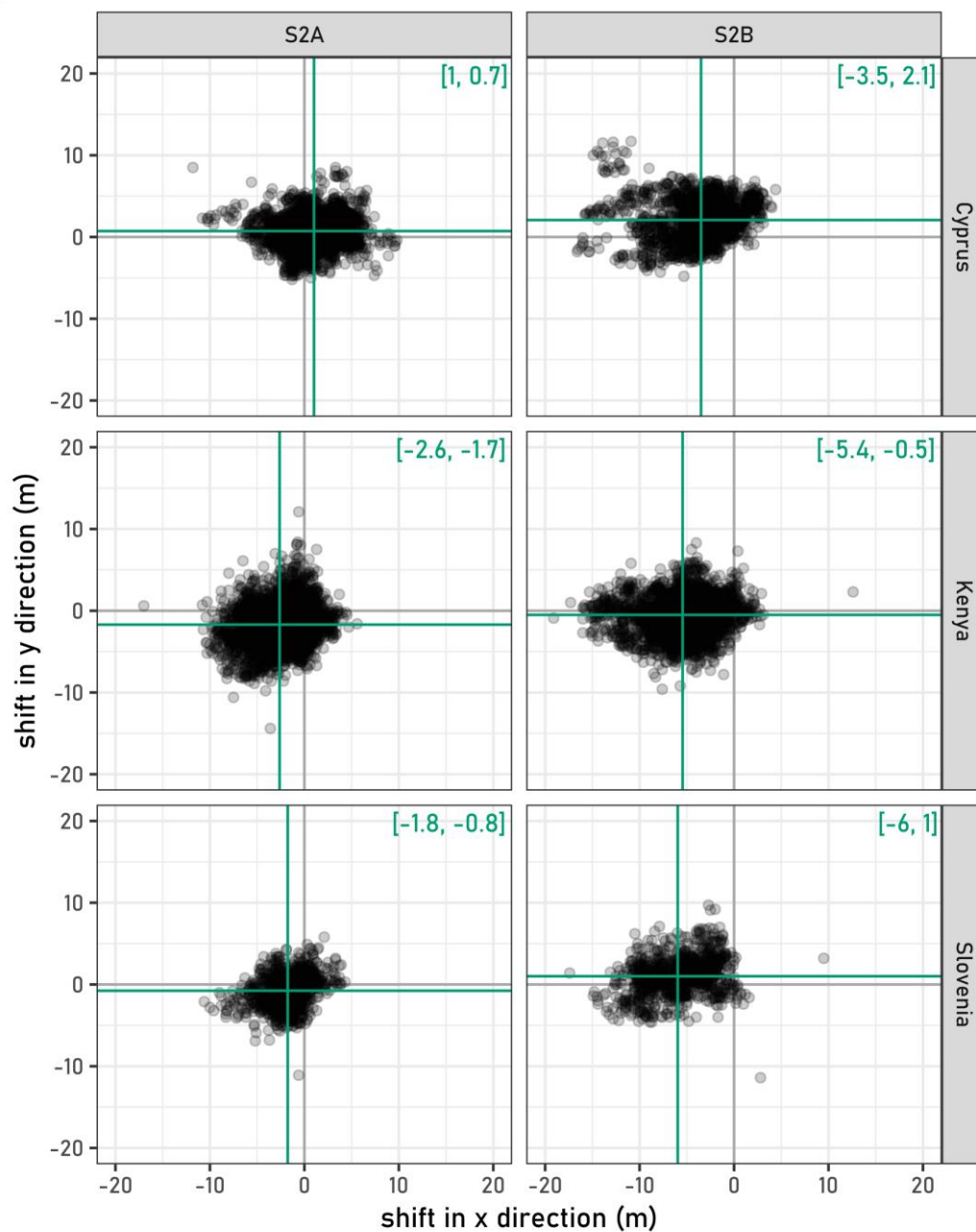
Figure 14: Geometric shifts of Sentinel-2 images for the selected study areas.

Slika 14: Geometrijskih premiki posnetkov Sentinel-2 za izbrana študijska območja.

The results show that average shifts of Sentinel-2 images are −2.88 m in the x-direction and −0.02 m in the y-direction. Notably, images acquired by the Sentinel-2B satellite are shifted more than those acquired by the Sentinel-2A. Average shifts on Sentinel-2B images across the different study areas are −4.56 m in the x-direction and 0.91 m in the y-direction compared to −0.86 m in the x-direction and −0.46 m in the y-direction observed on Sentinel-2A images. Slight differences can be seen between the different study areas, but the overall trends are the same. We found the accuracies to be higher than those reported in the literature which range from maximum shifts of 6 m (Vajsova and Åstrand, 2015), to 13 m (Pandžić et al., 2016), and 14 m (Rufin et al., 2021). Importantly, however, existing studies have

not differentiated between the Sentinel-2 satellites or in cases when they did, the reported differences were very small – within 2.5 m (Doshi et al., 2020). Despite the shifts that we found, we concluded that they are small and therefore we decided against re-aligning the images in subsequent analyses.

3.3.3   Influence of Radiometric Corrections on Fraction Map Accuracy

To reduce the effects of atmosphere and topography on reflectance values, radiometric corrections are applied to satellite images before the analysis. Various pre-processing functions for atmospheric and topographic corrections can be used for this purpose. We investigated how these image pre-processing affects the accuracy of the SMA. To compare and determine the stability of results, tests were performed using two Sentinel-2 images acquired in two different time periods with different atmospheric and Sun angle characteristics – the summer image, acquired on 11 July 2015, and the autumn image, acquired on 16 October 2017. The dates of the images were selected to match the acquisitions of aerial orthophotos which were used to generate reference data. We validated the maps based on the area covered by each of the land cover classes of interest by comparing the fraction maps to aerial orthophotos classified using RF with 2000 samples and 500 trees. The analysis involved three different levels of pre-processing of the same image:

- uncorrected image (top of atmosphere),
- atmospherically corrected image, and
- topographically corrected image.

Each subsequent pre-processing level included corrections from all previous levels. Atmospheric corrections were performed by ourselves using the ATCOR programme (Richter, 1996; Richter et al., 2006; Richter and Schläpfer, 2019). Topographic corrections were applied with the STORM processing chain which combines physical models and the Minnaert approach (Pehani et al., 2016; Zakšek et al., 2015).
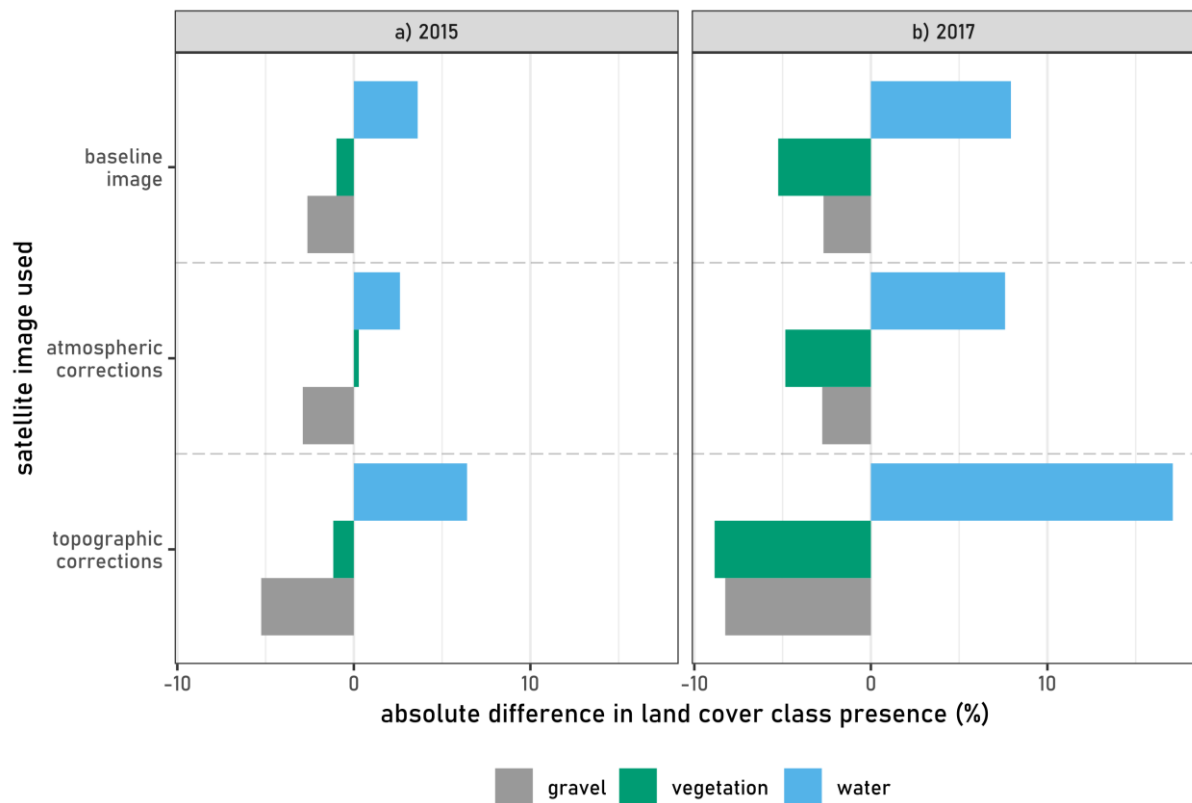
Figure 15: Accuracy of land cover fraction maps based on satellite images with different pre-processing levels.

Slika 15: Natančnost kart deležev pokrovnosti, izdelanih na podlagi satelitskih posnetkov z različnimi nivoji pred-procesiranja.

The results showed that atmospheric corrections slightly improved the map accuracy compared to the top of atmosphere reflectance image (Figure 15). Topographic corrections, on the other hand, introduced additional uncertainty that led to an increase in map error even compared to the baseline image. In particular, vegetation and gravel were frequently classified as water on the topographically corrected image. In subsequent analysis we therefore worked with atmospherically corrected images. The omission of topographic correction was not problematic because we focused on flat areas in river valleys, whereas topographic error is most pronounced on steep slopes.

3.3.4 Contribution of Improved Spatial Resolution of Input Satellite Images to Fraction Map Accuracy

The size of the pixel defines the size of area for which the land cover presence fractions are given. We investigated whether improved spatial resolution leads to more accurate results on an image acquired by the Sentinel-2 system on 11 July 2015. Of the ten Sentinel-2 spectral bands used in SMA, six are acquired with a 20 m spatial resolution. In the current pre-processing workflow, the remaining four bands with a 10 m resolution were downsampled to 20 m using bilinear interpolation. The resulting land cover fraction maps were thus produced with a 20 m spatial resolution.

To test the potential contribution of increasing spatial resolution to improve map accuracy, we applied the deep learning-based DSen2 algorithm (Lanaras et al., 2018) to resample the Sentinel-2 bands with a 20 and 60 m spatial resolution to 10 m. All of the 20 m and 60 m spectral bands are included in the resampling, apart from the cirrus band (B10) which contains too much noise.

The improvements gained by resampling were assessed by comparing the results with two fraction maps based on different input data:
- four spectral bands originally acquired with a 10 m resolution (blue, green, red, infrared) and
- ten spectral bands with a 20 m resolution.

Three endmembers for the SMA were selected automatically. The same land cover classes were chosen as endmembers on all images, namely gravel, vegetation, and water. With an increase in spatial resolution, the number of pixels that needed to be spectrally unmixed increased four-fold and so did the time required for the SMA. On the other hand, increasing the number of bands included in the SMA did not affect the duration of the SMA (Table 5).

Table 5: Computing time for automatic selection of three endmembers (ASEM) and the spectral mixture analysis (SMA) using different input images, derived from a Sentinel-2 image, acquired on 11 July 2015. S2 10 m – Sentinel-2 spectral bands acquired with a 10 m spatial resolution; S2 supres – Sentinel-2 image resampled to 10 m with the DSen2 algorithm; S2 20 m – Sentinel-2 spectral bands acquired with a 20 m spatial resolution, and the spectral bands acquired with a 10 m spatial resolution resampled to 20 m with bilinear interpolation.

Preglednica 5: Trajanje samodejnega izbora treh končnih pikslov (ASEM) in analize vsebnosti spektralnega signala (SMA) pri različnih vhodnih podatkih, pridobljenimi na podlagi posnetka Sentinel-2, zajetega 11. 7. 2015. S2 10 m – posnetek Sentinel-2 s spektralnimi kanali, zajetimi z 10-metrsko prostorsko ločljivostjo; S2 supres – posnetek Sentinel 2, prevzorčen na 10 m z algoritmom DSen2; S2 20 m – posnetek Sentinel-2 s spektralnimi kanali, zajetimi z 20-metrsko prostorsko ločljivostjo, in s spektralnimi kanali, zajetimi z 10-metrsko prostorsko ločljivostjo, prevzorčenimi na 20 m z bilinearno interpolacijo.

image	number of bands	number of pixels	ASEM (min:s)	SMA (min:s)	total (min:s)
S2 10 m	4	838,000	00:03	11:06	11:09
S2 supres	12	838,000	00:07	10:54	11:01
S2 20 m	10	210,000	00:01	02:35	02:36

Validation of the resulting land cover fraction maps was performed using the pixel-based method. The reference plot size was adjusted to the map with the coarsest spatial resolution, i.e. 20 m × 20 m. Comparison with the results based on the four spectral bands originally acquired in a 10 m resolution showed little or no improvement in map accuracy (Table 6). Similarly, no improvement in accuracy was observed when considering fraction maps based on the 20 m bands. Apparently, increasing the spatial resolution of the images with a deep learning algorithm did not produce sufficient supplementary information that could lead to a more successful spectral analysis.

Table 6: Mean absolute error of land cover fraction maps from different images, derived from a Sentinel-2 image, acquired on 11 July 2015. Endmembers selected automatically.

Preglednica 6: Povprečna absolutna napaka izračuna deležev pokrovnosti po razredih pokrovnosti za različne vhodne podatke na podlagi posnetka Sentinel-2, zajetega 11. 7. 2015. Končni piksli izbrani samodejno.

image	baseline-10m	baseline-20m	super-resolution
number of bands	4	10	12
spatial resolution (m)	10	20	10
gravel	0.140	0.110	0.138
vegetation	0.166	0.161	0.193
water	0.262	0.225	0.270
total	0.189	0.165	0.200

The pixel is still the basic unit for which land cover fractions are reported. We expected that by considering input satellite images with a higher spatial resolution we could improve the thematic accuracy of the produced fraction maps. However, the comparison of Landsat- and Sentinel-2-based maps in chapter 3.3.1 and Sentinel-2 10 m- and 20 m-based maps in the current chapter make it apparent that spectral resolution of input satellite images is more crucial for fraction map accuracy than spatial resolution. Because of the additional disadvantage of the high time intensity first for the super-resolution and then for the longer SMA, we decided to use the 20 m images in subsequent analysis.

3.3.5   Using Spectral Indices to Improve Fraction Map Accuracy

To increase the separability between the different land cover classes of interest, we calculated several spectral indices and included them along spectral bands reflectance values in the endmember selection process. We tested the contribution of the following spectral indices (Table 7):

- Anthocyanin Reflectance Index 1 (ARI1),
- Burn Area Index (BAI),
- Band Ration for Built-up Areas (BRBA),
- Enhanced Vegetation Index (EVI),
- Modified Normalised Difference Water Index (MNDWI),
- Modified Soil Adjusted Vegetation Index 2 (MSAVI2),
- Normalised Difference Infrared Index (NDII),
- Normalised Difference Vegetation Index (NDVI),
- NDVI multiplied by green band (NDVI-GREEN),
- Normalised Difference Water Index (NDWI),
- Normalised Pigment Chlorophyll Ratio Index (NPCRI), and
- Plant Senescence Reflectance Index (PSRI).

Table 7: Spectral indices selected to improve the separability of land cover classes.

Preglednica 7: Spektralni indeksi, izbrani za izboljšanje ločevanja med razredi pokrovnosti.

name	formula	reference
Anthocyanin Reflectance Index 1 (ARI1)	$ARI1 = \dfrac{1}{GREEN} - \dfrac{1}{RED\ EDGE}$	Gitelson et al., 2009
Burn Area Index (BAI)	$BAI = \dfrac{1}{(0.1 - RED)^2 + (0.06 - NIR)^2}$	Martín, 1998 cited in Chuvieco et al., 2002
Band Ratio for Built-up Areas (BRBA)	$BRBA = \dfrac{RED}{SWIR}$	Waqar et al., 2012
Enhanced Vegetation Index (EVI)	$EVI = 2.5\,\dfrac{NIR - RED}{NIR + 6RED - 7.5BLUE + 1}$	Huete et al., 1999, 1997
Modified Normalised Difference Water Index (MNDWI)	$MNDWI = \dfrac{GREEN - SWIR}{GREEN + SWIR}$	Du et al., 2016
Modified Soil Adjusted Vegetation Index (MSAVI2)	$MSAVI2 = \dfrac{2SWIR + 1 - \sqrt{(2SWIR + 1)^2 - 8(SWIR - NIR)}}{2}$	Qi et al., 1994
Normalised Difference Infrared Index (NDII)	$NDII = \dfrac{NIR - SWIR}{NIR + SWIR}$	Gao, 1996
Normalised Difference Vegetation Index (NDVI)	$NDVI = \dfrac{NIR - RED}{NIR + RED}$	Tucker, 1979
NDVI multiplied by green band (NDVI-GREEN)	$NDVIGREEN = \left(\dfrac{NIR - RED}{NIR + RED}\right) * GREEN$	Švab Lenarčič, 2018
Normalised Difference Water Index (NDWI)	$NDWI = \dfrac{GREEN - NIR}{GREEN + NIR}$	McFeeters, 1996
Normalised Pigment Chlorophyll Ratio Index (NPCRI)	$NPCRI = \dfrac{RED - BLUE}{RED + BLUE}$	Peñuelas et al., 1993, 1994
Plant Senescence Reflectance Index (PSRI)	$PSRI = \dfrac{RED - BLUE}{RED\ EDGE}$	Merzlyak et al., 1999

The potential contribution of each index to improved land cover separability was first assessed by visual comparison with reference data. We used Sentinel-2 images to test the contribution of spectral indices to SMA accuracy. Images from 2015, 2017, and 2020 were used, in line with the availability of reference data. For brevity, only the results based on the image acquired on 23 April 2020 and validated with field mapping data are shown.

Following these preliminary tests, a subset of spectral indices was chosen for further analysis. This subset of indices consisted of EVI, MNDWI, MSAVI2, NDII, NDVI, NDVI-GREEN, NDWI, and

46   Stančič, L. 2022. Monitoring Changes of Fluvial Gravel Bars with Remote Sensing.

PhD Th. Ljubljana, UL FGG, Interdisciplinary doctoral study programme Environmental Protection.

NPCRI. The final selection was made from indices which led to an increase in fraction map accuracy (Table 8).

Table 8: Improvement of the spectral mixture analysis by using spectral indices. Mean absolute error of fraction maps based on different input data derived from a Sentinel-2 image, acquired on 23 April 2020. Endmembers selected automatically.

Preglednica 8: Izboljšanje analize vsebnosti spektralnega signala z uporabo spektralnih indeksov. Povprečna absolutna napaka kart deležev pokrovnosti na podlagi različnih vhodnih podatkov, pridobljenih na podlagi posnetka Sentinel-2, zajetega 23. 4. 2020. Končni piksli izbrani samodejno.

image	baseline	all indices	selected indices
number of indices	0	8	5
gravel	0.062	0.058	0.056
vegetation	0.182	0.124	0.120
water	0.198	0.125	0.124
total	0.144	0.102	0.100
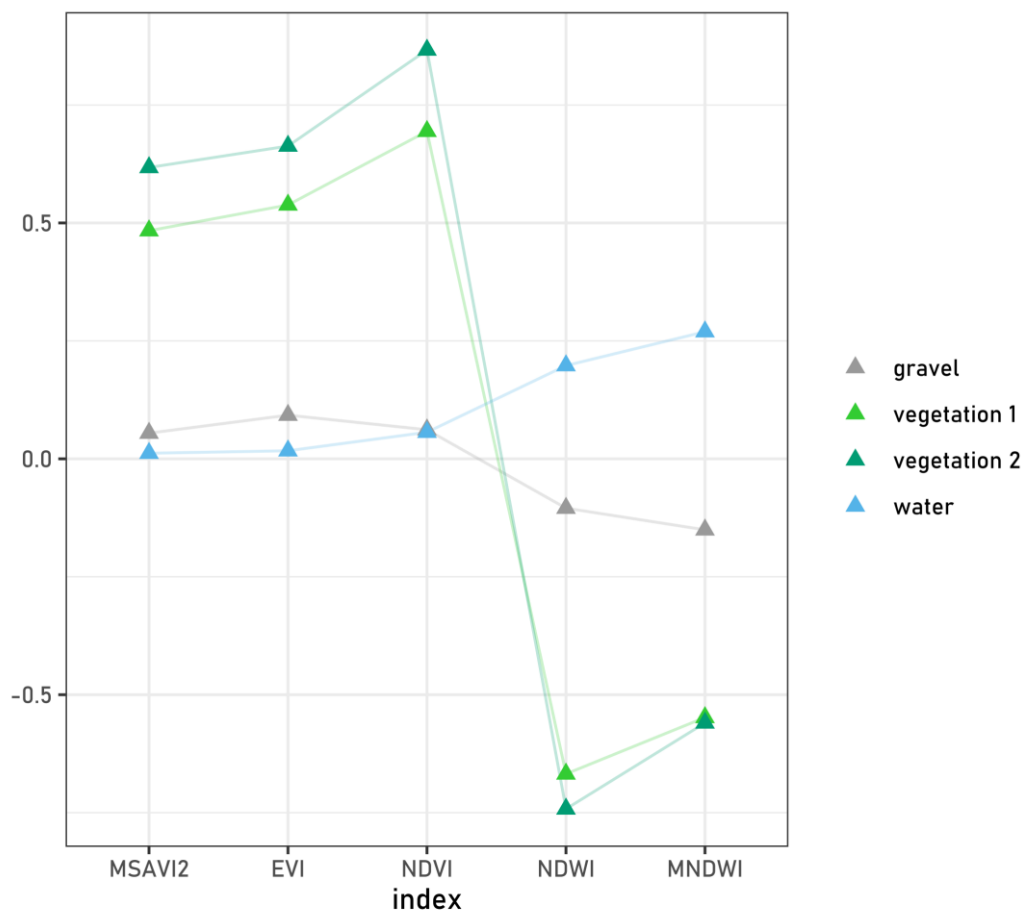
Figure 16: Values of the selected set of indices for the land cover classes of interest. Connecting lines are added for easier identification of values referring to the same land cover class.

Slika 16: Vrednosti izbranih indeksov za obravnavane razrede pokrovnosti. Povezovalne črte so dodane za lažje sledenje vrednostim posameznega razreda pokrovnosti.

We also selected indices with values which showed high separability between the land cover classes of interest (Figure 16). The presented endmembers were selected automatically. Two vegetation endmembers were selected before water and gravel were selected. Evidently, three endmembers were not sufficient to describe all of the land cover classes of interest. In further analysis, the fraction maps based on the two vegetation endmembers were added in subsequent analysis to result in a single vegetation fraction map. Index values for the different land cover classes of interest are similar to those in existing literature (Wu, 2004; Afrasinei et al., 2018). In particular, gravel bars have similar spectral index values to built-up areas (Xi et al., 2019). The selected spectral indices, which were thus chosen to complement the reflectance of the spectral bands, are EVI, MSAVI2, NDVI, NDWI, and MNDWI.

3.3.6   Conclusions on Input Satellite Images

Tests regarding the input satellite images for a successful SMA to map fluvial gravel bars led to four important findings for further analysis:

- Both Sentinel-2 and Landsat 8 images can be successfully used to produce accurate land cover fraction maps. Maps based on Landsat 7 have slightly lower accuracy, but still sufficient to provide meaningful information.

- Atmospheric correction improves the accuracy of fraction maps. Topographic correction introduces additional uncertainties and is therefore not recommended.

- For Sentinel-2, increasing the spatial and spectral resolution of input images to 10 m and 12 spectral bands using a deep neural network does not improve the accuracy of fraction maps compared to the baseline images with a 20 m spatial resolution and 10 spectral bands.

- The inclusion of spectral indices as input data for the SMA in addition to the spectral band information improves fraction map accuracies. The selected indices which lead to the highest separability between the land cover classes of interest and the most accurate fraction maps are EVI, MSAVI2, NDVI, NDWI, and MNDWI.

The next chapter explores the different methods and settings for endmember selection.

3.4   Endmember Selection

Endmembers are crucial for a successful SMA. We explored the impacts of different endmember selection strategies, namely a manual or automatic method, various numbers of selected endmembers, and diverse numbers of land cover classes for the endmembers to represent. Finally, we assessed the transferability of endmembers, i.e., the possibility of selecting endmembers on one image and using the same endmembers for the SMA of another image.
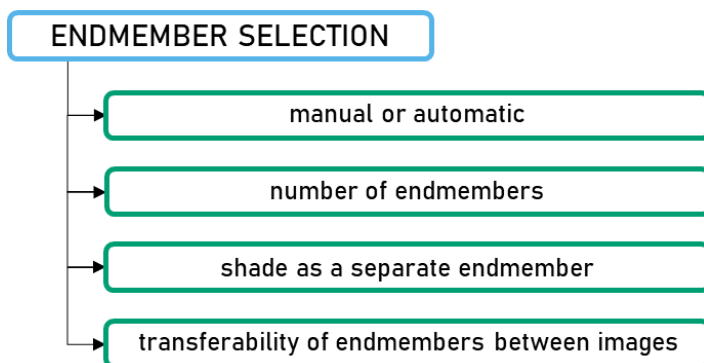
3.4.1   Manual or Automatic Endmember Selection

The manual endmember selection method is based on the use of reference data with a higher spatial resolution than the analysed satellite images to choose pure pixels where only a single land cover class is present. Several different pure pixels can be selected for one land cover class. Their spectral signatures and index values are combined by taking the average value, thus obtaining manual endmembers.

In the testing phase, we wanted to use the most representative and the best possible endmembers. At the same time, the method had to be comparable across different input satellite images. Therefore, we started with manual endmember selection on Landsat images, which have a lower spatial resolution and thus a lower probability of having pure pixels containing a single land cover class. For the endmember calculation, we selected all available spectrally pure pixels. This amounted to four pixels for gravel, twenty for vegetation, and nine for water. The same number of pixels was chosen for manual selection of endmembers on Sentinel-2 images. To increase comparability between the two different remote sensing systems, we selected endmembers at the same locations in each case.

Automatic endmember selection was done with an implementation of the N-FINDR algorithm in the Python package pysptools (version 0.15.0) (Therien, 2018). We started by defining three different endmembers. If the selected endmembers did not represent the three land cover classes of interest, we increased the number of endmembers until all desired land cover classes were represented with at least one endmember.

Table 9: Pixel-wise mean absolute error per land cover class for different images analysed using different endmember selection methods. Best results per land cover class in bold.

Preglednica 9: Povprečna absolutna napaka po pikslih za karte deležev pokrovnosti na podlagi različnih satelitskih posnetkov z različnimi metodami izbora končnih pikslov za izbrane razrede pokrovnosti. Najboljši rezultati za vsak razred pokrovnosti v krepki pisavi.

land cover class	Landsat 7, 9. 7. 2015		Sentinel-2, 11. 7. 2015		Landsat 8, 25. 4. 2020		Sentinel-2, 23. 4. 2020	
	manual	automatic	manual	automatic	manual	automatic	manual	automatic
gravel	0.087	0.094	0.078	0.082	**0.069**	0.071	0.095	0.124
vegetation	0.114	0.140	0.111	0.139	**0.108**	0.124	**0.108**	0.157
water	0.124	0.141	0.082	0.097	**0.074**	0.097	0.080	0.098
total	0.108	0.125	0.090	0.106	**0.084**	0.097	0.094	0.126

The two different endmember selection methods were compared on four satellite images: two Sentinel-2, one Landsat 7, and one Landsat 8. The results indicate that manually selected endmembers lead to more accurate land cover fraction maps (Table 9). Nevertheless, the accuracy achieved by using automatically selected endmembers is within 0.05 of that achieved by manually selected endmembers.

Importantly, gravel is mapped very successfully with both manually and automatically selected endmembers with little or no difference between the two selection methods.

When observing the errors at pixel level, it is clear that on a single pixel, the same land cover classes are frequently problematic for both the manually and the automatically selected pixels. Likewise, the direction and magnitude of the error are often very similar across endmember selection methods. Regarding the confusion of land cover classes, common misclassifications include the labelling of shallow water as gravel. This is not possible to overcome and has important implications, as the Soča is rarely over 2 m deep. The shallow depth means that electromagnetic radiation reaches the gravel riverbed, leading to reflectance values similar to surface gravel. Overall, gravel is mostly over-estimated, vegetation is under-estimated, while results for the water class are mixed.
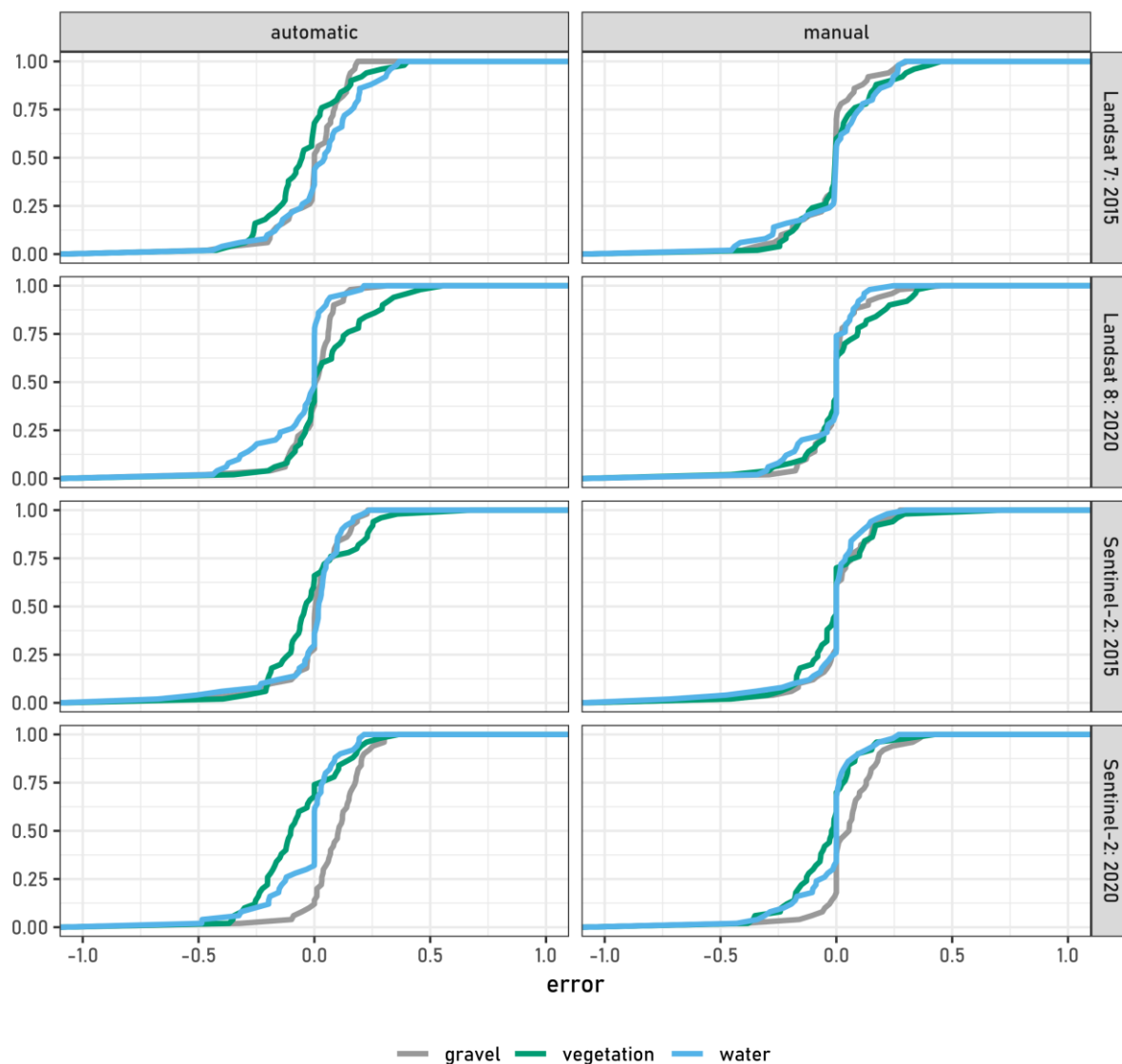
Figure 17: Cumulative distribution functions of pixel-wise errors per land cover class for different analysed images and different endmember selection methods.

Slika 17: Kumulativne porazdelitvene funkcije napak po pikslih za karte deležev pokrovnosti izbranih razredov na podlagi različnih satelitskih posnetkov z različnimi metodami izbora končnih pikslov.

The cumulative distribution functions have similar shapes regardless of the method used to select endmembers and the input satellite image (Figure 17). Nevertheless, the errors for manual endmember selection are generally closer to 0 than the errors for automatic endmember selection. Vegetation is the most problematic land cover class with the largest errors. The vegetation fraction is under-estimated in most cases. Water is generally well detected, with error values very close to 0, except on the Landsat 7 image. The Sentinel-2 image, acquired in 2020 and analysed with automatically selected endmembers, has the largest error, especially for vegetation and gravel.

This is also evident when comparing the average errors of the fraction maps (Table 10, Table 11). The errors for gravel are the lowest, except for the Sentinel-2 image acquired in 2020. The standard deviation of the errors is comparable for all land cover classes considered. However, in all analysed images, the standard deviation of errors is the lowest for gravel, which is important and beneficial for our study.

Table 10: Pixel-wise mean error with standard deviation per land cover class for different analysed images acquired in 2015 using different endmember selection methods.

Preglednica 10: Povprečna napaka s standardno deviacijo po pikslih za karte deležev pokrovnosti na podlagi različnih satelitskih posnetkov, zajetih leta 2015, z različnimi metodami izbora končnih pikslov za izbrane razrede pokrovnosti.

land cover	Landsat 7, 9. 7. 2015		Sentinel-2, 11. 7. 2015	
class	manual	automatic	manual	automatic
gravel	-0.018 ± 0.140	0.002 ± 0.134	0.013 ± 0.127	0.006 ± 0.132
vegetation	0.016 ± 0.165	-0.042 ± 0.177	0.001 ± 0.174	0.000 ± 0.189
water	0.002 ± 0.182	0.040 ± 0.181	-0.015 ± 0.159	-0.006 ± 0.163

Table 11: Pixel-wise mean error with standard deviation per land cover class for different analysed images acquired in 2020 using different endmember selection methods.

Preglednica 11: Povprečna napaka s standardno deviacijo po pikslih za karte deležev pokrovnosti na podlagi različnih satelitskih posnetkov, zajetih leta 2015, z različnimi metodami izbora končnih pikslov za izbrane razrede pokrovnosti.

land cover	Landsat 8, 25. 4. 2020		Sentinel-2, 23. 4. 2020	
class	manual	automatic	manual	automatic
gravel	0.005 ± 0.109	0.003 ± 0.134	0.062 ± 0.128	0.100 ± 0.113
vegetation	0.022 ± 0.172	0.061 ± 0.177	-0.038 ± 0.150	-0.070 ± 0.174
water	-0.026 ± 0.149	-0.064 ± 0.181	-0.026 ± 0.133	-0.033 ± 0.153

3.4.2   Different Numbers of Selected Endmembers

Automatic endmember selection may not result in the desired number of land cover classes when selecting the exact number of endmembers equal to the number of land cover classes of interest. In such cases, we increased the number of selected endmembers until all desired land cover classes were represented. We investigated whether increasing the number of endmembers leads to more accurate results covering the full land cover diversity, or whether endmembers tend to cluster around certain values. Such clustering would indicate that very similar endmembers are being selected.
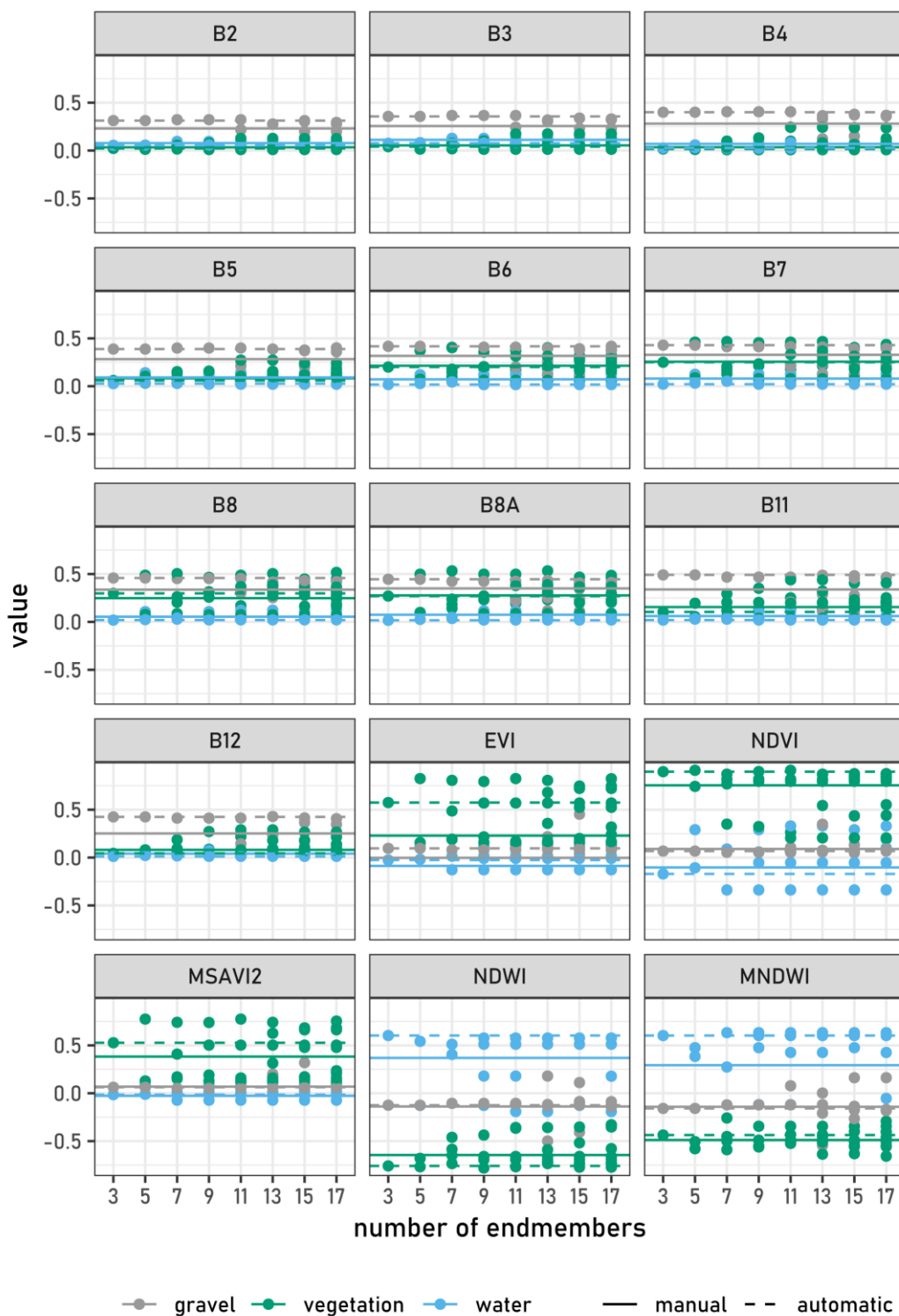
Figure 18: Values for all spectral bands and indices considered for different numbers of automatically selected endmembers. The dashed horizontal line shows the average value for all automatically selected endmembers. The solid horizontal line shows the values for manually selected endmembers.

Slika 18: Vrednosti odboja v vseh obravnavanih spektralnih kanalih in indeksih pri različnih številih samodejno izbranih končnih pikslov. Prekinjena vodoravna črta prikazuje povprečno vrednost vseh samodejno izbranih končnih pikslov. Neprekinjena vodoravna črta prikazuje vrednost ročno izbranih končnih pikslov.

The chosen algorithm for automatic endmember selection is implemented to allow the calculation of a maximum of 17 different endmembers. We started with the selection of three endmembers and increased this in steps of two up to 17. We looked for a possible clustering with plots of endmember values in selected spectral bands and indices (Figure 18, Figure 19).
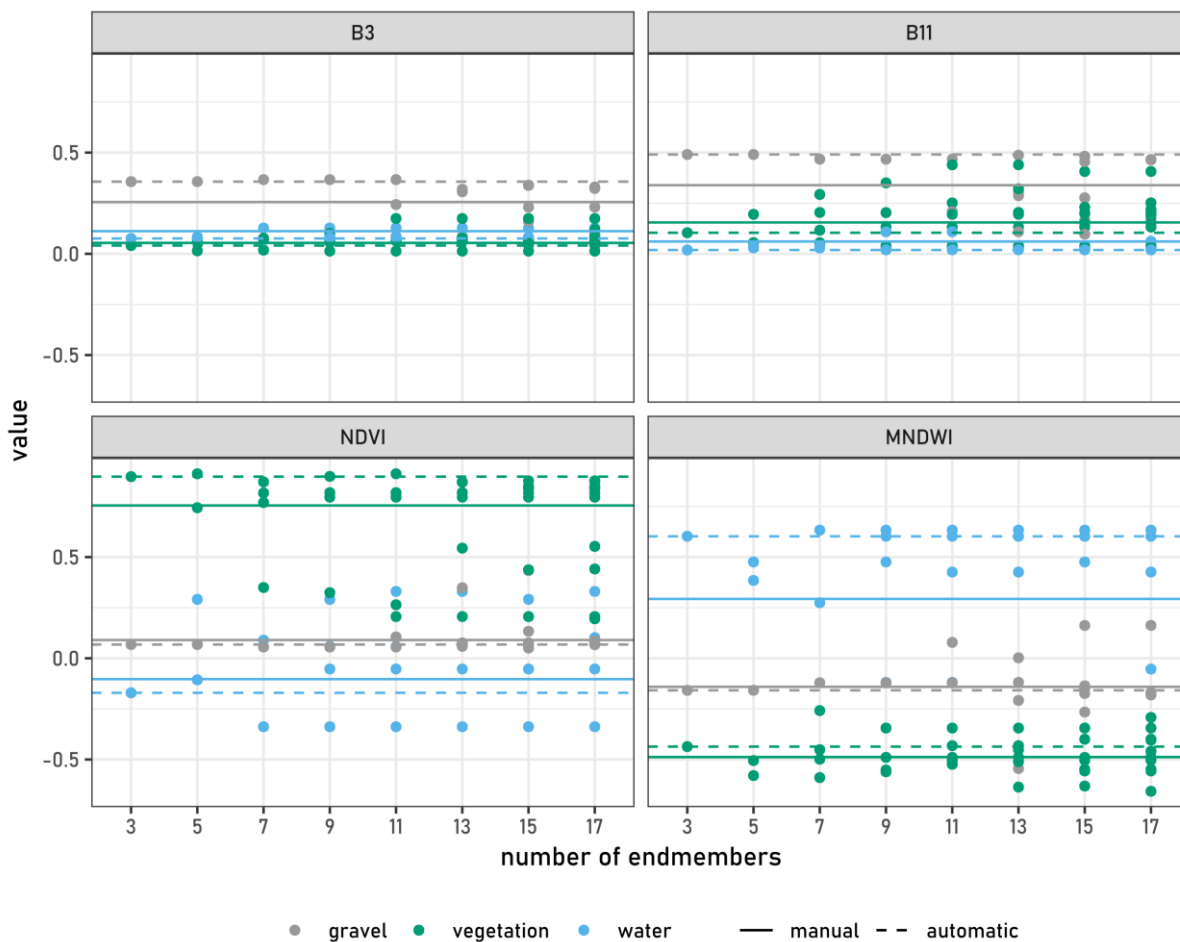
Figure 19: Values for selected spectral bands reflectance and indices for different numbers of automatically selected endmembers. The displayed bands and indices show the highest separability between the different land cover classes. The dashed horizontal line shows the average value of all automatically selected endmembers. The solid horizontal line shows the values for manually selected endmembers.

Slika 19: Vrednosti odboja v izbranih spektralnih kanalih in indeksih pri različnih številih samodejno izbranih končnih pikslov. Prikazana kanala in indeksa najbolje kažejo razlike med obravnavanimi razredi pokrovnosti. Prekinjena vodoravna črta prikazuje povprečno vrednost vseh samodejno izbranih končnih pikslov. Neprekinjena vodoravna črta prikazuje vrednost ročno izbranih končnih pikslov.

A visual inspection of the plots of endmember values shows that clustering starts at five automatically selected endmembers. As the number of endmembers is increased, the newly selected values are somewhere between the extreme values already selected with a set of five or even three endmembers.

3.4.3   Considering Shade as a Separate Endmember

Shade is a frequently selected endmember in SMA studies (e.g., Adams, 1995; Dennison and Roberts, 2003; Amaral et al., 2015). The reflectance of shaded pixels can be similar to that of surface water, so the inclusion of a shade endmember has been shown to be particularly important when mapping water (Liu et al., 2020). Areas detected as shade would then be masked out from the analysis. We therefore conducted a series of tests with shade as an additional endmember. Sentinel-2 satellite images were used for the analysis. Two time periods were considered, early summer 2015 and mid-autumn 2017. The selected time periods were primarily related to the availability of reference data, but also allowed comparison of the effects of different Sun angles and the consequent presence of shade. The resulting fraction maps were validated using the area-based approach by comparing the presence of each land cover class on the fraction map to that on the reference data (Figure 20).
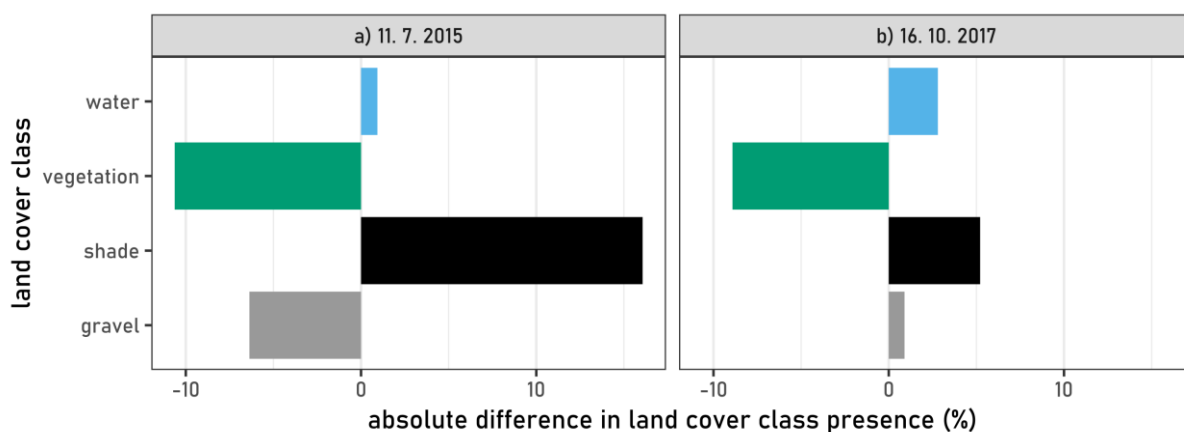
Figure 20: Absolute difference in the presence of land cover classes between the reference data and the satellite image-based land cover fraction map with shade as a separate endmember.

Slika 20: Absolutna razlika v prisotnosti razredov pokrovnosti med referenčnimi podatki in karto deležev pokrovnosti na podlagi satelitskih posnetkov s senco kot ločenim končnim pikslom.

The results show that the inclusion of shade as an additional endmember does not lead to more accurate fraction maps. Evidently, shade is a difficult class to map, as its detection accuracy is frequently the lowest of the classes considered. In both fraction maps examined, the presence of shade is over-estimated. This is interesting because one of the reference images was acquired earlier in the day and

the other later in the day than the analysed satellite images (Table 12). The over-estimation of shade is apparently larger than the variability of shade presence due to the different Sun angles.

Table 12: Acquisition times for the remote sensing data considered in the shade analysis (data source: ESA, 2021; Surveying and Mapping Authority of the Republic of Slovenia, 2021e).

Preglednica 12: Čas zajema daljinsko zaznanih podatkov, uporabljenih za analizo senc (vir podatkov: ESA, 2021; GURS, 2021e).

image ID	use	image system	acquisition date	acquisition time (UTC)
1	input	Sentinel-2	11. 07. 2015	10:00
2	reference	orthophoto	26. 05. 2015	07:29
3	input	Sentinel-2	16. 10. 2017	10:16
4	reference	orthophoto	14. 10. 2017	11:51

In addition to considering shade as a separate land cover class, we explored the impact of taking it into account as part of the training samples for other land cover classes. We included shade in the training samples for classifying the reference data to better represent the true spectral composition of the land cover class. The already acquired training samples for shade were reclassified to other land cover classes of interest, or discarded if they contained mixed land cover. Baseline reference data were produced from the remaining land cover classes only, excluding all shade training samples. Results were validated using the area-based method (Figure 21).
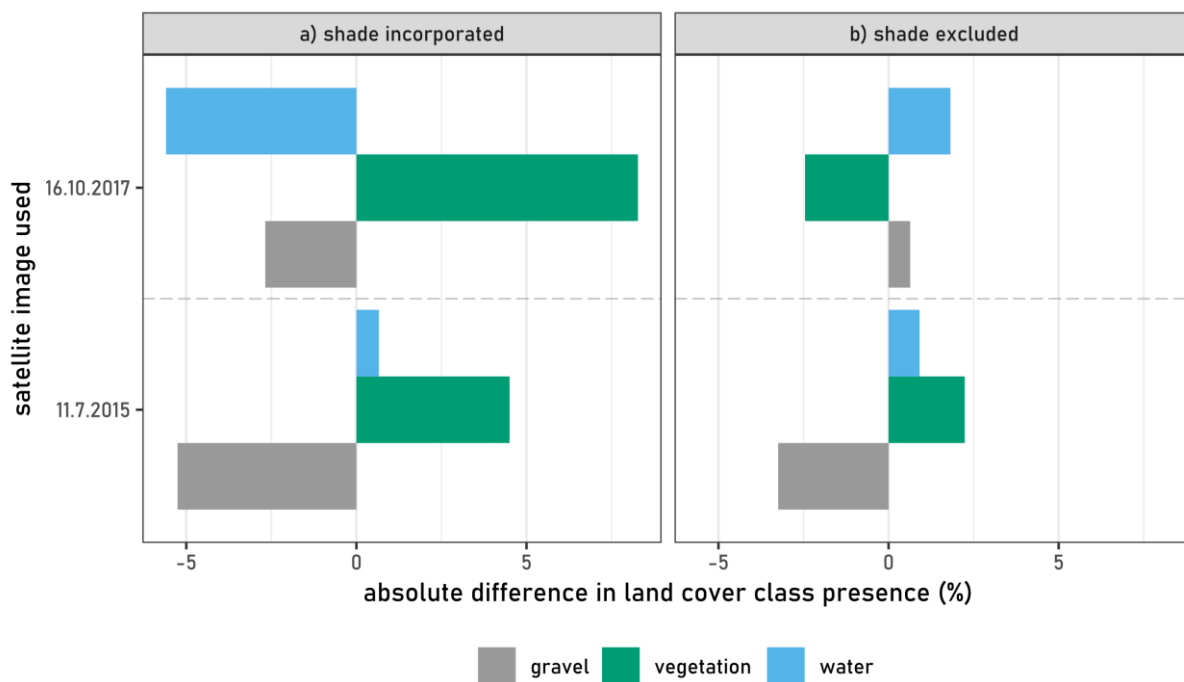
Figure 21: Absolute difference in the presence of land cover classes between the reference data and the satellite image-based land cover fraction map. For the reference data, shade is included in the training samples for other land cover classes (left) or completely excluded from the training samples (right).

Slika 21: Absolutna razlika v prisotnosti razredov pokrovnosti med referenčnimi podatki in karto deležev pokrovnosti na podlagi satelitskih posnetkov. Pri referenčnih podatkih je senca vključena med učne vzorce za druge razrede (levo) ali popolnoma izključena iz učnih vzorcev (desno).

The fraction maps that do not include shade as a separate endmember are more accurate than those that do. The best results are obtained when shade is completely excluded from the training samples for the reference data. Rather than providing a better representation of the land cover class of interest, shade appears to introduce additional variability that leads to confusion between classes and consequently lower map accuracy. When selecting training samples for reference data, it is therefore advisable to select only pixels that do not contain shade. In our case, the selection was manual so it was easily possible to exclude shade by visual interpretation. If applying an automatic training sample selection method, potential areas of shade can be masked out in advance, for example using a digital elevation model for terrain shadow and a buffer around forested areas for vegetation shade. Despite excluding shade from training samples, subsequent analysis classifies land cover classes with a satisfactory accuracy, even if they are covered with shade.

3.4.4 Transferability of Endmembers Selected on One Image for the Analysis of Different Images

We explored the possibility of applying a set of endmembers selected on one satellite image for the SMA of another image acquired with the same remote sensing system. In choosing the satellite images

to be considered, we followed the availability of reference data, both for the selection of endmembers and for the validation of fraction maps. Thus, for testing the Sentinel-2 images we used endmembers selected on an image from 23 April 2020 to unmix an image from 11 July 2015 (Table 13).

Table 13: Class-wise mean absolute error with endmembers (EM) chosen on the same or a different image, for images acquired with Sentinel-2. Values are deviations from averages. M – manual EM selection method; A – automatic EM selection method. Best results per land cover class in bold.

Preglednica 13: Povprečna absolutna napaka po razredih pokrovnosti, s končnimi piksli (EM), izbranimi na istem in na drugem posnetku, za posnetke Sentinel-2. Vrednosti so odstopanja od povprečja. M – ročna metoda izbora EM; A – samodejna metoda izbora EM. Najboljši rezultati za vsak razred pokrovnosti v krepki pisavi.

acquisition date of analysed image		11. 07. 2015		11. 07. 2015		23. 04. 2020		23. 04. 2020	
acquisition date of EM selection image	average	11. 07. 2015		23. 04. 2020		11. 07. 2015		23. 04. 2020	
EM selection method		M	A	M	A	M	A	M	A
gravel	0.093	**−0.015**	−0.011	−0.013	0.011	−0.009	0.005	0.002	0.030
vegetation	0.136	−0.025	0.004	**−0.037**	−0.010	0.024	0.052	−0.028	0.021
water	0.093	−0.011	0.004	**−0.014**	−0.011	0.023	0.019	**−0.014**	0.005
total	0.108	−0.017	−0.001	**−0.021**	−0.003	0.013	0.025	−0.013	0.019

We also considered the Landsat 8 system, where endmembers selected on an image from 25 April 2020 were taken for the SMA of an image from 17 July 2015 (Table 14). Endmembers were selected using both the manual and automatic methods. The same number of endmembers was considered for both selection methods. For Sentinel-2, we selected one endmember for gravel, two for vegetation, and two for water; for Landsat 8, there was one endmember for gravel, three for vegetation, and two for water.

Table 14: Class-wise mean absolute error with endmembers (EM) chosen on the same or a different image, for images acquired with Landsat 8. M – manual EM selection method; A – automatic EM selection method. Best results per land cover class in bold.

Preglednica 14: Povprečna absolutna napaka po razredih pokrovnosti, s končnimi piksli (EM), izbranimi na istem in na drugem posnetku, za posnetke Landsat 8. Vrednosti so odstopanja od povprečja. M – ročna metoda izbora EM; A – samodejna metoda izbora EM. Najboljši rezultati za vsak razred pokrovnosti v krepki pisavi.

acquisition date of analysed image		17. 07. 2015		17. 07. 2015		25. 04. 2020		25. 04. 2020	
acquisition date of EM selection image	average	17. 07. 2015		25. 04. 2020		17. 07. 2015		25. 04. 2020	
EM selection method		**M**	**A**	**M**	**A**	**M**	**A**	**M**	**A**
gravel	0.096	−0.022	0.019	−0.017	−0.001	**−0.027**	0.100	**−0.027**	−0.025
vegetation	0.132	−0.035	0.101	**−0.049**	−0.012	−0.009	0.035	−0.024	−0.008
water	0.101	−0.016	0.071	−0.021	0.015	−0.022	0.004	**−0.026**	−0.004
total	0.109	−0.024	0.063	**−0.029**	0.001	−0.019	0.046	−0.026	−0.012

The results show that the SMA can achieve high accuracy with transferred endmembers. Transferred endmembers can even lead to better results than those selected on the analysed image. The transfer of endmember is successful for all land cover classes considered. Mapping accuracy changes the least for gravel endmember transfer. Transfer of water endmembers is the most uncertain and results in the largest differences in mapping accuracy. Both manually and automatically selected endmembers can be successfully transferred. Differences in accuracies due to the transfer of endmembers are smaller when using manually selected endmembers.

3.4.5   Conclusions on Endmember Selection

In this chapter, several features related to the selection of endmembers for SMA were explored and the following observations were made:

-   Automatically selected endmembers can be used to produce fraction maps with similar accuracy as manually selected endmembers. However, it is necessary to inspect the automatically selected endmembers because various spectral and land cover outliers can inherently be selected as endmembers.
-   The optimal total number of endmembers for SMA using multispectral images is between three and five. Fraction maps based on endmembers representing the same land cover class can be combined after the SMA. Increasing the number of automatically selected endmembers to more

than five leads to many different endmembers being considered for a single land cover class of interest, and thus to redundant information.

- The developed method does not allow accurate detection of shade. On the other hand, the inclusion of shade pixels in other land cover classes does not seem to affect the accuracy of the fraction maps.
- In the study area during the leaf-on season, the endmembers selected on one satellite image can be successfully used for the SMA of another satellite image acquired with the same remote sensing system.

Having established the endmember selection process, the next section presents the resulting land cover fraction maps and compares their accuracy to the accuracy of land cover maps produced using a hard classification method.

3.5   Soft Image Classification

In this section, the fraction maps produced using SMA are presented. The maps for different remote sensing systems are shown and compared with a hard classification method using the spectral angle mapper (SAM) (Kruse et al., 1993).
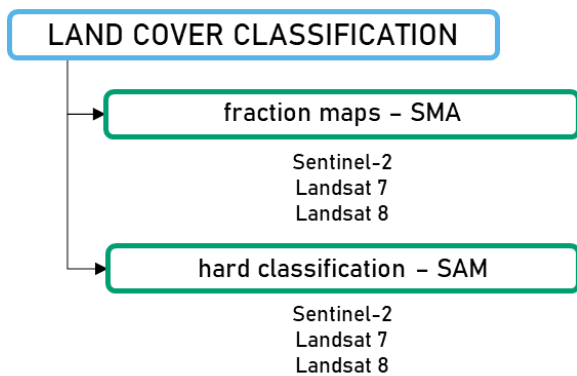
3.5.1   Land Cover Fraction Maps

Using the SMA-based mapping method, we produced land cover fraction maps for the three classes of interest – gravel, vegetation, and water. The maps were generated using Sentinel-2, Landsat 7, and Landsat 8 satellite images. Upon visual inspection, the maps look informative, with gravel occurring in rounded, elongated shapes, resembling gravel bars. Different types of gravel bars can be distinguished, including those forming in the middle of the river and those developing along the river bank. Vegetation is detected in the riparian zone along the river banks. Water surfaces are linear and connected. Comparing the 2015 and 2020 maps, changes in the size and location of gravel bars are evident. The dynamics of gravel bars confirm findings from the literature that one type of gravel bar can be

transformed into another over time (Robert, 2003). Fraction maps produced with manually and automatically selected endmembers show no visible differences (Figure 22).
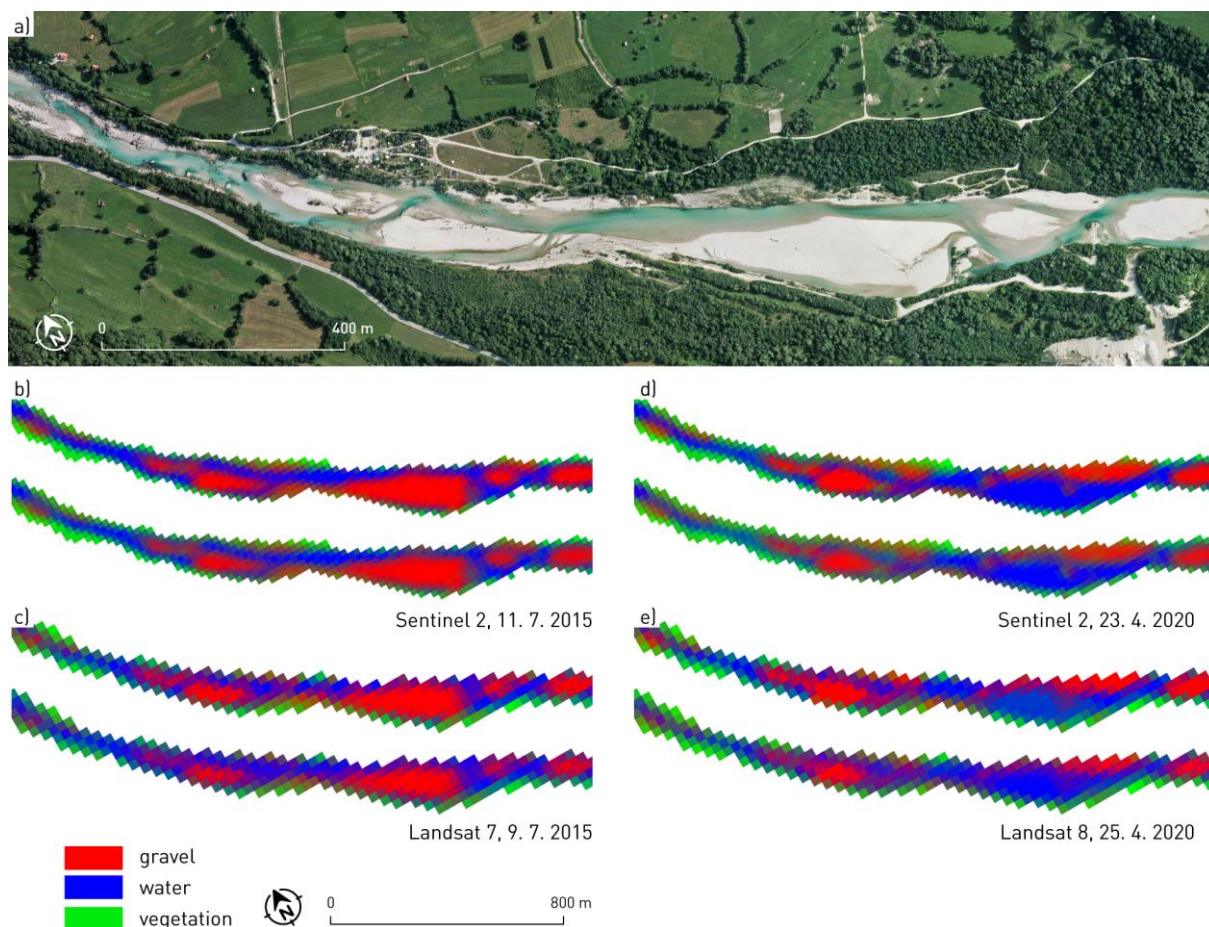
Figure 22: Land cover fraction maps for a section of the study area on the Soča River. a) Observed river section on a true colour orthophoto (data source: Surveying and Mapping Authority of the Republic of Slovenia, 2021e). b) – c) Resulting fraction maps. Maps produced with manually selected endmembers shown at the top and maps produced with automatically selected endmembers shown at the bottom.

Slika 22: Karte deležev pokrovnosti za izsek študijskega območja na reki Soči. a) Prikaz opazovanega izseka na barvnem ortofotu (vir podatkov: GURS, 2021e). b) – c) Izdelane karte deležev pokrovnosti. Karte na podlagi ročno izbranih končnih pikslov prikazane zgoraj in karte na podlagi samodejno izbranih končnih pikslov prikazane spodaj.

3.5.2   Comparison of Results with Hard Classification

To additionally assess the proposed soft classification mapping method, we compared it with a hard classification method. We selected the spectral angle mapper (SAM) classification (Kruse et al., 1993) based on the existing literature and because similar input data can be used, making the two methods easy to compare (Dennison et al., 2004). The endmember spectral signatures from SMA were used as input spectra for SAM. We compared the two classification methods based on accuracy assessment with

reference to VHR data and by comparing their respective error metrics. For SMA, we observed the root-mean-square error (RMSE), which is a commonly used metric to describe the error of the unmixed signal (Dubovyk et al., 2015; Somers et al., 2011). For each pixel, the predicted reflectance values are calculated based on the land cover class fraction determined by the SMA. The RMSE is then computed as the mean difference between the modelled and observed reflectance. For SAM, we reported the spectral angle between the reflectance values of a single pixel and the reflectance values of the endmember representing the land cover class as which that pixel was classified. Thus, a large spectral angle signifies that the spectral signature of the pixel is very different from the spectral signature of the endmember representing the land cover class to which the particular pixel was assigned. To compare SMA and SAM, the two respective error values were extracted for 1000 randomly selected pixels. Additionally, accuracy was evaluated both pixel-wise and study area-wise. The pixel-wise assessment was performed for 50 randomly selected map pixels by comparing their land cover with that obtained based on VHR reference images. In this case, we expected the soft classification to perform better, as it is able to detect sub-pixel land cover presence fractions. We also assessed the mapping accuracy for the whole study area by looking at the detected land cover presence for each class of interest and comparing it to the reference data.
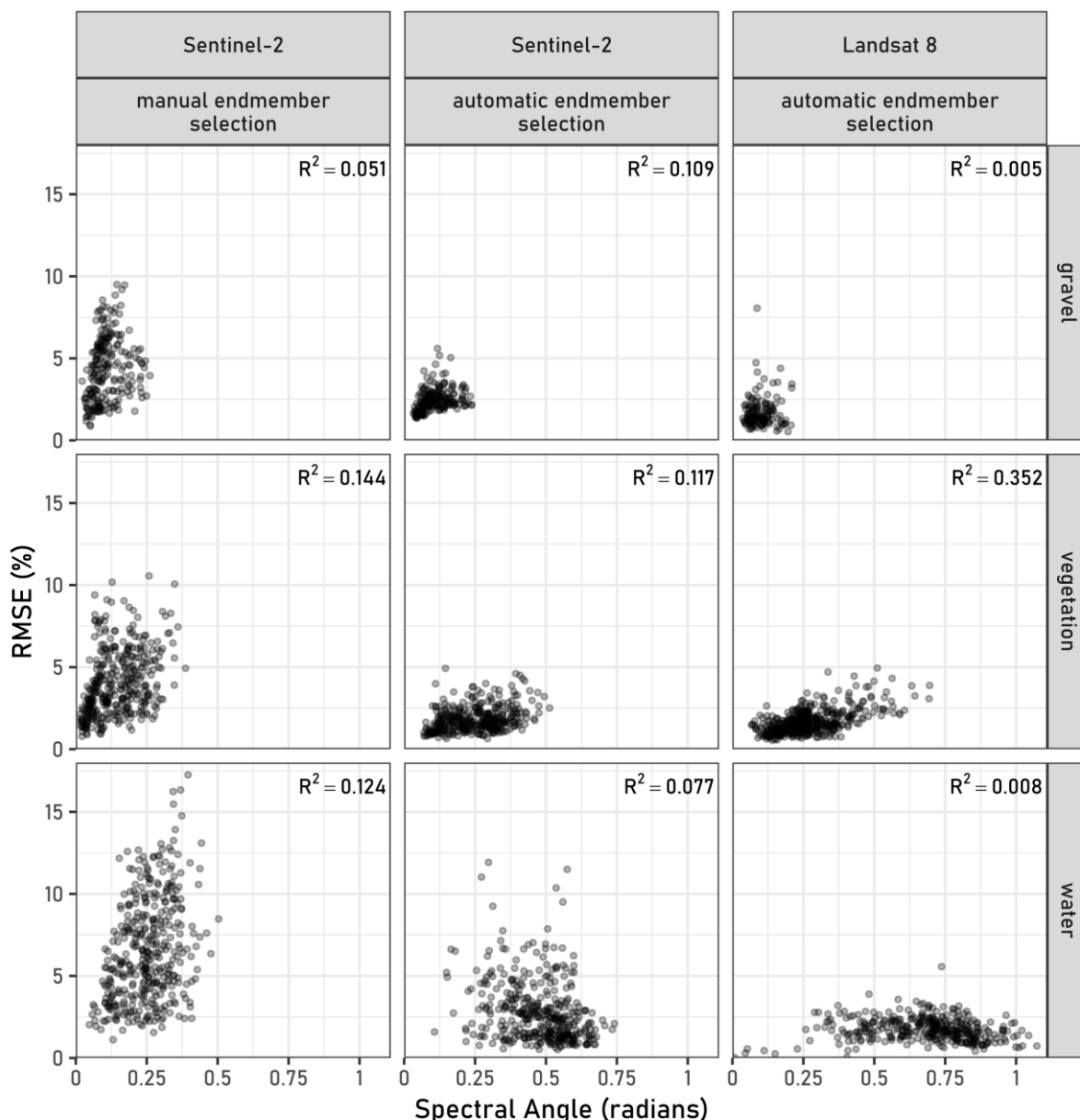
Figure 23: Comparison of RMSE and spectral angle for different land cover classes, remote sensing systems, and endmember selection methods. Values are for land cover maps based on images from 23 April 2020 (Sentinel-2) and 25 April 2020 (Landsat 8).

Slika 23:   Primerjava RMSE in spektralnega kota za različne razrede pokrovnosti, sisteme daljinskega zaznavanja in metode izbora končnih pikslov. Vrednosti se nanašajo na karte pokrovnosti na podlagi posnetkov, zajetih 23. 4. 2020 (Sentinel-2) in 25. 4. 2020 (Landsat 8).

We present the comparison of error metrics for images acquired in 2020 (Figure 23). The Sentinel-2 and Landsat 8 were compared based on models that use automatically selected endmembers. The two different endmember selection methods – manual and automatic – were assessed using Sentinel-2 images. The results show that the error metrics of the two classification methods are not strongly linearly correlated. The highest R^2 value (0.352) was obtained for vegetation on the Landsat 8 image. This

indicates that, for example, a pixel that was accurately classified by the soft classification was not necessarily classified equally well by the hard classification. For the Landsat 8 image, water pixels were classified well by SMA, but not by SAM. Both soft and hard classification produced the most accurate models for gravel, while water proved the most difficult to classify. Gravel has a uniform spectral response that can be modelled well even with few samples. Water appears to have a highly variable spectral response which is difficult to model accurately. One of the possible reasons for this variability is the non-uniform depth of water, which ranges from a few centimetres to several metres, leading to the occasional inclusion of the riverbed in the spectral signal. Additionally, the presence of rapids in the river causes whitewater, which has a different spectral response than the less turbulent sections of the river. Regarding the endmember selection methods, manually selected endmembers lead to smaller spectral angles, but a higher RMSE than automatically selected endmembers. One explanation for this lies in the inherent characteristics of the two endmember selection methods. The automatic method searches for endmembers with the extreme spectral properties and, consequently, the largest spectral angle relative to the spectral responses of other pixels. The manual method, on the other hand, uses endmembers that are the average spectra, more similar to a wider range of other pixels and result in smaller spectral angles. However, the manually selected endmembers cannot account for the full range of spectral variability in the image, which leads to a high RMSE. For gravel, a low RMSE and small spectral angles were achieved for the models for both Landsat 8 and Sentinel-2. The hard classification of vegetation was slightly better with Landsat 8, possibly due to the larger number of spectral bands in the red edge range. Water was modelled with very large spectral angles for Sentinel-2 and even larger ones for Landsat 8, again most likely due to the high spectral variability of water surfaces.

The comparison with the hard classification was also made based on the accuracy of the representation of the actual land cover. For brevity, only results based on images acquired in 2020 are shown. In situ data from field mapping were used as reference. First, we assessed the pixel-wise accuracy using MAE (Table 15). As expected, the soft classification performed much better, because the hard classification is not able to convey information about land cover at the sub-pixel level.

Table 15: Mean absolute error for a pixel-wise comparison of soft and hard classification per land cover class. The Sentinel-2 image was acquired on 23 April 2020. The Landsat 8 image was acquired on 25 April 2020. EM – endmember. Best results per land cover class in bold.

Preglednica 15: Povprečna absolutna napaka za primerjavo mehke in trde klasifikacije po pikslih glede na razrede pokrovnosti. Posnetek Sentinel-2 je bil zajet 23. 4. 2020. Posnetek Landsat 8 je bil zajet 25. 4. 2020. EM – končni piksel. Najboljši rezultati za vsak razred pokrovnosti v krepki pisavi.

| image | Sentinel-2 | | | | Landsat 8 | |
| EM selection | manual | | automatic | | automatic | |
classification	soft	hard	soft	hard	soft	hard
gravel	0.095	0.254	0.124	0.273	**0.071**	0.249
vegetation	**0.108**	0.131	0.157	0.131	0.124	0.193
water	**0.080**	0.159	0.098	0.180	0.097	0.213
total	**0.094**	0.181	0.126	0.195	0.097	0.218

Next, we examined the values for validating the area-wise presence of land cover classes (Table 16). The soft classification performed much better in modelling the presence of gravel and water. No important difference was found between the two classification methods for vegetation.

Table 16: Comparison of soft and hard classification accuracy based on land cover class presence in the validation area. Values indicate the difference to reference land cover class presence. The Sentinel-2 image was acquired on 23 April 2020. The Landsat 8 image was acquired on 25 April 2020. EM – endmember. Best results per land cover class in bold.

Preglednica 16: Primerjava mehke in trde klasifikacije po prisotnosti razredov pokrovnosti na območju validacije. Vrednosti prikazujejo razliko od prisotnosti razredov pokrovnosti na referenčnih podatkih. Posnetek Sentinel-2 je bil zajet 23. 4. 2020. Posnetek Landsat 8 je bil zajet 25. 4. 2020. EM – končni piksel. Najboljši rezultati za vsak razred pokrovnosti v krepki pisavi.

| image | Sentinel-2 | | | | Landsat 8 | |
| EM selection | manual | | automatic | | automatic | |
classification	soft	hard	soft	hard	soft	hard
gravel	0.062	0.190	0.100	0.210	**0.003**	0.163
vegetation	**−0.038**	−0.045	−0.070	−0.045	0.061	0.042
water	**−0.026**	−0.147	−0.033	−0.167	−0.064	−0.205

3.5.3   Conclusions on Image Classification

The tests described in the previous chapters can be successfully used to produce land cover fraction maps. Both pixel-wise and study-area wise validation showed that such land cover maps derived from the so-called soft classification are more accurate than maps produced using hard classification methods. The proposed method can therefore be used for the development of a land cover time series and

subsequent monitoring of gravel bars. The construction of a land cover time series is presented in the next section.

3.6 Land Cover Time Series Development

In order to track the changes in land cover we analysed all of the available Sentinel-2 images for the study area that had less than 10% cloud cover on the whole image. For clarity, the results of the different endmember selection and data smoothing methods are presented based only on data for the time period from the years 2019 and 2020.
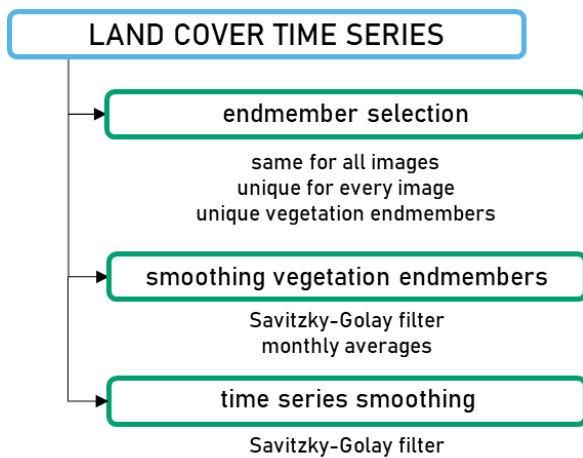
3.6.1 Endmember Selection for Time Series Analysis

We started with one endmember selected automatically for gravel, one for water, and two for vegetation. The two fraction maps based on the two vegetation endmembers were combined after the SMA to obtain a single fraction map of vegetation presence. Three different approaches were applied to determine which endmembers were used for the SMA:

- Same endmembers for all images: the endmembers selected on the image from 11 July 2015 were used to unmix all images in the time series.
- Unique endmembers for every image: endmembers were selected separately for each image, but always at the same location. The selected locations were visually inspected to ensure that the desired land cover was actually present.
- Unique vegetation endmembers: only vegetation endmembers were selected separately for each image. The gravel and water endmembers were transferred from the image acquired on 11 July 2015.

Land cover class and pixel purity were verified using satellite images and reference aerial orthophotos (Figure 24). The endmembers were selected automatically using the N-FINDR algorithm as described in Chapter 3.4.1 above. They therefore represent pixels with the most diverse spectral characteristics. In future studies, if the selection is done manually, in the case of water endmembers, a pixel closer to the centre of the river flow could be selected. In this way, it would be easier to ensure that water is indeed present on the selected pixel in different hydrological conditions.
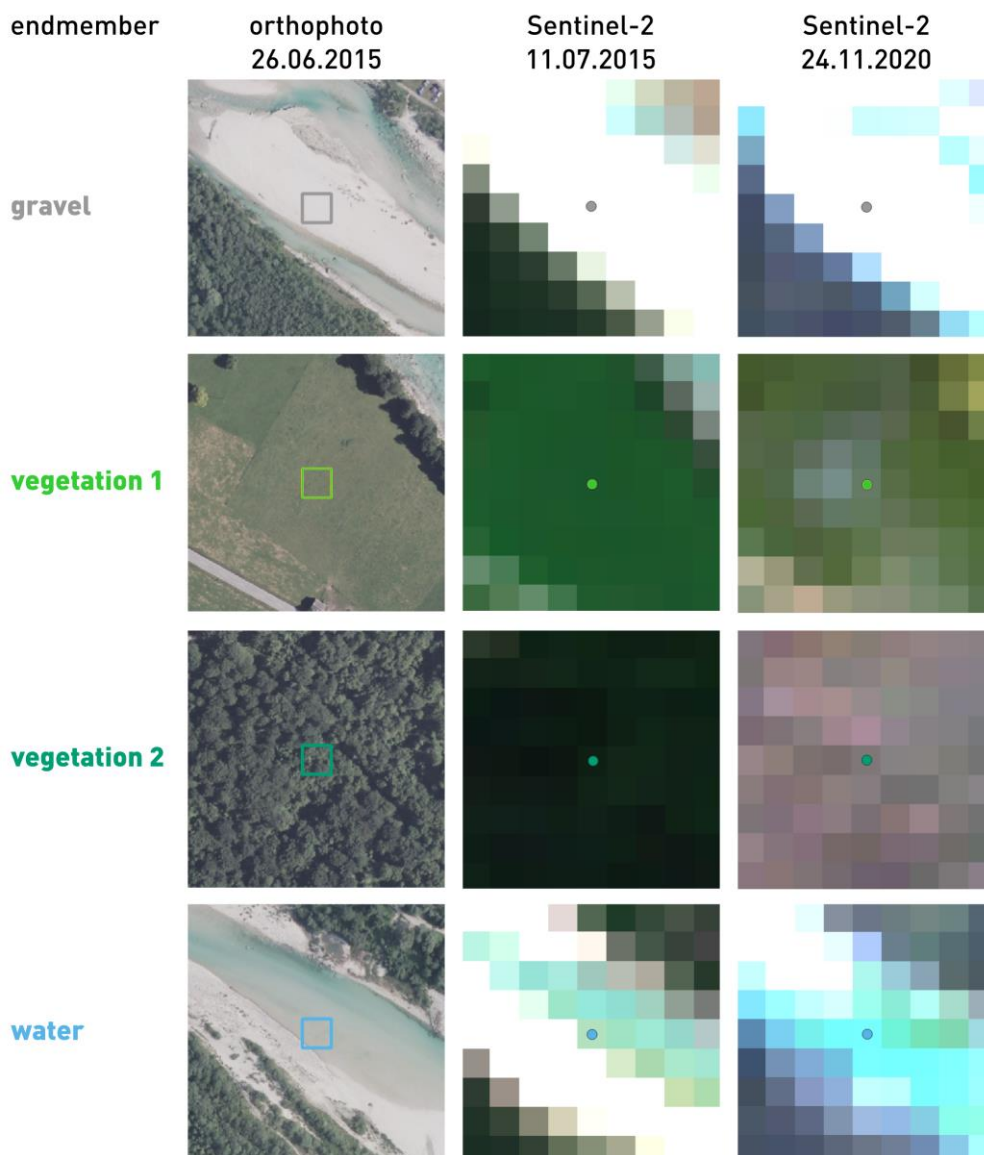
Figure 24: Pixels selected for unmixing on the first and last Sentinel-2 image of the time series used and on the aerial orthophoto, acquired on 26 June 2015 (basemap: ESA, 2021; Surveying and Mapping Authority of the Republic of Slovenia, 2021e).

Slika 24: Piksli, izbrani za analizo spektralnega signala na prvi in na zadnji sliki uporabljene časovne vrste posnetkov Sentinel-2 ter na letalskem ortofotu, zajetem 26.6.2015 (podlaga: ESA 2021; GURS, 2021e).

The location of the pixel for which the endmember values were extracted remained the same for all different endmember selection methods. However, the endmember values changed in accordance with the image reflectance values. For the uniquely selected endmembers, the fluctuations of their values over the year were evident (Figure 25).
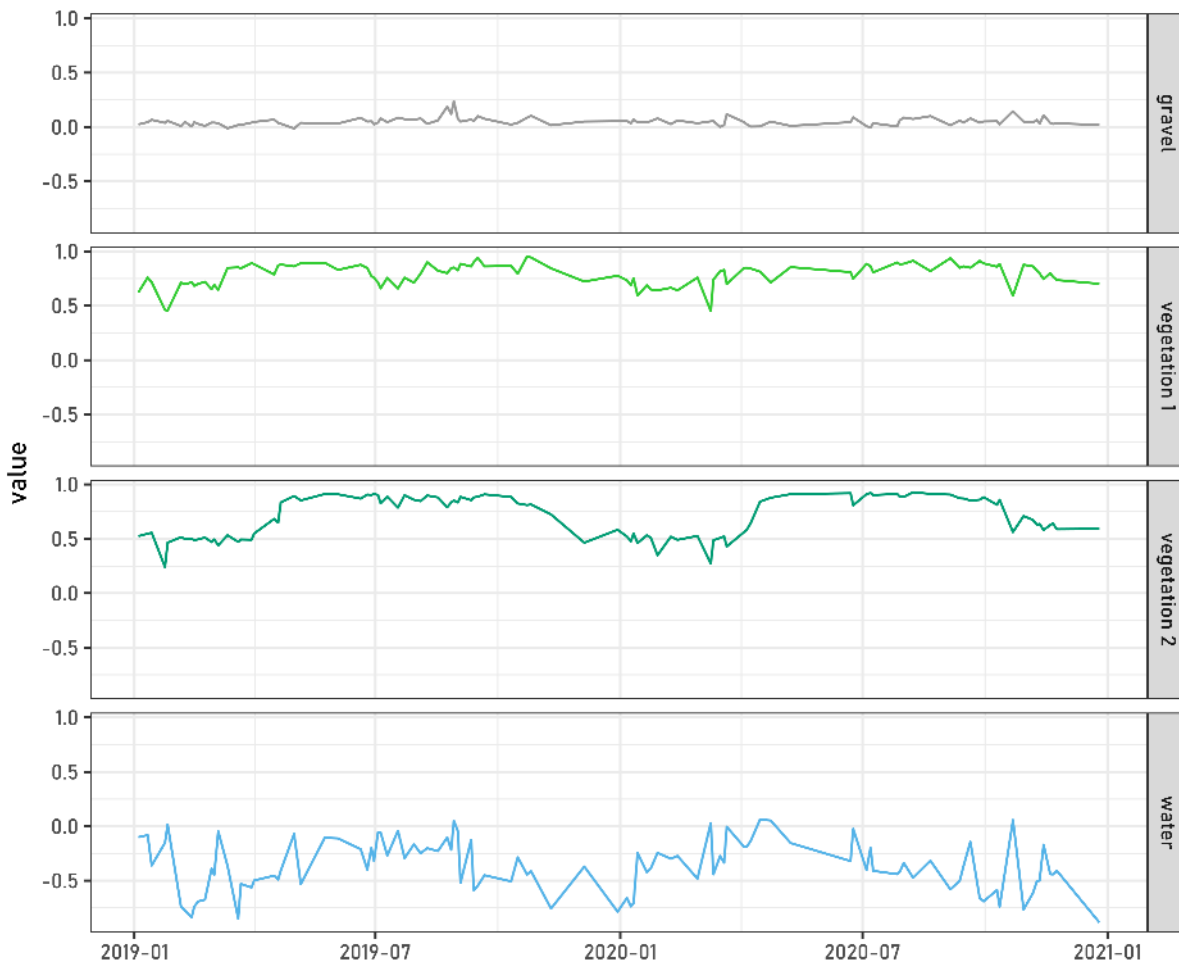
Figure 25: Time series of Sentinel-2 NDVI for the different selected endmembers.

Slika 25:   Časovna vrsta NDVI na podlagi posnetkov Sentinel-2 za izbrane končne piksle.

A visual comparison of the time series for the land cover classes of interest shows similar general trends and plot shapes, but also considerable differences in magnitude (Figure 26). The time series based on the same endmembers transferred to all images analysed appears to be the most stable.
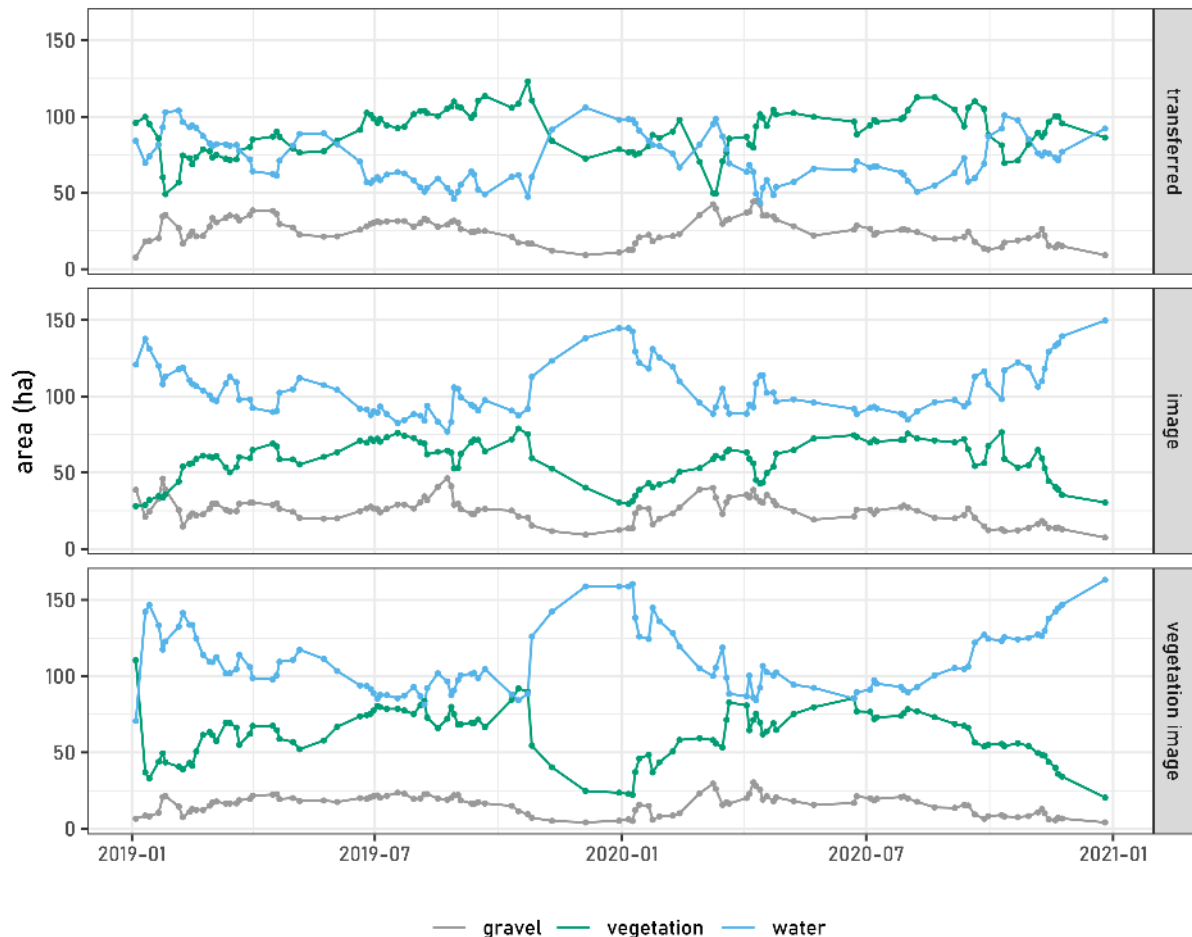
Figure 26: Time series of presence of different land cover classes in the study area based on three different endmember selection strategies.

Slika 26: Časovne vrste prisotnosti izbranih razredov pokrovnosti na študijskem območju glede na tri različne pristope izbora končnih pikslov.

The high presence of water in the winter months is not only due to the rise in water level, but also due to topographic shadow classified as surface water (Figure 27). Topographic shadow is therefore a cause for error. However, as described in chapter 3.4.3 above, this problem cannot be solved with the available topographic corrections. Moreover, the accuracy of shade detection with the proposed method is much lower than the accuracy for other land cover classes of interest. Further shade detection and elimination is beyond the scope of this work.
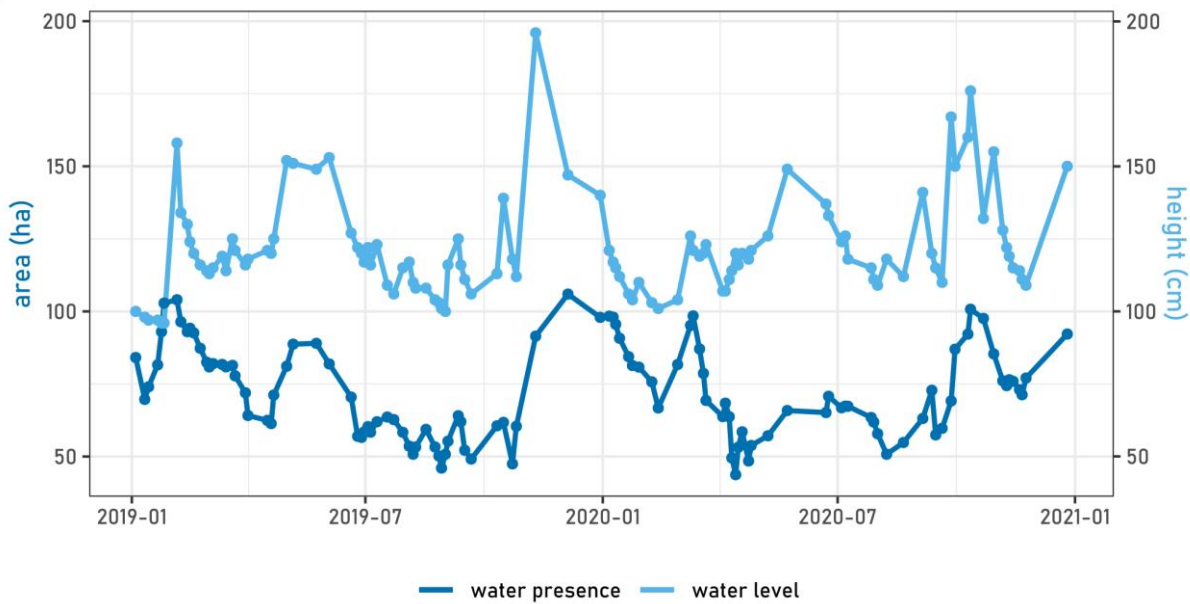
Figure 27: Time series of water presence, based on transferred endmembers, and water level measured at a gauging station in Kobarid (data source: Slovenian Environment Agency, 2021b).

Slika 27: Časovni vrsti prisotnosti vode na podlagi prenesenih končnih pikslov in vodostaja, izmerjenega na merilni postaji Kobarid (vir podatkov: Agencija RS za okolje, 2021b).

3.6.2   Smoothing Vegetation Endmembers for Time Series Analysis

A large variability in the presence of land cover classes is observed in the time series plots (Figure 26), particularly for vegetation. One possible reason for this could be the continuous change in spectral characteristics of vegetation due to phenology, and thus a difficulty in accurately identifying the vegetation land cover class on all images. We therefore performed additional tests using two approaches of averaging vegetation endmembers to make them more general and appropriate for analysing different images (Figure 28):

- The first method locally smooths the time series of vegetation endmember reflectance and index values with a Savitzky-Golay filter and uses the smoothed values for unmixing. We used a Savitzky-Golay filter implementation from the R package Signal (Signal developers, 2013).
- The second method calculates monthly averages of vegetation endmember values and then uses these averages to unmix all images acquired in that month.
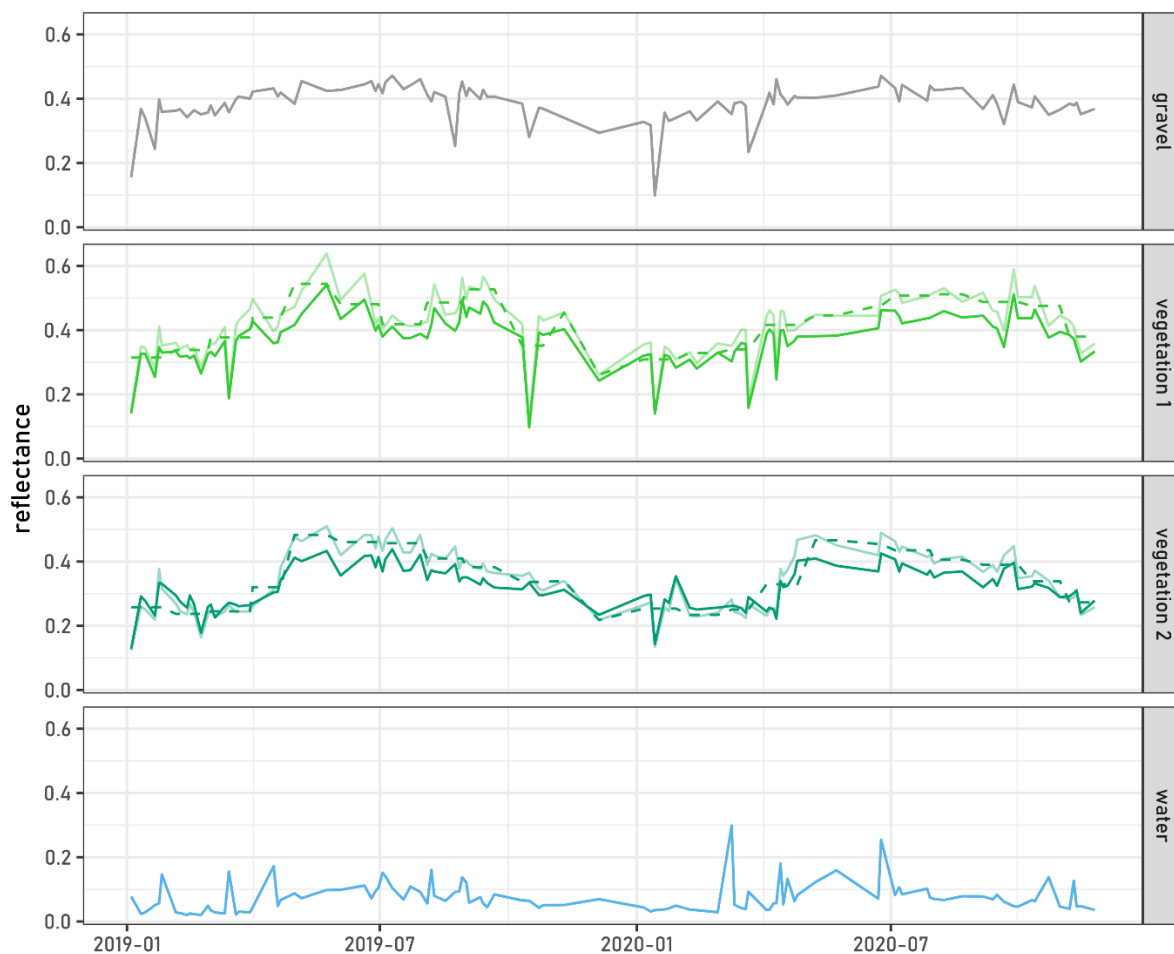
Figure 28: Time series for the different selected endmembers in the Sentinel-2 band 8A. Vegetation endmember values smoothed using a Savitzky-Golay filter. Vegetation endmember values averaged for each month shown with a dashed line. Unsmoothed vegetation endmember values shown in the background in lighter colours.

Slika 28: Časovna vrsta izbranih končnih pikslov v spektralnem pasu 8A na podlagi posnetkov Sentinel-2. Vrednosti končnih pikslov za vegetacijo zglajene s filtrom Savitzky-Golay. Vrednosti končnih pikslov za vegetacijo povprečene po mesecih prikazane s črtkano črto. Nezglajene vrednosti končnih pikslov za vegetacijo prikazane v ozadju z večjo prosojnostjo.

Plots of the time series data for selected land cover presence show no considerable difference between the different smoothing strategies for the vegetation endmembers (Figure 29). Since smoothing represents an additional processing step and lengthens the analysis process, we decided to omit it in further work.
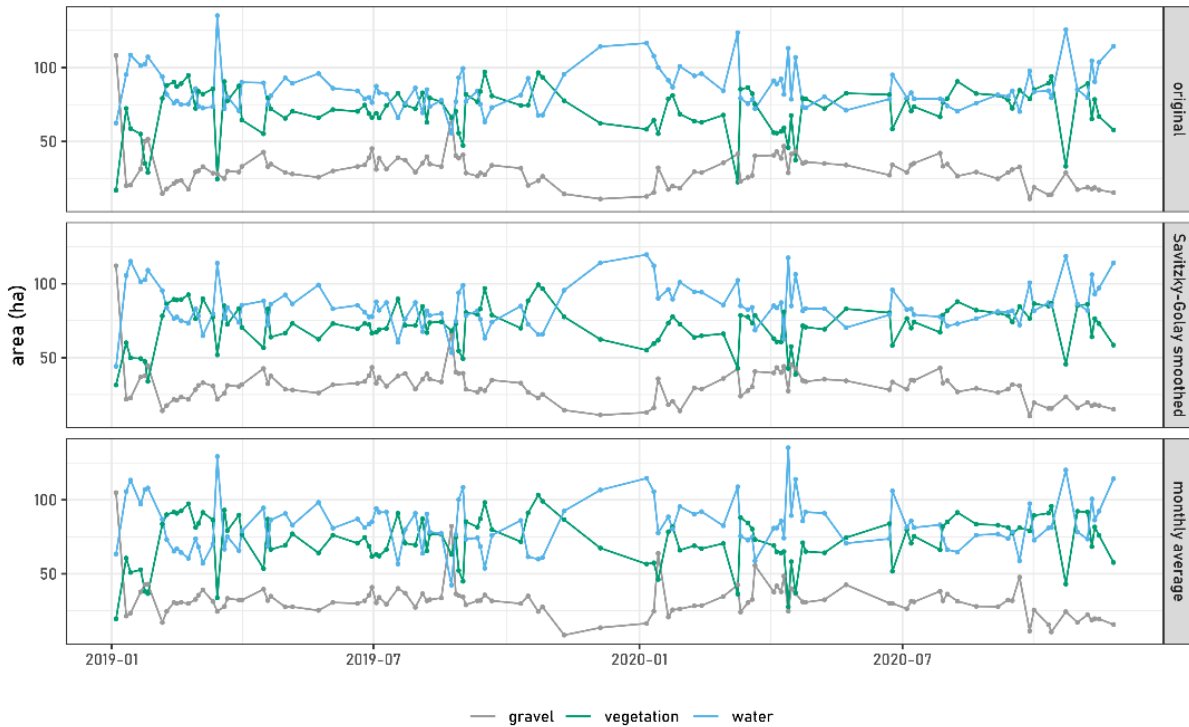
Figure 29: Time series of the presence of the selected land cover class based on different methods for smoothing the vegetation endmembers.

Slika 29: Časovna vrsta prisotnosti izbranih razredov pokrovnosti na podlagi različnih načinov glajenja signala končnih pikslov za vegetacijo.

3.6.3   Land Cover Time Series Smoothing

To better detect long-term changes in gravel bars, we attempted to remove outliers with smoothing. We used the Savitzky-Golay filter, which is implemented in the R package Signal (Signal developers, 2013). The contribution of smoothing was considerable, as significant changes and important trends were much easier to detect with visual inspection (Figure 30).
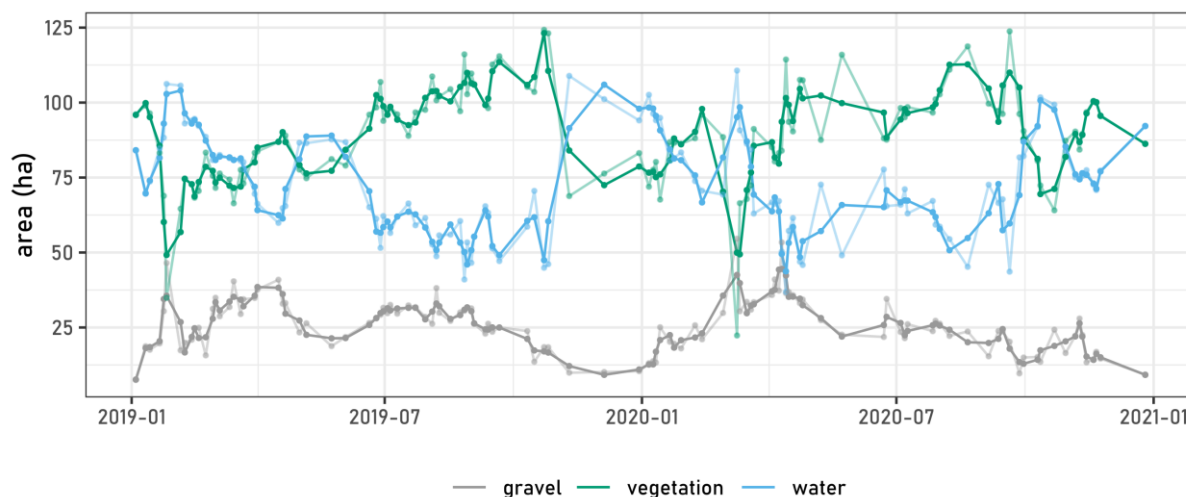
Figure 30: Time series of different land cover classes presence smoothed with a Savitzky-Golay filter. Unsmoothed values shown in the background in lighter colours.

Slika 30:   Časovna vrsta prisotnosti izbranih razredov pokrovnosti, zglajena s filtrom Savitzky-Golay. Nezglajene vrednosti prikazane v ozadju z večjo prosojnostjo.

3.6.4   Conclusions on Land Cover Time Series

Based on a time series of cloudless Sentinel-2 images acquired in the years 2019 and 2020, we made several observations regarding the development of land cover time series from fraction maps:

-   The spectral signatures of endmembers selected on one satellite image can be used to successfully unmix a time series of different satellite images acquired in various seasons.
-   When acquired separately for each satellite image, vegetation endmembers show the largest variations. However, temporally smoothing or averaging the spectral signatures of the vegetation endmembers does not lead to better fraction maps or more stable land cover time series.
-   Smoothing the land cover time series using a Savitzky-Golay filter results in a more stable dataset where meaningful disruptions can be more easily identified.

3.7   Conclusions on the Proposed Method

We tested various settings to determine the optimal characteristics of a spectral mixture analysis (SMA)-based method for mapping and monitoring gravel bars. The method was developed and tested on a 15 km section of the Soča River in Slovenia, between the settlements of Kobarid and Tolmin. The different options were validated using either a pixel-wise or a study area-wise accuracy assessment, as both were shown to give similar results when comparing different settings.

Regarding the input satellite images, we found that both Sentinel-2 and Landsat 8 images can be used to accurately map land cover fractions. Landsat 7 images result in slightly less accurate results, but the difference is within 0.02 MAE and thus still acceptable. The atmospheric correction improves the mapping accuracy, but the topographic correction introduces additional uncertainty and does not contribute to map improvement. Additionally, increasing the spatial and spectral resolution using a deep neural network, as tested for Sentinel-2 images, does not lead to more accurate fraction maps. On the other hand, the inclusion of selected spectral indices in addition to spectral bands leads to more accurate results.

The endmember selection is one of the most important steps in SMA; we therefore tested different configurations. The results show that both manual and automatic endmember selection can produce accurate fraction maps. Nevertheless, even the automatic method requires manual inspection of the selected endmembers to ensure that all of the land cover classes of interest are included. To cover the three land cover types of interest, the optimal number of endmembers is between three and five. Based on the existing literature, shade is an additional endmember that can lead to better fraction maps. However, we found that shade is difficult to detect with the proposed method. Moreover, including shade in other land cover classes of interest does not significantly reduce map accuracy. Therefore, we did not consider shade as a separate endmember. Finally, we found that the endmembers selected based on one satellite image can be successfully transferred to another satellite image to perform SMA.

The land cover fraction maps produced using SMA look informative and show the land cover classes of interest well. Compared to a hard classification based on spectral angle mapper, the fraction maps are more accurate, which is another incentive for the proposed method. We therefore used the method to produce land cover fraction maps for different time points and built a time series of land cover data. Tests with different methods for developing time series showed that the same endmembers can be used for unmixing all images. Different smoothing and averaging approaches applied to the vegetation endmembers, which have the largest annual fluctuations, do not lead to more stable and accurate time series. However, visual inspection of land cover presence plots shows that smoothing the entire time

series with a Savitzky-Golay filter produces clearer results where disturbances can be more easily detected.

These findings were a base for developing the steps of the complete workflow for mapping and monitoring fluvial gravel bars as defined in Figure 31. The main contribution of the proposed method to the existing body of work on land cover monitoring is the combination of sub-pixel mapping and time series analysis. The SMA enables the detection of features and processes that are smaller than the input satellite image pixel and cannot be mapped using hard classification. Land cover time series based on fraction maps therefore more accurately represent the conditions in the environment and are more sensitive to changes in the observed features.
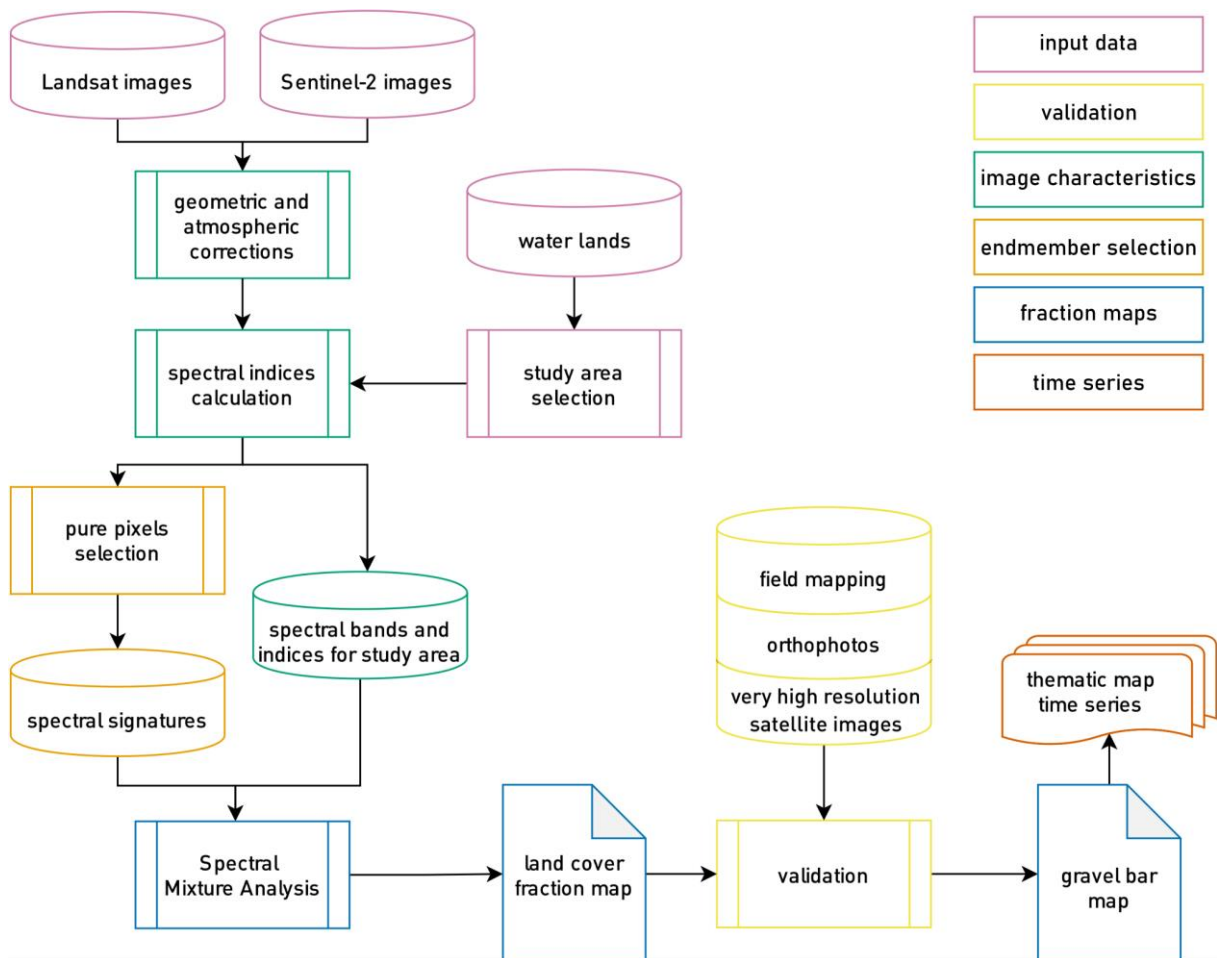
Figure 31: Workflow for the proposed method for monitoring fluvial gravel bars.

Slika 31:   Potek predlagane metode za spremljanje rečnih prodišč.

We established the validation method, input data characteristics, endmember selection strategy, satellite image classification method, and land cover time series development. The next chapter illustrates the application of the method for mapping different study areas as well as detecting changes in gravel bars.

»This page is intentionally blank.«

4   MONITORING GRAVEL BARS

This chapter describes the application of the developed land cover fraction mapping method to map and monitor fluvial gravel bars. First, land cover fraction maps of water lands for the Soča, Sava, and Vjosa rivers are presented. The first proposed hypothesis on the accuracy of the fraction maps is tested. Next, the second hypothesis of the ability of the fraction maps to detect changes is verified. Finally, we demonstrate the use of fraction maps to develop land cover time series, compare the data to selected hydrologic parameters, and explore potential applications of the time series.

4.1   Fraction Maps of Gravel for Different Rivers

To validate the SMA-based method for mapping gravel bars that was developed on a smaller study area, we applied the method to larger river areas. For this purpose, three different rivers known to transport large amounts of gravel were selected. The first river is the Soča, a section of which also served as the study area for the development of the method. The second was the upper section of the Sava, which also flows through north-western Slovenia. The third river was the Vjosa in southern Albania, which is known for extensive gravel bars and natural process dynamics. The combined length of the river sections under consideration was over 250 km.

We used Landsat 5 and Landsat 8 images to generate fraction maps in all study sites to gain a temporal overview of changes in gravel presence. Three images were chosen for each river for classification over a period of 30 – 35 years. All of the selected images were acquired during leaves-on period. Where available, the hydrological characteristics during image acquisition time were also checked to minimise the effect of water level differences on changes of gravel presence (Slovenian Environment Agency, 2021b). The resulting gravel fraction maps and their assessment are presented in the next chapters.

4.1.1   Soča River, Slovenia

The satellite images used for gravel fraction mapping on the Soča river were a Landsat 5 image from 12 July 1990, a Landsat 5 image from 27 June 2002, and a Landsat 8 image from 26 June 2019. Endmembers used for the SMA of Landsat 5 images were selected on the image from 2002 with reference from aerial orthophotos acquired on 18 July 2006, and transferred to the 1990 image. Endmembers used for the SMA of the Landsat 8 image were selected on the image based on reference from aerial orthophotos acquired on 5 September 2020. The water lands with a 100 m buffer on each side of the whole Soča river course in Slovenia were analysed. For a better view of the details, the resulting map of the whole river course was split into several sections (Figure 32).
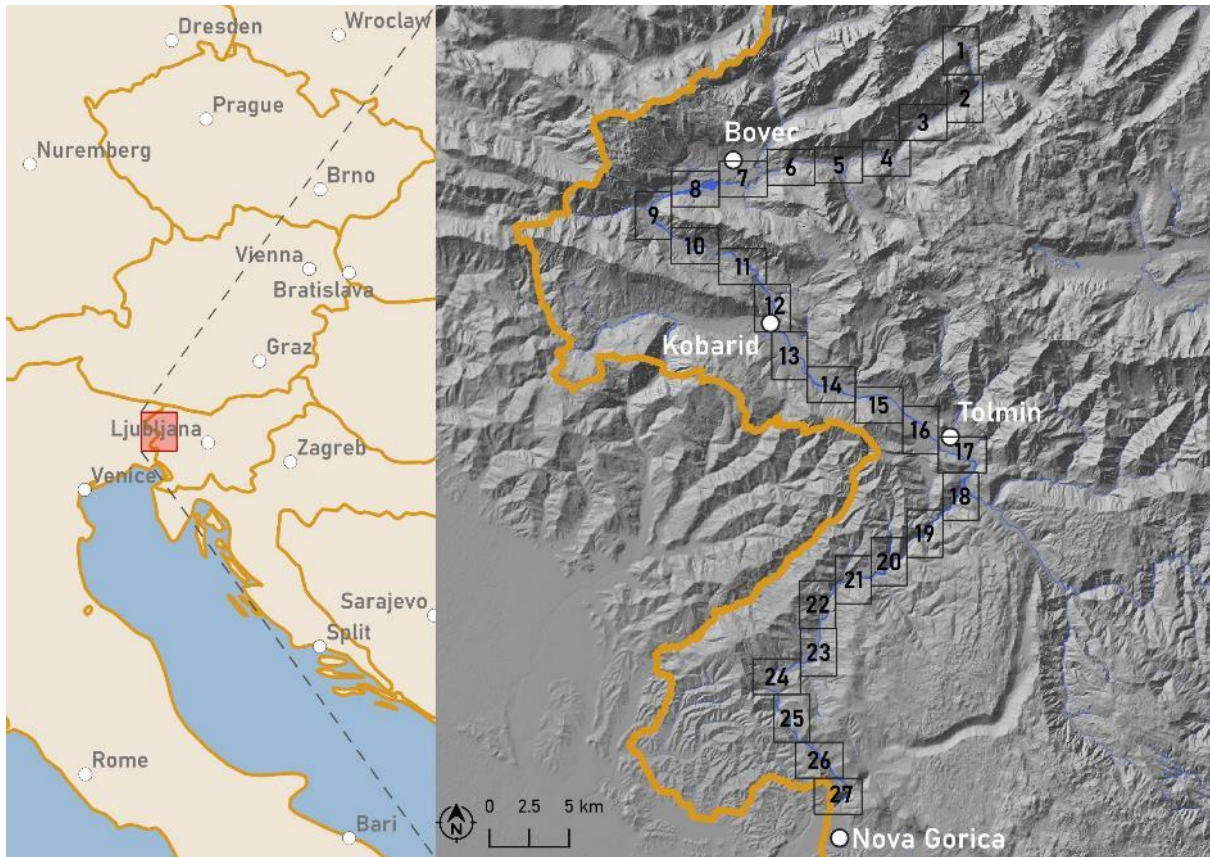
Figure 32: Sections of gravel presence maps on the Soča river in Slovenia (data source: Natural Earth, 2020; Slovenian Water Agency, 2021c; Surveying and Mapping Authority of the Republic of Slovenia, 2016, 2021b).

Slika 32: Sekcije kart prisotnosti proda na Soči v Sloveniji (vir podatkov: Natural Earth, 2020; DRSV, 2021c; GURS, 2016, 2021b).

Each section shows the presence of gravel on fraction maps for three different timestamps (Figure 33). Fraction maps of all sections are available in Appendix A. Many different types of gravel bars can be observed on the Soča river. Most commonly, gravel bars appear along the banks of the river, but there are also some gravels bars in the middle of the river. Gravel bars are complex, formed by a combination of erosion and deposition.
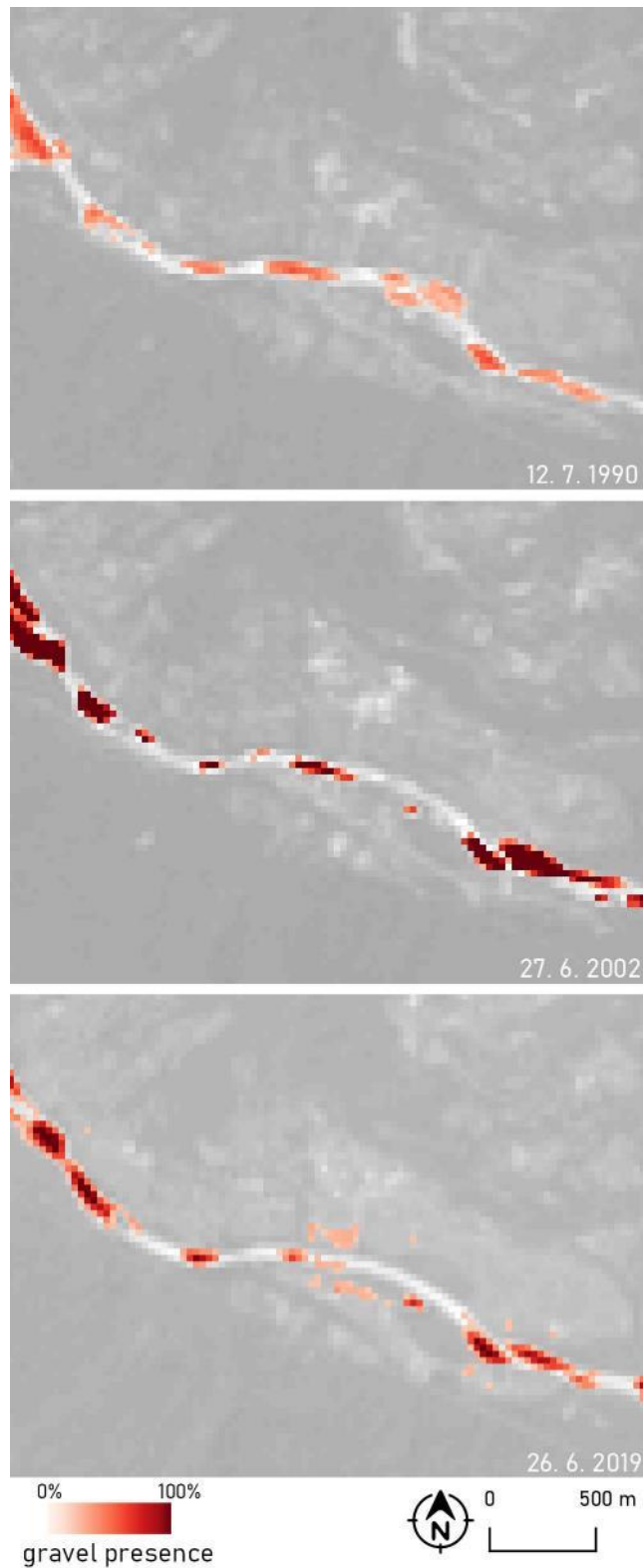
Figure 33: Gravel presence on the Soča river near the Kamno settlement (Section 14) in three different timestamps based on Landsat images.

Slika 33: Prisotnost proda na Soči v bližini naselja Kamno (sekcija 14) v treh različnih časovnih obdobjih na podlagi posnetkov Landsat.

4.1.2 Sava River, Slovenia

The satellite images used for gravel fraction mapping on the Sava river were a Landsat 5 image from 11 July 1984, a Landsat 5 image from 18 July 2004, and a Landsat 8 image from 30 July 2020. Endmembers used for the SMA of Landsat 5 images were selected on the image from 2004 with reference from aerial orthophotos acquired on 22 July 2006, and transferred to the 1984 image. Endmembers used for the SMA of the Landsat 8 image were selected on the image based on reference from aerial orthophotos acquired on 28 July 2020. The water lands with a 100 m buffer on each side of the upper section of the Sava river course in Slovenia were analysed. For a better view of the details, the resulting map of the river course was split into several sections (Figure 34).
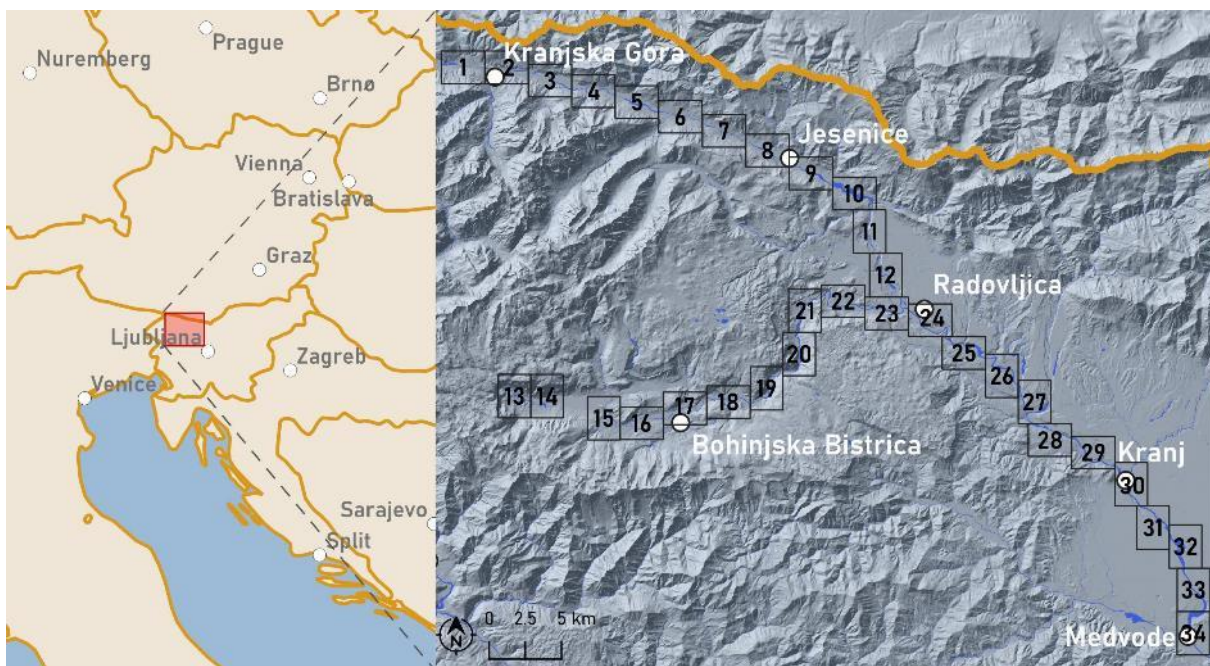
Figure 34: Sections of gravel presence maps on the upper Sava river between the spring and the Medvode settlement (data source: (Natural Earth, 2020; Slovenian Water Agency, 2021c; Surveying and Mapping Authority of the Republic of Slovenia, 2016, 2021b).

Slika 34:   Sekcije kart prisotnosti proda na Zgornji Savi med izvirom in Medvodami (vir podatkov: Natural Earth, 2020; DRSV, 2021c; GURS, 2016, 2021b).

Each section shows the presence of gravel on fraction maps for three different timestamps (Figure 35). Fraction maps of all sections are available in Appendix B. The Sava river has fewer gravel bars than the Soča, but a diversity of forms can still be seen. Lateral gravel bars forming along the river bar in a series of erosion and deposition processes are the most common. We can also see how one type of gravel can be transformed into another over time, for example from a mid-channel bar to a point bar.
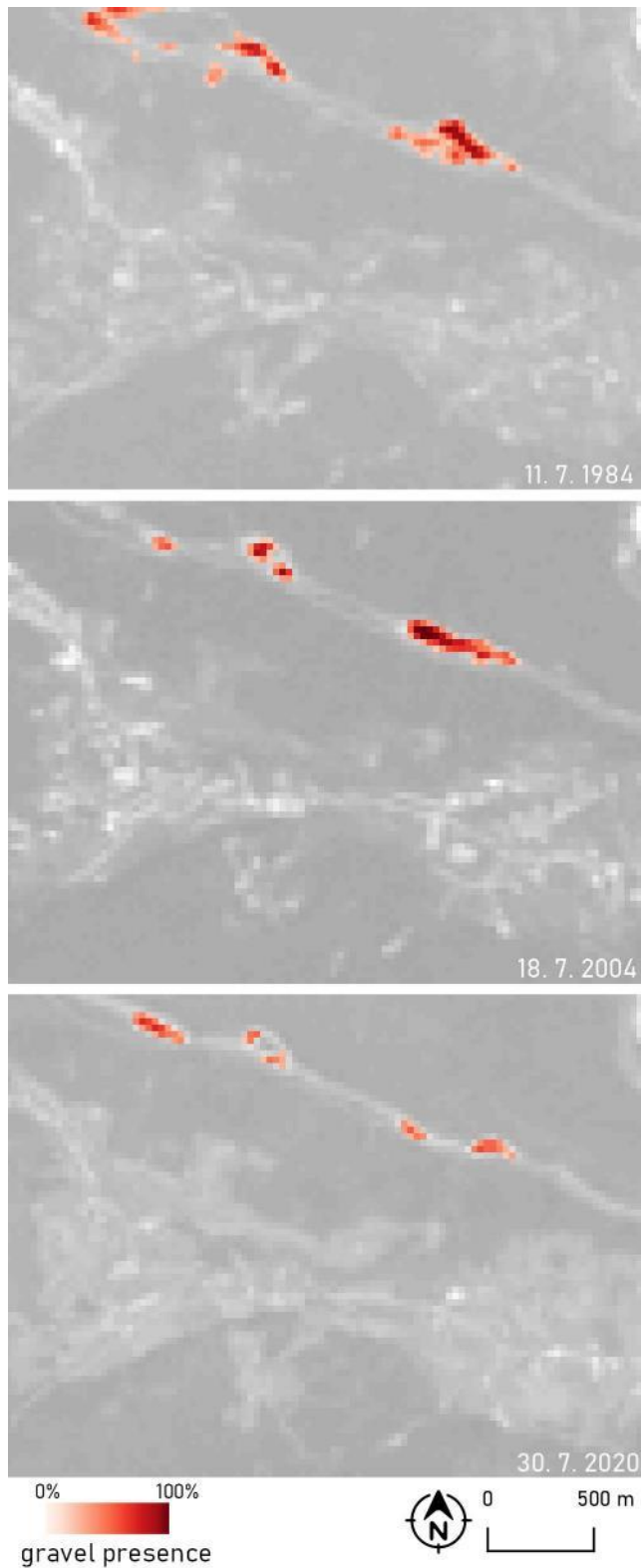
Figure 35: Gravel presence on the Sava river near the Besnica settlement (Section 28) in three different timestamps based on Landsat images.

Slika 35: Prisotnost proda na Savi v bližini naselja Besnica (sekcija 28) v treh različnih časovnih obdobjih na podlagi posnetkov Landsat.

4.1.3   Vjosa River, Albania

The satellite images used for gravel fraction mapping on the Vjosa river were a Landsat 5 image from 24 July 1984, a Landsat 5 image from 24 June 2002, and a Landsat 8 image from 7 June 2019. We analysed an over 60 km long section of the Vjosa river between the Memaliaj settlement and the confluence with the Shushica river. As no official map of water lands was at our disposal, an openly available polygon of the river delineated based on VHR satellite data with a 100 m buffer on each side was used to narrow down the area of observation (OpenStreetMap contributors, 2021).

Endmembers used for the SMA of Landsat 5 images were selected on the image from 2002, and transferred to the 1984 image. Endmembers used for the SMA of the Landsat 8 image were selected on the image based on the newest openly available VHR data (Bing, 2021; Esri, 2021). For a better view of the details, the resulting map of the river course was split into several sections (Figure 36).
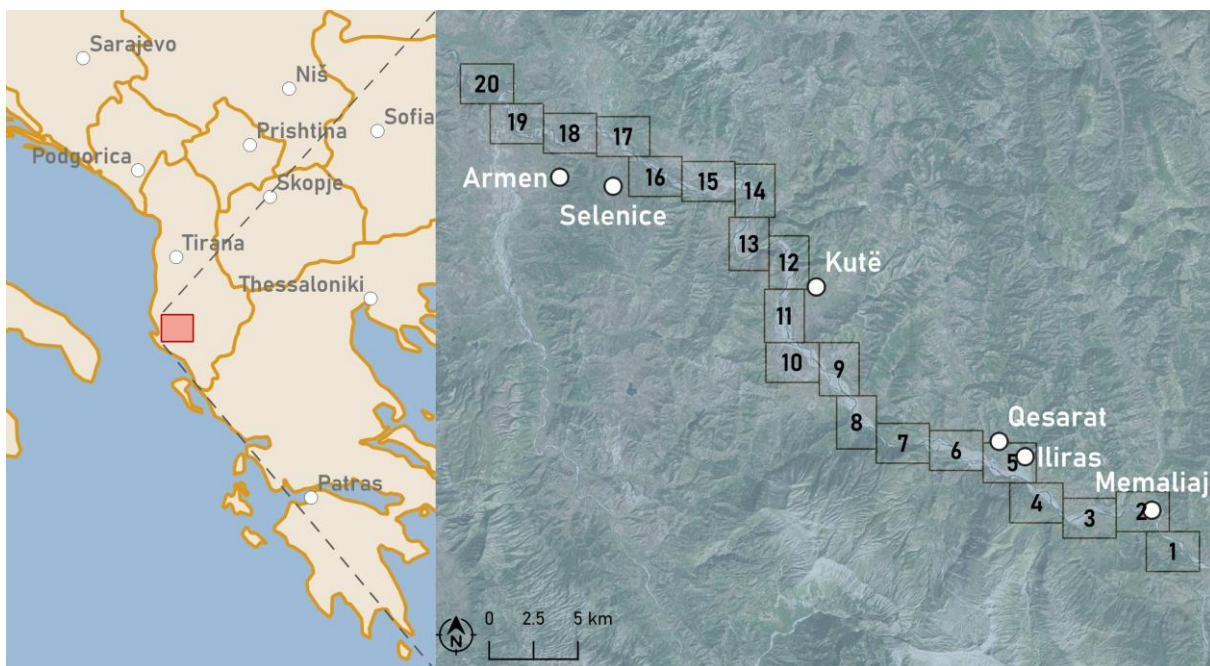
Figure 36:   Sections of gravel presence maps on the Vjosa river between the Memaliaj settlement and the confluence with the Shushica river (data source: Natural Earth, 2020; Bing, 2021).

Slika 36:   Sekcije kart prisotnosti proda na reki Vjosi med naseljem Memaliaj in sotočjem z reko Šušico (vir podatkov: Natural Earth, 2020; Bing, 2021).

Each section shows the presence of gravel on fraction maps for three different timestamps (Figure 37). Fraction maps of all sections are available in Appendix C. An issue that can be seen on fraction maps is the presence of single pixels with very low gravel presence in the middle of gravel bars. This is observed only on Landsat 5 images. The issue is not present on the Soča and Sava rivers, so it could be related to the endmembers used for analysis of the Vjosa river. Additionally, we needed to limit the area of

observation to the riparian zone. In absence of other data, we used the openly available river polygon with a buffer as described above. However, this polygon is based on recent data and does not take the historical river extent into account. Furthermore, the polygon includes the surface water only, and not the water lands as a whole. We mapped only gravel that is located within this polygon and so parts of gravel bars further from the present-day river were missed.

The Vjosa river is known for its extensive gravel bars (Fouache et al., 2001; Rössler et al., 2018; Spada et al., 2018; Schiemer et al., 2020). The fraction maps clearly show this and also highlight the fast speed of changes in gravel bar location. The gravel bars on the Vjosa are mostly complex, formed by a succession of deposition and erosion. One of the reasons for this abundance and complexity of gravel bars is that Vjosa is one of the last large European rivers without a dam that would trap the sediment.
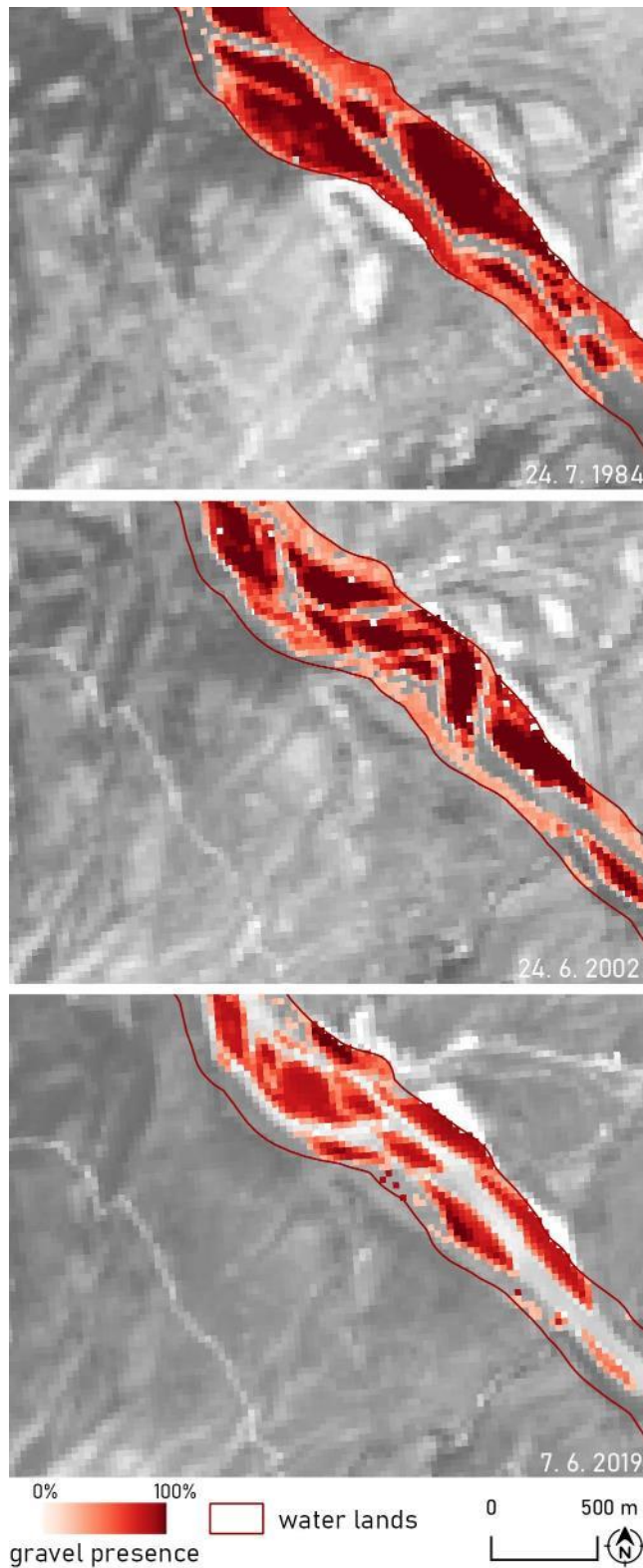
Figure 37: Gravel presence on the Vjosa river near the Iliras settlement (Section 4) in three different timestamps based on Landsat images.

Slika 37:   Prisotnost proda na reki Vjosi v bližini naselja Iliras (sekcija 4) v treh različnih časovnih obdobjih na podlagi posnetkov Landsat.

4.1.4   Validation of the Land Cover Fraction Maps of Water Lands

The most recent fraction maps were validated with VHR remote sensing data. The maps were not validated in their whole extent. Instead, parts of the fraction maps that matched the extent of available VHR data were taken into consideration. Different sources of VHR data were used. The gravel map of the Soča river was validated with a WorldView-2 satellite image with a 2 m spatial resolution, acquired on 3 July 2019 and covering the extent between the settlements Kobarid and Tolmin in the length of almost 15 km. The gravel map of the Sava river was validated with aerial orthophotos with a 0.5 m spatial resolution, acquired on 28 July 2020 and covering the extent between the river spring at Zelenci, and the settlements Bohinjska Bela and Posavec. The total length of the validated map is over 60 km. The gravel map of the Vjosa river was validated with a WorldView-2 satellite image with a 2 m spatial resolution acquired on 16 July 2019. The validated section is located between the settlements Poçem and Qesarat with the total length of almost 25 km.

We validated the presence of all of the land cover classes of interest – gravel, vegetation, and water – using the area-based approach as described in Chapter 3.2.3 above. Most of the land cover classes of interest were mapped with less than a 10% error (Figure 38). Vegetation was an exception with mapping errors slightly over 10% for the Sava and Vjosa river maps. Gravel was mapped with maximum errors around 5% on all rivers. The results indicate that gravel can be mapped accurately using the proposed SMA-based method on diverse rivers.
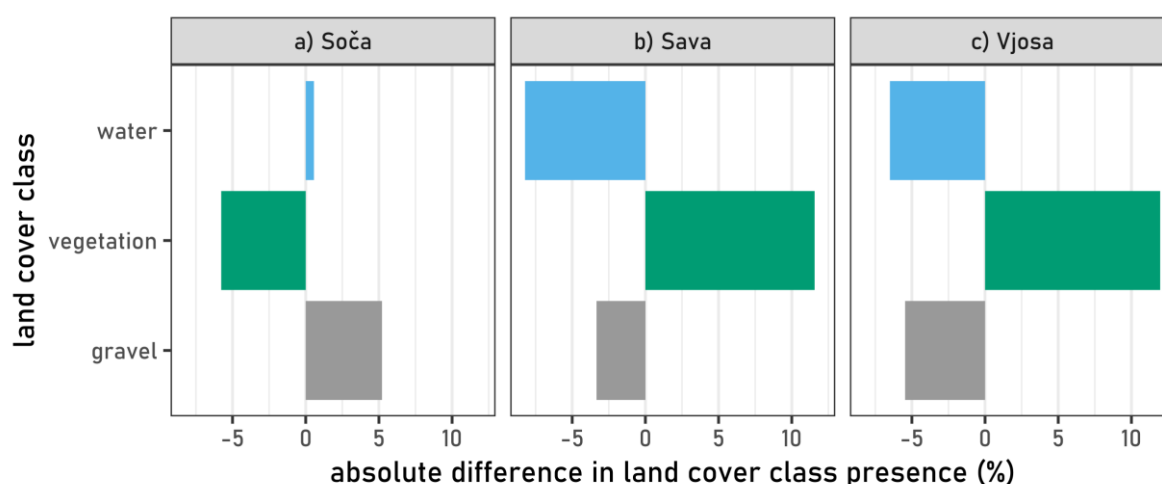
Figure 38: Absolute difference in the presence of land cover classes between reference data and satellite image-based land cover fraction maps for different rivers.

Slika 38: Absolutna razlika v prisotnosti razredov pokrovnosti med referenčnimi podatki in kartami deležev pokrovnosti za različne reke na podlagi satelitskih posnetkov.

4.2   Detection of Changes in Gravel Presence

We investigated the extent to which fraction maps are able to detect gravel bar changes. Rapid change detection is one of the most important advantages of using satellite images from remote sensing systems with a revisit time of only a few days. We focused the change detection on the gravel land cover class. Gravel bars are dynamic geomorphological features that change rapidly. The reasons for changes may be natural, such as increased water levels or fluvial transport ability, or anthropogenic, such as in-channel gravel mining or dam construction.

To begin with, we evaluated the ability of fraction maps to detect changes using simple image differencing. The results were validated with VHR reference data. Aerial orthophotos with a spatial resolution of 0.5 m acquired on 14 October 2017 and 5 September 2020 were used as reference data. Additionally, a classified VHR WorldView-2 satellite image of the study area, acquired on 3 July 2019, with a spatial resolution of 2 m was used as a reference. The reference images were classified into the three land cover classes of interest using a random forest (RF) supervised classification. The satellite images used for the test were selected as close as possible to the acquisition of the reference data. We used Sentinel-2 images acquired on 13 October 2017, 3 July 2019, and 5 September 2020.

The extent of gravel bars changes due to floods and other exceptional events but also due to changes in discharge. To make meaningful analysis of change detection, it is therefore important to ensure that dates with comparable hydrological conditions are considered. The hydrological conditions on the observed dates were similar, with daily discharges ranging from 11.6 to 35.9 m^3/s (Table 17). Existing research shows that factors such as endmember quality and radiometric, spatial, and spectral resolutions of satellite images influence gravel bar mapping accuracy more than observed changes in hydrological conditions (Stančič et al., 2021). The differences are particularly negligible when considering that the discharge in the study area in the years 2017 to 2020 had a much wider variability – between 7.1 and 460 m^3/s (Slovenian Environment Agency, 2021b).

Table 17: Hydrological conditions at the time of input and reference data acquisition (data source: Slovenian Environment Agency, 2021b).

Preglednica 17:   Hidrološki pogoji v času zajema vhodnih in referenčnih podatkov (vir podatkov: Agencija RS za okolje, 2021b).

image ID	use	image system	acquisition date	discharge (m³/s)
1	input	Sentinel-2	16. 10. 2017	11.6
2	reference	orthophoto	14. 10. 2017	12.3
3	input	Sentinel-2	03. 07. 2019	19.8
4	reference	WorldView-2	03. 07. 2019	19.8
5	input	Sentinel-2	05. 09. 2020	35.9
6	reference	orthophoto	05. 09. 2020	35.9

We first investigated whether the fraction maps were able to detect changes observed on the reference data (sensitivity), and then verified whether the changes detected on the fraction maps could be confirmed with the reference data (precision).

4.2.1   Sensitivity of Fraction Maps to Changes in Gravel Presence

The sensitivity of change detection using land cover fraction maps is defined as the ability of the change maps to indicate the processes observed on the reference data. To assess this, we first created a reference map of gravel change by differencing the classified reference images. We vectorised the resulting change map and calculated the areas of the change polygons. In line with our second hypothesis, we selected areas of change larger than 400 m^2 which is equal to the size of one pixels of the input satellite image. All detected areas of change were validated by visual inspection of the reference data to confirm that change had indeed occurred. In parallel, we produced maps of gravel change fractions, again using image differencing. We then calculated the mean pixel values of the change maps within the reference change polygons.

The calculated values show that a decrease or removal of gravel can be detected well, with negative values observed on the fraction change maps (Table 18). The extent of gravel removal was stable and evenly distributed from 2017 to 2020.

Table 18: Fraction change for reference data-based areas of gravel decrease.

Preglednica 18: Spremembe deležev za območja zmanjšanja proda glede na referenčne podatke.

time period	fraction change map mean value	number of change areas	total change extent (ha)
2017–2019	−0.283	15	3.859
2019–2020	−0.165	26	3.335
2017–2020	−0.394	31	6.172

Gravel increase or deposition can also be detected well with fraction maps, but the change values are smaller and therefore less evident (Table 19). Most of the deposition areas formed between 2017 and 2019. There was very little deposition between 2019 and 2020, and some of the existing deposition areas were removed.

Table 19: Fraction change for reference data-based areas of gravel increase.

Preglednica 19: Spremembe deležev za območja povečanja proda glede na referenčne podatke.

time period	fraction change map mean value	number of change areas	total change extent (ha)
2017–2019	0.106	23	3.676
2019–2020	0.214	6	0.857
2017–2020	0.177	14	2.446
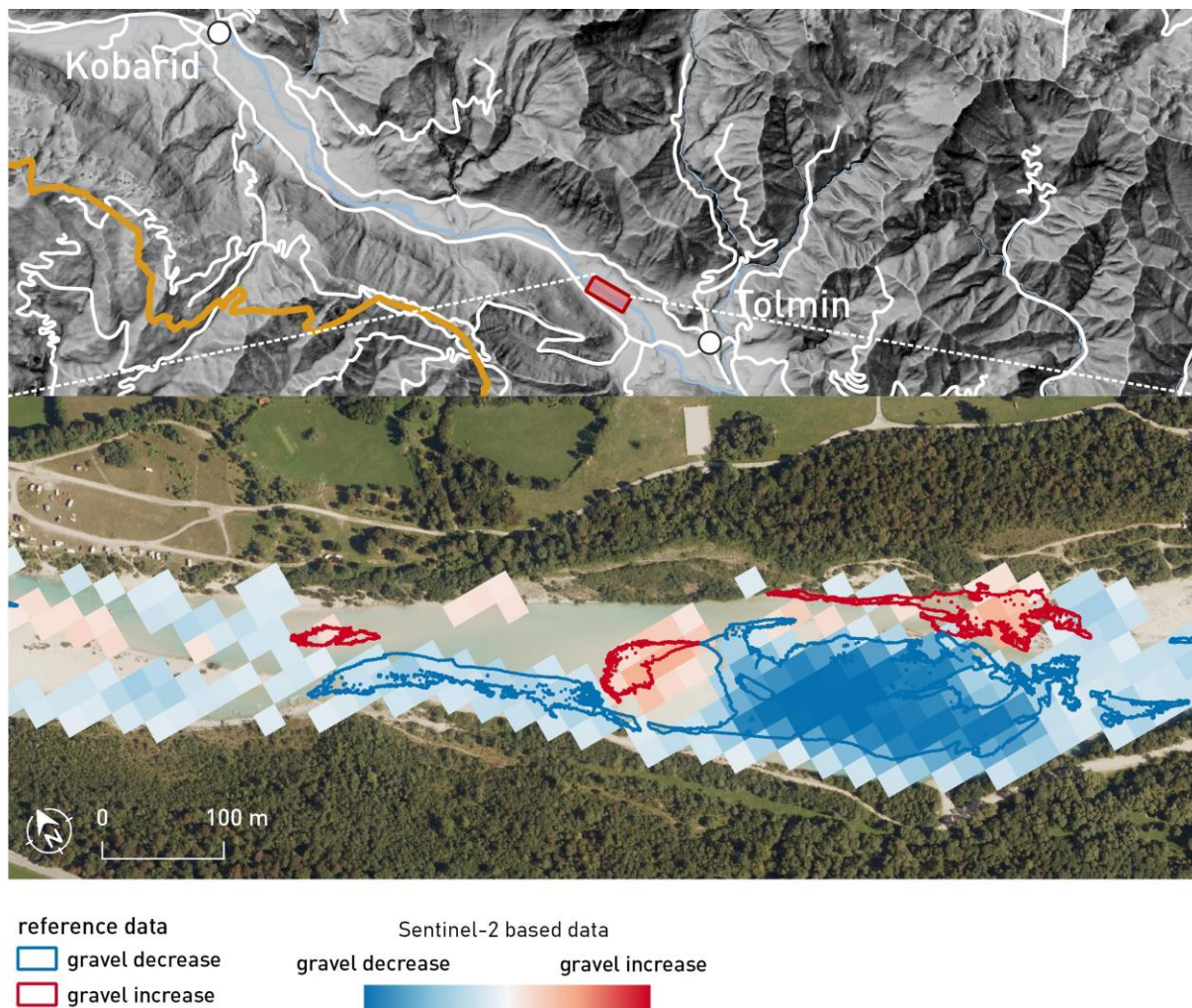
Figure 39: Reference dataset and fraction map of changes in gravel between the years 2017 and 2020 on a subset of the study area on the Soča River (data source: Surveying and Mapping Authority of the Republic of Slovenia, 2016, 2021a, 2021b, 2021e; Slovenian Water Agency, 2021c).

Slika 39:   Referenčni podatki in karta deležev za spremembe v prisotnosti proda med leti 2007 in 2020 na manjšem območju testnega odseka reke Soče (vir podatkov: DRSV, 2021c; GURS, 2016, 2021a, 2021b, 2021e).

The good general overlap between the changes on the reference data and the fraction maps can also be seen visually by comparing the two mapped datasets (Figure 39). As can be seen, the areas of change are often narrow and do not cover the entire satellite image pixel. This may be a reason for low values of fraction change on maps.

4.2.2   Precision of Changes Detected on Land Cover Fraction Maps

In a second line of investigation, we tested whether the changes detected by fraction map differencing actually occurred and can be confirmed by VHR reference data. The preparation of the input data followed the method described above. Namely, we examined a simple image differencing of the various

90   Stančič, L. 2022. Monitoring Changes of Fluvial Gravel Bars with Remote Sensing.

PhD Th. Ljubljana, UL FGG, Interdisciplinary doctoral study programme Environmental Protection.

time steps and compared the results based on fraction maps with those observed on reference data. We focused on the period from October 2017 to September 2020.

We selected 62 non-adjacent pixels that were located in the middle of the areas of gravel change detected on the fraction maps (Figure 40). Gravel change areas were defined as those with at least ± 10% change per pixel. The identified changes were then checked against reference data.

☐ gravel decrease ☐ gravel increase
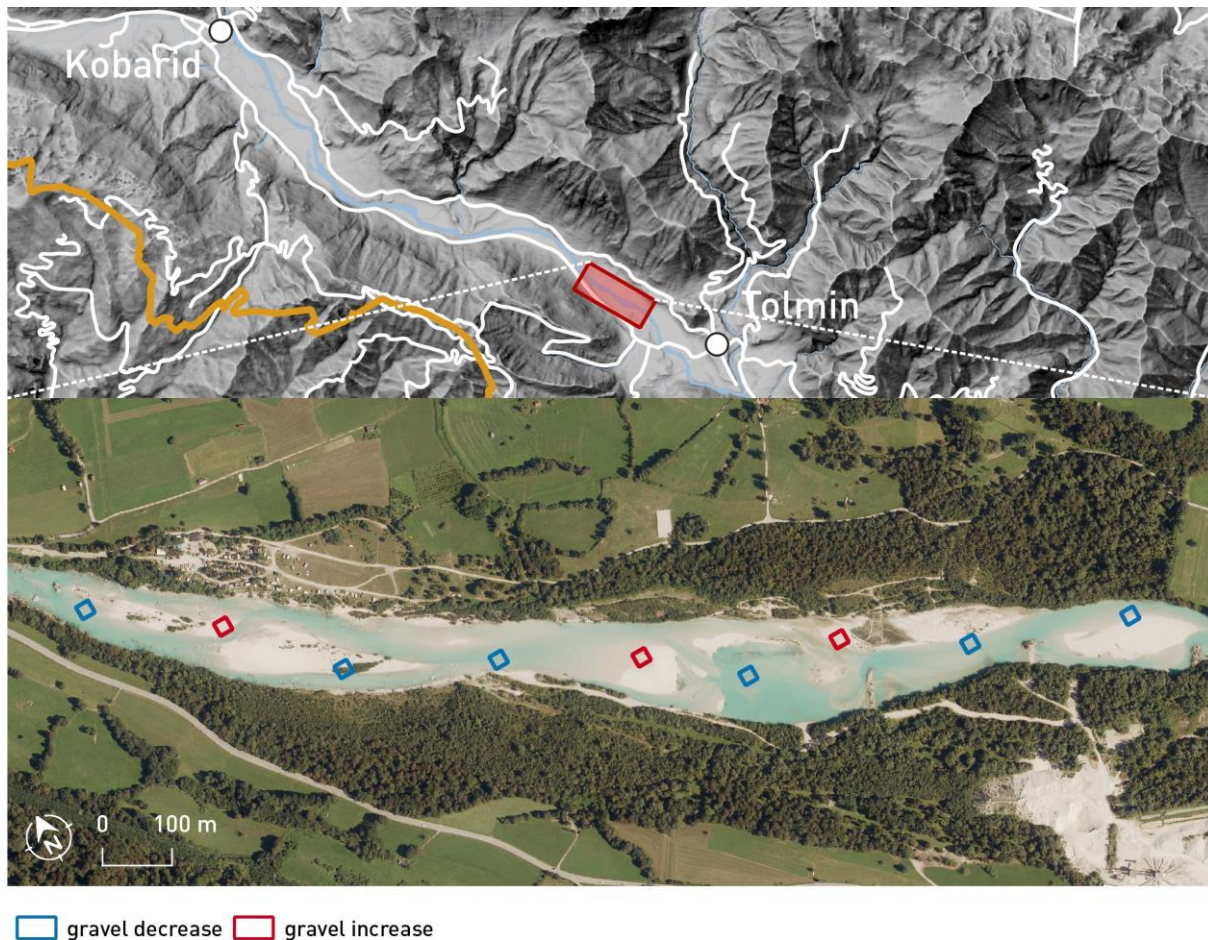
Figure 40: An extract of pixels selected to verify the precision of the land cover fraction change map (data source: Surveying and Mapping Authority of the Republic of Slovenia, 2016, 2021a, 2021b, 2021e; Slovenian Water Agency, 2021b).

Slika 40: Izrez primera pikslov za preverjanje točnosti karte s spremembami deležev razredov pokrovnosti (vir podatkov: DRSV, 2021b; GURS, 2016, 2021a, 2021b, 2021e).

Almost 75% of the identified changes were confirmed with reference data (Table 20). The most common change was from gravel to water, which accounted for almost half of all changes detected. The hydrological conditions on the observed dates were similar, therefore we can assume that the changes are not due only to different water levels. The change from water to gravel accounted for only 16% of all changes detected. One-tenth of the detected changes was due to gravel overgrowth. A change was falsely reported in 16% of cases. Most commonly, an increase of gravel was noted in areas where gravel was removed. In 10% of cases, no change could be detected on the reference data even though maps of fraction change indicated otherwise. Pixels where no change could be confirmed had the lowest average values of fraction change, below 20%. For comparison, pixels where gravel deposition occurred had an average fraction change value of 30%. Where gravel removal took place, the average fraction change value was −47%. We conclude that values of fraction change above ± 30% are indicative of real change.

Table 20: Fraction change for the analysed areas of change, identified on the land cover fraction change map for the period 2017–2020.

Preglednica 20: Spremembe deležev za analizirana območja sprememb na podlagi karte s spremembami deležev razredov pokrovnosti za obdobje 2017–2020.

type of change	number of instances	share of instances (%)	average fraction change map value
water to gravel	10	16	0.304
gravel to vegetation	6	10	−0.446
gravel to water	30	48	−0.479
gravel to water (error)	9	15	0.254
gravel to vegetation (error)	1	2	0.127
no change	6	10	−0.175
total	62	100	−0.198

4.2.3   Correlation of Observed Changes Between Fraction Maps and Reference Data

A third and final validation of change detection was the correlation between the change values observed on the fraction maps and the reference data. The reference data were first resampled to the spatial resolution of the fraction maps, i.e. 20 m. Then, the values were extracted for all the pixels in the validation areas and only for the pixels in the change areas that were detected on the VHR reference data. The extracted values of the fraction maps and the reference data were then compared using the Pearson correlation coefficient.

The results show that the change maps are highly correlated, especially in areas of change (Pearson's $r > 0.85$, $p < 0.0001$). The lowest correlation is observed for the 2019 to 2020 period with $r = 0.469$ for the whole area and $r = 0.663$ for the change areas (Table 21).

Table 21: Correlation between fraction and reference change maps. $p < 0.0001$.

Preglednica 21: Korelacija med vrednostmi na kartah s spremembami deležev in na referenčnih kartah sprememb. $p < 0.0001$.

time period	whole area		change areas	
	r value	number of instances	r value	number of instances
2017–2019	0.542	4,691	0.860	250
2019–2020	0.469	4,691	0.663	199
2017–2020	0.606	4,691	0.860	254

Monitoring changes of fluvial gravel bars must be carried out at time points with comparable hydrological conditions. This can be challenging since the acquisition of input satellite images as well as reference remote sensing data is fixed in time. Cloud obstruction further limits the amount of data that can be used for monitoring. When validating change detection, the task is particularly complex as the hydrological conditions need to be matched between the input satellite images and also the reference data. In our study case, the daily discharges ranged from 11.6 to 35.9 m^3/s. Reference data were acquired very close to the input satellite images, mostly on the same day. When reference data were from a different date, the difference in daily discharges between reference and input data was 0.7 m^3/s. Such fluctuations evidently do not alter the gravel bar extent too significantly, as the overlap between changes observed on reference and input data was very high.

4.3 Assessment of Land Cover Time Series Based on Fraction Maps for Monitoring

In the following section, we aim to verify whether the land cover fraction maps produced with SMA can be used to monitor the presence of land cover classes and whether these data can provide information about possible changes in water lands. To this end, we first tested the stability of land cover presence data and their correlation with changes in hydrologic data. Next, we examined how known gravel bar changes manifest on plots of gravel presence through time.

4.3.1 Comparison of Land Cover Time Series Based on Fraction Maps with Hydrological Data

Rising water levels inundate parts of gravel bars, reducing their extent. We checked whether this process could be detected in time series of gravel presence based on remote sensing relative to water levels measured in situ. The analysis was performed for the study area on the Soča between the settlements of Kobarid and Tolmin. Hydrologic data were obtained from a gauging station in Kobarid, located at 46.247481° N, 13.586414° E. The data are collected by the Slovenian Environment Agency and are

publicly available (Slovenian Environment Agency, 2021b). The plotted graphs show a clear negative correlation between the area covered with gravel and the water level (Figure 41). This was confirmed by the Pearson correlation coefficient of −0.643 (p < 0.0001).
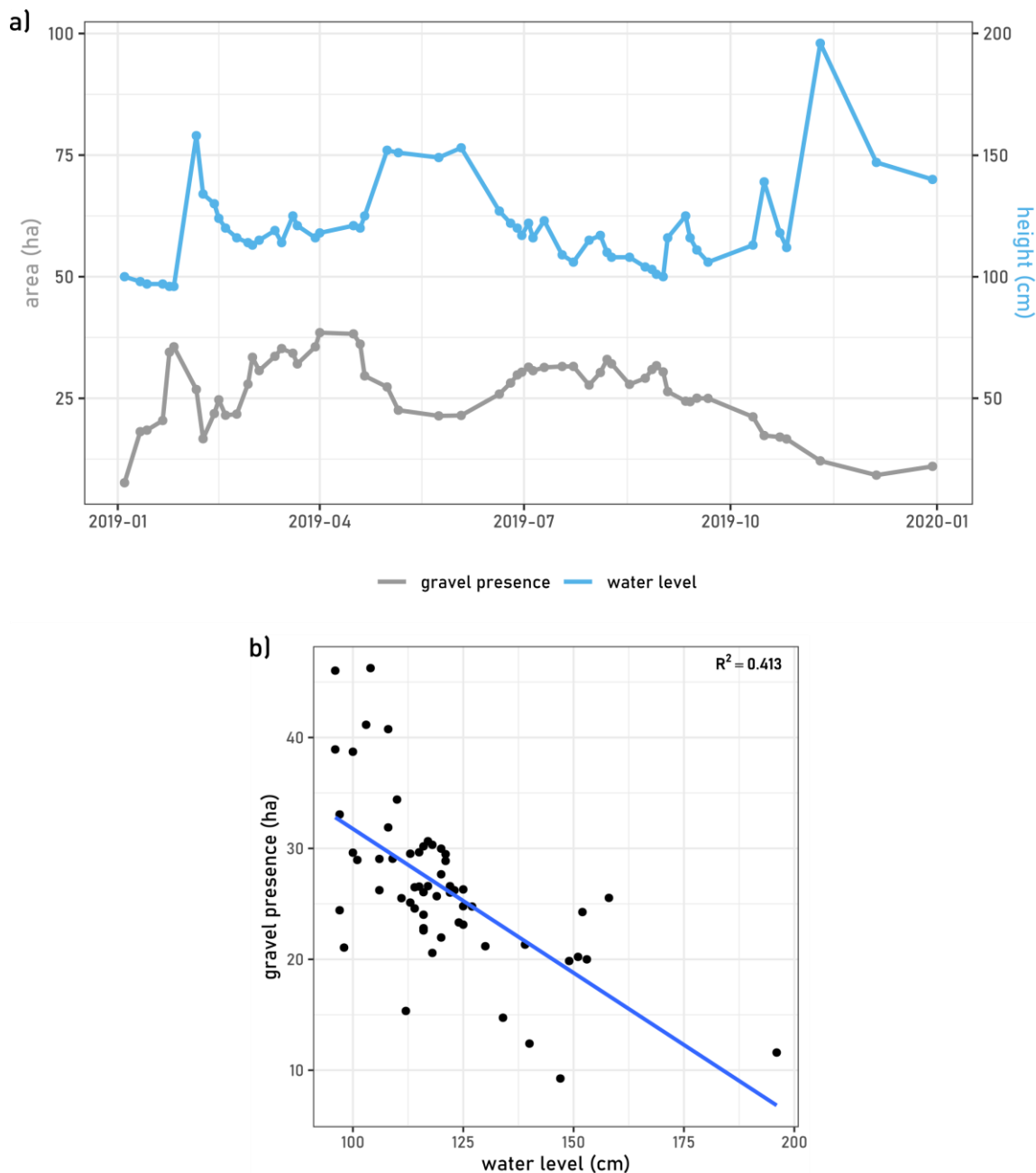
Figure 41: Gravel presence in the study area and water level at the Kobarid gauging station. a) Time series of the data. b) Scatter plot with the linear regression line and coefficient of determination (data source: Slovenian Environment Agency, 2021b).

Slika 41: Prisotnost proda na študijskem območju in vodostaj na merilni postaji Kobarid. a) Časovna vrsta podatkov. b) Razsevni diagram s črto linearne regresije in koeficientom določanja (vir podatkov: Agencija RS za okolje, 2021b).

After some extreme weather events, abrupt changes in water level may occur. Such changes may happen too rapidly to be reflected in the change of gravel bar area and may not even be captured within the return period of the remote sensing system. This could reduce the correlation between the water level and gravel area datasets. To account for these abrupt processes, we tested the influence of different smoothing methods. For water level, we calculated a five-day moving average for each date, with the date in question as the last data point in the averaging calculations. We also smoothed the data using a Savitzky-Golay filter. The same filter was applied for smoothing the gravel area. We calculated the correlation between values measured on the same day. We considered a total of 58 different dates from 2019.

The results show a good correlation between the non-smoothed gravel area and water level datasets (Table 22). Using a Savitzky-Golay filter to smooth either the gravel area or the water level increases the correlation between the two datasets. The highest correlation (-0.729) is found when both datasets are smoothed with a Savitzky-Golay filter. Taking the five-day average water level instead of the daily value decreases the correlation slightly. This supports the body of existing knowledge that the five-day moving average provides useful information only in stable conditions without precipitation.

Table 22: Correlation between water level and gravel area in the study area on the Soča River. Data from 58 different dates in 2019 were considered. $p < 0.0001$.

Preglednica 22: Korelacija med vodostajem in pokrovnostjo proda na študijskem območju na reki Soči. Upoštevali smo podatke za 58 datumov v letu 2019. $p < 0.0001$.

		water level		
		no smoothing	five-day average	Savitzky-Golay
gravel area	**no smoothing**	-0.643	-0.601	-0.724
	Savitzky-Golay	-0.656	-0.617	-0.729

From the correlation, we can conclude that the land cover maps are consistent with the expected physical processes and can be considered as valid data sources.

4.3.2   Using Time Series to Detect Changes in Gravel Presence

In this subchapter we test if known change events could be detected from the time series data of gravel presence. The change events considered were selected based on field data and confirmed with reference data. Two different change events were chosen, one on the Soča near the settlement of Dolje and another on the Sava river near the city of Kranj.

4.3.2.1   Case Study at Dolje on the Soča River

Large gravel bars are present on the left bank of the Soča near the settlement of Dolje (Figure 42). Reference images of the area show that large changes in the form of gravel bar removal occurred between 31 October 2019 and 5 December 2019. We focused the analysis of land cover presence on the smaller study area at Dolje, 15 ha in size, to check whether the changes also manifested in the gravel area.

Figure 42: Overview of the study area for small-scale gravel change detection on the Soča river near the settlement of Dolje (data source: Surveying and Mapping Authority of the Republic of Slovenia, 2016, 2021a, 2021b, 2021e; Slovenian Water Agency, 2021c).

Slika 42: Pregled študijskega območja za zaznavanje sprememb na manjših površinah na Soči v bližini naselja Dolje (vir podatkov: DRSV, 2021c; GURS, 2016, 2021a, 2021b, 2021e).

We plotted a time series of gravel presence in the Dolje study area for the years 2019 and 2020 (Figure 43). The average area covered by gravel in the observed period is 4 ha. Reviewing the input satellite images, we found that a decrease in gravel presence up to two standard deviations, i.e. by a total of 2 ha, indicates actual changes in the size of gravel bars.
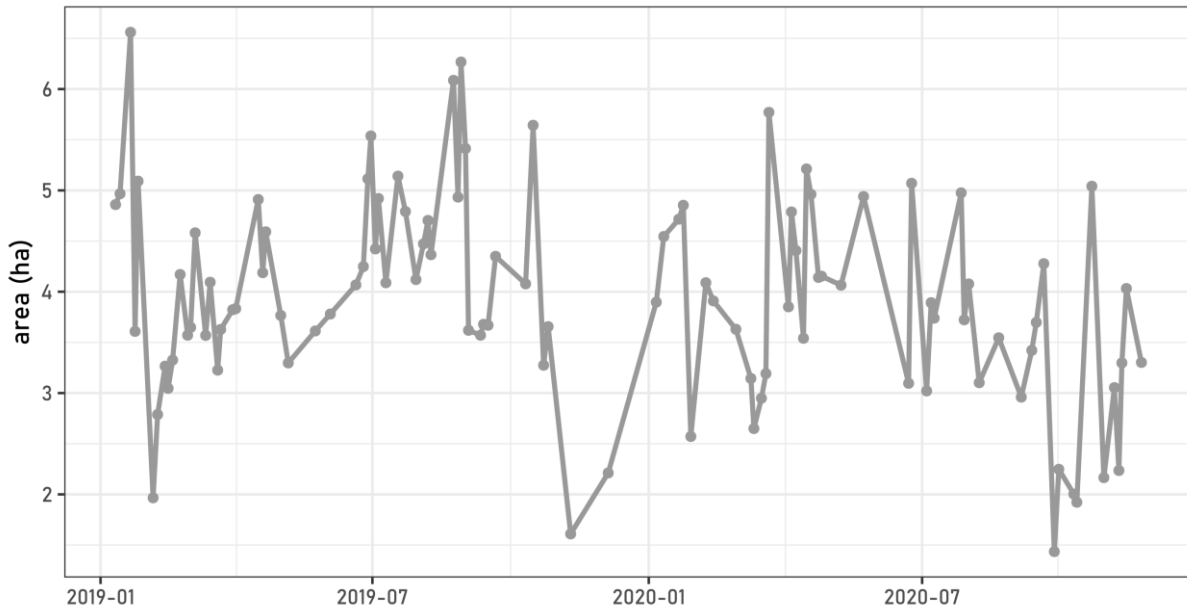
Figure 43: Presence of gravel in the Dolje study area in 2019 and 2020.

Slika 43:   Prisotnost proda na študijskem območju Dolje v letih 2019 in 2020.

The changes can be clearly seen on satellite images (Figure 44). The processes of re-formation of gravel bars at similar locations to where they were present before is in line with reports in existing literature (Robert, 2003).
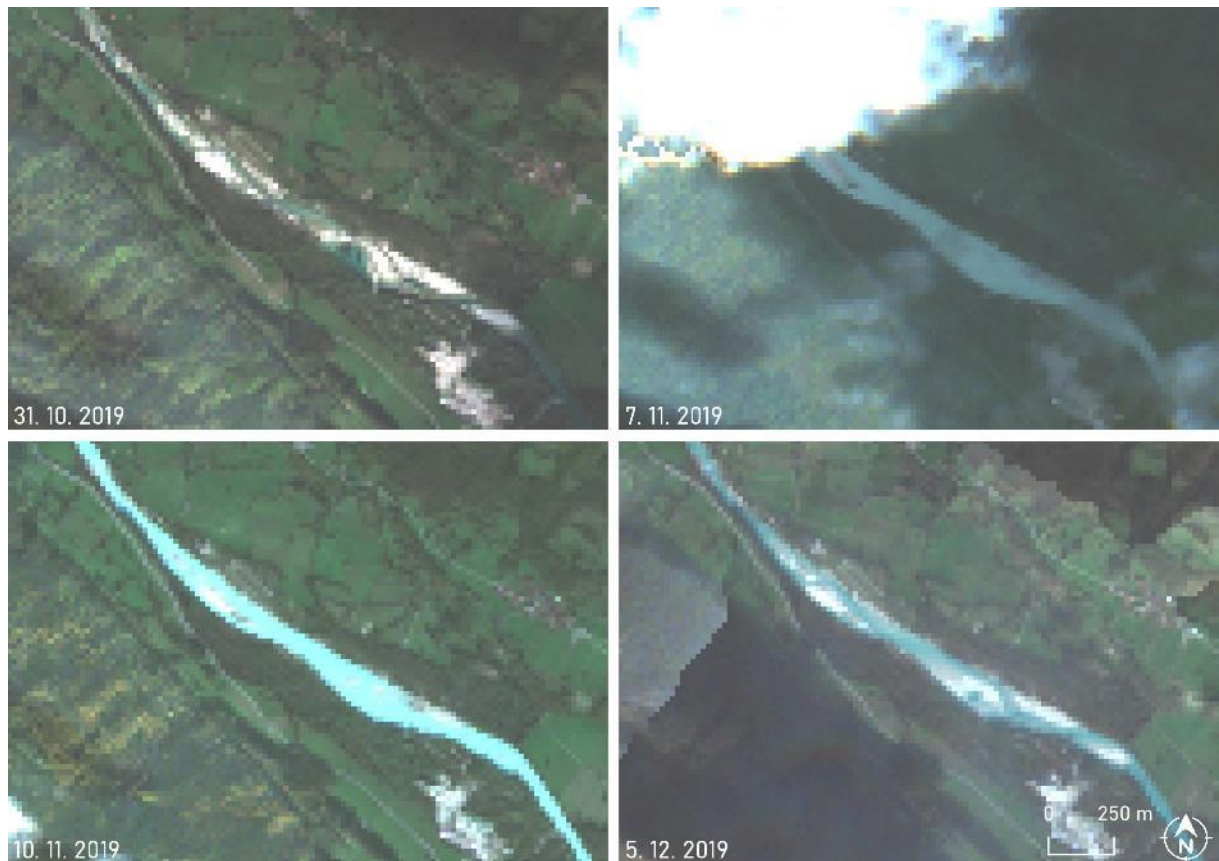
Figure 44:   Sentinel-2 true colour images showing the removal of gravel from the Soča river at the Dolje study area and the subsequent formation of new gravel bars. The extent of gravel bars under observation is shown on Figure 42 (data source: Modified Copernicus Sentinel data, 2021).

Slika 44:   Naravno barvni kompoziti Sentinel-2, ki prikazujejo odstranjevanje proda na študijskem območju na Soči blizu naselja Dolje in kasnejše oblikovanje novih prodišč. Obseg prodišč, ki smo jih opazovali, je prikazan na Slika 42 (vir podatkov: Modified Copernicus Sentinel data, 2021).

4.3.2.2   Case Study at Kranj on the Sava River

Extensive gravel deposits are present on the Sava river near the town of Kranj, downstream of a soft dam for a hydroelectric power plant (HPP) (Papler and Basej, 2014) (Figure 45). Satellite images of the area show that large gravel bar removal took place between 2 July 2020 and 27 July 2020. We focused the analysis of land cover presence on the smaller study area at Kranj, 15 ha in size, to check whether the changes can be detected in a time series of gravel presence.

Figure 45: Overview of the study area for small-scale gravel change detection on the Sava river near the town of Kranj (data source: Surveying and Mapping Authority of the Republic of Slovenia, 2016, 2021a, 2021b, 2021e; Slovenian Water Agency, 2021c).

Slika 45:   Pregled študijskega območja za zaznavanje sprememb na manjših površinah na Savi v bližini Kranja (vir podatkov: DRSV, 2021b; GURS, 2016, 2021a, 2021b, 2021e).

We plotted a time series of gravel presence in the Kranj study area for the years 2019 and 2020 (Figure 46). The average area covered by gravel in the observed period is 2.7 ha. Reviewing the input satellite images, we found – similar to the results at the Dolje study area – that a decrease in gravel presence up to two standard deviations, indicates actual changes in the size of gravel bars.
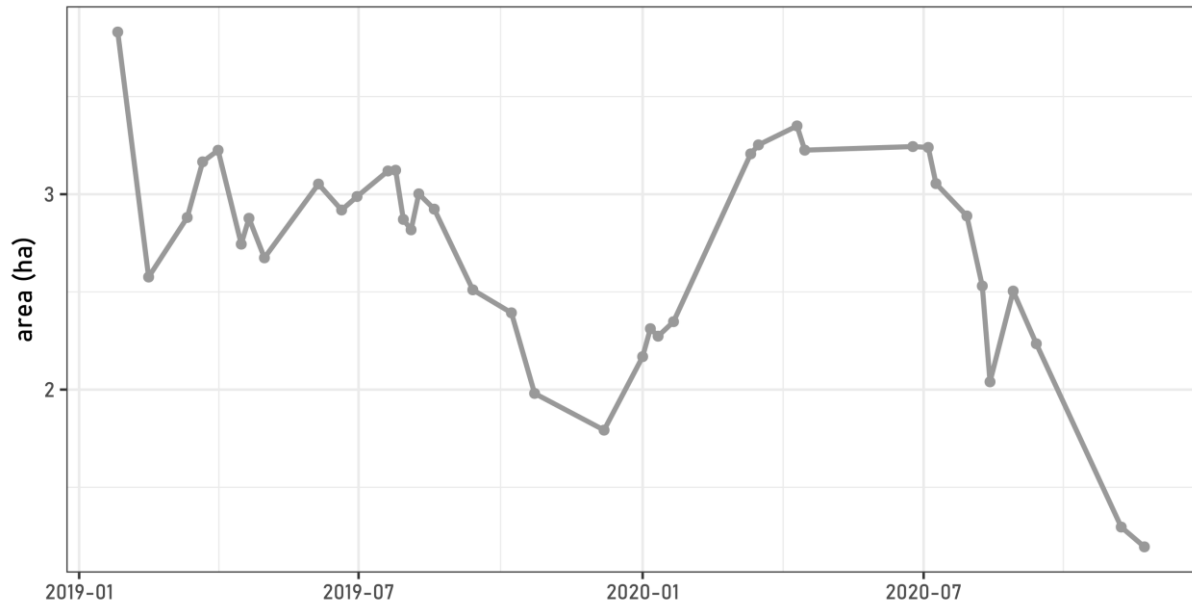
Figure 46: Presence of gravel in the Kranj study area in 2019 and 2020.

Slika 46:   Prisotnost proda na študijskem območju Kranj v letih 2019 in 2020.

The changes can also be confirmed visually on satellite images (Figure 47).

Figure 47: Sentinel-2 true colour images showing the removal of gravel from the Sava river at the Kranj study area. The extent of gravel bars under observation is shown on Figure 45 (data source: Modified Copernicus Sentinel data, 2021).

Slika 47: Naravno barvni kompoziti Sentinel-2, ki prikazujejo odstranjevanje proda na študijskem območju na Savi pri Kranju. Obseg prodišč, ki smo jih opazovali, je prikazan na Slika 45 (vir podatkov: Modified Copernicus Sentinel data, 2021).

5   DISCUSSION

The dissertation proposes a method for sub-pixel mapping of fluvial gravel bars based on spectral mixture analysis (SMA) using freely available Earth observation (EO) data. We tested several configurations to determine the most appropriate method for fraction map validation, optimal characteristics of the input satellite image, the most successful process of endmember selection, the production of fraction maps, and the final development of a time series of land cover presence. The method was developed on a section of the upper Soča river in Slovenia. Subsequently, we transferred the method to map gravel bars in multiple timestamps on the whole Soča river in Slovenia, the upper Sava river in Slovenia, and the middle Vjosa river in Albania. We also tested the ability of fraction maps to detect small-scale changes in the extent of gravel bars. Finally, we evaluated the usefulness of time series based on fraction maps to derive information on the hydrological characteristics of rivers and to detect the removal of gravel bars.

The final chapter with discussion summarises the tests of the proposed research hypotheses, outlines the contribution of the dissertation to science, describes the limitations of the proposed method, and highlights opportunities for further work.

5.1   Hypotheses Testing

The first part of the dissertation describes the tests that were conducted to develop the method for producing accurate land cover fraction maps of fluvial environments. The focus of the dissertation is on the gravel land cover class, but to gain an overview of the environment studied, we also mapped surface water and vegetation. These land cover classes were considered in accuracy assessments. Validation was performed at two different levels, where we first focused on the land cover fractions mapped on selected single pixels (pixel-based validation), and then examined the land cover presence on the entire study area (area-based validation). We assessed the mapping results based on different input images – four-band 10 m Sentinel-2 images, ten-band 20 m Sentinel-2 images, six-band 30 m Landsat images, and various spectral indices derived from the input spectral bands. The validation areas ranged in size from a 15 km long section on the Soča to a 25 km section on the Vjosa and a 60 km section on the Sava.

The best results of the pixel-based validation showed a total mean absolute error (MAE) of 0.084. That means that the presence of all land cover classes of interest was mapped on average with the accuracy of ± 8.4% per pixel. The highest total MAE for a different image with a different endmember selection strategy was 0.126. The relative variation of MAE between the different fraction maps is low in absolute terms (± 4.2%). This indicates the stability and robustness of the proposed method. However, accuracy of the mapping varies between the different land cover classes of interest. Gravel is mapped the most accurately in all cases, with an average MAE of 0.088 ± 0.016 across different fraction maps. Vegetation

is mapped with the least accuracy, with an average MAE of 0.125 ± 0.017. Water is mapped more accurately than vegetation, but has a higher standard deviation in mapping accuracy with an average MAE of 0.099 ± 0.021. The area-based validation shows similar trends to the pixel-based validation. In most maps, gravel presence is mapped the most accurately, followed by water and vegetation. The absolute differences in land cover presence between the fraction maps and the reference data are mostly within 10%. The only exception is vegetation along the Sava and Vjosa rivers, which is overestimated by more than 11%.

Based on the results summarised above, we can therefore **confirm** the *Hypothesis 1: Using spectral mixture analysis, it is possible to distinguish gravel bars, surface water, and vegetation in fluvial ecosystems. The land cover of river ecosystems can be determined with a thematic accuracy of 90% by analysing the spectral signal composition of freely available satellite images with a spatial resolution of up to 10 m.* Using freely available satellite images with spatial resolutions of 10 m, 20 m, and 30 m, an overall mapping accuracy of 90% was achieved. However, some caveats regarding the method need to be considered. Namely, vegetation mapping with SMA is less accurate and often does not reach accuracies of 90% both on a sub-pixel level and on the study area-wide scale.

In the second part of the dissertation, we investigate the ability of SMA-based fraction maps to monitor gravel bars. We first produced fraction maps for river sections up to over 90 km long in three different timestamps over a 30-year period. Gravel bars were successfully mapped in all timestamps on different rivers. Subsequently, we were interested in the possibilities of change detection on fraction maps. To do this, we began by using simple map differencing. First, we tested the sensitivity of fraction maps, also known as recall and true positive rate, i.e. whether changes observed on very high resolution (VHR) reference data could be detected by fraction maps. We focused on areas of change with a size of at least 400 m^2, which corresponds to one pixel of the selected input satellite image (the 20 m bands of the Sentinel-2). The results showed that gravel removal could be successfully detected using fraction maps with negative values of gravel presence change. Gravel accumulation could also be detected, but the positive change values were smaller in our case and therefore less distinct. Second, we evaluated the precision of the fraction maps, i.e. whether the changes detected on the fraction maps could be verified with VHR reference data. We examined pixels of the fraction maps that were found to have a change of at least $\pm$ 10% between 2017 and 2020, and checked whether the change could also be seen on the reference data. We were able to confirm almost 75% of the changes reported by the fraction maps. The pixels where a change actually occurred showed a gravel presence change of at least $\pm$ 30%. From this we can infer that a change in gravel presence in a pixel of at least $\pm$ 30% indicates definite gravel removal or deposition.

The second part of the change detection assessment tested the potential of using time series data. We plotted the total presence of gravel in a selected smaller study area where gravel removal was known to have occurred. The selected study areas were located near the Dolje village on the Soča and near the Kranj city on the Sava. The average extent of gravel bars was 4 ha at Dolje and 3 ha at Kranj. The extents of gravel bars varied with changes in water level. However, we found that a decrease in gravel bar size within two standard deviations of the mean indicated regular variations, while a larger decrease pointed to gravel bar removal. In agreement with the outlined results, we can thus also **confirm** the *Hypothesis 2: Time series analysis of sub-pixel land cover maps allows the detection of seasonal changes in gravel bar extent and location. In addition to seasonal dynamics, changes in the extent of gravel bars due to exceptional anthropogenic and natural events larger than 500 m^2 can also be detected.* The extent of changes that can be detected is also influenced by the spatial resolution of the input satellite images. Nevertheless, we showed that freely available satellite images can be successfully used to detect changes in gravel bars down to 400 m^2 (one pixel) in size.

5.2   Contribution to Science

The application of EO data to collect environmental variables and monitor the state of the natural environment is an important field that has also been highlighted in the United Nations 2030 Agenda which formulated the Sustainable Development Goals (SDGs) (UN, 2015). The main motivation that guided the topic of this dissertation was to contribute to the work on SDG indicator 6.6.1: Change in the extent of water-related ecosystems over time (UN, 2017). Fluvial gravel bars are important water-related features that are often difficult to map and monitor due to their small extent. Therefore, by applying the SMA to map fluvial gravel bars, we contributed to the development of new knowledge and experience in using EO data to monitor progress towards the SDGs.

The main contribution of the dissertation to science was the development of a new procedure for rapid and accurate mapping of gravel bars and other water-related ecosystems. The proposed workflow uses freely available satellite images with a short revisit period, making it well suited for monitoring purposes. We have also produced land cover maps of water-related ecosystems that can be used to inform planning and management decisions. Comprehensive maps covering a large area are particularly useful for managing fluvial ecosystems, where changes in one part of the basin may have effects far downstream.

The production of land cover maps for a long period provided a good overview of the dynamics of gravel bars in the past. Additionally, with frequently available input satellite images we were able to rapidly detect and monitor changes over a short time period. This supplementary information on past characteristics and timely information on changes combine to contribute to a better understanding of the dynamics of fluvial gravel bars. Our results show that gravel bars are very dynamic with rapidly

changing extents. Water level has a major influence on the extent of gravel bars. Despite changes in size and shape, the locations where gravel bars occur in a river channel are constant. Even after gravel bars are removed, new deposits quickly form at the same location.

The proposed method was developed on river sections for which several different VHR remote sensing as well as in situ data were available. This allowed validation of the results and determination of the optimal workflow. We analysed the transferability of the workflow to other areas and found that it is possible and provides accurate results. The method can be used to study other rivers for which there may not be as much data available. Studying different rivers may lead to a new understanding of the effects of natural and anthropogenic changes on the land cover of water-related ecosystems.

5.3 Limitations of the Proposed Method

The main limitations of the proposed method are related to cloud cover and terrain shadows, which are well-known problems of optical images. Mountainous areas, which were the focus of many of our observations, are frequently covered by clouds due to rising air masses. Additionally, river valleys are located between steep slopes, resulting in shadowing. This issue is particularly pressing during the winter months when the Sun incidence angle is low. We mitigated cloud obstruction problems by using a cloud masking algorithm (Sinergise, 2021). We attempted to address topographic normalisation with radiometric corrections, but the results were not satisfactory. Future work could test different radiometric correction algorithms, such as the Teillet regression or the Statistical Empirical model (Teillet et al., 1982), the b correction (Vincini et al., 2002), the Modified Sun-Canopy-Sensor correction (SCS+C) (Soenen et al., 2005), the Variable Empirical Coefficient Algorithm (VECA) (Gao and Zhang, 2007), or the Path Length Correction (PLC) (Yin et al., 2018), which have been shown to be successful in other studies (Ma et al., 2021).

The difficulty in distinguishing land cover classes is partly due to their physical characteristics. Rivers are often shallow in many of the areas observed, so the sensor detects gravel reflectance from the riverbed in addition to surface water, which can lead to misclassification. Problems with vegetation detection occur primarily when foliage is not fully developed and the sensor detects bare ground or shade under trees.

In addition to the limitations that apply generally to land cover classification based on multispectral optical images, issues related to SMA in particular are also important. The SMA determines the fraction of land cover presence on an individual pixel by examining the spectral signal from the observed pixel and comparing it to the spectral signals of the input endmembers. The land cover fractions are determined based on the degree of similarity between the spectral signals of the observed pixel and the endmembers. The selected endmembers must therefore have sufficiently different spectral properties for

the SMA to be able to differentiate between their respective contributions to the spectral signal of the observed pixel. It is therefore necessary to make simplifications and generalisations when selecting the land cover classes that are considered in the analysis. In our study of mapping gravel bars, the most severe simplification was the inclusion of built-up areas in the gravel class. The gravel presence maps therefore do not differentiate between gravel bars and built-up areas. We mitigated this problem by limiting the study area to water lands in order to include only riparian areas in the analysis. However, some built-up is present even in water lands, particularly in larger settlements. This could be addressed with the addition of different EO data such as synthetic aperture radar (SAR), or in the post-processing stage with the use of auxiliary datasets of buildings and infrastructure for masking.

The accuracy of the SMA depends on the ability of the selected endmembers to represent the land cover classes of interest. Validation of our fraction maps indicates that gravel can generally be modelled well with the selected endmembers. On the other hand, vegetation and water are more problematic for mapping. Vegetation in the study areas occurs in diverse forms, mostly as mixed forest, but also as shrubs and grasslands. The general shapes of the spectral signatures are similar across different vegetation forms, but each plant species still has slightly different spectral characteristics. These differences can lead to errors when a single endmember is used to model all of the different vegetation classes. Similarly, water can have different spectral responses depending on Sun glint, surface waves, depth, sediment content, microorganisms, and dissolved organic matter (Guneroglu et al., 2013; Japitana et al., 2019; Vouvé et al., 2009). Thus, different models could be used to represent water based on different endmembers. The model with the smallest RMSE could then be selected as the final model for mapping water (Cavanaugh et al., 2011). A similar strategy could be used for vegetation.

Real changes of gravel bars can only be detected with observations during times of similar hydrological conditions. Otherwise, the detected changes could be the result of different water levels and not changes in bedload. This could be a limitation in studies of rivers with fewer gauging stations. Radar altimetry has been shown to provide good ancillary data in the case of ungauged rivers and could be used to inform further analysis and allow an unbiased change detection (Bogning et al., 2018).

5.4   Opportunities for Further Work

The proposed method can be used to study and monitor other rivers where important gravel bar habitats are present. A well-known European example is the Tagliamento river in Italy, which forms extensive gravel bars with high biodiversity. The river is also very dynamic and therefore interesting to observe frequently (Gurnell et al., 2001; Henshaw et al., 2013). Rivers in different climatic zones and with various geologic characteristics of the basins can be studied to learn more about the geomorphological processes that shape them.

This study explored several characteristics that are important for improving the accuracy of SMA-based land cover fraction maps. These findings and the proposed workflow can be used for mapping various phenomena. The only limitation in using this method is that the observed land cover classes must have very distinct and different spectral properties. This is necessary for the SMA to accurately determine the contributions of the different land cover classes to the mixed signal in a single pixel (de Vries et al., 2021). For example, it is difficult to correctly map different tree species that have a very similar spectral signature shape with SMA. However, delineation of bare ground or built-up areas and vegetation or water can be successfully performed. Therefore, examples of other possible applications of the proposed method are monitoring of urban sprawl, rock-fall, deforestation, and open-pit mining.

Monitoring gravel bars with the proposed method could be complemented with additional data in the future. In particular, the use of SAR could lead to better results. The SAR data could be integrated in a pre-processing stage, to more accurately delineate the area of observation or in the post-processing stage to mask out areas that are not of interest. Differences in texture are picked up well by SAR, which could help in differentiating between gravel bars and built-up areas. Data from SAR have been shown to be successful in separating water from other land cover classes (Musa et al., 2015). Additionally, SAR is not affected by clouds, which is an important consideration when studying mountainous regions where cloudy conditions are frequent. The successful use of combined SAR and multispectral data for land cover classification has already been demonstrated (Sukawattanavijit et al., 2017). Importantly, with the Copernicus programme supporting the operation of the Sentinel-1 SAR system, the long-term operational data availability is assured.

Hydrological conditions influence the reliability of monitoring changes of gravel bars. If changes are assessed between two time points with very different conditions, the differences in water level could induce changes that are not due to flood events or infrastructural interventions. In the present study of change detection, we selected images from the same season and thus ensured comparable hydrological conditions. However, this aspect of change detection can be developed further with more emphasis placed on selecting dates with very similar conditions.

6   CONCLUSION

The dissertation proposes a novel method for monitoring gravel bars in rivers using Earth observation (EO) data. Gravel bars are dynamic geomorphological features that provide many important ecological functions. Natural and anthropogenic changes in the fluvial environment rapidly lead to changes in the gravel bar extent and location. Gravel bars can therefore be considered indicators of alterations and disturbances in the fluvial environment. Monitoring gravel bars using field mapping is time consuming and therefore unfeasible for covering a large area simultaneously to provide an overview of the impact on the wider river system. Satellite remote sensing, with its frequent observations, increasingly open availability, and uniform, wide-area coverage, provides an ideal data source for monitoring natural processes. However, freely and openly available satellite images have a spatial resolution of 10 m at best, which may be too coarse to accurately detect gravel bars. We therefore tested soft classification as a method to observe features smaller than the spatial resolution of the EO sensor. Sub-pixel mapping was performed using spectral mixture analysis (SMA). We set several research objectives to develop a SMA-based mapping method for fluvial gravel bars that is transferable to different locations and requires only openly available data. The study area used for method development and related testing was located on the Soča river in northwestern Slovenia between the settlements of Kobarid and Tolmin.

Gravel bars can form in different parts of the river channel by both deposition and erosion processes. Once formed, their general location remains relatively stable, but their extent varies depending on the water level. Even where gravel bars are completely removed during resource excavation operations, they usually re-form quickly in the same location and with a similar extent. These characteristics of gravel bar development were also confirmed by our observations. We were able to obtain this information from time series of fraction maps showing the presence of gravel bars. The development of these maps was the result of many different tests that allowed us to gain a better understanding of the SMA and the features that define its accuracy.

We used very high resolution (VHR) aerial orthophotos and satellite images and classified them into the land cover types of interest using a Random Forest classifier with 500 trees. These classifications were used as reference data for validating the land cover fraction maps. We used two different validation methods, one focusing on pixel-level accuracy and a second evaluating the accuracy of land cover detection across the entire study area. The input data for the sub-pixel mapping were openly available satellite images from the Sentinel-2 and Landsat programmes. When working with Sentinel-2, we used the 20 m spectral bands because the majority of bands are acquired at this spatial resolution. The bands originally acquired at 10 m were resampled to 20 m. Detailed and abundant spectral information is critical for a successful SMA. Therefore, we supplemented the information from the spectral bands with selected spectral indices to better discriminate between gravel, vegetation, and water.

As described in the literature, appropriate endmembers are key to accurate fraction maps. We tested several configurations to determine the optimal characteristics for endmember selection for mapping gravel bars. Automatic endmember extraction was found to result in products with similar accuracy as using manually selected endmembers. However, even with automatic endmember extraction, operator intervention is required to ensure that the selected endmembers actually represent the land cover of interest and are not outliers. The approach that produces the most accurate fraction maps must therefore be semi-automatic. We found that three to five endmembers per SMA are optimal and that, contrary to results from the literature, adding shade as a separate endmember does not contribute to the accuracy of the fraction maps. In addition, endmembers selected on one satellite image can be used for the SMA of another satellite image from a similar geographic zone and phenological phase.

We compared the produced fraction maps of gravel bars with the results of a hard classification using the Spectral Angle Mapper with the same input data to determine the contribution of soft classification to increased accuracy of gravel bar monitoring. The results showed that the soft classification more accurately represents the land cover of the selected riparian environment in a mountainous area. After confirming the suitability of the fraction maps, we further developed and applied the proposed method. We produced time series of land cover presence in the study area based on fraction maps. The time series were smoothed using a Savitzky-Golay filter to minimise outliers but maintain distinct changes. The fraction mapping method was then extended to the upper and middle sections of the Soča river in Slovenia, the upper section of the Sava river in Slovenia, and the middle section of the Vjosa river in Albania. The total length of the combined river course mapped was over 250 km. We used Landsat images to produce fraction maps of gravel bars over the last 35 years.

Finally, we evaluated the ability of the fraction maps produced to detect changes in gravel bars. First, we tested simple image differencing of two fraction maps. To ensure that the observed changes resulted from flood events, gravel mining, or other interventions, and not just changes in water level, we selected dates with similar hydrologic conditions. We were able to show that change detection using this method had high sensitivity, detecting areas of change with an extent of at least 400 m^2 or one pixel of input satellite images. The change maps also showed satisfactory precision, with nearly 75% of detected changes confirmed by VHR reference data. Next, we investigated whether time series of gravel presence could also be used to detect change. The extents of water and gravel can vary following changes in water level. However, we found that a decrease in gravel bar size within two standard deviations of the mean indicated regular variations, while a larger decrease pointed to gravel bar removal.

Additionally, we compared the EO-based time series of land cover presence with in situ hydrological data. We found a high statistically significant negative correlation between the gravel presence and the water level measured at a gauging station in the study area. This suggests that remote sensing results

can be used to provide information about processes in areas where accurate and long-term in situ measurements are not established.

Thus, we achieved the research objectives set at the beginning of the study and obtained the expected results. These results can serve as a starting point for mapping different land cover types, such as built-up areas, bare ground, or anything else with distinct spectral properties and a tendency to occur at extents too small to be detected with openly available satellite images. In the case of extending the method to other land cover types, the tests defined by the workflow for deriving the method proposed in this dissertation would need to be repeated to determine the optimal mapping method for the particular land cover type under observation. The questions relating to endmembers are particularly important to accurately detect the land cover type of interest. Nevertheless, we believe that our study provides a good framework for further research and extension of the method to other land cover types.

A well known axiom in nature conservation is that processes which cannot be observed cannot be understood and features which cannot be monitored cannot be protected. Increasing volumes of EO data offer an opportunity to address such concerns about data gaps. We hope that the workflow that was developed in the scope of our research in addition to our findings will contribute to leverage the available data. The sub-pixel mapping method ensures that smaller features, which may have an important influence on environmental functions, are also considered in monitoring programmes. New insights into gravel bar dynamics may inform future efforts in protecting natural river ecosystems and restoring altered ecosystems closer to their natural state. This will enable a full functioning of river ecosystems with all the social and ecological benefits that they bring. Additionally, the developed method is opening several intersting possibilites for further technical solutions and thematic applications. There is therfore ample space to use available data in improved workflows to increase our understanding about the world and consequently lead a more responsible existence.

»This page is intentionally blank.«

7   SUMMARY

Earth observation (EO) has been established as an important source of environmental information. A globally uniform coverage of openly available data and a new observation every few days make EO data well suited for a variety of monitoring tasks. Despite advances in the field, there are many opportunities to expand the application of EO data, for example in sustainable development and hydrology. In this study, we explore the potential for monitoring gravel bars in rivers using freely available satellite images. Gravel bars are areas of sedimentation formed by deposition, but they can be transformed and reformed during successive periods of erosion and deposition. They are characteristic of braided river systems and may form in the middle of the riverbed or along the bank. Gravel bars are usually reshaped by events of high water level. As they become higher and are overgrown with vegetation, they are transformed into more stable fluvial islands. Gravel bars consist of underwater parts with rapids and deposits that form above the water surface. Our study focused on bare, non-vegetated gravel bars, which are the most dynamic, and their parts that extend above the water surface and can be observed with optical satellite images.

The habitats of several plant and animal species are tied to gravel bars. Filtration of water, infiltration into ground water, and mitigation of riverbank erosion are influenced by gravel bars. Their conservation importance has been recognised in several international and national directives. The most direct process that damages gravel bars is the in-channel mining of material for use in construction. The construction of dams, flood protection, and riverbed regulation also affect the sediment balance and consequently the extent of gravel bars. To better understand the impacts of these various processes on gravel bars, we developed a mapping and monitoring method based on openly available optical satellite images. We used data acquired since 1982 with the Landsat system in six (Landsat 4, Landsat 5, Landsat 7) or seven (Landsat 8) spectral bands with a spatial resolution of 30 m and a revisit time of 16 days. For more recent events, we used data from the Sentinel-2 system, which has been in operation since 2015. In 2017, the first Sentinel-2 satellite was complemented by a second satellite, increasing the revisit time to the current five days. Sentinel-2 acquires ten spectral bands – in similar wavelengths to the Landsat system – with a spatial resolution of 10 m or 20 m, depending on the band.

The spatial resolution of the input satellite images is adequate for many applications, but may be too coarse for observing rivers in their upper sections where they are still narrow. Gravel bars also often take forms that are narrower than the spatial resolution of the input images. A hard image classification, where each pixel is assigned one land cover class, may therefore not capture the full extent of gravel bars. Thus, we based the gravel bar mapping on soft classification, which reports the fractions that different land cover classes occupy in each pixel. The classification is based on linear spectral mixture analysis (SMA). The SMA calculates the degree to which the spectral response of a particular pixel

112

Stančič, L. 2022. Monitoring Changes of Fluvial Gravel Bars with Remote Sensing.
PhD Th. Ljubljana, UL FGG, Interdisciplinary doctoral study programme Environmental Protection.

matches the spectral responses of the input endmembers, i.e. pure pixels containing only one land cover class. In this way, features that have distinct spectral characteristics, but are smaller than the spatial resolution of the input images can be detected. Based on the SMA results, fraction maps of land cover class presence can be produced and plotted as time series for monitoring.

The SMA has been used for a variety of applications, from forest disturbance detection and soil degradation monitoring to urban expansion mapping. The principal input for a successful SMA are endmembers that accurately represent the land cover classes of interest. The endmember selection, also known as endmember extraction, can be done directly from the input satellite images, resulting in what are known as image endmembers. If the image contains a very heterogeneous landscape and all pixels are mixed, the endmembers can be modelled based on the image data. A third possibility is to obtain endmembers by field or laboratory measurements with spectroradiometers. We used image endmembers in our analyses, but selected them both manually and automatically. Manual selection was done with reference to very high resolution (VHR) aerial orthophoto or satellite images, or field mapping to ensure that only pure pixels were selected. Automatic selection was performed using the N-FINDR algorithm, which begins with a predefined number of pixels and replaces them until they outline a geometric body with the largest possible volume in the multidimensional space defined by the number of input image bands. Using the defined endmembers, we modelled the reflectances of the input mixed pixels with linear unmixing. Linear spectral unmixing occurs when different land cover classes are present in patches smaller than the instantaneous field of view (IFOV) of the remote sensing sensor, but nevertheless form distinct and separate forms. Non-linear spectral mixtures, on the other hand, are characteristic of formations where different materials are very closely intertwined, such as when analysing the composition of sand or soil. However, in gravel bar mapping, we assumed a linear spectral mixing mechanism. We use linear spectral unmixing to model the land cover class fractions or abundances in each pixel to produce sub-pixel maps of the fluvial environment.

The study consists of two main parts. The first part contains various tests to establish the workflow for the most accurate sub-pixel mapping. The tests are conducted in a study area on the Soča river in north-western Slovenia on a 15 km long river section between the settlements of Kobarid and Tolmin. This section was chosen because it contains many gravel bars, but also because there is a lot of ancillary data available that can be used for the development and validation of the method. The study focused on the river and riparian environment as defined by the official Water Lands spatial dataset, which comprises the riverbed and banks up to the first geomorphological change. The resulting maps were validated at both the pixel level and the entire study area level. Pixel-level validation involves a close-up view of the fraction maps, while the study area-wide validation was implemented to account for possible geometric shifts in the input images that would wrongly manifest as errors on the pixel level. The two validation

methods address different aspects of classification accuracy, but have been shown to produce similar results when comparing fraction maps with different configurations.

We first investigated different characteristics of the input satellite images that affect the accuracy of the fraction maps. We found that both Landsat and Sentinel-2 images can be used for accurate mapping. The geometric accuracy of the Sentinel-2 images was within 3 m on average, which is better than what is reported in the literature. The high geometric accuracy is a possible explanation for the minimal discrepancies between the pixel- and area-wide accuracy assessments. Atmospheric corrections improve the accuracy of the fraction maps, but topographic corrections introduce new uncertainties and do not result in better mapping. Super resolution of the 20 m Sentinel-2 bands to 10 m also did not result in more accurate fraction maps. Spectral indices are important to improve differentiation between the land cover classes of interest and increase the accuracy of fraction maps. This improvement has an upper limit after which additional indices no longer have a positive contribution. We supplemented the spectral bands with five different indices, namely Enhanced Vegetation Index (EVI), Modified Normalised Difference Vegetation Index 2 (MSAVI2), Normalised Difference Vegetation Index (NDVI), Normalised Difference Water Index (NDWI), and Modified Normalised Difference Water Index (MNDWI).

We showed that the automatically selected endmembers can produce comparable results to the manually selected endmembers. Despite the automation, it is necessary to review the selected endmembers to ensure that they represent the land cover classes of interest and not spectral or land cover outliers. The optimal number of all endmembers used for SMA is between three and five. Multiple endmembers can be used to represent the same land cover class and combine their fractions after SMA, e.g. forest and grassland pixels used to determine vegetation fractions. We considered three different land cover classes – gravel, vegetation, and water. Several studies in the existing literature include shade as a separate endmember. We assumed that this would improve the mapping accuracy because topographic shadow in a narrow river valley surrounded by steep slopes and vegetation shadows obscuring underlying surface water and gravel are common in our study area. However, shade was not accurately mapped by the proposed method, and including shade into other land cover classes did not improve fraction maps. Finally, we found that endmembers selected on one image of the study area during the leaf-on season could be accurately used for the SMA of another image of the same area acquired with the same remote sensing system at a different time during the leaf-on period.

Once the input data and workflow for endmember selection were established, we produced fraction maps of the study area using Sentinel-2, Landsat 7, and Landsat 8 images at different timestamps. Gravel bars are easily distinguished on the maps and their changes over the years are evident. The fraction maps produced using the soft classification were compared with the maps resulting from the hard classification

with the Spectral Angle Mapper (SAM). The same satellite images and endmember spectra were used for SAM as for the SMA. Different input images and endmembers were tested. Gravel was mapped more accurately by the soft classification than by the hard classification in all cases.

Next, we produced a time series of land cover class presence based on available satellite images. We focused on the Sentinel-2 data because they have a higher temporal density. When analysing a series of different satellite images, one of the main questions is which endmembers to use. First, three different configurations for the selection of endmembers for all land cover classes of interest were tested. In the first configuration, the same set of endmembers was applied for the analysis of all images. In the second configuration, endmembers were selected separately for each image. In the third configuration, only vegetation endmembers were selected separately for each image, while for gravel and water the same set of endmembers was used for all images. The general trends shown by the land cover time series were similar for all configurations. The time series with the same set of endmembers transferred for analysis of all images was the most stable with the least fluctuations, therefore this method was recommended for further analysis. To account for seasonal variations in vegetation reflectance, we performed tests to smooth the vegetation endmembers selected separately on each input satellite image. In the first method, the time series of vegetation endmembers were smoothed using a Savitzky-Golay filter, while in the second method monthly averages of vegetation endmember values were calculated. The differences in the resulting time series are negligible. Because smoothing and averaging of vegetation endmembers require additional processing time, we do not recommend them. Finally, we attempted to remove the outliers in land cover presence using a Savitzky-Golay filter. The smoothed time series more clearly showed meaningful changes in the environment.

The mapping method established on the study area was then applied for the analysis of more extensive river sections and over longer time periods. We mapped a total of over 250 km on the Soča and Sava rivers in Slovenia and on the Vjosa river in Albania. Landsat images were used as input to cover a time period of over 30 years. The gravel fraction maps provide an overview of changes in the extent and location of gravel bars. We used VHR reference data to validate the fraction maps produced. The gravel class was detected with 95% accuracy for all rivers considered.

We then investigated the most important characteristic of the produced fraction maps – their ability to detect change. First, we examined the capabilities of simple image differencing. We compared three fraction maps produced from Sentinel-2 images from a three-year time span and validated the detected changes with VHR reference data from the same timestamps. We paid attention to the hydrological conditions during the time of input and reference data acquisition to ensure that the detected changes arise from actual changes in river processes and not just different water levels. The change maps were assessed in terms of sensitivity, i.e. the ability to detect actual changes on the ground as observed in the

reference data, and precision, i.e. that the changes shown on the change maps actually occurred and could be confirmed with the reference data. The evaluation of sensitivity focused on areas of change that were at least 400 m^2 in size, which is equal to the extent of one pixel of the input satellite image. We verified the values of the fraction change maps in the reference change areas. A total of 72 areas with gravel removal (decrease in gravel fraction) and 43 areas with gravel deposition (increase in gravel fraction) were considered. Both removal and deposition of gravel were detected well on the change maps. Deposition occurred in narrower strips that often did not reach the width of an entire pixel. Therefore, the change values in the areas of deposition were lower than the change values in the areas of removal. This could be a specificity of the study area. The assessment of change detection precision focused on 62 non-adjacent pixels where a change of at least ± 10% was detected. Reference data were then used to verify that a change had indeed occurred on these selected pixels. Almost 75% of the detected changes were confirmed, with half of them showing a change from gravel to water. In 10% of the cases, no change could be detected on the reference data, while in 15% a false change was reported. An examination of the change values in areas with true changes showed that the values were much higher than in areas with false or no changes. Values of fraction change higher than ± 30% were indicative of a true change. Final validation of the simple fraction change maps was performed by correlation with change maps based on reference data. The reference change maps were resampled to the spatial resolution of fraction change maps, i.e. 20 m. The pixel values of the fraction maps and the reference maps were then compared at the level of the entire study area and also only in the areas of change detected in the reference data. The results confirmed that the two datasets are highly correlated, especially in the areas of change (Pearson's r > 0.85, p < 0.0001).

In addition to fraction change maps produced by image differencing, we tested whether time series of data of land cover presence could be used to monitor gravel bars. First, we compared the time series of gravel presence in the study area on the Soča river with in situ water level data from a gauging station in the study area. There was a significant negative correlation between the two datasets (Pearson's r < −0.64, p < 0.0001), showing agreement of the fraction maps with the expected physical processes on the ground. Next, we investigated whether time series of gravel presence could be used to detect change. We focused on two known gravel removal sites, one on the Soča near the settlement of Dolje and another on the Sava near the city of Kranj. We plotted the time series of gravel presence at a smaller study area encompassing the gravel removal sites over a period of 2019 and 2020. All available Sentinel-2 images with cloud cover of 10% or less were used to produce fraction maps. The presence of gravel at the study sites varied with relation to the water level, and these fluctuations were substantial. However, we found that a decrease in gravel presence of more than two standard deviations below the value of the average gravel presence in the study area indicated gravel removal. For example, in the Dolje study area, the average gravel presence during the two years of observation was 4 ha with a standard deviation of 1 ha.

A decrease of 2 ha therefore indicated removal. The same process was observed in Kranj. Thus, the time series of gravel presence can be used to detect changes that are above the specified threshold in size.

The tests and applications of the proposed method for gravel bar mapping on different rivers confirmed our first hypothesis that using SMA it is possible to distinguish gravel bars, surface water, and vegetation in fluvial ecosystems with a thematic accuracy of 90%. In particular, gravel was mapped very accurately, while vegetation was more problematic, sometimes not achieving 90% accuracy. The change detection evaluation also confirmed the second proposed hypothesis that sub-pixel land cover maps can be used to monitor changes in gravel bars that are at least 500 m^2 in size. The extent of change that can be detected depends on the spatial resolution of the input satellite images, but we showed that Sentinel-2 images with a spatial resolution of 20 m can detect changes of 400 m^2, i.e. the area equal to the size of one pixel of the input image. By using SMA, we aimed to contribute to new knowledge in the use of EO data for monitoring natural processes. The main contribution of the dissertation to science is the development of a new workflow for mapping gravel bars and other water-related features using freely available satellite images. The method was developed on a river section for which an abundance of ancillary data is available, which enabled validation of the results and development of an optimal mapping configuration. We also studied the transferability of the method and confirmed that it can be used to study areas where not as much data is available. This could lead to new insights into river dynamics and better management of the fluvial environment.

The main limitations of the proposed method are related to the use of optical satellite images. Cloud obstruction and terrain shadow prevent observation and monitoring of processes on the ground and are particularly problematic in mountainous areas surrounded by steep slopes and frequent cloud cover. Gravel is generally detected very well, but detection of water is difficult in areas with rapids and shallow sections where gravel reflectance from the riverbed can be detected by the sensor. Vegetation mapping is problematic when foliage is not fully developed and the sensor detects bare ground under trees. The SMA can successfully map land cover classes that have very different spectral signatures. Generalisations of diverse land cover classes with similar spectral signatures into a single land cover class are therefore necessary. The most problematic generalisation in our case is the inclusion of built-up areas in the gravel class. The gravel presence maps therefore do not differentiate between gravel bars and built-up. This is mitigated by focusing the analysis on water lands but remains problematic particularly in settlements. The accuracy of SMA depends on the quality of the endmembers used. It is difficult to select endmembers that accurately reflect the spectral properties of land cover classes that are very diverse. Water can have very different spectral responses depending on Sun glint, surface waves, depth, sediment content, presence of microorganisms, and dissolved organic matter, making it difficult to always accurately map it with SMA. This is even more pressing for vegetation, which occurs in many different forms in the area under observation. While the general shapes of the spectral signatures

of different vegetation forms are similar, there are some discrepancies depending on the plant species present. These differences could lead to errors if a single endmember is used to model all vegetation forms. Therefore, further work could explore the possibility of using several different models to represent water and vegetation based on different endmembers and selecting the model with the least error for further mapping. Monitoring of gravel bars could also be supplemented with synthetic aperture radar (SAR), which is not affected by clouds and is known for successful water detection. Further studies could also be done using the currently developed sub-pixel mapping method, extending it to other river systems. Several other phenomena and land cover classes could also be mapped using the proposed workflow, such as deforestation and urbanisation. The abundance of openly available satellite images with frequent revisit times allows monitoring of diverse processes and making more informed decisions.

»This page is intentionally blank.«

8   RAZŠIRJEN POVZETEK

Opazovanje Zemlje se je uveljavilo kot pomemben vir podatkov o okolju. Enotna pokritost vseh svetovnih kopnih površin s prosto dostopnimi podatki vsakih nekaj dni pomeni, da so podatki opazovanja Zemlje primerni za različne naloge spremljanja spremembe. Kljub dosedanjemu napredku na tem področju obstaja še veliko možnosti za razširitev, na primer z vidika trajnostnega razvoja in hidrologije. Pričujoča raziskava proučuje možnosti za spremljanje rečnih prodišč z uporabo prosto dostopnih satelitskih posnetkov. Najboljša prostorska ločljivost prosto dostopnih satelitskih posnetkov je 10 m, to pa pogosto ni dovolj dobro za natančno zaznavanje prodišč, ki so lahko zelo ozka. Za izboljšanje kartiranja in spremljanja prodišč smo razvili metodo za podpikselsko kartiranje na podlagi analize vsebnosti spektralnega signala (ang. Spectral Mixture Analyis, SMA).

V doktorski disertaciji smo preverili naslednji dve raziskovalni hipotezi.

Hipoteza 1: Z analizo sestave spektralnega signala je mogoče ločiti prodišča, vodo in vegetacijo v rečnih ekosistemih.
Podhipoteza 1.1: Pokrovnost rečnih ekosistemov je mogoče z analizo sestave spektralnega signala prosto dostopnih satelitskih posnetkov prostorske ločljivosti do 10 m določiti z 90% tematsko natančnostjo.

Testirali smo različne pristope za določitev postopka, ki vodi do najbolj natančnih kart deležev pokrovnosti. Preverili smo različne značilnosti vhodnih satelitskih posnetkov, ki vplivajo na natančnost kartiranja – uporabljen sistem daljinskega zaznavanja, geometrijska in radiometrična natančnost, prostorska ločljivost in uporaba spektralnih indeksov. Poleg tega smo proučili lastnosti končnih pikslov, ki prav tako določajo natančnost kartiranja – možnost samodejnega izbora končnih pikslov, optimalno število izbranih končnih pikslov, senca kot dodaten končni piksel in premos končnih pikslov, izbranih na enem posnetku, za analizo drugega posnetka. Pri preizkusih smo za referenco uporabili terensko kartiranje, letalske ortofote in satelitske posnetke zelo visoke ločljivosti (ang. very high resolution, VHR).

Hipoteza 2: Z analizo časovne vrste tematskih kart podpikselske pokrovnosti lahko določimo sezonske spremembe v obsegu in lokaciji prodišč.
Podhipoteza 2.1: Ob sezonski dinamiki lahko zaznamo spremembe v površini prodišč zaradi izrednih antropogenih in naravnih dogodkov, ki so večje od 500 m².

Razvito metodo za podpikselsko kartiranje smo preizkusili na časovni vrsti satelitskih posnetkov. Pri tem smo preverili vpliv različnih pristopov pri razvoju časovne vrste – izbor končnih pikslov,

modeliranje vegetacije v različnih fenoloških fazah in časovno glajenje izračunane prisotnosti izbranih razredov pokrovnosti. Časovno vrsto izračunane prisotnosti razredov pokrovnosti smo primerjali s hidrološkimi podatki merilne postaje. V nadaljevanju smo izdelali karte deležev prisotnosti proda za odseke na treh izbranih rekah v skupni dolžini prek 250 km in s časovnim obsegom prek 30 let. Nazadnje smo preverili sposobnost predlagane metode za zaznavo sprememb prodišč z vidika občutljivosti in natančnosti na podlagi referenčnih VHR posnetkov. Z opazovanjem vpliva sprememb na grafični prikaz prisotnosti proda smo proučili tudi možnost za spremljanje prodišč s podatki časovnih vrst.

8.1   Značilnosti rečnih prodišč

Prodišča so območja začasne sedimentacije v rečnih koritih, ki nastanejo z odlaganjem, vendar so lahko tudi preoblikovana v zaporednem delovanju erozije in odlaganja. Značilna so za pramenaste rečne sisteme in lahko nastanejo na sredini struge ali ob bregu. Gorvodno nad prodiščem se navadno nahaja tolmun, poglobitev rečnega dna, kjer se vodni tok upočasni. Na čelu prodišča prečno na strugo nastanejo plitve brzice ali brazde, kjer vodni tok plitev in hiter. Glavni razlog za nastanek prodišč je lokalno zmanjšanje transportne moči vodnega toka. Do tega pogosto pride tudi na notranjem delu rečnih meandrov (Tarbuck in Lutgens, 2005). Oblika prodišč in velikost odloženega zrna sta odvisni od povprečnega strmca vodnega telesa in od pretoka. Ob povečanih pretokih se sestavni material prodišč navadno zamenja, njihova lokacija v strugi pa se ne spreminja. Obstaja več različnih klasifikacij tipov prodišč (npr. glede na kompleksnost ali glede na mesto nastanka v strugi), vendar lahko en tip prodišča s časom preide v drugega. Dogodki z visokim vodostajem običajno preoblikujejo prodišča. Z odlaganjem dodatnega material postanejo prodišča višja, poraste jih vegetacija in tako se s časom preoblikujejo v stabilnejše rečne otoke (Robert, 2003). Prodišča so sestavljena tudi iz delov pod vodno gladino, kot so brzice in podvodni sedimenti, naša raziskava pa se je osredotočila na gola, neporasla prodišča, ki so najbolj dinamična, in specifično na njihove nadvodne dele, ki jih je mogoče opazovati z optičnimi satelitskimi posnetki.

Prodišča so habitati za več rastlinskih in živalskih vrst. Kot območja na stiku vodnega in kopnega sta za njih značilni velika vrstna pestrost in prisotnost redkih vrst (Langhans in Tockner, 2014; Zeng in sod., 2015). V Sloveniji imamo primere živalskih vrst, kot je ptica mali deževnik (*Charadrius dubius*), in rastlinskih vrst, kot je prodiščna hrustavka (*Chondrilla chondrilloides*), ki so vezane na rečna prodišča. Poleg tega prodišča vplivajo na filtracijo vode, vnos vode v podtalnico in blažitev erozije rečnih bregov. Različne mednarodne in državne direktive poudarjajo pomen ohranjevanja prodišč (OJ L 206, 1992; Uradni list RS št. 112/03, 2003; EC DG ENVIRONMENT, 2013). Gre namreč za habitat, ki je spremenljiv, nestabilen in občutljiv na hidrološke spremembe ter kot tak dober pokazatelj motenj v fluvialnem okolju.

Dejavnost, ki najbolj neposredno uničuje prodišča, je izkop materiala za uporabo v gradbeništvu (Jogan in sod., 2004). Gradnja jezov, protipoplavne zaščite in ureditev struge vplivajo tudi na ravnovesje v količini sedimenta ter posledično na obseg prodišč. Večdesetletno proučevanje zajezenih rek je pokazalo, da delovanje hidroelektrarn lahko povzroči razširitev rečne struge, zmanjšanje števila brzic in tolmunov in povečanje števila izdankov matične podlage v strugi. Dnevni izpusti vode vodijo do odnašanja drobnejših delcev. Zaradi zmanjšane vijugavosti in zaporedij brzic ter tolmunov se zmanjša hrapavost dna in poveča premestitvena zmogljivost vodotoka, kar lahko vodi do poglabljanja rečnega korita (Assani in Petit, 2004; Kiss in Andrasi, 2014).

Prodišča skupaj s tolmuni in brazdami sestavljajo osnovno enoto razvejanih rek. Njihovo število, lokacija, oblika, sestava in velikost nakazujejo potek geomorfoloških procesov v rečnem koritu. Za boljše razumevanje vpliva različnih procesov na prodišča smo razvili metodo kartiranja in spremljanja, ki temelji na prosto dostopnih optičnih satelitskih posnetkih.

8.2   Osnove analize vsebnosti spektralnega signala

Prostorska ločljivost prosto dostopnih satelitskih posnetkov je dobra za številne aplikacije, vendar je lahko preveč groba za opazovanje rek v njihovih zgornjih delih, kjer so navadno ozke. Tudi prodišča so pogosto ožja od prostorske ločljivosti vhodnih satelitskih posnetkov. Trda klasifikacija posnetkov, pri kateri je vsakemu pikslu (slikovnemu elementu) dodeljen en razred pokrovnosti, zato morda ne zazna celotnega obsega prodišč. Kartiranje prodišč smo zato zasnovali na uporabi mehke klasifikacije, ki opredeli deleže pristnosti različnih razredov pokrovnosti na vsakem pikslu. Klasifikacija temelji na linearni SMA. Metoda SMA izračuna stopnjo ujemanja spektralnega signala določenega piksla s spektralnimi signali vhodnih končnih pikslov (ang. endmembers), to je čistih pikslov, ki vsebujejo samo en razred pokrovnosti (Keshava 2003; Veganzones in Graña, 2008). Na ta način je mogoče zaznati pojave, ki imajo značilne spektralne lastnosti, vendar so manjši od prostorske ločljivosti vhodnih posnetkov. Na podlagi rezultatov SMA je mogoče izdelati karte deležev prisotnosti izbranih razredov pokritosti in z njimi izrisati časovne vrste za spremljanje stanja na površju.

Metoda SMA je bila razvita za opazovanje kamnin in mineralov na Marsu (Adams in sod., 1986) ter kasneje uporabljena za različne namene – od odkrivanja poškodb gozdov (Hirschmugl in sod., 2014) in spremljanja degradacije tal (Dubovyk in sod., 2015) do kartiranja širitve mest (Aina in sod., 2019). Ključni vhodni podatki za uspešno SMA je zadostno število primernih končnih pikslov, ki natančno predstavljajo spektralne lastnosti izbranih razredov pokrovnosti. Določitev primernega števila končnih pikslov, s katerimi lahko opišemo značilnosti opazovanega območja, navadno vključuje preizkušanje različnih možnosti in izbor tiste, ki vodi do najmanjše napake (Somers in sod. 2011). Izbor spektralnih značilnosti končnega piksla lahko naredimo neposredno na vhodnih satelitskih posnetkih. Če posnetek vsebuje zelo heterogeno pokrajino in so vsi piksli mešani, lahko končne piksle modeliramo na podlagi

podatkov o posnetku in tako dobimo končne piksle, ki niso izbrani na posnetku (ang. non-pixel endmembers). Tretja možnost je pridobitev končnih pikslov s terenskimi ali laboratorijskimi meritvami s spektro-radiometri (Du, 2018). V naših analizah smo uporabili končne piksle, izbrane na posnetku (ang. image endmembers), vendar smo jih izbrali tako ročno kot samodejno. Ročni izbor smo naredili glede na letalski ortofoto, podatke VHR ali terensko kartiranje. S tem smo zagotovili izbor resnično čistih pikslov, ki so vsebovali le en razred pokrovnosti. Samodejni izbor smo opravili z uporabo algoritma N-FINDR, ki se začne z vnaprej določenim željenim številom pikslov. Algoritem začetne izbrane piksle nato zamenjuje z drugimi, dokler ne začrtajo geometrijskega telesa z največjim možnim volumnom v večdimenzionalnem prostoru, določenem s številom spektralnih kanalov na vhodnem posnetku (Slika 48).
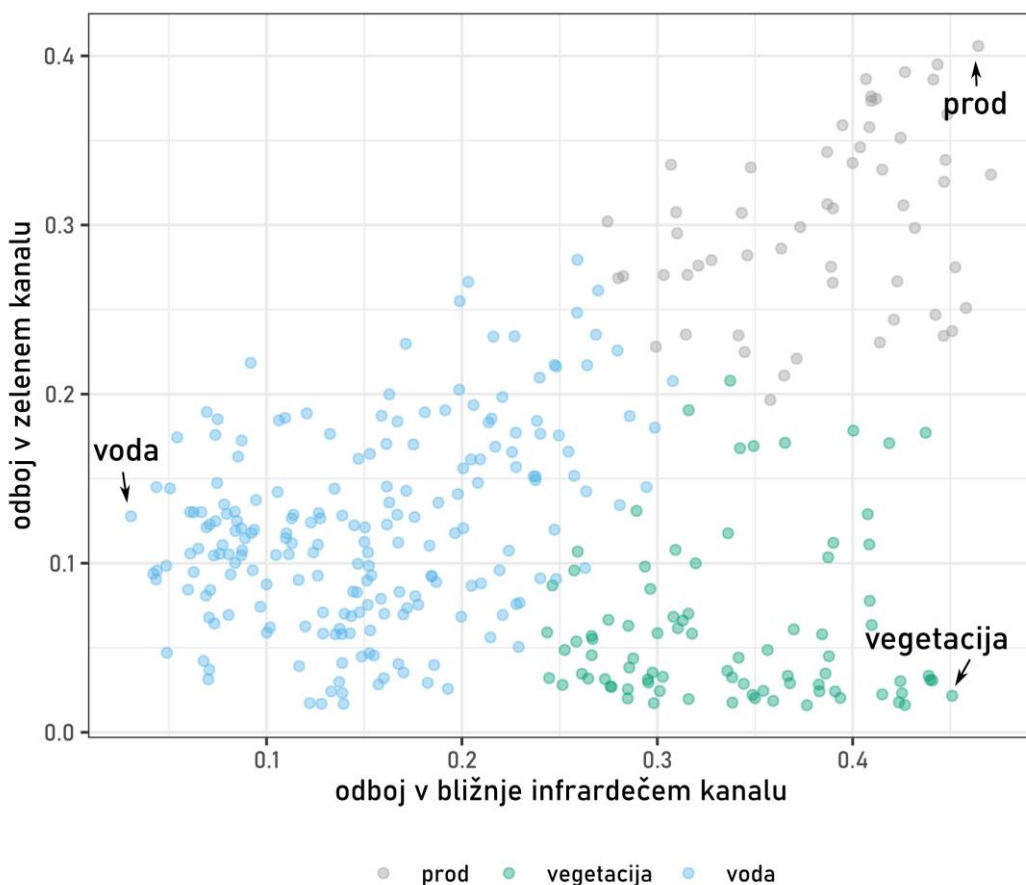
Slika 48:   Primer končnih pikslov, izbranih kot skrajne točke v trodimenzijskem spektralnem prostoru.

Figure 48:   An example of endmembers selected as extreme points in a three-dimensional spectral space.

Tako definirane končne piksle smo uporabili za modeliranje odbojnosti vhodnih linearno mešanih pikslov. Linearne spektralne mešanice so prisotne, ko se različni razredi pokrovnosti pojavljajo v oblikah, ki so manjše od trenutnega vidnega polja (ang. instantaneous field of view, IFOV) senzorja, vendar so kljub temu jasno zamejene. Po drugi strani so nelinearne spektralne mešanice značilne za

oblike, kjer so različni materiali zelo tesno prepleteni, na primer pri analizi sestave peska ali prsti. V primeru kartiranja prodišč smo predpostavili linearni spektralni mehanizem mešanja. V tem primeru je spektralni signal mešanega piksla (r) določen kot kombinacija spektralnih signalov končnih pikslov, obteženih s podpikselsko prisotnostjo razredov pokrovnosti. Model opiše spodnja enačba

$$r = Mf + \varepsilon \tag{4}$$

kjer je M matrika v kateri stolpci predstavljajo spektralne podpise izbranih končnih pikslov, f je vektor deležev prisotnosti razredov pokrovnosti in ε je šum ali delež signala, ki ga ni mogoče opisati z izbranimi končnimi piksli.

Za reševanje enačbe lahko uporabimo kvadratno programiranje, metod največje verejtnosti ali metodo najmanjših kvadratov. Metodo SMA lahko izvedemo brez omejitev, a če želimo pridobiti fizikalno smiselne rezultate, vrednosti koeficientov v enačbi 4 pogosto omejimo na pozitivna števila. Implementiramo lahko tudi pogoj, da mora biti seštevek vrednosti koeficientov enak ena. Na ta način dobimo polno omejeno analizo vsebnosti spektralnega signala (ang. fully constrained spectral mixture analysis), ki smo jo izvedli tudi v tej raziskavi. Uporabili smo torej linearno SMA za modeliranje deležev (ang. fractions, abundances) razredov pokrovnosti na vsakem pikslu in tako naredili podpikselske karte rečnega okolja.

8.3   Razvoj metode za podpikselsko kartiranje prodišč

Disertacija je sestavljena iz dveh glavnih delov. V prvem delu smo se ukvarjali z različnimi testi za vzpostavitev pristopa za najbolj natančno podpikselsko kartiranje. Za kartiranje prodišč smo uporabili podatke, pridobljene s sistemom za daljinsko zaznavanje Landsat od leta 1982 v šestih (Landsat 4, Landsat 5, Landsat 7) ali sedmih (Landsat 8) spektralnih kanalih s prostorsko ločljivostjo 30 m in novim posnetkom istega območja vsakih 16 dni (Barsi in sod., 2014). Pri opazovanju novejših dogodkov smo uporabili podatke sistema Sentinel-2, ki deluje od leta 2015. Leta 2017 je bil prvi satelit Sentinel-2 dopolnjen z drugim satelitom, s čimer se je čas ponovnega obiska skrajšal na zdajšnjih pet dni. Satelit Sentinel-2 opazuje Zemljo v desetih spektralnih kanalih – v podobnih valovnih dolžinah kot Landsat – s prostorsko ločljivostjo 10 ali 20 m, odvisno od kanala (Drusch in sod., 2012).

Pri kartiranju smo se osredotočili na obvodna območja, kakor jih določa sloj vodnih zemljišč. Gre za prosto dostopne vektorske podatke, ki so dostopni v vodnem katastru Direkcije RS za vode (DRSV, 2021). Vodno zemljišče obsega rečno korito do prve večje geomorfološke spremembe. Rečni bregovi in prodišča so tako vključeni v območje analize. Podatkovni sloj je bil pripravljen v skladu z Zakonom o vodah (Uradni list RS št. 67/02, 2002) na podlagi ortofotov iz Cikličnega aerofotografiranja Slovenije in podatkov Laserskega skeniranja Slovenije.

V analizi smo se ukvarjali s tremi različnimi razredi pokrovnosti, ki sestavljajo večino obrečnega okolja – prod, vegetacija in voda. Za uspešno SMA morajo imeti obravnavani razredi čim bolj različne spektralne podpise. Če bi obravnavali razrede z zelo podobnimi spektralnimi podpisi, bi bilo zelo težko ločiti doprinose posameznih razredov k spektralnemu signalu opazovanega piksla. Zato je bilo pri izboru obravnavanih razredov potrebno narediti določene poenostavitve. Razred prod je vključeval prodišča, skale, pesek in pozidana območja. Mešanje prodišč in pozidanih območij smo zmanjševali z omejitvijo opazovanega območja na vodna zemljišča. Razred vegetacija je vključeval drevesa, grmišča in travišča. Razred voda je vključeval reke, potoke in stoječo vodo. V izogib mešanju osenčenih površin z vodo smo testirali smo tudi kartiranje sence kot ločenega razreda.

Preizkuse smo izvedli na študijskem območju na reki Soči v severozahodni Sloveniji na 15 km dolgem rečnem odseku med Kobaridom in Tolminom (Slika 49). Ta odsek smo izbrali, ker vsebuje veliko prodišč, pa tudi zato, ker je za to območje na voljo veliko dodatnih podatkov, ki smo jih lahko uporabili pri razvoju in validaciji različnih metod.
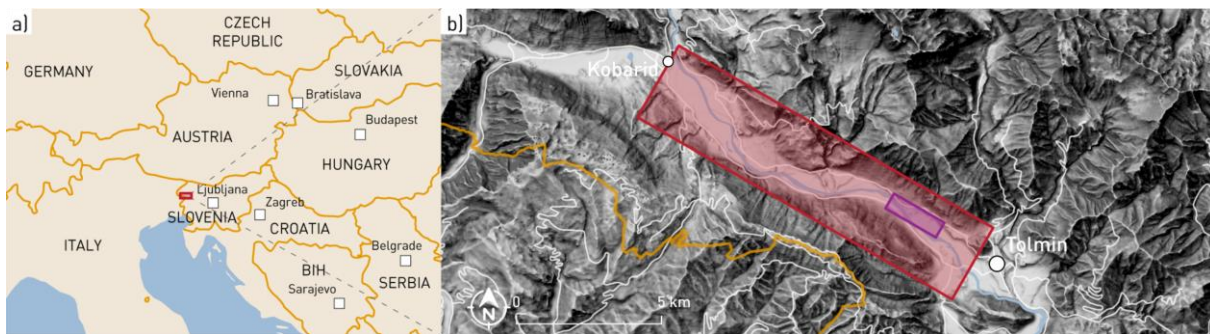
Slika 49:   Pregled študijskega območja. a) Lokacija študijskega območja (rdeč pravokotnik) v porečju zgornje Soče, v severozahodni Sloveniji, s sredinskimi koordinati 46.2° severno in 13.6° vzhodno (vir podatkov: Natural Earth, 2020). b) Bližnji pogled študijskega območja. Rdeč pravokotnik označuje celotno območje, vijolični pravokotnik pa lokacijo bližnjega pogleda na Slika 52 (vir podatkov: GURS, 2016, 2021a, 2021b).

Figure 49: Overview of the study area. a) Location of the study area (red rectangle) in the upper Soča river basin, north-western Slovenia, Central Europe, centred on 46.2° N, 13.6° E (data source: Natural Earth, 2020). b) A closer view of the study area. The red rectangle indicates the entire study area, while the purple rectangle marks the location of the enlarged view in Figure 52 (data source: Surveying and Mapping Authority of the Republic of Slovenia, 2016, 2021a, 2021b).

Rezultate v obliki kart smo ovrednotili tako na ravni pikslov kot na ravni študijskega območja. Ocena kakovosti na ravni pikslov proučuje karte deležev pokrovnosti od blizu. Deleže prisotnosti razredov pokrovnosti na podlagi SMA primerjamo z deleži zaznanimi na referenčnih podatkih (Schug in sod., 2018). Za referenčne podatke smo uporabili letalske ortofote, VHR satelitske posnetke (WorldView-2,

Pléiades) in lastno terensko kartiranje. Primerjavo smo naredili z izračunom povprečne absolutne napake (ang. mean absolute error, MAE):

$$MAE = \frac{1}{n} \sum_{i=1}^{n} |x_i - x|$$ (5)

kot absolutna razlika med deleži pokrovnosti na referenčnih podatkih (x) in deleži pokrovnosti na podlagi SMA (x_i). Vrednosti MAE smo izračunali za 50 naključno izbranih območij v velikosti enega piksla satelitskega posnetka na študijskem območju ($n = 50$).

Glavni doprinos ocene kakovosti na ravni celotnega študijskega območja je omilitev vpliva možnih geometrijskih premikov vhodnih posnetkov, ki bi jih lahko napačno zaznali kot napake na ravni pikslov. Za referenco smo uporabili klasifikacijo letalskih ortofotov in VHR satelitskih posnetkov. Preizkusili smo različne metode klasifikacije, vključno z ročno digitalizacijo in strojnim učenjem z različnimi algoritmi ter raznovrstnimi značlinostmi. Kot najboljši pristop tako z vidika natančnosti produktov kot tudi časovne in računske učinkovitosti smo izbrali klasifikacijo z algoritmom naključnih dreves (ang. random forest, RF) s 500 drevesi.

Obe metodi ocene kakovosti obravnavata različne vidike natančnosti klasifikacije, vendar se je pokazalo, da dajeta podobne rezultate pri primerjavi različnih kart deležev pokrovnosti. V nadaljevanju smo zato izmenično uporabljali tako validacijo na nivoju pikslov kot na nivoju celotnega študijskega območja.

8.3.1 Značilnosti vhodnih satelitskih posnetkov

V raziskavi smo naprej preverili značilnosti vhodnih satelitskih posnetkov, ki vplivajo na natančnost kart deležev pokrovnosti. Primerjali smo natančnost klasifikacije na podlagi različnih sistemov za daljinsko zaznavanje. Uporabili smo posnetke Sentinel-2, zajete 11.7.2015 in 23.4.2020, posnetek Landsat 7, zajet 9.7.2015 ter posnetek Landsat 8, zajet 25.4.2020 (Slika 50). Ugotovili smo, da se lahko posnetki Landsat in Sentinel-2 uporabljajo za natančno kartiranje.

126

Stančič, L. 2022. Monitoring Changes of Fluvial Gravel Bars with Remote Sensing.
PhD Th. Ljubljana, UL FGG, Interdisciplinary doctoral study programme Environmental Protection.
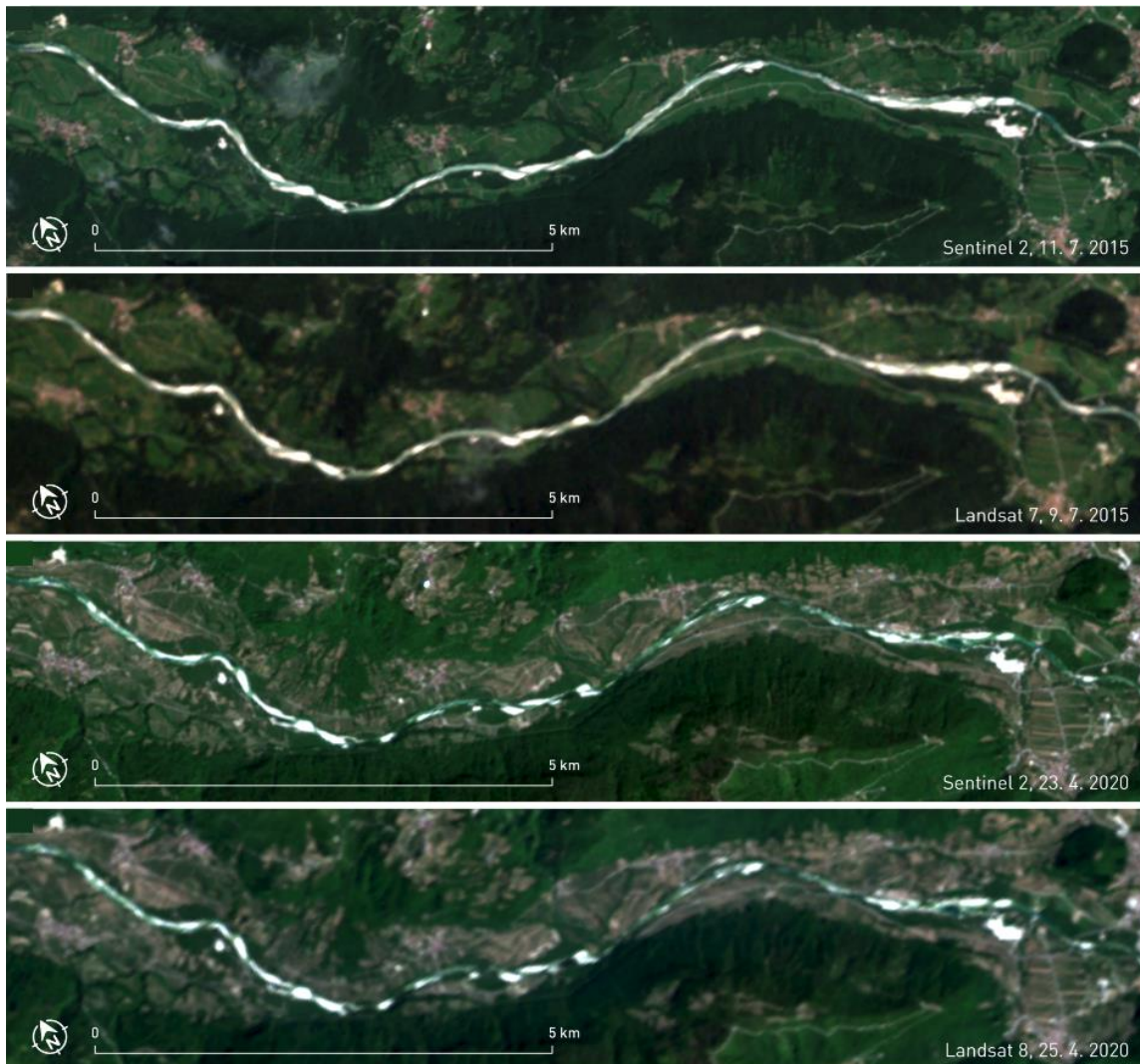
Slika 50: Pregled satelitskih posnetkov, uporabljenih v analizi. Naravno barvni kompoziti s posnetkov, uporabljenih v analizi (vir podatkov: ESA, 2021, U. S. Geological Survey, 2021a, 2021b).

Figure 50: Overview of the satellite images used in the analysis. True colour composites of the images used in the analysis (data source: ESA, 2021; U. S. Geological Survey, 2021a, 2021b).

Pri primerjavi satelitskih posnetkov, iskanju sprememb in analiza časovnih vrst je dobra geometrijska natančnost ključna lastnost posnetkov. Želeli smo preveriti realno geometrijsko natančnost posnetkov Sentinel-2. Za to smo izbrali tri različna študijska območja – v Sloveniji, na Cipru in v Keniji. Na vsakem območju smo izbrali 10 do 20 referenčnih točk, večinoma cestnih križišč, ki so služile za primerjavo različnih posnetkov. V analizo smo vključili vse posnetke, zajete med 2017 in 2020 z največ 10% oblačnosti. Rezultati so pokazali, da je bila geometrijska natančnost posnetkov Sentinel-2 v povprečju manjša od 3 m, kar je bolje, kot navaja literatura (Vajsova in Åstrand, 2015; Pandžić in sod., 2016; Rufin in sod., 2021). Z visoko geometrijsko natančnostjo lahko razlagamo tudi minimalna odstopanja med ocenami kakovosti na ravni pikslov in celotnega študijskega območja.

Stančič, L. 2022. Monitoring Changes of Fluvial Gravel Bars with Remote Sensing.
PhD Th. Ljubljana, UL FGG, Interdisciplinary doctoral study programme Environmental Protection.

127

Radiometrični popravki so pomemben korak v pred-procesiranju za analizo satelitskih posnetkov. Zmanjšajo vpliv atmosfere in reliefa na odbojnost površja in s tem omogočajo bolj natančne analize brez učinka artefaktov in boljšo primerjavo različnih posnetkov. Proučili smo doprinos atmosferskih in topografskih popravkov k natančnosti SMA. Atmosferske porpavke smo naredili s programom ATCOR (Richter in Schläpfer, 2019), topografske pa s procesno verigo STORM (Zakšek in sod., 2015; Pehani in sod. 2016). Rezultati so pokazali, da atmosferski popravki izboljšajo natančnost kart deležev pokrovnosti. Topografski popravki v posnetke vnašajo dodatne negotovosti in ne vodijo do boljšega kartiranja.

Velikost piksla satelitskega posnetka določa velikost površine, za katero z SMA izračunamo deleže prisotnosti razredov pokrovnosti. Preverili smo, ali bi izboljšanje prostorske ločljivosti satelitskih posnetkov lahko vodilo do bolj natančnih kart deležev pokrovnosti. Za izboljšanje prostorske ločljivosti smo uporabili algoritem DSen2, ki temelji na globokem učenju (Lanaras in sod., 2018). Teste smo naredili na posnetku Sentinel-2, zajetem 11.7.2915. Vse spektralne kanale, ki so bili zajeti z 20 m ali 60 m ločljivostjo, smo z globokim učenjem prevzorčili na 10 m. Izvzeli smo le 10. kanal (cirus), ki vsebuje preveč šuma. Rezultate kartiranja z izboljšanimi posnetki smo primerjali z rezultati na podlagi a) štirih spektralnih kanalov, ki so v izhodišču zajeti v 10 m, in z rezultati na podlagi b) kombinacije šestih spektralnih kanalov, ki so zajeti v 20 m ter štirih 10 m kanalov, prevzorčenih na 20 m z bilinearno interpolacijo. Izboljšanje prostorske ločljivost ni vodilo do natančnejših kart deležev pokrovnosti, zahteva pa dodaten čas za izvedbo, zato smo v nadaljevanju uporabili kanale v 20 m ločljivosti (opcija b, opisana zgoraj).

Spektralni indeksi so pomembni za boljše razlikovanje med različnimi razredi pokrovnosti in izboljšanje natančnosti karte deležev pokrovnosti. To izboljšanje ima zgornjo mejo, po kateri dodatni indeksi nimajo več pozitivnega vpliva na natančnost. Testirali smo zmožnost 12 različnih spektralnih indeksov za razločevanje izbranih razredov pokrovnosti in med njimi izbrali pet indekov z največjim doprinosom k boljši natančnosti kartiranja (Preglednica 23). Spektralne kanale smo tako dopolnili z naslednjimi indeksi: izboljšani vegetacijski indeks (ang. Enhanced Vegetation Index, EVI), spremenjen vegetacijski indeks, prilagojen za odbojnost prsti 2 (ang. Modified Soil Adjusted Vegetation Index 2, MSAVI2), normiran diferencialni vegetacijski indeks (ang. Normalised Difference Vegetation Index, NDVI), normiran diferencialni vodni indeks (ang. Normalised Difference Water Index, NDWI) in spremenjen normiran diferencialni vodni indeks (ang. Modified Normalised Difference Water Index, MNDWI).

128
Stančič, L. 2022. Monitoring Changes of Fluvial Gravel Bars with Remote Sensing.
PhD Th. Ljubljana, UL FGG, Interdisciplinary doctoral study programme Environmental Protection.

Preglednica 23: Spektralni indeksi, izbrani za izboljšanje ločevanja med razredi pokrovnosti.

Table 23: Spectral indices selected to improve the separability of land cover classes.

indeks	enačba	vir
izboljšani vegetacijski indeks (EVI)	$EVI = 2.5 \dfrac{NIR - RED}{NIR + 6RED - 7.5BLUE + 1}$	Huete in sod., 1999, 1997
spremenjen normiran diferencialni vodni indeks (MNDWI)	$MNDWI = \dfrac{GREEN - SWIR}{GREEN + SWIR}$	Du in sod., 2016
spremenjen vegetacijski indeks, prilagojen za odbojnost prsti 2 (MSAVI2)	$MSAVI2 = \dfrac{2SWIR + 1 - \sqrt{(2SWIR + 1)^2 - 8(SWIR - NIR)}}{2}$	Qi in sod., 1994
normiran diferencialni vegetacijski indeks (NDVI)	$NDVI = \dfrac{NIR - RED}{NIR + RED}$	Tucker, 1979
normiran diferencialni vodni indeks (NDWI)	$NDWI = \dfrac{GREEN - NIR}{GREEN + NIR}$	McFeeters, 1996

8.3.2 Izbor končnih pikslov

Končni piksli so ključni za uspešno SMA, zato je njihov izbor pomemben korak v analizi. Preverili smo vpliv različnih strategij izbora končnih pikslov na natančnost kartiranja deležev prisotnosti izbranih razredov pokrovnosti. Najprej smo proučili zmožnosti samodejnega izbora končnih pikslov. Samodejni izbor smo naredili z implementacijo algoritma N-FINDR v Python paketu pysptools (verzija 0.15.0) (Therien, 2018). Rezultate smo primerjali s kartiranjem na podlagi enakega števila končnih pikslov, ki smo jih ročno izbrali z vizualno interpretacijo referenčnih podatkov z visoko prostorsko ločljivostjo. Analizirali smo posnetke Sentinel-2, Landsat 7 in Landsat 8. Pokazali smo, da lahko samodejno izbrani končni piksli vodijo do rezultatov, primerljivih z ročno izbranimi končnimi piksli. Kljub samodejnosti je potrebno ob koncu analize ročno pregledati izbrane končne piksle in se s tem prepričamo, da predstavljajo izbrane razrede pokrovnosti in ne različnih osamelcev.

V nadaljevanju smo preverili, koliko končnih pikslov je smiselno uporabiti, preden pride do gručenja in podvajanja spektralnih informacij zaradi zelo velike podobnosti med razredi pokrovnosti. Ugotovili smo, da je optimalno število vseh končnih pikslov, ki se uporabljajo za SMA, med tri in pet (Slika 51). Za modeliranje prisotnosti enega izbranega razreda pokrovnosti lahko uporabimo več končnih pikslov in njihove deleže združimo po končani SMA. Tako lahko na primer uporabimo piksla gozdov in travnikov ter z njima določimo delež vegetacije.
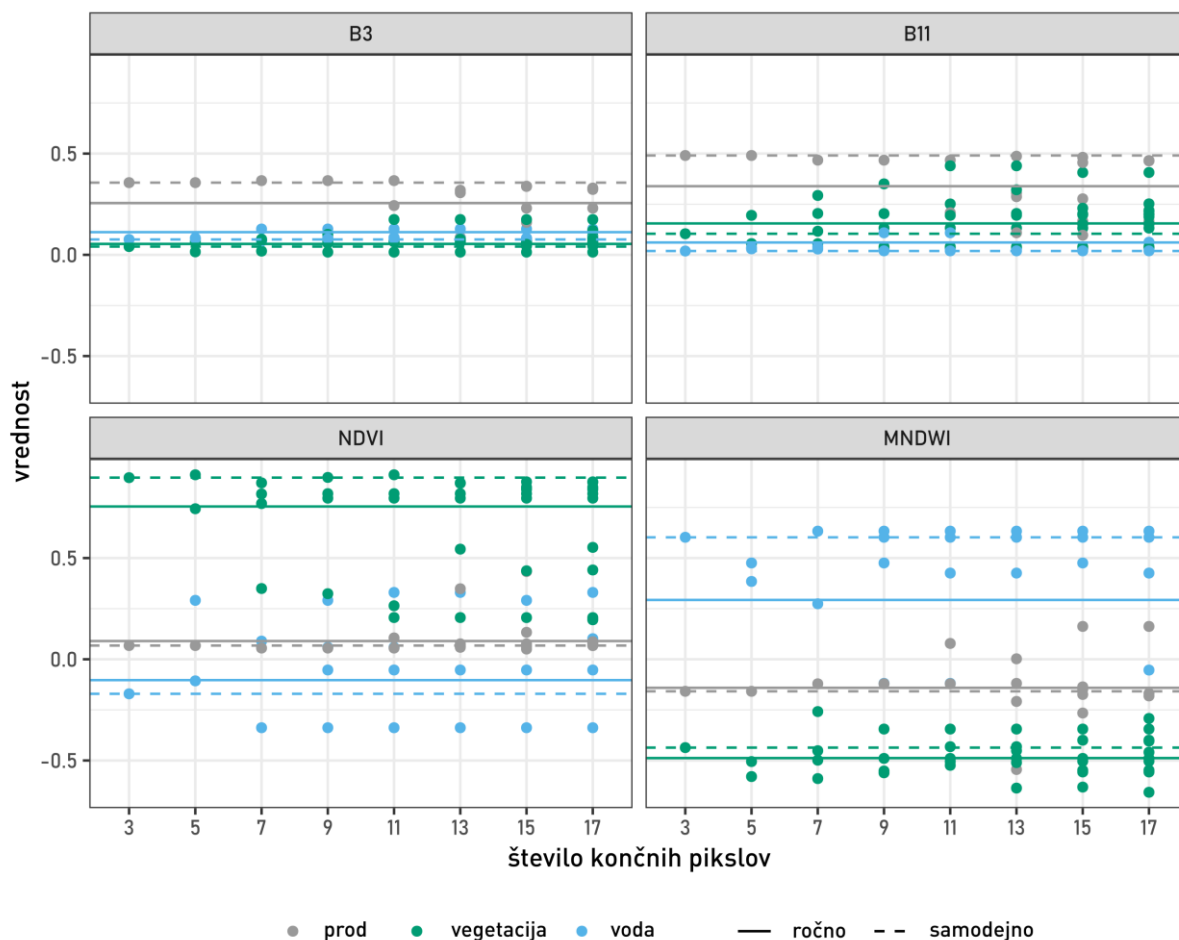
Slika 51: Vrednosti odboja v izbranih spektralnih kanalih in indeksih pri različnih številih samodejno izbranih končnih pikslov. Prikazana kanala in indeksa najbolje kažejo razlike med obravnavanimi razredi pokrovnosti. Prekinjena vodoravna črta prikazuje povprečno vrednost vseh samodejno izbranih končnih pikslov. Neprekinjena vodoravna črta prikazuje vrednost ročno izbranih končnih pikslov.

Figure 51: Values for selected spectral bands reflectance and indices for different numbers of automatically selected endmembers. The displayed bands and indices show the highest separability between the different land cover classes. The dashed horizontal line shows the average value of all automatically selected endmembers. The solid horizontal line shows the values for manually selected endmembers.

Obravnavali smo tri različne razrede pokrovnosti – prod, vegetacijo in vodo. Več študij v obstoječi literaturi k izbranim razredom pokrovnosti dodajajo senco kot ločen končni piksel (npr. Adams, 1995; Dennison in Roberts, 2003; Amaral in sod., 2015). Pričakovali smo, da bo to izboljšalo natančnost kartiranja, saj so topografske sence v ozki rečni dolini s strmimi pobočji in sence vegetacije, ki zakrivajo vodo in prod, pogosti pojavi na našem študijskem območju. Analizirali smo posnetke Sentinel-2, zajete 11.7.2015 in 16.10.2017. Izbrali smo časovna obdobja z različnimi koti Sonca nad obzorjem in posledično različnimi obsegi senc. Rezultati so pokazali, da sence niso bile natančno kartirane s predlagano metodo, poleg tega vključevanje senčnih vzorcev v druge razrede pokrovnosti ni izboljšalo

kart deležev pokrovnosti. V nadaljnjih analizah smo zato obravnavali le tri izhodiščne razrede pokrovnosti – prod, vegetacijo in vodo.

Nazadnje smo v testih izbora končnih pikslov preverili, ali lahko končne piksle, izbrane na enem satelitskem posnetku, uporabimo za analizo drugega satelitskega posnetka. Prenosljivost končnih pikslov smo preverili na posnetkih Sentinel-2 in Landsat 8 iz let 2015 in 2020. Ugotovili smo, da lahko končne piksle, izbrane na enem posnetku študijskega območja med sezono olistanja, uspešno uporabimo za SMA drugih posnetkov istega območja, pridobljene z istim sistemom daljinskega zaznavanja na drugi točki sezone olistanosti (ang. leaf-on period).

8.3.3   Karte pokrovnosti na podlagi mehke klasifikacije

Po določitvi najbolj primernih vhodnih podatkov in procesa za izbor končnih pikslov, smo izdelali karte deležev pokrovnosti za celotno študijsko območje na podlagi posnetkov Sentinel-2, Landsat 7 in Landsat 8 za različne časovne točke (Slika 52). Prodišča je na kartah enostavno razločiti; njihove spremembe skozi leta so očitne. Med kartami na podlagi ročno in samodejno izbranih končnih pikslov ni vidnih razlik.
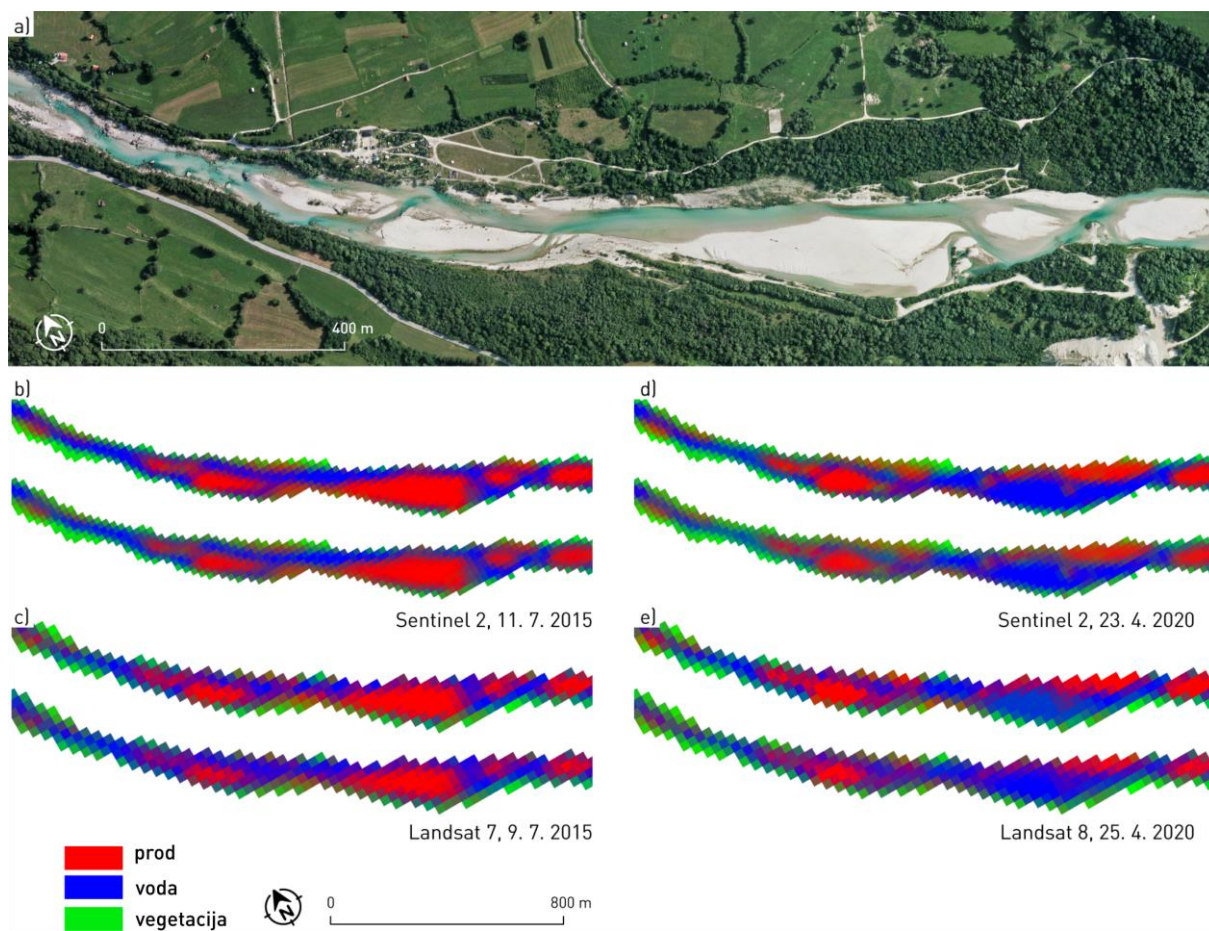
Slika 52: Karte deležev pokrovnosti za izsek študijskega območja na reki Soči. a) Prikaz opazovanega izseka na barvnem ortofotu (vir podatkov: GURS, 2021e). b) – c) Izdelane karte deležev pokrovnosti. Karte na podlagi ročno izbranih končnih pikslov prikazane zgoraj in karte na podlagi samodejno izbranih končnih pikslov prikazane spodaj.

Figure 52: Land cover fraction maps for a section of the study area on the Soča River. a) Observed river section on a true colour orthophoto (data source: Surveying and Mapping Authority of the Republic of Slovenia, 2021e). b) – c) Resulting fraction maps. Maps produced with manually selected endmembers shown at the top and maps produced with automatically selected endmembers shown at the bottom.

Karte deležev pokrovnosti, izdelane z uporabo mehke klasifikacije, smo primerjali s kartami, izdelanimi s trdo klasifikacijo na podlagi kota med spektri (ang. Spectral Angle Mapper, SAM). Za SAM smo uporabili iste satelitske posnetke in spektre končnih pikslov kot za SMA. Preizkusili smo različne vhodne posnetke in končne piksle. V vseh primerih je bil prod natančneje kartiran z mehko klasifikacijo kot s trdo. Primerjali smo tudi napake na nivoju pikslov za mehko in trdo klasifikacijo. Obstoječe raziskave so namreč pokazale močno povezanost med napakami različnih pristopov klasifikacije (Dennison in sod., 2004). V našem primeru na vzorcu 1000 pikslov nismo zaznali visoke korelacije med različnima metrikama napak; najvišji R^2 je znašal le 0.352. To pomeni, da piksel, ki je bil natančno klasificiran z mehko klasifikacijo, ni bil nujno enako natančno klasificiran s trdo klasifikacijo in obratno.

### 8.3.4   Razvoj časovne vrste podatkov o pokrovnosti

V naslednjem koraku smo na podlagi razpoložljivih satelitskih posnetkov izdelali časovno vrsto prisotnosti izbranih razredov pokrovnosti. Osredotočili smo se na podatke Sentinel-2 zaradi njihove večje časovne gostote. Pri analizi časovne vrste različnih satelitskih posnetkov je eno glavnih vprašanj, katere končne piksle uporabiti. Najprej smo preizkusili tri različne pristope za izbor končnih pikslov za vse izbrane razrede pokrovnosti. V prvem pristopu smo uporabili isti nabor končnih pikslov za analizo vseh posnetkov. V drugem pristopu smo končne piksle izbrali ločeno za vsak posnetek posebej. V tretjem pristopu smo za vsak posnetek posebej izbrali samo končni piksel za vegetacijo, medtem ko je bil za prod in vodo uporabljen isti nabor končnih pikslov za vse posnetke. Splošni trendi časovnih vrst pokrovnosti so bili podobni pri vseh različnih pristopih. Časovna vrsta z istim naborom končnih pikslov, prenesenih za analizo vseh posnetkov, je bila najbolj stabilna z najmanj nihanji, zato to metodo priporočamo za nadaljnjo analizo. Za upoštevanje sezonskih razlik v odbojnosti vegetacije, smo naredili dodatne teste za glajenje končnih pikslov za vegetacijo, izbranih na vsakem vhodnem satelitskem posnetku posebej. Pri prvem testu smo zgladili časovno vrsto končnih pikslov za vegetacijo s filtrom Savitzky-Golay, pri drugem testu pa smo izračunali mesečna povprečja vrednosti končnih pikslov za vegetacijo. Razlike v nastalih časovnih vrstah so bile zanemarljive. Glajenje in povprečje končnih pikslov za vegetacijo podaljša čas obdelave brez očitnih koristi, zato teh pristopov ne priporočamo. Nazadnje smo s filtrom Savitzky-Golay skušali odstraniti osamelce v časovni vrsti prisotnosti razredov pokrovnosti (Slika 53). Ugotovili smo, da je zglajena časovna vrsta bolj stabilna in bolj jasno kaže pomembne spremembe v okolju.
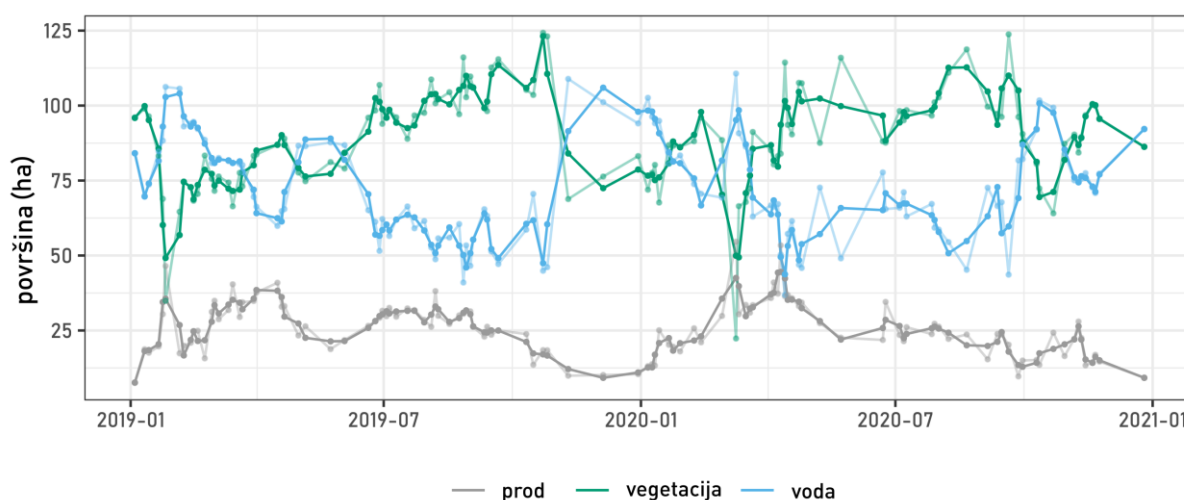
Slika 53: Časovna vrsta prisotnosti izbranih razredov pokrovnosti, zglajena s filtrom Savitzky-Golay. Nezglajene vrednosti prikazane v ozadju z večjo prosojnostjo.

Figure 53: Time series of different land cover classes presence smoothed with a Savitzky-Golay filter. Unsmoothed values shown in the background in lighter colours.

Stančič, L. 2022. Monitoring Changes of Fluvial Gravel Bars with Remote Sensing.
PhD Th. Ljubljana, UL FGG, Interdisciplinary doctoral study programme Environmental Protection.

133

Na podlagi navedenih testov smo oblikovali postopek za kartiranje in spremljanje prodišč s satelitskimi posnetki (Slika 54).
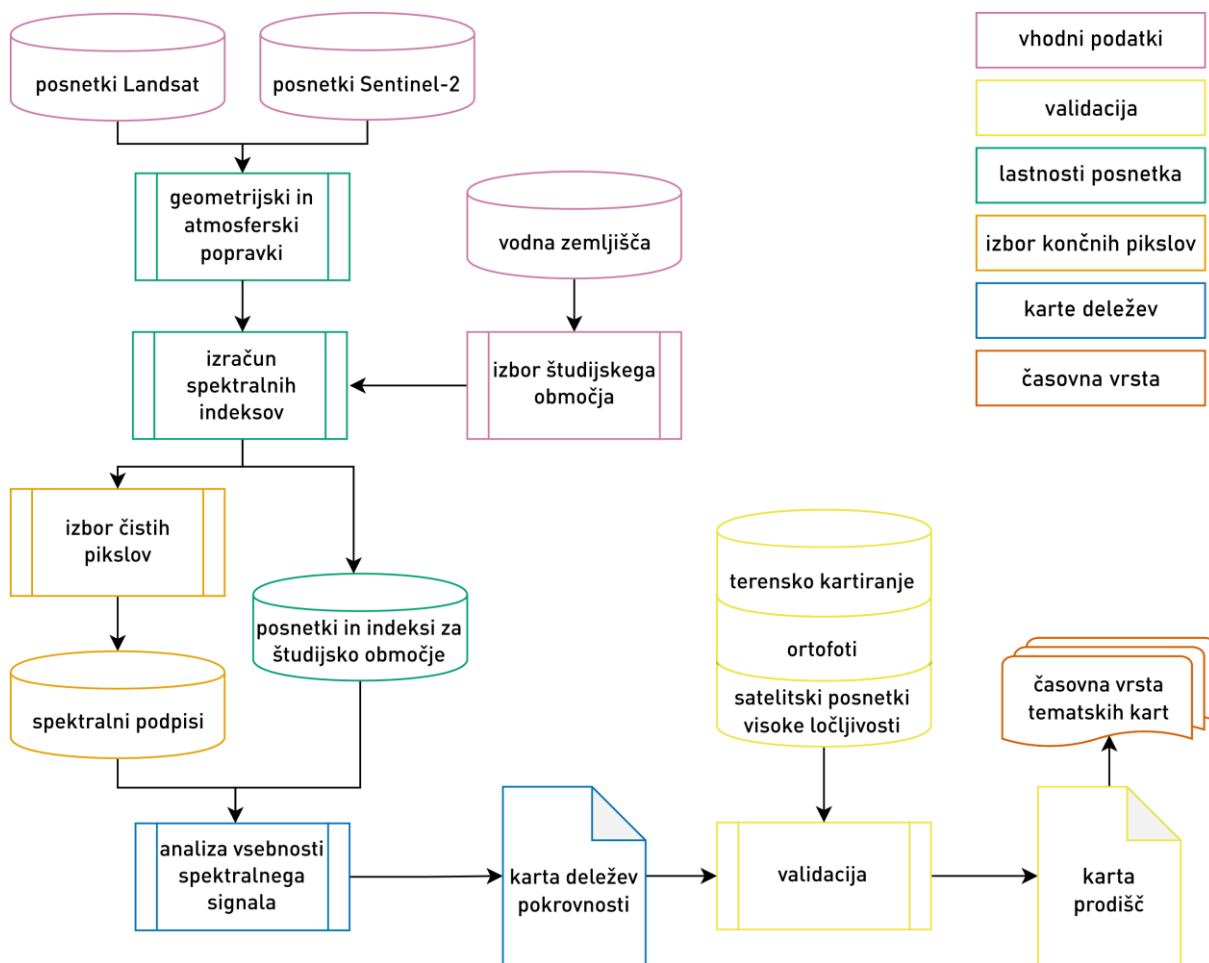
Slika 54:   Potek predlagane metode za spremljanje rečnih prodišč.

Figure 54: Workflow for the proposed method for monitoring fluvial gravel bars.

8.4   Uporaba razvite metode za spremljanje prodišč

Metodo kartiranja, ki smo jo razvili na študijskem območju, smo nato uporabili za analizo večjih rečnih odsekov v daljših časovnih obdobjih. Nato smo preverili, kako dobro lahko z razvito metodo zaznavamo spremembe, tako s primerjavo dveh različnih kart, kot z opazovanjem nihanj v časovni vrsti prisotnosti proda.

8.4.1   Karte deleža proda za izbrane reke

Kartirali smo območja v skupni dolžini preko 250 km na Soči in Savi v Sloveniji ter na reki Vjosa v Albaniji. Uporabili smo posnetke Landsat, ki so zajemali časovno obdobje 35 let. Karte deleža proda, ki smo jih naredili, omogočajo pregled sprememb obsega in lokacije prodišč (Slika 55). Karte prodišč na Soči so v prilogi A, karte prodišč na Savi v prilogi B in karte prodišč na Vjosi v prilogi C.
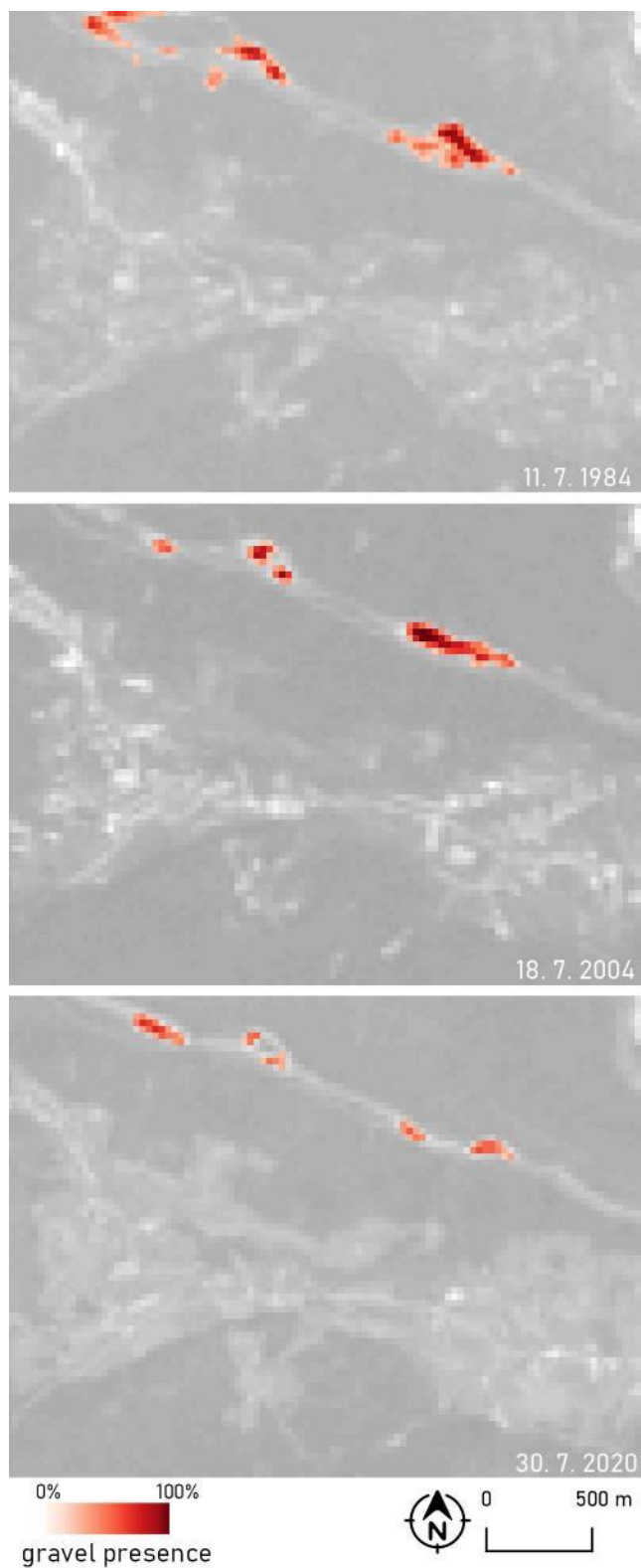
Slika 55: Prisotnost proda na Savi v bližini naselja Besnica v treh različnih časovnih obdobjih (podlaga: GURS, 2021e).

Figure 55: Gravel presence on the Sava river near the Besnica settlement in three different timestamps (basemap: Surveying and Mapping Authority of the Republic of Slovenia, 2021e).

Za validacijo izdelanih kart deležev pokrovnosti smo uporabili referenčne podatke VHR. Na vseh obravnavanih rekah je bil prod zaznan s 95% natančnostjo (Slika 56).
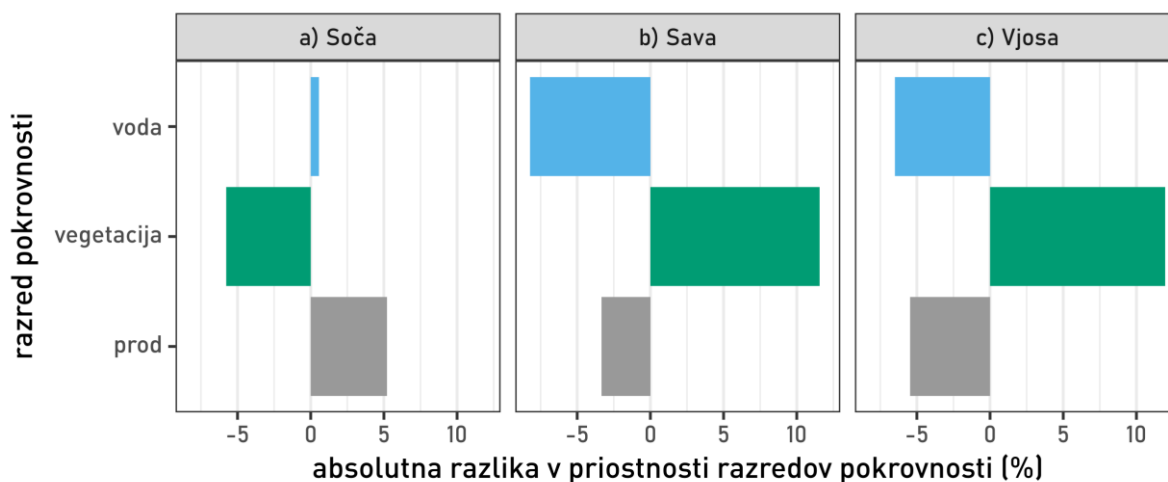
Slika 56: Absolutna razlika v prisotnosti razredov pokrovnosti med referenčnimi podatki in kartami deležev pokrovnosti za različne reke na podlagi satelitskih posnetkov.

Figure 56: Absolute difference in the presence of land cover classes between reference data and satellite image-based land cover fraction maps for different rivers.

8.4.2   Zaznavanje sprememb v prisotnosti proda

V nadaljevanju smo preverili sposobnost zaznavanja sprememb na izdelanih kartah deležev pokrovnosti. Najprej smo proučili zmožnosti preprostega izračuna razlike kart. Primerjali smo karte deležev pokrovnosti, izdelane s posnetki Sentinel-2 iz časovnega obdobja treh let, in preverili zaznane spremembe z referenčnimi podatki VHR z istih časovnih točk. Pri izbiri posnetkov za primerjavo smo se prepričali, da so bili hidrološki pogoji na datume zajema primerljivi. Dnevni srednji pretoki, izmerjeni znotraj proučevanega območja na hidrološki postaji Kobarid, so se gibali med 11.6 in 35.9 m^3/s (Agencija RS za okolje, 2021b). Referenčni podatki so bili v dveh primerih zajeti na isti dan kot vhodni satelitski posnetki, le enkrat so bili zajeti z zamikom dveh dni in 0.7 m^3/s razlike v dnevnem srednjem pretoku. S primerljivostjo hidroloških pogojev smo zagotovili, da so opažene spremembe rečnih prodišč posledica poplav, odvzema proda ali drugih izjemnih dogodkov in ne zgolj rezultat spremembe pretoka.

Karte sprememb smo ocenili z vidika občutljivosti (ang. sensitivity), to je zmožnosti zaznavanja dejanskih sprememb na terenu, ki smo jih določili z referenčnimi podatki, in natančnosti (ang. precision), to je, da so se spremembe, prikazane na kartah sprememb, zgodile v resnici in jih je bilo mogoče potrditi z referenčnimi podatki. V oceni občutljivosti smo se osredotočili na območja sprememb v obsegu vsaj 400 m^2, kar je enako velikosti enega piksla vhodnih satelitskih posnetkov Sentinel-2. Nato

smo za izbrana referenčna območja sprememb preverili vrednosti kart sprememb deležev pokrovnosti. Skupno smo opazovali 72 območij odstranitve proda (zmanjšanje deleža proda) in 43 območij odlaganja proda (povečanje deleža proda). Tako odstranjevanje kot odlaganje proda je bilo na kartah sprememb dobro zaznano (Slika 57). Odlaganje je potekalo v ožjih pasovih, ki pogosto niso dosegli širine celotnega piksla, zato so bile vrednosti sprememb na območjih odlaganja nižje od vrednosti sprememb na območjih odstranitve. Tu gre lahko za posebnost študijskega območja.
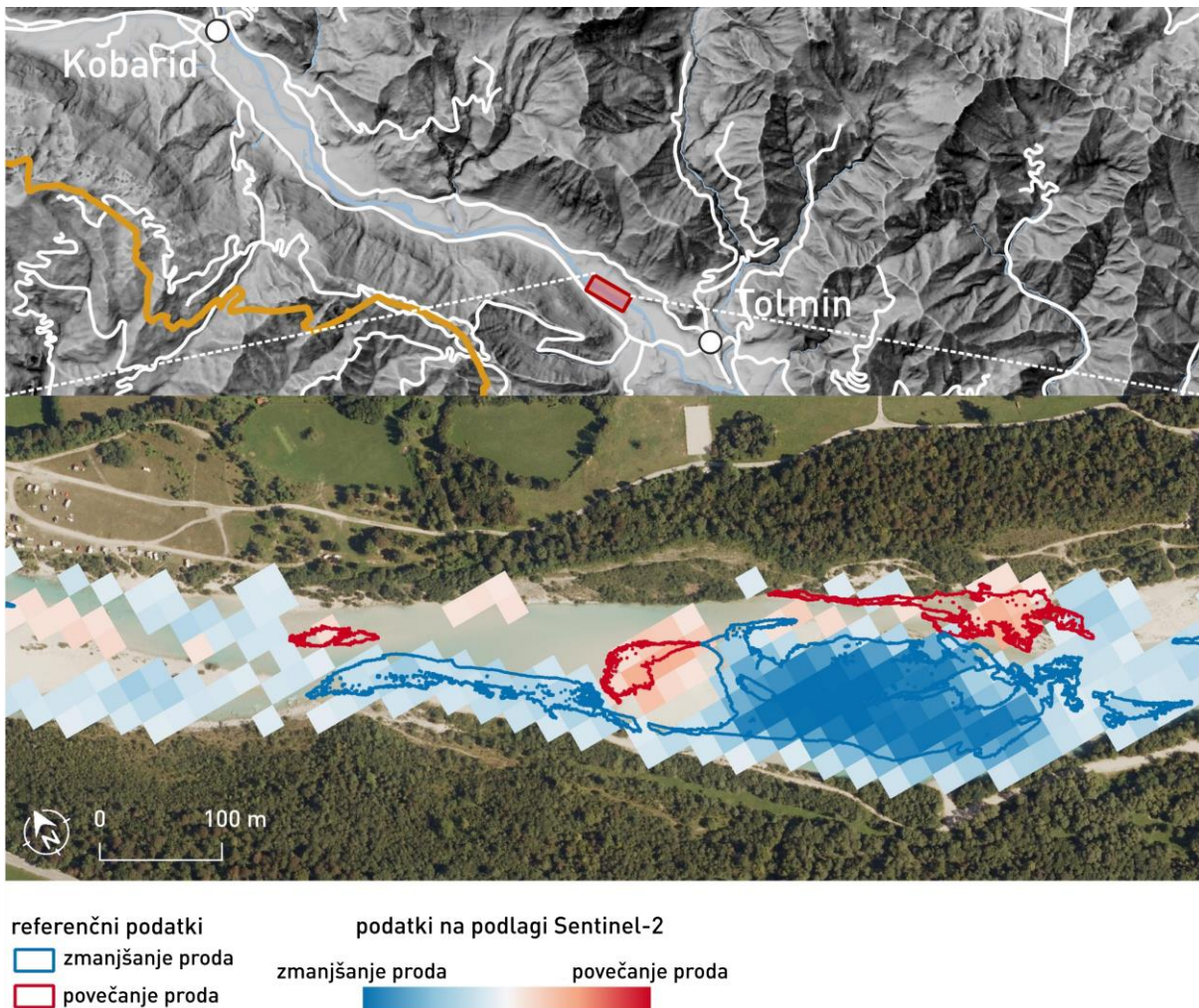
Slika 57:   Referenčni podatki in karta deležev za spremembe v prisotnosti proda med leti 2007 in 2020 na manjšem območju testnega odseka reke Soče (vir podatkov: DRSV, 2021c; GURS, 2016, 2021a, 2021b, 2021e).

Figure 57: Reference dataset and fraction map of changes in gravel between the years 2017 and 2020 on a subset of the study area on the Soča River (data source: Surveying and Mapping Authority of the Republic of Slovenia, 2016, 2021a, 2021b, 2021e; Slovenian Water Agency, 2021c).


V oceni natančnosti zaznavanja sprememb smo se osredotočili na 62 pikslov, ki niso bili v sosedstvu in na katerih je bila zaznana najmanj ± 10% sprememba. Z referenčnimi podatki smo nato preverili, ali je na izbranih pikslih res prišlo do spremembe. Potrdili smo skoraj 75% zaznanih sprememb pokrovnosti,

pri čemer je pri polovici šlo za spremembo iz proda v vodo. V 10% primerov na referenčnih podatkih ni bilo mogoče opaziti nobene spremembe, v 15% pa je bila zaznana napačna sprememba. Pregled vrednosti sprememb na območjih s potrjenimi spremembami je pokazal, da so bile vrednosti veliko višje kot na območjih z napačno zaznanimi spremembami ali brez vsakršnih sprememb. Vrednosti spremembe deležev pokrovnosti, višje od ± 30%, so nakazovale resnično spremembo.

Končno oceno kakovosti preprostih kart sprememb deležev pokrovnosti smo naredili s primerjavo s kartami sprememb deležev na podlagi referenčnih podatkov VHR. Referenčne karte sprememb smo prevzorčili na prostorsko ločljivost kart sprememb deležev pokrovnosti na podlagi satelitskih posnetkov, to je 20 m. Vrednosti pikslov kart deležev pokrovnosti in referenčnih kart smo primerjali na ravni celotnega študijskega območja in nato na območjih sprememb, zaznanih na referenčnih podatkih. Rezultati so potrdili, da sta karti močno povezani, zlasti na območjih sprememb (Pearsonov r > 0,85, p < 0,0001).

8.4.3   Ocena časovnih vrst podatkov o pokrovnosti za spremljanje prodišč

Poleg kart sprememb deležev pokrovnosti, izdelanih z izračunom razlike posnetkov, smo preverili, ali je mogoče časovne vrste podatkov o prisotnosti razredov pokrovnosti uporabiti za spremljanje prodišč. Najprej smo časovno vrsto prisotnosti proda na proučevanem območju na Soči primerjali s podatki o vodostaju s hidrološke postaje, ki se nahaja na študijskem območju (Slika 58). Podatkovna niza sta statistično značilno negativno povezana (Pearsonov r = −0,64, p < 0,0001), kar kaže na skladnost kart deležev pokrovnosti s pričakovanimi procesi na terenu.
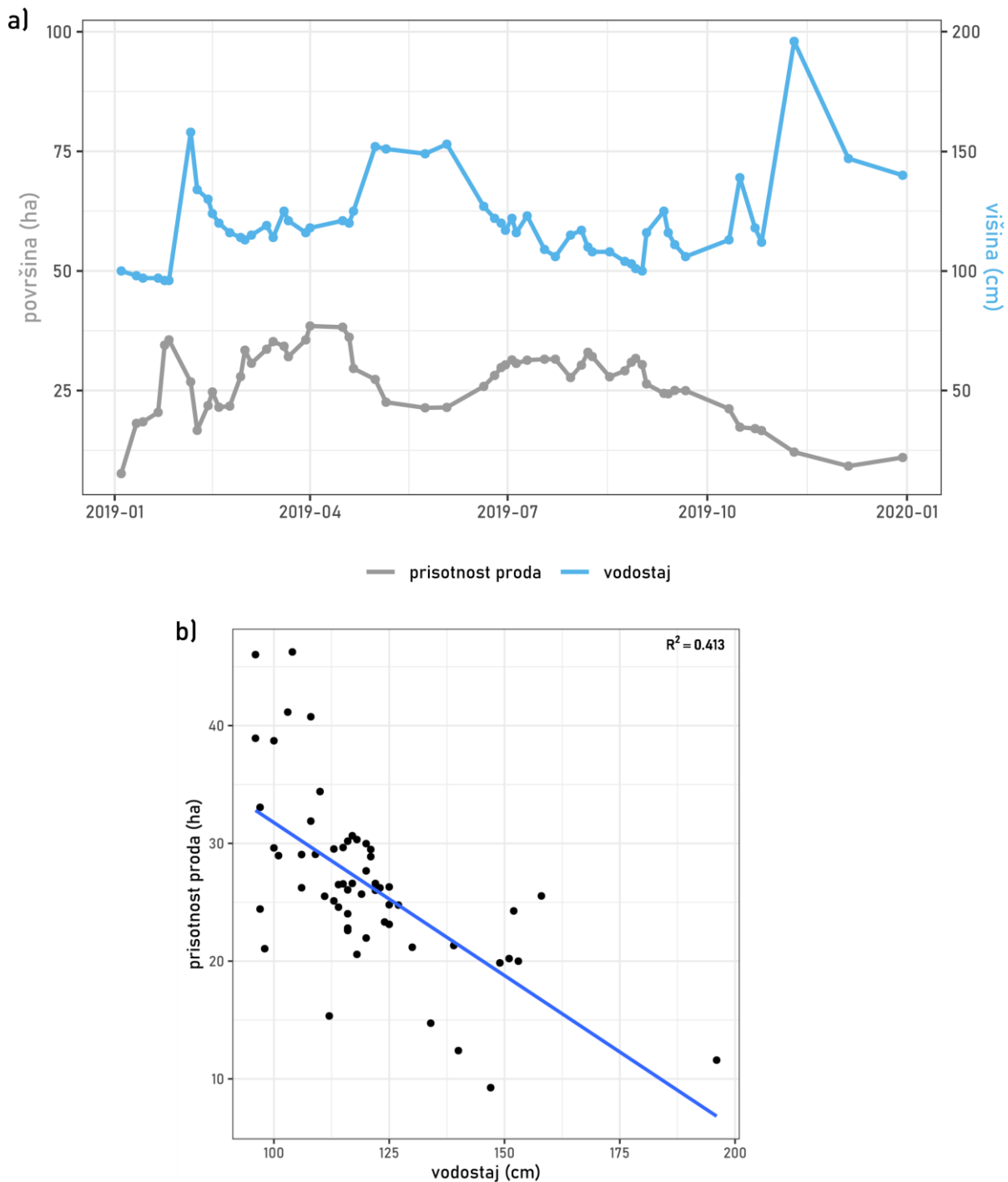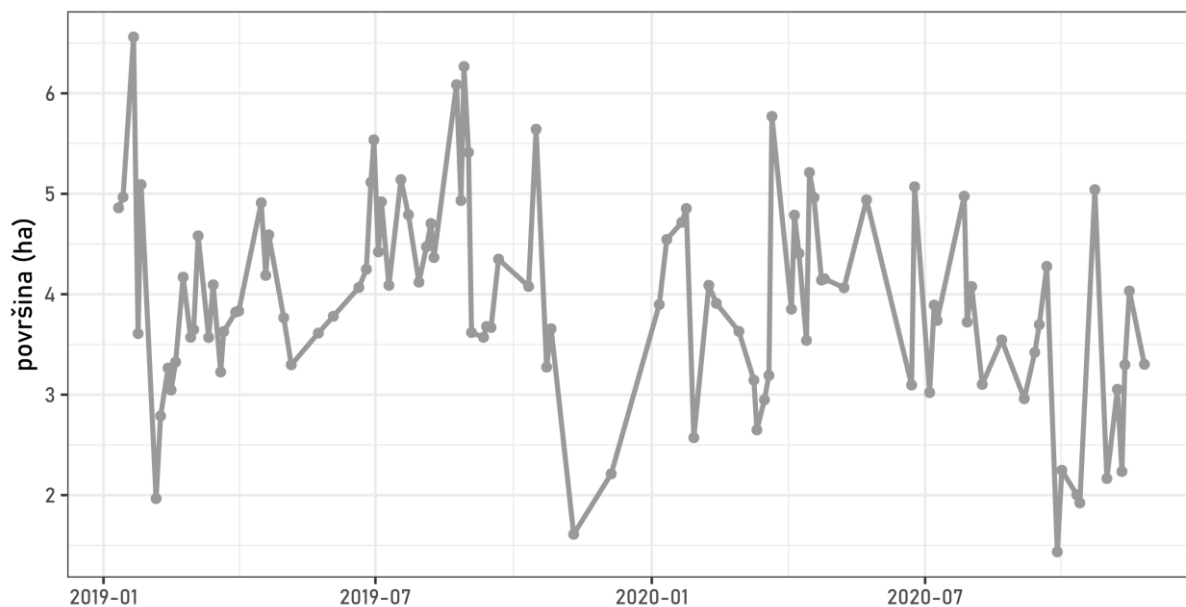
Slika 58: Prisotnost proda na študijskem območju in vodostaj na merilni postaji Kobarid a) Časovna vrsta podatkov. b) Razsevni diagram s črto linearne regresije in koeficientom določanja (vir podatkov: Agencija RS za okolje, 2021b).

Figure 58: Gravel presence in the study area and water level at the Kobarid gauging station. a) Time series of the data. b) Scatter plot with the linear regression line and coefficient of determination (data source: Slovenian Environment Agency, 2021b).

V nadaljevanju smo preverili, ali je mogoče časovne vrste prisotnosti proda uporabiti za zaznavanje sprememb. Osredotočili smo se na dve znani lokaciji odvzema proda, eno na Soči pri naselju Dolje in

drugo na Savi pri Kranju. Izrisali smo časovno vrsto prisotnosti proda na manjšem študijskem območju, ki je zajemalo mesta odvzema proda v letih 2019 in 2020 (Slika 59). Za izdelavo kart deležev pokrovnosti smo uporabili vse razpoložljive posnetke Sentinel-2 z največ 10% oblačnosti na celotnem posnetku.

Slika 59: Prisotnost proda na študijskem območju Dolje v letih 2019 in 2020.

Figure 59: Presence of gravel in the Dolje study area in 2019 and 2020.

Prisotnost proda na proučevanih območjih je močno nihala v skladu s spremembami vodostaja. Kljub velikim nihanjem smo ugotovili, da zmanjšanje prisotnosti proda za več kot dva standardna odklona pod vrednostjo povprečne prisotnosti proda na proučevanem območju pomeni odvzem proda. Na študijskem območju Dolje, na primer, je bila povprečna prisotnost proda v letih 2019 in 2020 4 ha s standardnim odklonom 1 ha. Zmanjšanje za 2 ha je torej kazalo na odvzem (Slika 60). Enak proces smo opazili v Kranju. Časovne vrste prisotnosti proda se torej lahko uporabijo za odkrivanje sprememb nad omenjenim velikostnim pragom.
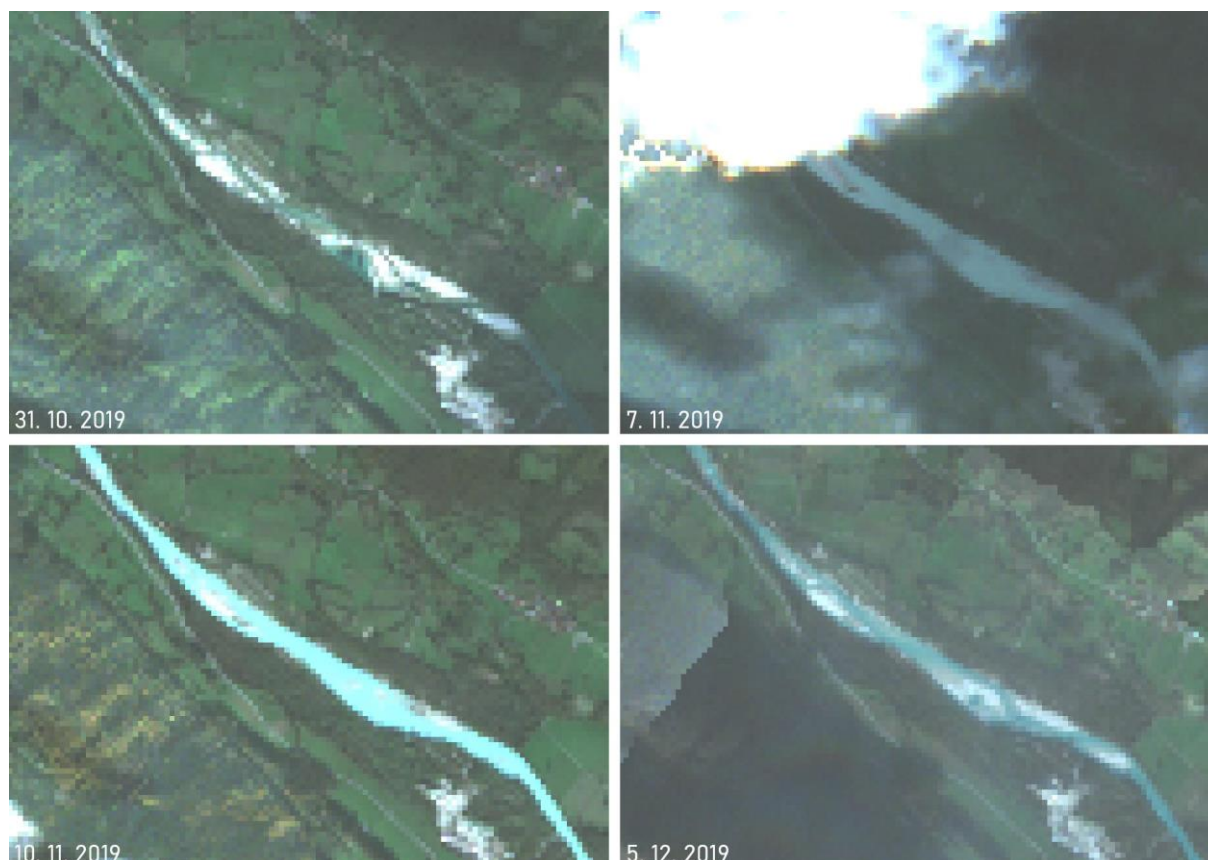
Slika 60: Naravno barvni kompoziti Sentinel-2, ki prikazujejo odstranjevanje proda na študijskem območju na Soči blizu naselja Dolje in kasnejše oblikovanje novih prodišč (vir podatkov: Modified Copernicus Sentinel data, 2021).

Figure 60: Sentinel-2 true colour images showing the removal of gravel from the Soča river at the Dolje study area and the subsequent formation of new gravel bars (data source: Modified Copernicus Sentinel data, 2021).

8.5 Razprava in zaključki

Uporaba in preverjanje predlagane metode kartiranja prodišč na različnih rekah so potrdili našo prvo hipotezo, da je z uporabo SMA mogoče razlikovati prod, površinsko vodo in vegetacijo v rečnih ekosistemih z 90% tematsko natančnostjo. Predvsem prod je bil kartiran z zelo visoko natančnostjo, medtem ko je bila vegetacija bolj problematična in včasih ni dosegla 90% natančnosti. Ovrednotenje zaznavanja sprememb je potrdilo tudi drugo hipotezo, da je mogoče s podpikselskimi kartami pokrovnosti spremljati spremembe prodišč, ki so velike vsaj 500 m^2. Na obseg sprememb, ki jih je mogoče zaznati, vpliva prostorska ločljivost vhodnih satelitskih posnetkov. Pokazali smo, da lahko posnetke Sentinel-2 s prostorsko ločljivostjo 20 m uporabimo za zaznavanje sprememb v velikosti 400 m^2, kar je velikost enega piksla vhodnih posnetkov. Z uporabo SMA smo želeli prispevati k novemu znanju o uporabi podatkov daljinskega zaznavanja za spremljanje naravnih procesov. Glavni prispevek disertacije k znanosti je razvoj novega postopka za kartiranje prodišč in drugih oblik, povezanih z vodo, z uporabo prosto dostopnih satelitskih posnetkov. Metodo smo razvili na rečnem odseku, kjer je bilo na voljo veliko referenčnih podatkov, s katerimi smo lahko ocenili kakovost rezultatov in tako določili

Stančič, L. 2022. Monitoring Changes of Fluvial Gravel Bars with Remote Sensing.
PhD Th. Ljubljana, UL FGG, Interdisciplinary doctoral study programme Environmental Protection.

141

najboljši pristop kartiranja. Proučili smo tudi prenosljivost metode in potrdili, da jo je mogoče uporabiti za opazovanje območij, kjer morda ni na voljo toliko pomožnih podatkov. Razširjena uporaba razvitega postopka kartiranje bi lahko pripeljala do novih ugotovitev o dinamiki rek in do boljšega upravljanja z rečnim okoljem.

Glavne omejitve predlagane metode so povezane z uporabo optičnih satelitskih posnetkov. Oblaki in topografske sence onemogočajo opazovanje in spremljanje procesov na površju ter so še posebej problematični v gorskih območjih z visokimi strmimi pobočji in pogosto oblačnostjo. Prod je na splošno zelo dobro zaznan, po drugi strani pa je zaznavanje vode težavno na območjih brzic in plitvin, kjer lahko senzor zazna odboj proda z rečnega dna. Kartiranje vegetacije je problematično, če listje ni v celoti razvito in senzor zazna golo površje pod drevesi. Iz značilnosti SMA izhaja, da moramo za obravnavo izbrati razrede s kar najbolj različnimi spektralnimi značilnostmi. V nasprotnem primeru je težko določiti vpliv posameznih razredov na spektralni signal opazovanega piksla. Pri izboru obravnavanih razredov smo zato morali narediti poenostavitve. Z vidika spremljanja prodišč je najhujša poenostavitev, da smo v razred prod vključili pozidana območja. Karte prisotnosti proda tako ne razlikujejo med prodišči in pozidanimi območji. To težavo smo naslovili z zamejitvijo območja opazovanja na vodna zemljišča, kjer je pozidave manj. Vseeno pa so tudi na vodnih zemljiščih posamezna pozidana območja, sploh v večjih naseljih. V nadaljnih analizah bi lahko poskusili z ločevanjem proda in pozidanih območij z dodatnimi podatki daljinskega zaznavanja, na primer z umetno odprtinskim radarjem (ang. Synthetic Aperture Radar, SAR), lahko pa bi tudi v postopku poobdelave karte prodišč maskirali s pomožnimi sloji stavb in infrastrukture. Natančnost SMA je odvisna od kakovosti uporabljenih končnih pikslov. Težko je izbrati končne piksle, ki natančno predstavljajo spektralne lastnosti zelo raznolikih razredov pokrovnosti. Voda ima lahko zelo različen spektralni odzivi glede na sončno bleščanje, površinske valove, globino, vsebnost sedimentov, prisotnost mikroorganizmov in raztopljene organske snovi, zato jo je težko vedno natančno kartirati s SMA. Ta težava je še bolj pereča pri vegetaciji, ki se na opazovanem območju pojavlja v različnih oblikah. Čeprav so oblike spektralnih podpisov različnih vegetacijskih oblik podobne, obstajajo razlike med posameznimi rastlinskimi vrstami. Te razlike lahko povzročijo napake, če za modeliranje vseh vegetacijskih oblik uporabimo en sam končni piksel. V prihodnjih raziskavah bi zato lahko proučili možnost uporabe več različnih modelov za zaznavanje vode in vegetacije na podlagi različnih končnih pikslov. Za nadaljnje kartiranje bi nato izbrali model z najmanjšo napako. Spremljanje prodišč bi lahko dopolnili tudi s SAR, ki lahko prodre skozi oblake in je znan po uspešnem zaznavanju vode. Dodatne raziskave bi lahko opravili tudi s kartiranjem dodatnih rečnih sistemov s predlagano podpikselsko metodo. Z razvitim postopkom bi lahko kartirali tudi druge razrede pokrovnosti in pojave, kot so krčenje gozdov in urbanizacija. Veliko število prosto dostopnih satelitskih posnetkov s kratkim časom ponovnega obiska omogočajo spremljanje različnih procesov in sprejemanje bolj utemeljenih odločitev.

»This page is intentionally blank.«

9   REFERENCES

Adams, J. 1995. Classification of multispectral images based on fractions of endmembers: Application to land-cover change in the Brazilian Amazon. Remote Sensing of Environment 52: 137–154. https://doi.org/10.1016/0034-4257(94)00098-8

Adams, J.B., Smith, M.O., Johnson, P.E. 1986. Spectral mixture modeling: A new analysis of rock and soil types at the Viking Lander 1 site. Journal of Geophysical Research 91: 8098–8112. https://doi.org/10.1029/JB091iB08p08098

Afrasinei, G.M., Melis, M.T., Arras, C., Pistis, M., Buttau, C., Ghiglieri, G. 2018. Spatiotemporal and spectral analysis of sand encroachment dynamics in southern Tunisia. European Journal of Remote Sensing 51: 352–374. https://doi.org/10.1080/22797254.2018.1439343

Aina, Y.A., Adam, E., Ahmed, F., Wafer, A., Alshuwaikhat, H.M. 2019. Using multisource data and the V-I-S model in assessing the urban expansion of Riyadh city, Saudi Arabia. European Journal of Remote Sensing 52: 557–571. https://doi.org/10.1080/22797254.2019.1691469

Allen, G.H., Pavelsky, T.M. 2018. Global extent of rivers and streams. Science 361: 585–588. https://doi.org/10.1126/science.aat0636

Amaral, C.H., Roberts, D.A., Almeida, T.I.R., Souza Filho, C.R. 2015. Mapping invasive species and spectral mixture relationships with neotropical woody formations in southeastern Brazil. ISPRS Journal of Photogrammetry and Remote Sensing 108: 80–93. https://doi.org/10.1016/j.isprsjprs.2015.06.009

Assani, A.A., Petit, F. 2004. Impact of hydroelectric power releases on the morphology and sedimentology of the bed of the Warche River (Belgium). Earth Surface Processes and Landforms 29: 133–143. https://doi.org/10.1002/esp.1004

Atkinson, P.M. 2005. Sub-pixel target mapping from soft-classified, remotely sensed imagery. Photogrammetric Engineering & Remote Sensing 71: 839–846. https://doi.org/10.14358/PERS.71.7.839

Barsi, J., Lee, K., Kvaran, G., Markham, B., Pedelty, J. 2014. The spectral response of the Landsat-8 Operational Land Imager. Remote Sensing 6: 10232–10251. https://doi.org/10.3390/rs61010232

Berger, M., Moreno, J., Johannessen, J.A., Levelt, P.F., Hanssen, R.F. 2012. ESA's sentinel missions in support of Earth system science. Remote Sensing of Environment 120: 84–90. https://doi.org/10.1016/j.rse.2011.07.023

Bing. 2021. VirtualEarth. https://www.bingmapsportal.com/ (Accessed 15. 11. 2021).

Bishop-Taylor, R., Sagar, S., Lymburner, L., Alam, I., Sixsmith, J. 2019. Sub-pixel waterline extraction: Characterising accuracy and sensitivity to indices and spectra. Remote Sensing 11: 2984. https://doi.org/10.3390/rs11242984

Blöschl, G., Bierkens, M.F.P., Chambel, A., Cudennec, C., Destouni, G., Fiori, A., Kirchner, J.W., McDonnell, J.J., Savenije, H.H.G., Sivapalan, M., Stumpp, C., Toth, E., Volpi, E., Carr, G., Lupton, C., Salinas, J., Széles, B., Viglione, A., Aksoy, H., Allen, S.T., Amin, A., Andréassian, V., Arheimer, B., Aryal, S.K., Baker, V., Bardsley, E., Barendrecht, M.H., Bartosova, A., Batelaan, O., Berghuijs, W.R., Beven, K., Blume, T., Bogaard, T., Borges de Amorim, P., Böttcher, M.E., Boulet, G., Breinl, K., Brilly, M., Brocca, L., Buytaert, W., Castellarin, A., Castelletti, A., Chen, X., Chen, Yangbo, Chen, Yuanfang, Chifflard, P., Claps, P., Clark, M.P., Collins, A.L., Croke, B., Dathe, A., David, P.C., de Barros, F.P.J., de Rooij, G., Di Baldassarre, G., Driscoll, J.M., Duethmann, D., Dwivedi, R., Eris, E., Farmer, W.H., Feiccabrino, J., Ferguson, G., Ferrari, E., Ferraris, S., Fersch, B., Finger, D., Foglia, L., Fowler, K., Gartsman, B., Gascoin, S., Gaume, E., Gelfan, A., Geris, J., Gharari, S., Gleeson, T., Glendell, M., Gonzalez Bevacqua, A., González-Dugo, M.P., Grimaldi, S., Gupta, A.B., Guse, B., Han, D., Hannah, D., Harpold, A., Haun, S., Heal, K., Helfricht, K., Herrnegger, M., Hipsey, M., Hlaváčiková, H., Hohmann, C., Holko, L., Hopkinson, C., Hrachowitz, M., Illangasekare, T.H., Inam, A., Innocente, C., Istanbulluoglu, E., Jarihani, B., Kalantari, Z., Kalvans, A., Khanal, S., Khatami, S., Kiesel, J., Kirkby, M., Knoben, W., Kochanek, K., Kohnová, S., Kolechkina, A., Krause, S., Kreamer, D., Kreibich, H., Kunstmann, H., Lange, H., Liberato, M.L.R., Lindquist, E., Link, T., Liu, J., Loucks, D.P., Luce, C., Mahé, G., Makarieva, O., Malard, J., Mashtayeva, S., Maskey, S., Mas-Pla, J., Mavrova-Guirguinova, M., Mazzoleni, M., Mernild, S., Misstear, B.D., Montanari, A., Müller-Thomy, H., Nabizadeh, A., Nardi, F., Neale, C., Nesterova, N., Nurtaev, B., Odongo, V.O., Panda, S., Pande, S., Pang, Z., Papacharalampous, G., Perrin, C., Pfister, L., Pimentel, R., Polo, M.J., Post, D., Prieto Sierra, C., Ramos, M.-H., Renner, M., Reynolds, J.E., Ridolfi, E., Rigon, R., Riva, M., Robertson, D.E., Rosso, R., Roy, T., Sá, J.H.M., Salvadori, G., Sandells, M., Schaefli, B., Schumann, A., Scolobig, A., Seibert, J., Servat, E., Shafiei, M., Sharma, A., Sidibe, M., Sidle, R.C., Skaugen, T., Smith, H., Spiessl, S.M., Stein, L., Steinsland, I., Strasser, U., Su, B., Szolgay, J., Tarboton, D., Tauro, F., Thirel, G., Tian, F., Tong, R., Tussupova, K., Tyralis, H., Uijlenhoet, R., van Beek, R., van der Ent, R.J., van der Ploeg, M., Van Loon, A.F., van Meerveld, I., van Nooijen, R., van Oel, P.R., Vidal, J.-P., von Freyberg, J., Vorogushyn, S., Wachniew, P., Wade, A.J., Ward, P., Westerberg, I.K., White, C., Wood, E.F., Woods, R., Xu, Z., Yilmaz, K.K., Zhang, Y. 2019. Twenty-three unsolved problems in hydrology (UPH) – a community perspective. Hydrological Sciences Journal 64: 1141–1158. https://doi.org/10.1080/02626667.2019.1620507

Bogning, S., Frappart, F., Blarel, F., Niño, F., Mahé, G., Bricquet, J.-P., Seyler, F., Onguéné, R., Etamé, J., Paiz, M.-C., Braun, J.-J. 2018. Monitoring water levels and discharges using radar altimetry in an ungauged river basin: The case of the Ogooué. Remote Sensing 10: 350. https://doi.org/10.3390/rs10020350

Campbell, J.B., Wynne, R.H. 2011. Introduction to remote sensing, 5th ed. ed. New York, Guilford Press: 667 p.

Carlotto, M.J. 2009. Effect of errors in ground truth on classification accuracy. International Journal of Remote Sensing 30: 4831–4849. https://doi.org/10.1080/01431160802672864

Cavanaugh, K.C., Siegel, D.A., Reed, D.C., Dennison, P.E. 2011. Environmental controls of giant-kelp biomass in the Santa Barbara Channel, California. Marine Ecology Progress Series 429: 1–17. https://doi.org/10.3354/meps09141

Chehdi, K., Cariou, C. 2019. Learning or assessment of classification algorithms relying on biased ground truth data: What interest? Journal of Applied Remote Sensing 13: 1. https://doi.org/10.1117/1.JRS.13.034522

Chuvieco, E., Martín, M.P., Palacios, A. 2002. Assessment of different spectral indices in the red-near-infrared spectral domain for burned land discrimination. International Journal of Remote Sensing 23: 5103–5110. https://doi.org/10.1080/01431160210153129

Clerc, S., MPC Team. 2021. Sentinel-2: L1C data quality report. Reference S2-PDGS-MPC-DQR. https://sentinels.copernicus.eu/documents/247904/685211/Sentinel-2_L1C_Data_Quality_Report (Accessed 5. 3. 2021).

de Sherbinin, A., Levy, M.A., Zell, E., Weber, S., Jaiteh, M. 2014. Using satellite data to develop environmental indicators. Environmental Research Letters 9: 084013. https://doi.org/10.1088/1748-9326/9/8/084013

de Vries, J., van Maanen, B., Ruessink, G., Verweij, P.A., de Jong, S.M. 2021. Unmixing water and mud: Characterizing diffuse boundaries of subtidal mud banks from individual satellite observations. International Journal of Applied Earth Observation and Geoinformation 95: 102252. https://doi.org/10.1016/j.jag.2020.102252

Dechoz, C., Poulain, V., Massera, S., Languille, F., Greslou, D., de Lussy, F., Gaudel, A., L'Helguen, C., Picard, C., Trémas, T. 2015. Sentinel 2 Global Reference Image. In: Bruzzone, L. (Ed.). SPIE Remote Sensing, Toulouse, France. p. 96430A. https://doi.org/10.1117/12.2195046

Demarchi, L., Chan, J.C.-W., Ma, J., Canters, F. 2012. Mapping impervious surfaces from superresolution enhanced CHRIS/Proba imagery using multiple endmember unmixing. ISPRS Journal of Photogrammetry and Remote Sensing 72: 99–112. https://doi.org/10.1016/j.isprsjprs.2012.05.015

Dennison, P.E., Halligan, K.Q., Roberts, D.A. 2004. A comparison of error metrics and constraints for multiple endmember spectral mixture analysis and spectral angle mapper. Remote Sensing of Environment 93: 359–367. https://doi.org/10.1016/j.rse.2004.07.013

Dennison, P.E., Roberts, D.A. 2003. Endmember selection for multiple endmember spectral mixture analysis using endmember average RMSE. Remote Sensing of Environment 87: 123–135. https://doi.org/10.1016/S0034-4257(03)00135-4

Dobigeon, N., Tourneret, J.-Y., Richard, C., Bermudez, J.C.M., McLaughlin, S., Hero, A.O. 2014. Nonlinear unmixing of hyperspectral images: Models and algorithms. IEEE Signal Processing Magazine 31: 82–94. https://doi.org/10.1109/MSP.2013.2279274

Donchyts, G., Baart, F., Winsemius, H., Gorelick, N., Kwadijk, J., van de Giesen, N. 2016. Earth's surface water change over the past 30 years. Nature Climate Change 6: 810–813. https://doi.org/10.1038/nclimate3111

Doshi, N., Koringa, P.A., Ghosh, R. 2020. Geometric and radiometric assessment of Sentinel-2A and Sentinel-2B sensors. In: 2020 7th International Conference on Signal Processing and Integrated Networks (SPIN). IEEE, Noida, India, pp. 975–980. https://doi.org/10.1109/SPIN48934.2020.9071261

Drusch, M., Del Bello, U., Carlier, S., Colin, O., Fernandez, V., Gascon, F., Hoersch, B., Isola, C., Laberinti, P., Martimort, P., Meygret, A., Spoto, F., Sy, O., Marchese, F., Bargellini, P. 2012. Sentinel-2: ESA's Optical High-Resolution Mission for GMES Operational Services. Remote Sensing of Environment 120: 25–36. https://doi.org/10.1016/j.rse.2011.11.026

Du, Q. 2018. Pixel unmixing. In: Comprehensive Remote Sensing. Elsevier, pp. 186–198. https://doi.org/10.1016/B978-0-12-409548-9.10337-9

Du, Y., Zhang, Y., Ling, F., Wang, Q., Li, W., Li, X. 2016. Water bodies' mapping from Sentinel-2 imagery with Modified Normalized Difference Water Index at 10-m spatial resolution produced by sharpening the SWIR band. Remote Sensing 8: 354. https://doi.org/10.3390/rs8040354

Dubovyk, O., Menz, G., Lee, A., Schellberg, J., Thonfeld, F., Khamzina, A. 2015. SPOT-based sub-field level monitoring of vegetation cover dynamics: A case of irrigated croplands. Remote Sensing 7: 6763–6783. https://doi.org/10.3390/rs70606763

EC DG ENVIRONMENT. 2013. Interpretation manual of European habitats.

ESA. 2021. Sentinel-2 imagery. https://scihub.copernicus.eu/ (Accessed 15. 11. 2021).

Esri. 2021. Satellite. https://server.arcgisonline.com/ArcGIS/rest/services/World_Imagery/MapServer/tile/{z}/{y}/{x} (Accessed 15. 11. 2021).

Foody, G.M., Muslim, A.M., Atkinson, P.M. 2005. Super-resolution mapping of the waterline from remotely sensed data. International Journal of Remote Sensing 26: 5381–5392. https://doi.org/10.1080/01431160500213292

Foški, M. 2017. Determination of plot patterns and their changes in Slovenian rural areas (in Slovenian). Doctoral thesis. Ljubljana, University of Ljubljana, Faculty of Civil and Geodetic Engineering (self-published M. Foški): 240 pp.

Fouache, E., Gruda, G., Mucaj, S., Nikolli, P. 2001. Recent geomorphological evolution of the deltas of the rivers Seman and Vjosa, Albania. Earth Surface Processes and Landforms 26: 793–802. https://doi.org/10.1002/esp.222

Gao, B. 1996. NDWI—A normalized difference water index for remote sensing of vegetation liquid water from space. Remote Sensing of Environment 58: 257–266. https://doi.org/10.1016/S0034-4257(96)00067-3

Gao, Y., Zhang, W. 2007. Variable empirical coefficient algorithm for removal of topographic effects on remotely sensed data from rugged terrain, in: 2007 IEEE International Geoscience and Remote Sensing Symposium. Presented at the 2007 IEEE International Geoscience and Remote Sensing Symposium, IEEE, Barcelona, Spain, pp. 4733–4736. https://doi.org/10.1109/IGARSS.2007.4423917

Gatti, A., Galoppo, A. 2018. Sentinel-2 products specification document. https://sentinel.esa.int/documents/247904/685211/Sentinel-2-Products-Specification-Document (Accessed 14. 1. 2019).

GEO. 2017. Earth Observations in support of the 2030 Agenda for Sustainable Development. https://www.earthobservations.org/documents/publications/201703_geo_eo_for_2030_agenda.pdf (Accessed 1. 11. 2019).

Geodetic Institute of Slovenia. 2021. Methodology for hydrography and water lands data acquisition. Data model and rules for acquisition. Version 3.0.4. Technical report (in Slovenian). http://www.evode.gov.si/fileadmin/user_upload/EHVZ/Metodologija_EHVZ_v304_2021_04_14a.pdf (Accessed 22. 6. 2021).

Geological Survey of Slovenia. 2019. Basic Geologic map 1:100,000. http://biotit.geo-zs.si/ogk100/ (Accessed 15. 1. 2019).

Geršič, M. 2010. Succession on the point bars of the Sava river. Dela 33: 5–19. https://doi.org/10.4312/dela.33.1.5-19

Geršič, M., Repe, Blaž, Blatnik, M., Brečko Grubar, V., Kovač, B., Pozvek, N., Seifert, A. 2014. Geography and plant succession: Selected examples from Slovenian regions. Ljubljana, Založba ZRC: 137 p.

Gitelson, A.A., Chivkunova, O.B., Merzlyak, M.N. 2009. Nondestructive estimation of anthocyanins and chlorophylls in anthocyanic leaves. American Journal of Botany 96: 1861–1868. https://doi.org/10.3732/ajb.0800395

Guizar-Sicairos, M., Thurman, S.T., Fienup, J.R. 2008. Efficient subpixel image registration algorithms. Optics Letters 33: 156–158. https://doi.org/10.1364/OL.33.000156

Guneroglu, A., Karsli, F., Dihkan, M. 2013. Automatic detection of coastal plumes using Landsat TM/ETM+ images. International Journal of Remote Sensing 34: 4702–4714. https://doi.org/ 10.1080/01431161.2013.782116

Gurnell, A.M., Petts, G.E., Hannah, D.M., Smith, B.P.G., Edwards, P.J., Kollmann, J., Ward, J.V., Tockner, K. 2001. Riparian vegetation and island formation along the gravel-bed Fiume Tagliamento, Italy. Earth Surface Processes and Landforms 26: 31–62. https://doi.org/10.1002/ 1096-9837(200101)26:1<31::AID-ESP155>3.0.CO;2-Y

Henshaw, A.J., Gurnell, A.M., Bertoldi, W., Drake, N.A. 2013. An assessment of the degree to which Landsat TM data can support the assessment of fluvial dynamics, as revealed by changes in vegetation extent and channel position, along a large river. Geomorphology 202: 74–85. https://doi.org/10.1016/j.geomorph.2013.01.011

Heylen, R., Parente, M., Gader, P. 2014. A review of nonlinear hyperspectral unmixing methods. IEEE Journal of Selected Topics in Applied Earth Observations and Remote Sensing 7: 1844–1868. https://doi.org/10.1109/JSTARS.2014.2320576

Hirschmugl, M., Steinegger, M., Gallaun, H., Schardt, M. 2014. Mapping forest degradation due to selective logging by means of time series analysis: Case studies in Central Africa. Remote Sensing 6: 756–775. https://doi.org/10.3390/rs6010756

Hladnik, D. 2005. Spatial structure of disturbed landscapes in Slovenia. Ecological Engineering 24: 17–27. https://doi.org/10.1016/j.ecoleng.2004.12.004

Hölbling, D., Eisank, C., Albrecht, F., Vecchiotti, F., Friedl, B., Weinke, E., Kociu, A. 2017. Comparing manual and semi-automated landslide mapping based on optical satellite images from different sensors. Geosciences 7: 37. https://doi.org/10.3390/geosciences7020037

Huang, C., Chen, Y., Zhang, S., Wu, J. 2018. Detecting, extracting, and monitoring surface water from space using optical sensors: A review. Reviews of Geophysics 56: 333–360. https://doi.org/ 10.1029/2018RG000598

Huete, A., Justice, C., van Leeuwen, W. 1999. MODIS vegetation Index (MOD 13): Algorithm Theoretical Basis Document. Version 3. https://eospso.gsfc.nasa.gov/sites/default/files/atbd/ atbd_mod13.pdf (Accessed 9. 10. 2020).

Huete, A., Liu, H.Q., Batchily, K., van Leeuwen, W. 1997. A comparison of vegetation indices over a global set of TM images for EOS-MODIS. Remote Sensing of Environment 59: 440–451. https://doi.org/10.1016/S0034-4257(96)00112-5

Ilsever, M., Unsalan, C. 2013. Locating the urban area in satellite images to detect changes in them, in: 2013 6th International Conference on Recent Advances in Space Technologies (RAST). 6th International Conference on Recent Advances in Space Technologies (RAST), IEEE, Istanbul, Turkey. pp. 109–114. https://doi.org/10.1109/RAST.2013.6581165

Irons, J.R., Dwyer, J.L., Barsi, J.A. 2012. The next Landsat satellite: The Landsat Data Continuity Mission. Remote Sensing of Environment 122: 11–21. https://doi.org/10.1016/j.rse.2011.08.026

Japitana, M.V., Demetillo, A.T., Burce, M.E.C., B. Taboada, E. 2019. Catchment characterization to support water monitoring and management decisions using remote sensing. Sustainable Environment Research 29: 8. https://doi.org/10.1186/s42834-019-0008-5

Jogan, N., Kotarac, M., Lešnik, A. (Eds.). 2004. Identification of European-scale priority areas of non-forest habitat types by means of the prevalence of typical plant species. Technical report (in Slovenian). Miklavž na Dravskem polju, Center za kartografijo favne in flore: 64 p.

Kamal, M., Phinn, S. 2011. Hyperspectral data for mangrove species mapping: A comparison of pixel-based and object-based approach. Remote Sensing 3: 2222–2242. https://doi.org/10.3390/rs3102222

Kärdi, T. 2007. Remote sensing of urban areas: Linear spectral unmixing of Landsat Thematic Mapper images acquired over Tartu (Estonia). Proceedings of the Estonian Academy of Sciences, Biology and Ecology 56: 19–32. https://www.kirj.ee/public/Ecology/2007/issue_1/bio-2007-1-2.pdf

Keshava, N. 2003. A survey of spectral unmixing algorithms. Lincoln Laboratory Journal 14: 55–78. https://archive.ll.mit.edu/publications/journal/pdf/vol14_no1/14_1survey.pdf

Keshava, N., Mustard, J.F. 2002. Spectral unmixing. IEEE Signal Processing 19: 44–57. https://doi.org/10.1109/79.974727

Kiss, T., Balogh, M. 2015. Characteristics of point-bar development under the influence of a dam: Case study on the Dráva River at Sigetec, Croatia. Journal of Environmental Geography 8. https://doi.org/10.1515/jengeo-2015-0003

Klaneček, M., Čuš, I., Hojnik, T. 2005. Prodišča na Dravi med Markovci in Zavrčem ter možnost učinkovitejših vzdrževalnih ukrepov = Gravelbars on the Drava river between Markovci and Zavrč and possibilities of more effective maintenance measures. Acta hydrotechinca 23: 57–76.

Kraff, N.J., Wurm, M., Taubenbock, H. 2020. Uncertainties of human perception in visual image interpretation in complex urban environments. IEEE Journal of Selected Topics in Applied Earth Observations and Remote Sensing 13: 4229–4241. https://doi.org/10.1109/JSTARS.2020.3011543

Kruse, F.A., Heidebrecht, K.B., Shapiro, A.T., Barloon, P.J., Goetz, A.F.H. 1993. The Spectral Image Processing System (SIPS) interactive visualization and analysis of imaging spectrometer data. Remote Sensing of Environment 44: 145–163. https://doi.org/10.1016/0034-4257(93)90013-N

Kryniecka, K., Magnuszewski, A. 2021. Application of satellite Sentinel-2 images to study alternate sandbars movement at lower Vistula River (Poland). Remote Sensing 13: 1505. https://doi.org/10.3390/rs13081505

Lanaras, C., Bioucas-Dias, J., Galliani, S., Baltsavias, E., Schindler, K. 2018. Super-resolution of Sentinel-2 images: Learning a globally applicable deep neural network. ISPRS Journal of Photogrammetry and Remote Sensing 146: 305–319. https://doi.org/10.1016/j.isprsjprs.2018.09.018

Langhans, S.D., Tockner, K. 2014. Edge effects are important in supporting beetle biodiversity in a gravel-bed river floodplain. PLoS ONE 9: e114415. https://doi.org/10.1371/journal.pone.0114415

Li, W. 2021. Improving urban impervious surfaces mapping through integrating statistical methods and spectral mixture analysis. Remote Sensing 13: 2474. https://doi.org/10.3390/rs13132474

Li, X., Chen, R., Foody, G.M., Wang, L., Yang, X., Du, Y., Ling, F. 2020. Spatio-temporal sub-pixel land cover mapping of remote sensing imagery using spatial distribution information from same-class pixels. Remote Sensing 12: 503. https://doi.org/10.3390/rs12030503

Liaw, A., Wiener, M. 2002. Classification and regression by randomForest. R News 2: 18–22. https://cogns.northwestern.edu/cbmg/LiawAndWiener2002.pdf

Ling, F., Zhang, Y., Foody, G.M., Li, X., Zhang, X., Fang, S., Li, W., Du, Y. 2016. Learning-based superresolution land cover mapping. IEEE Transactions on Geoscience and Remote Sensing 54: 3794–3810. https://doi.org/10.1109/TGRS.2016.2527841

Liu, C., Shi, J., Liu, X., Shi, Z., Zhu, J. 2020. Subpixel mapping of surface water in the Tibetan Plateau with MODIS data. Remote Sensing 12: 1154. https://doi.org/10.3390/rs12071154

Liu, Q., Trinder, J., Turner, I. 2016. A comparison of sub-pixel mapping methods for coastal areas. ISPRS Annals of the Photogrammetry, Remote Sensing and Spatial Information Sciences 3: 67–74. https://doi.org/10.5194/isprsannals-III-7-67-2016

Stančič, L. 2022. Monitoring Changes of Fluvial Gravel Bars with Remote Sensing.
PhD Th. Ljubljana, UL FGG, Interdisciplinary doctoral study programme Environmental Protection.

151

Ma, Y., He, T., Li, A., Li, S. 2021. Evaluation and intercomparison of topographic correction methods based on Landsat images and simulated data. Remote Sensing 13: 4120. https://doi.org/10.3390/rs13204120

Masek, J.G., Wulder, M.A., Markham, B., McCorkel, J., Crawford, C.J., Storey, J., Jenstrom, D.T. 2020. Landsat 9: Empowering open science and applications through continuity. Remote Sensing of Environment 248: 111968. https://doi.org/10.1016/j.rse.2020.111968

McFeeters, S.K. 1996. The use of the Normalized Difference Water Index (NDWI) in the delineation of open water features. International Journal of Remote Sensing 17: 1425–1432. https://doi.org/10.1080/01431169608948714

Merzlyak, M.N., Gitelson, A.A., Chivkunova, O.B., Rakitin, V.YU. 1999. Non-destructive optical detection of pigment changes during leaf senescence and fruit ripening. Physiologia Plantarum 106: 135–141. https://doi.org/10.1034/j.1399-3054.1999.106119.x

Meyer, D., Dimitriadou, E., Hornik, K., Weingessel, A., Leisch, F. 2021. e1071: Misc functions of the Department of Statistics, Probability Theory Group (Formerly: E1071). https://CRAN.R-project.org/package=e1071 (Accessed 25. 6. 2021).

Mikoš, M., Kranjc, A., Mati, B., Müller, J., Rakovec, J., Roš, M., Brilly, M. 2002a. Terminology in hydrology. Acta hydrotechnica 20: 32, 3–325.

Mikoš, M., Štravs, L., Petkovšek, G., Brilly, M. 2002b. Sediment budget of the Koritnica River basin: 1. Yearly sediment transport rates (in Slovenian). Gradbeni vestnik 51: 316–321.

Ministry of Agriculture, Forestry and Food of the Republic of Slovenia 2020. Map of actual land use. http://rkg.gov.si/GERK/documents/RABA_2020_05_31.RAR (Accessed 6. 6. 2020).

Modified Copernicus Sentinel data. 2021. Sentinel Hub. https://www.sentinel-hub.com/ (Accessed 10. 11. 2021).

Musa, Z.N., Popescu, I., Mynett, A. 2015. A review of applications of satellite SAR, optical, altimetry and DEM data for surface water modelling, mapping and parameter estimation. Hydrology and Earth System Sciences 19: 3755–3769. https://doi.org/10.5194/hess-19-3755-2015

Muslim, A.M., Foody, G.M., Atkinson, P.M. 2007. Shoreline mapping from coarse–spatial resolution remote sensing imagery of Seberang Takir, Malaysia. Journal of Coastal Research 236: 1399–1408. https://doi.org/10.2112/04-0421.1

Mylona, E., Daskalopoulou, V., Sykioti, O., Koutroumbas, K., Rontogiannis, A. 2018. Classification of Sentinel-2 images utilizing abundance representation. Proceedings 2: 328. https://doi.org/10.3390/ecrs-2-05141

NASA. 2015. Comparison of Landsat 7 and 8 bands with Sentinel-2. https://web.archive.org/web/20170515022022/https://landsat.gsfc.nasa.gov/wp-content/uploads/2015/06/Landsat.v.Sentinel-2.png (Accessed 10. 7. 2021).

Natural Earth. 2020. 1 : 10m cultural vectors. Admin 0 - countries. https://www.naturalearthdata.com/http//www.naturalearthdata.com/download/10m/cultural/ne_10m_admin_0_countries.zip (Accessed 3. 8. 2021).

Nichols, G. 2009. Sedimentology and stratigraphy. 2nd ed. Chichester, Hoboken, Wiley-Blackwell: 419 p.

Niroumand-Jadidi, M., Vitti, A. 2017. Reconstruction of river boundaries at sub-pixel resolution: Estimation and spatial allocation of water fractions. ISPRS International Journal of Geo-Information 6: 383. https://doi.org/10.3390/ijgi6120383

Nistor, C., Săvulescu, I., Mihai, B.-A., Zaharia, L., Vîrghileanu, M., Carablaisă, S. 2021. The impact of large dams on fluvial sedimentation: The Iron Gates Reservoir on the Danube River. Acta geographica Slovenica 61: 41–55. https://doi.org/10.3986/AGS.7856

Official Gazette of the Republic of Slovenia, No. 67/02. 2002. Water act.

Official Gazette of the Republic of Slovenia, No. 112/03. 2003. Decree on habitat types.

Ogrin, D. 1996. The climate types in Slovenia (in Slovenian). Geografski vestnik 68: 39–56. http://zgs.zrc-sazu.si/Portals/8/Geografski_vestnik/Pred1999/GV_6801_039_056.pdf

Ogrin, D., Plut, D. 2009. Applied physical geography of Slovenia. Ljubljana, Ljubljana University Press, Faculty of Arts: 246 p.

OJ L 206. 1992. Council Directive 92/43/EEC of 21 May 1992 on the conservation of natural habitats and of wild fauna and flora.

Okujeni, A., Canters, F., Cooper, S.D., Degerickx, J., Heiden, U., Hostert, P., Priem, F., Roberts, D.A., Somers, B., van der Linden, S. 2018. Generalizing machine learning regression models using multi-site spectral libraries for mapping vegetation-impervious-soil fractions across multiple cities. Remote Sensing of Environment 216: 482–496. https://doi.org/10.1016/j.rse.2018.07.011

OpenStreetMap contributors. 2021. OpenStreetMap data retrieved from https://download.geofabrik.de/.

Oštir, K. 2006. Daljinsko zaznavanje. Ljubljana, Založba ZRC: 250 p.

Pandžić, M., Mihajlović, D., Pandžić, J., Pfeifer, N. 2016. Assessment of the geometric quality of Sentinel-2 data. ISPRS - International Archives of the Photogrammetry, Remote Sensing and Spatial Information Sciences XLI-B1: 489–494. https://doi.org/10.5194/isprsarchives-XLI-B1-489-2016

Papler, D., Basej, J. 2014. Rehabilitation and rehabilitation effects of the Sava HPP soft dam, in: Transmission of Innovations, Knowledge and Practical Experience into Everyday Practice. Conference VIVUS – on Agriculture, Environmentalism, Horticulture and Floristics, Food Production and Processing and Nutrition. Naklo, Biotechnical Centre Naklo: pp. 429–441. http://www.bc-naklo.si/fileadmin/visja_sola/2014/2sekcijaNaravovarstvo/49-Papler-Basej-Z.pdf

Pehani, P., Čotar, K., Marsetič, A., Zaletelj, J. Oštir, K.. 2016. Automatic geometric processing for very high resolution optical satellite data based on vector roads and orthophotos. Remote Sensing 8: 343. https://doi.org/10.3390/rs8040343

Pekel, J.-F., Cottam, A., Gorelick, N., Belward, A.S. 2016. High-resolution mapping of global surface water and its long-term changes. Nature 540: 418–422. https://doi.org/10.1038/nature20584

Peñuelas, J., Gamon, J.A., Fredeen, A.L., Merino, J., Field, C.B. 1994. Reflectance indices associated with physiological changes in nitrogen- and water-limited sunflower leaves. Remote Sensing of Environment 48: 135–146. https://doi.org/10.1016/0034-4257(94)90136-8

Peñuelas, J., Gamon, J.A., Griffin, K.L., Field, C.B. 1993. Assessing community type, plant biomass, pigment composition, and photosynthetic efficiency of aquatic vegetation from spectral reflectance. Remote Sensing of Environment 46: 110–118. https://doi.org/10.1016/0034-4257(93)90088-F

Priem, F., Okujeni, A., van der Linden, S., Canters, F. 2019. Comparing map-based and library-based training approaches for urban land-cover fraction mapping from Sentinel-2 imagery. International Journal of Applied Earth Observation and Geoinformation 78: 295–305. https://doi.org/10.1016/j.jag.2019.02.003

Prigent, C., Matthews, E., Aires, F., Rossow, W.B. 2001. Remote sensing of global wetland dynamics with multiple satellite data sets. Geophysical Research Letters 28: 4631–4634. https://doi.org/10.1029/2001GL013263

QGIS Development Team. 2020. QGIS Geographic Information System. Open Source Geospatial Foundation Project.

Qi, J., Kerr, Y., Chehbouni, A. 1994. External factor consideration in vegetation index development, in: Proceedings of Physical Measurements and Signatures in Remote Sensing, ISPRS. International Symposium on Physical Measurements and Signatures in Remote Sensing: pp. 723–730.

R Core Team 2021. R: A language and environment for statistical computing. Vienna, R Foundation for Statistical Computing.

Ranfl, I. 2010. Braiding river Soča in the Bovec basin (in Slovenian). Bachelor thesis. Ljubljana, University of Ljubljana, Faculty of Civil and Geodetic Engineering (self-published I. Ranfl): 96 p.

Rastiveis, H., Samadzadegan, F., Reinartz, P. 2013. A fuzzy decision making system for building damage map creation using high resolution satellite imagery. Natural Hazards and Earth System Sciences 13: 455–472. https://doi.org/10.5194/nhess-13-455-2013

Reschke, J., Hüttich, C. 2014. Continuous field mapping of Mediterranean wetlands using sub-pixel spectral signatures and multi-temporal Landsat data. International Journal of Applied Earth Observation and Geoinformation 28: 220–229. https://doi.org/10.1016/j.jag.2013.12.014

Richards, A. 1990. Seabirds of the northern hemisphere. Limpsfield, UK, Dragon's World Ltd: 192 p.

Richter, R. 1996. A spatially adaptive fast atmospheric correction algorithm. International Journal of Remote Sensing 17: 1201–1214. http://dx.doi.org/10.1080/01431169608949077

Richter, R., Schläpfer, D. 2019. Atmospheric / topographic correction for satellite imagery (ATCOR-2/3 user guide, version 9.3.0, April 2019). https://www.rese-apps.com/pdf/atcor3_manual.pdf (Accessed 2. 8. 2019).

Richter, R., Schläpfer, D., Müller, A. 2006. An automatic atmospheric correction algorithm for visible / NIR imagery. International Journal of Remote Sensing 27: 2077–2085. https://doi.org/ 10.1080/01431160500486690

Robert, A. 2003. River processes: An introduction to fluvial dynamics. London, Arnold: 214 p.

Rössler, N., Egger, G., Drescher, A. 2018. Fluvial processes and changes in the floodplain vegetation of the Vjosa river (Albania). Acta ZooBot Austria 155: 73–84. https://www.zobodat.at/pdf/ VZBG_155_1_0073-0084.pdf

Roy, D.P., Li, J., Zhang, H.K., Yan, L. 2016. Best practices for the reprojection and resampling of Sentinel-2 Multi Spectral Instrument Level 1C data. Remote Sensing Letters 7: 1023–1032. https://doi.org/10.1080/2150704X.2016.1212419

Rufin, P., Frantz, D., Yan, L., Hostert, P. 2021. Operational coregistration of the Sentinel-2A/B image archive using multitemporal Landsat spectral averages. IEEE Geoscience and Remote Sensing Letters 18: 712–716. https://doi.org/10.1109/LGRS.2020.2982245

Schiemer, F., Beqiraj, S., Drescher, A., Graf, W., Egger, G., Essl, F., Frank, T., Hauer, C., Hohensinner, S., Miho, A., Meulenbroek, P., Paill, W., Schwarz, U., Vitecek, S. 2020. The Vjosa River corridor: a model of natural hydro-morphodynamics and a hotspot of highly threatened ecosystems of European significance. Landscape Ecology 35: 953–968. https://doi.org/10.1007/s10980-020-00993-y

Stančič, L. 2022. Monitoring Changes of Fluvial Gravel Bars with Remote Sensing.
PhD Th. Ljubljana, UL FGG, Interdisciplinary doctoral study programme Environmental Protection.

155

Schmidt, M., Scarth, P. 2009. Spectral mixture analysis for ground-cover mapping. In: Jones, S., Reinke, K. (Eds.). Innovations in remote sensing and photogrammetry. Berlin, Heidelberg, Springer: pp. 349–359. https://doi.org/10.1007/978-3-540-93962-7_27

Schug, F., Okujeni, A., Hauer, J., Hostert, P., Nielsen, J.Ø., van der Linden, S. 2018. Mapping patterns of urban development in Ouagadougou, Burkina Faso, using machine learning regression modeling with bi-seasonal Landsat time series. Remote Sensing of Environment 210: 217–228. https://doi.org/10.1016/j.rse.2018.03.022

Schwarz, M., Steinmeier, C., Holecz, F., Stebler, O., Wagner, H. 2003. Detection of windthrow in mountainous regions with different remote sensing data and classification methods. Scandinavian Journal of Forest Research 18: 525–536. https://doi.org/10.1080/02827580310018023

Scott, G., Rajabifard, A. 2017. Sustainable development and geospatial information: A strategic framework for integrating a global policy agenda into national geospatial capabilities. Geospatial Information Science 20: 59–76. https://doi.org/10.1080/10095020.2017.1325594

Serlet, A.J., Gurnell, A.M., Zolezzi, G., Wharton, G., Belleudy, P., Jourdain, C. 2018. Biomorphodynamics of alternate bars in a channelized, regulated river: An integrated historical and modelling analysis. Earth Surface Processes and Landforms 43: 1739–1756. https://doi.org/10.1002/esp.4349

Shao, Q., Shi, Y., Xiang, Z., Shao, H., Xian, W., Peng, P., Li, C., Li, Q. 2018. Monitoring the grassland change in the Qinghai-Tibetan plateau: A case study on Aba county. Journal of the Indian Society of Remote Sensing 46: 569–580. https://doi.org/10.1007/s12524-017-0721-7

Signal developers. 2013. Signal: Signal processing. http://r-forge.r-project.org/projects/signal/ (Accessed 4. 7. 2021).

Sinergise. 2021. s2cloudless v1.5.0. GitHub. https://github.com/sentinel-hub/sentinel2-cloud-detector/releases/tag/v1.5.0 (Accessed 8. 12. 2021).

Slovenian Environment Agency. 2021a. Archive of meteorological data. Ljubljana, Ministry of the Environment and Spatial Planning of the Republic of Slovenia. http://www.meteo.si/met/sl/archive/ (Accessed 25. 6. 2021).

Slovenian Environment Agency. 2021b. Archive of surface waters: Daily data. Ljubljana, Ministry of the Environment and Spatial Planning of the Republic of Slovenia. http://vode.arso.gov.si/hidarhiv/pov_arhiv_tab.php (Accessed 16. 9. 2019).

Slovenian Water Agency. 2021a. Water lands of running inland water. Ljubljana, Ministry of the Environment and Spatial Planning of the Republic of Slovenia. http://www.statika.evode.gov.si/fileadmin/vodkat/DRSV_VZ_TEK_CV.zip (Accessed 25. 8. 2021).

156   Stančič, L. 2022. Monitoring Changes of Fluvial Gravel Bars with Remote Sensing.

PhD Th. Ljubljana, UL FGG, Interdisciplinary doctoral study programme Environmental Protection.

Slovenian Water Agency. 2021b. Polygon data layer of hydrography: Infrastructure and other. Ljubljana, Ministry of the Environment and Spatial Planning of the Republic of Slovenia. http://www.statika.evode.gov.si/fileadmin/vodkat/DRSV_HIDRO5_OBM_OBJ.zip (Accessed 15. 1. 2021).

Slovenian Water Agency. 2021c. Polygon data layer of hydrography: Surface waters. Ljubljana, Ministry of the Environment and Spatial Planning of the Republic of Slovenia. http://www.statika.evode.gov.si/fileadmin/vodkat/DRSV_HIDRO5_OBM_PV.zip (Accessed 15. 1. 2021).

Snow, D.W., Perrins, C.M. 1998. The birds of the western palearctics vol. 1: Non-passerines. Oxford, Oxford University Press: 1008 p.

Soenen, S.A., Peddle, D.R., Coburn, C.A. 2005. SCS+C: A modified Sun-canopy-sensor topographic correction in forested terrain. IEEE Transactions on Geoscience and Remote Sensing 43: 2148–2159. https://doi.org/10.1109/TGRS.2005.852480

Somers, B., Asner, G.P., Tits, L., Coppin, P. 2011. Endmember variability in spectral mixture analysis: A review. Remote Sensing of Environment 115: 1603–1616. https://doi.org/10.1016/j.rse.2011.03.003

Spada, D., Molinari, P., Bertoldi, W., Vitti, A., Zolezzi, G. 2018. Multi-temporal image analysis for fluvial morphological characterization with application to Albanian rivers. ISPRS International Journal of Geo-Information 7: 314. https://doi.org/10.3390/ijgi7080314

Stančič, L., Oštir, K., Kokalj, Ž. 2021. Fluvial gravel bar mapping with spectral signal mixture analysis. European Journal of Remote Sensing 54: 31–46. https://doi.org/10.1080/22797254.2020.1811776

Strahler, A.H., Strahler, A.N. 2005. Physical geography: Science and systems of the human environment. 3rd ed. New York, John Wiley & Sons: 794 p.

Suess, S., van der Linden, S., Okujeni, A., Griffiths, P., Leitão, P.J., Schwieder, M., Hostert, P. 2018. Characterizing 32 years of shrub cover dynamics in southern Portugal using annual Landsat composites and machine learning regression modeling. Remote Sensing of Environment 219: 353–364. https://doi.org/10.1016/j.rse.2018.10.004

Sukawattanavijit, C., Chen, J., Zhang, H. 2017. GA-SVM algorithm for improving land-cover classification using SAR and optical remote sensing data. IEEE Geoscience and Remote Sensing Letters 14: 284–288. https://doi.org/10.1109/LGRS.2016.2628406

Surveying and Mapping Authority of the Republic of Slovenia. 2021a. National General Map at 1 : 250 000 Scale - vector data. Communication infrastructure. Ljubljana, Ministry of the Environment

and Spatial Planning of the Republic of Slovenia. http://egp.gu.gov.si/egp/ (Accessed 11. 10. 2021).

Surveying and Mapping Authority of the Republic of Slovenia. 2021b. National Border Record. Ljubljana, Ministry of the Environment and Spatial Planning of the Republic of Slovenia. http://egp.gu.gov.si/egp/ (Accessed 11. 10. 2021).

Surveying and Mapping Authority of the Republic of Slovenia. 2021c. Orthophotos. Ljubljana, Ministry of the Environment and Spatial Planning of the Republic of Slovenia. http://egp.gu.gov.si/egp/ (Accessed 15. 10. 2021).

Surveying and Mapping Authority of the Republic of Slovenia. 2016. Digital Elevation Model. DEM 0125. Ljubljana, Ministry of the Environment and Spatial Planning of the Republic of Slovenia. http://egp.gu.gov.si/egp/ (Accessed 17. 1. 2019).

Surveying and Mapping Authority of the Republic of Slovenia. 2015. Orthophotos. Ljubljana, Ministry of the Environment and Spatial Planning of the Republic of Slovenia. http://egp.gu.gov.si/egp/ (Accessed 17. 1. 2019).

Szoszkiewicz, K., Jusik, S., Gebler, D., Achtenberg, K., Adynkiewicz-Piragas, M., Artur Radecki-Pawlik, A., Okruszko, T., Pietruczuk, K., Przesmycki, M., Nawrocki, P. 2020. Hydromorphological index for rivers: A new method for hydromorphological assessment and classification for flowing waters in Poland. Journal of Ecological Engineering 21: 261–271. https://doi.org/10.12911/22998993/126879

Škornik, S., Meznarič, M., Kaligarič, M. 2017. Factors affecting composition of gravel bar vegetation in middle reach of a lowland river. Polish Journal of Ecology 65: 194–210. https://doi.org/10.3161/15052249PJE2017.65.2.003

Škornik, S., Meznarič, M., Kaligarič, M. 2016. Functional composition of mid-stream gravel bar vegetation (Middle Drava River, NE Slovenia). Annales : anali za istrske in mediteranske študije, Series historia naturalis 26: 171–182.

Švab Lenarčič, A. 2018. Multitemporal land cover classification of optical satellite imagery (in Slovenian). Doctoral thesis. Ljubljana, University of Ljubljana, Faculty of Civil and Geodetic Engineering (self-published A. Švab Lenarčič): 175 p.

Tarbuck, E.J., Lutgens, F.K. 2005. Earth: An introduction to physical geology, 8th ed. Upper Saddle River, Prentice Hall: 711 p.

Tarko, A., de Bruin, S., Bregt, A.K. 2018. Comparison of manual and automated shadow detection on satellite imagery for agricultural land delineation. International Journal of Applied Earth Observation and Geoinformation 73: 493–502. https://doi.org/10.1016/j.jag.2018.07.020

Teillet, P.M., Guindon, B., Goodenough, D.G. 1982. On the slope-aspect correction of Multispectral Scanner data. Canadian Journal of Remote Sensing 8: 84–106. https://doi.org/10.1080/07038992.1982.10855028

Therien, C. 2018. PySptools documentation. https://pysptools.sourceforge.io/index.html (Accessed 21. 2. 2020).

Tucker, C.J. 1979. Red and photographic infrared linear combinations for monitoring vegetation. Remote Sensing of Environment 8: 127–150. https://doi.org/10.1016/ 0034-4257(79)90013-0

U. S. Geological Survey. 2021a. Landsat-7 imagery. https://earthexplorer.usgs.gov/ (Accessed 10. 11. 2021).

U. S. Geological Survey. 2021b. Landsat-8 imagery. https://earthexplorer.usgs.gov/ (Accessed 10. 11. 2021).

UN. 2017. Resolution adopted by the General Assembly on 6 July 2017: 71/313. Work of the Statistical Commission pertaining to the 2030 Agenda for Sustainable Development.

UN. 2015. Resolution adopted by the General Assembly on 25 September 2015: 70/1. Transforming our world: the 2030 Agenda for Sustainable Development. https://doi.org/10.1891/ 9780826190123.ap02

Vajsova, B., Åstrand, P.J. 2015. New sensors benchmark report on Sentinel-2A: Geometric benchmarking over Maussane test site for CAP purposes. https://data.europa.eu/doi/10.2788/ 544302 (Accessed 7. 4. 2021).

van der Walt, S., Schönberger, J.L., Nunez-Iglesias, J., Boulogne, F., Warner, J.D., Yager, N., Gouillart, E., Yu, T. 2014. scikit-image: image processing in Python. PeerJ 2: e453. https://doi.org/ 10.7717/peerj.453

Veganzones, M.A., Graña, M. 2008. Endmember extraction methods: A short review. Knowledge-Based Intelligent Information and Engineering Systems, 12th International Conference, pp. 400–407. http://www.ehu.eus/ccwintco/uploads/d/d6/Kes2008.pdf

Verpoorter, C., Kutser, T., Seekell, D.A., Tranvik, L.J. 2014. A global inventory of lakes based on high-resolution satellite imagery. Geophysical Research Letters 41: 6396–6402. https://doi.org/ 10.1002/2014GL060641

Vincini, M., Reeder, D., Frazzi, E. 2002. An empirical topographic normalization method for forest TM data, in: IEEE International Geoscience and Remote Sensing Symposium. IEEE International Geoscience and Remote Sensing Symposium. Toronto, IGARSS 2002, IEEE: pp. 2091–2093. https://doi.org/10.1109/IGARSS.2002.1026454

Vouvé, F., Cotrim da Cunha, L., Serve, L., Vigo, J., Salmon, J.-M. 2009. Spatio-temporal variations of fluorescence properties of dissolved organic matter along the River Têt (Pyrénées-Orientales, France). Chemistry and Ecology 25: 435–452. https://doi.org/10.1080/02757540903325104

Waqar, M.M., Mirza, J.F., Mumtaz, R., Hussain, E. 2012. Development of new indices for extraction of built-up area & bare soil from Landsat data. Open Access Scientific Reports 1: 1, 1–4. https://doi.org/10.4172/scientificreports.136

Winter, M.E. 1999. N-FINDR: an algorithm for fast autonomous spectral end-member determination in hyperspectral data. In: Descour, M.R., Shen, S.S. (Eds.). SPIE's International Symposium on Optical Science, Engineering, and Instrumentation. Denver: pp. 266–275. https://doi.org/10.1117/12.366289

Woodcock, C.E., Allen, R., Anderson, M., Belward, A., Bindschadler, R., Cohen, W., Gao, F., Goward, S.F., Helder, D., Helmer, E., Nemani, R., Oreopoulos, L., Schott, J., Thenkabail, P.S., Vermote, E.F., Vogelmann, J., Wulder, M.A., Wynne, R. 2008. Free access to Landsat imagery. Science 320: 1011.

Woodhouse, I.H. 2021. On 'ground' truth and why we should abandon the term. Journal of Applied Remote Sensing 15. https://doi.org/10.1117/1.JRS.15.041501

Wu, C. 2004. Normalized spectral mixture analysis for monitoring urban composition using ETM+ imagery. Remote Sensing of Environment 93: 480–492. https://doi.org/10.1016/j.rse.2004.08.003

Wulder, M.A., Loveland, T.R., Roy, D.P., Crawford, C.J., Masek, J.G., Woodcock, C.E., Allen, R.G., Anderson, M.C., Belward, A.S., Cohen, W.B., Dwyer, J., Erb, A., Gao, F., Griffiths, P., Helder, D., Hermosilla, T., Hipple, J.D., Hostert, P., Hughes, M.J., Huntington, J., Johnson, D.M., Kennedy, R., Kilic, A., Li, Z., Lymburner, L., McCorkel, J., Pahlevan, N., Scambos, T.A., Schaaf, C., Schott, J.R., Sheng, Y., Storey, J., Vermote, E., Vogelmann, J., White, J.C., Wynne, R.H., Zhu, Z. 2019. Current status of Landsat program, science, and applications. Remote Sensing of Environment 225: 127–147. https://doi.org/10.1016/j.rse.2019.02.015

Xi, Y., Thinh, N.X., Li, C. 2019. Preliminary comparative assessment of various spectral indices for built-up land derived from Landsat-8 OLI and Sentinel-2A MSI imageries. European Journal of Remote Sensing 52: 240–252. https://doi.org/10.1080/22797254.2019.1584737

Yin, G., Li, A., Wu, S., Fan, W., Zeng, Y., Yan, K., Xu, B., Li, J., Liu, Q. 2018. PLC: A simple and semi-physical topographic correction method for vegetation canopies based on path length correction. Remote Sensing of Environment 215: 184–198. https://doi.org/10.1016/j.rse.2018.06.009

160   Stančič, L. 2022. Monitoring Changes of Fluvial Gravel Bars with Remote Sensing.

PhD Th. Ljubljana, UL FGG, Interdisciplinary doctoral study programme Environmental Protection.

Zakšek, K., Čotar, K., Veljanovski, T., Pehani, P., Oštir, K. 2015. Topographic correction module at STORM (TC@Storm). ISPRS - International Archives of the Photogrammetry, Remote Sensing and Spatial Information Sciences XL-7/W3: 721–728. https://doi.org/10.5194/isprsarchives-XL-7-W3-721-2015

Zeng, Q., Shi, L., Wen, L., Chen, J., Duo, H., Lei, G. 2015. Gravel bars can be critical for biodiversity conservation: A case study on Scaly-sided Merganser in South China. PLoS ONE 10: e0127387. https://doi.org/10.1371/journal.pone.0127387

10 APPENDICES

APPENDIX A: Gravel Fraction Maps of the Soča River

APPENDIX B: Gravel Fraction Maps of the Sava River

APPENDIX C: Gravel Fraction Maps of the Vjosa River

»This page is intentionally blank.«

APPENDIX A : Gravel Fraction Maps of the Soča River
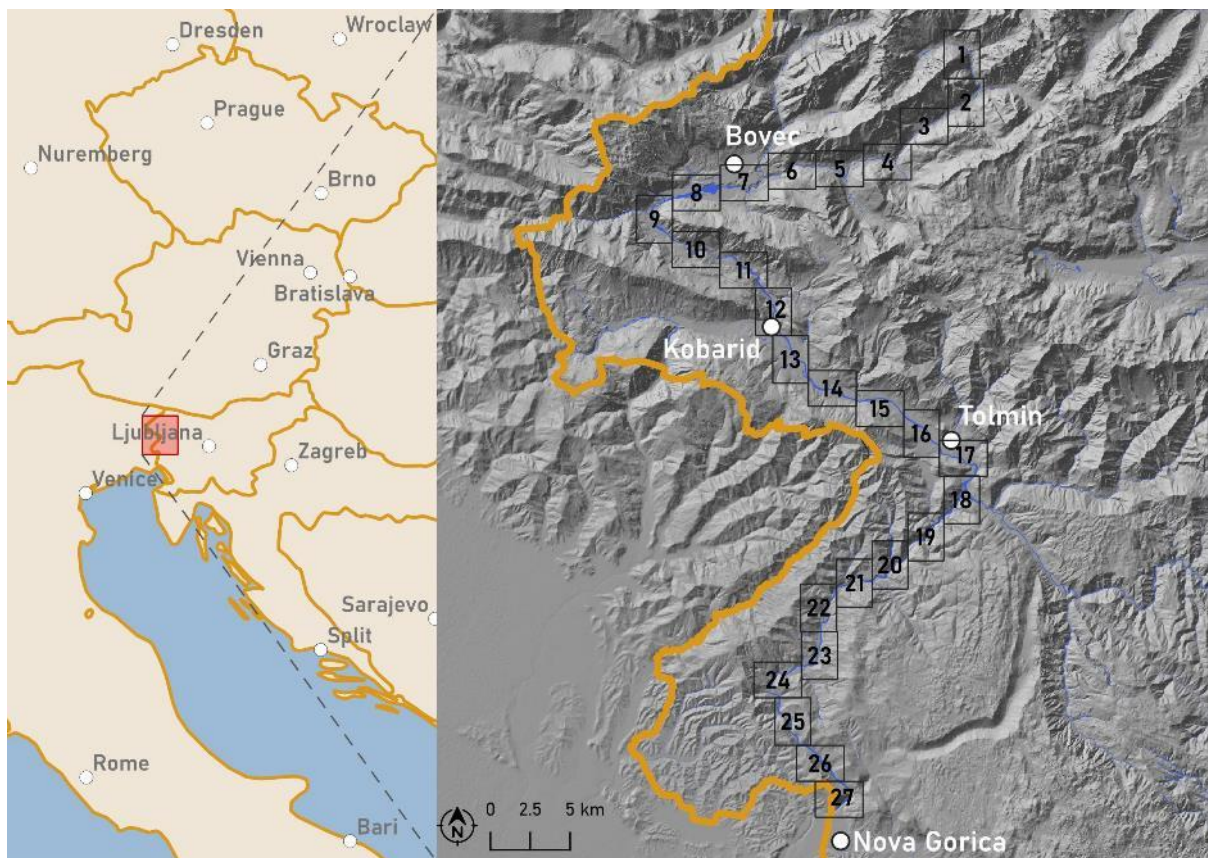
Figure A-1: Sections of the gravel presence maps on the Soča river in Slovenia (data source: Natural Earth, 2020; Slovenian Water Agency, 2021b; Surveying and Mapping Authority of the Republic of Slovenia, 2016, 2021b).

Slika A-1: Sekcije kart prisotnosti proda na Soči v Sloveniji (vir podatkov: Natural Earth, 2020; DRSV, 2021b; GURS, 2016, 2021b).
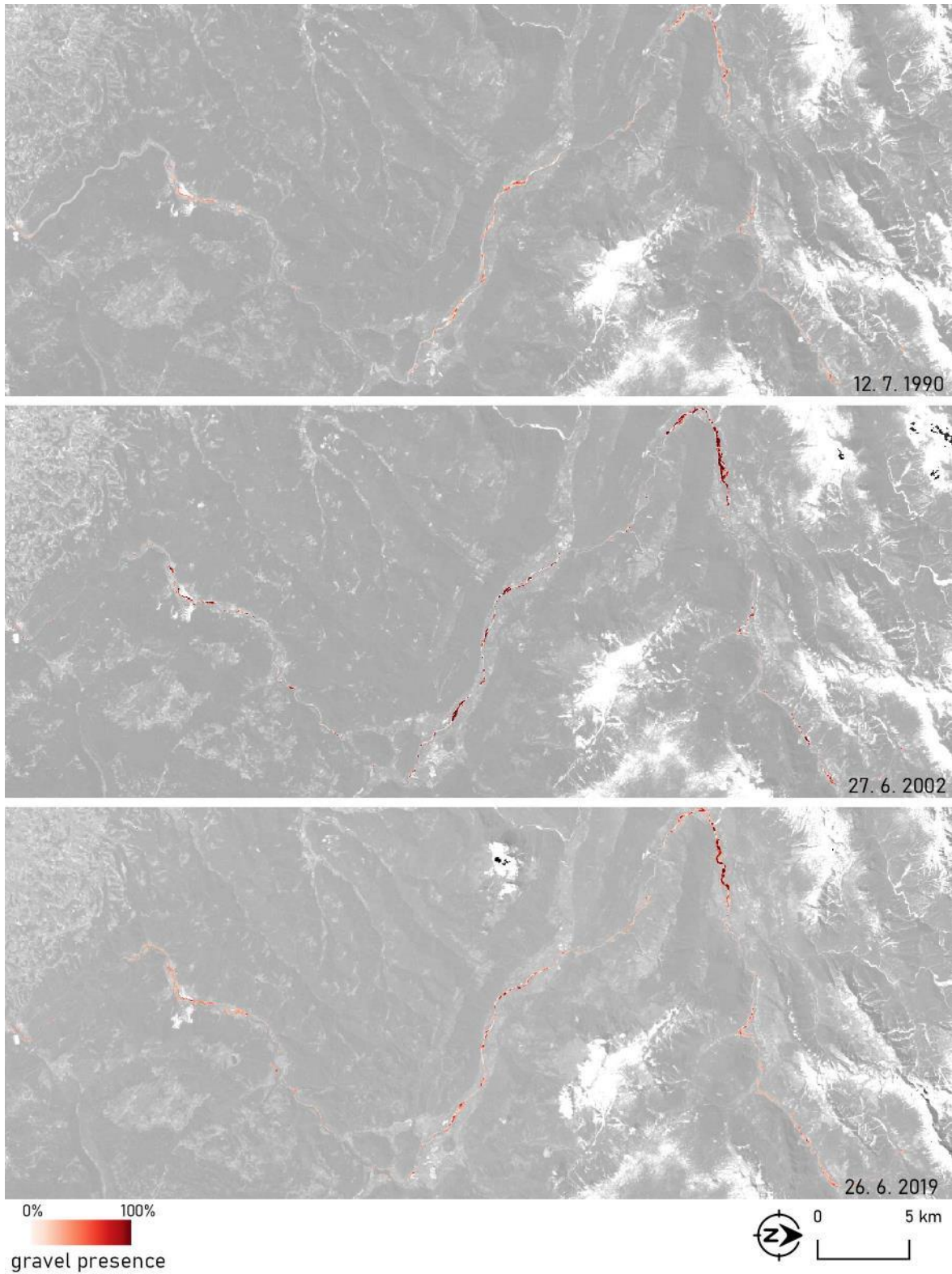
Figure A-2: Gravel presence on the Soča river in Slovenia in three different timestamps based on Landsat images.

Slika A-2: Prisotnost proda na Soči v Sloveniji v treh različnih časovnih obdobjih na podlagi posnetkov Landsat.
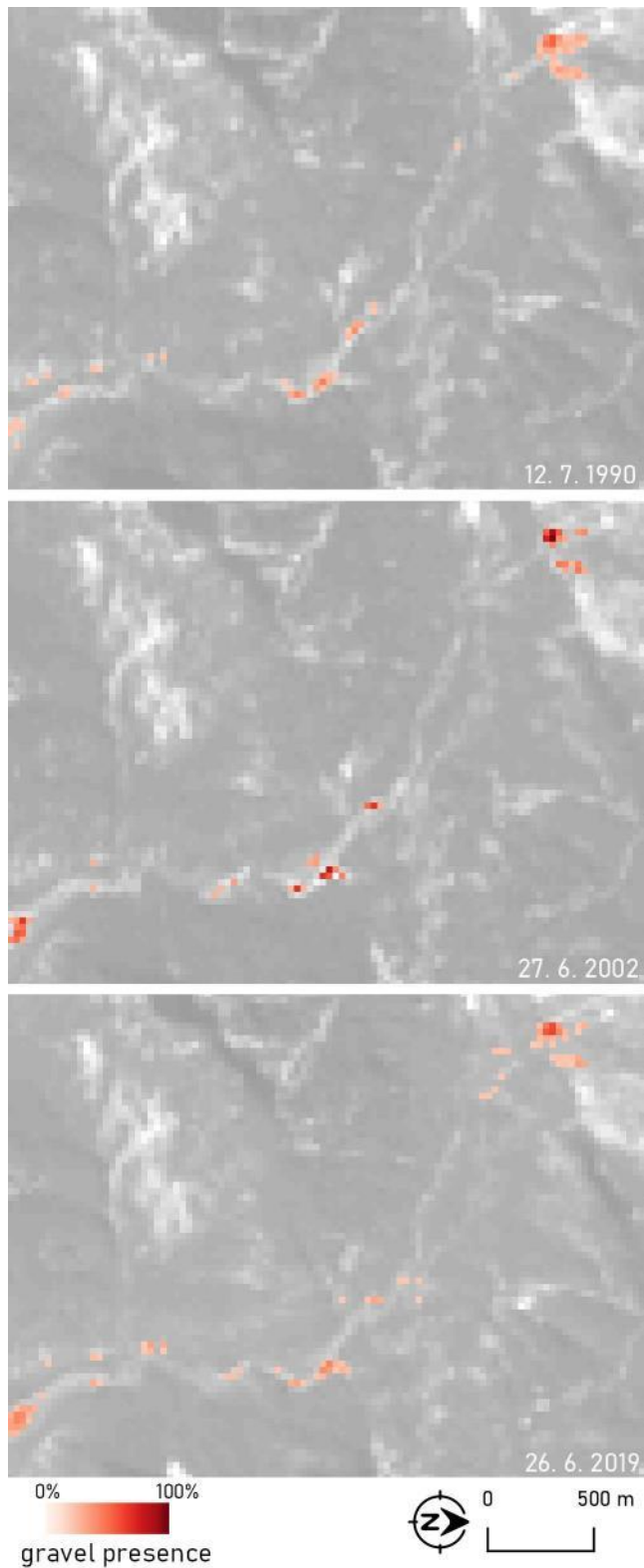
Figure A-3: Gravel presence on the Soča river on section 1 in three different timestamps based on Landsat images.

Slika A-3: Prisotnost proda na Soči na sekciji številka 1 v treh različnih časovnih obdobjih na podlagi posnetkov Landsat.
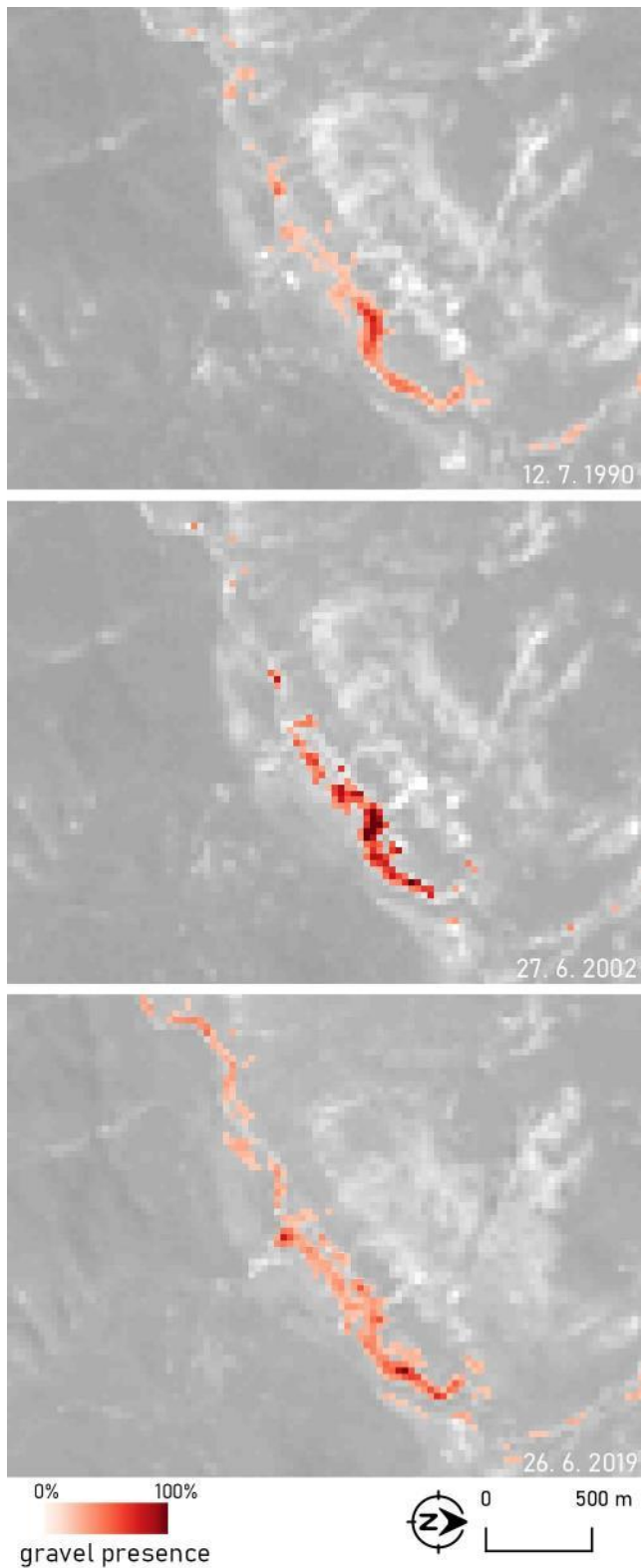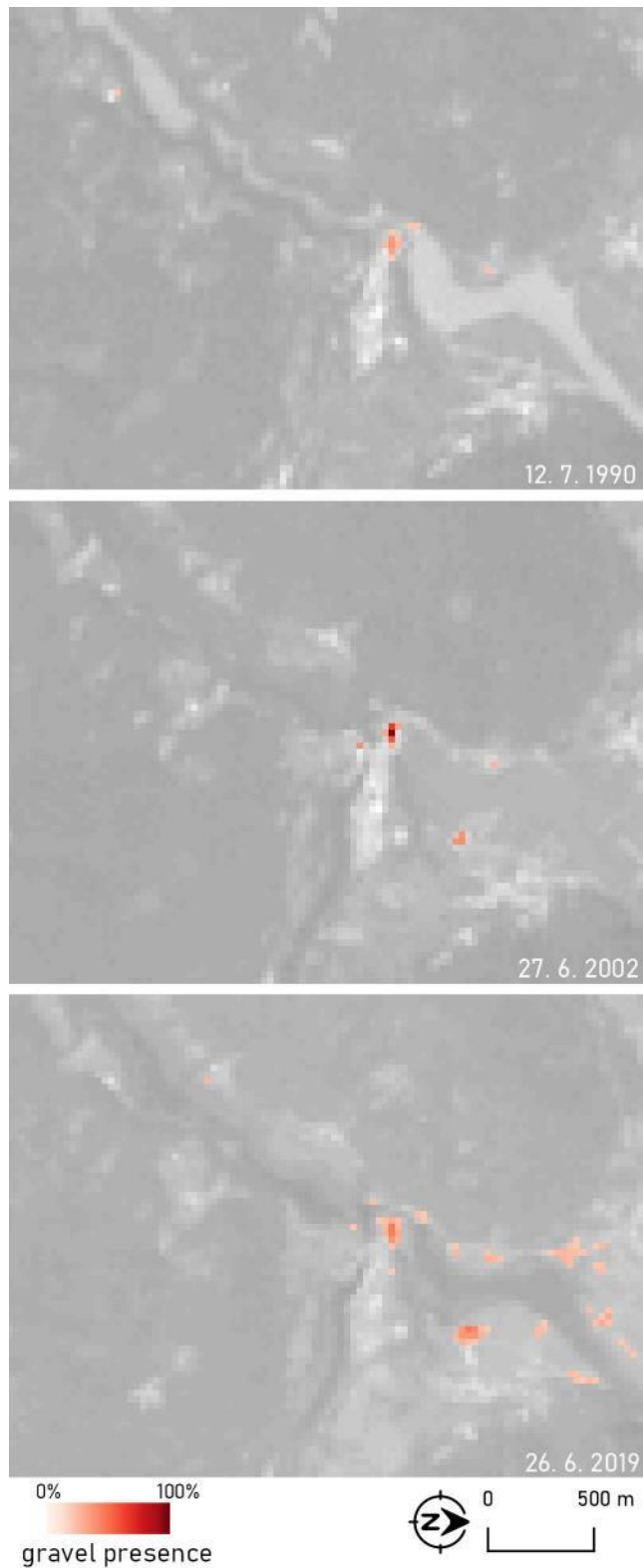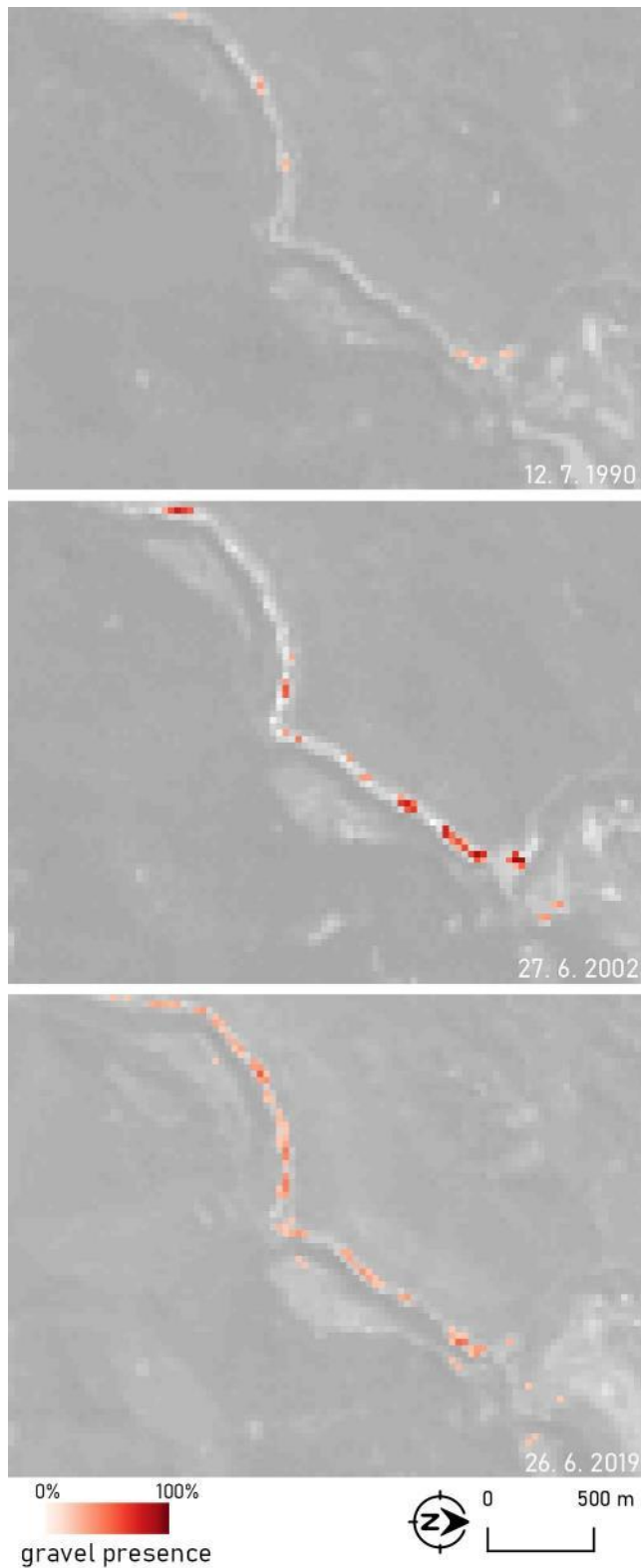
Figure A-4: Gravel presence on the Soča river on section 2 in three different timestamps based on Landsat images.

Slika A-4: Prisotnost proda na Soči na sekciji številka 2 v treh različnih časovnih obdobjih na podlagi posnetkov Landsat.
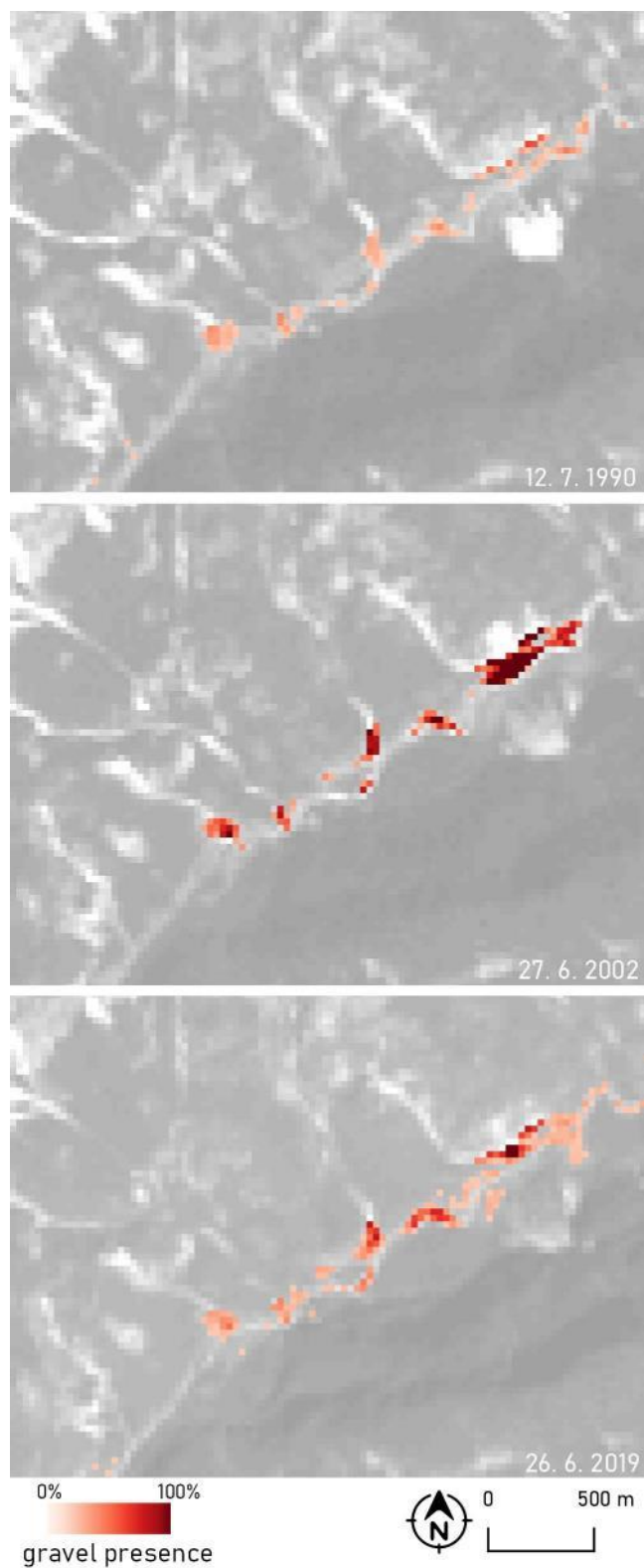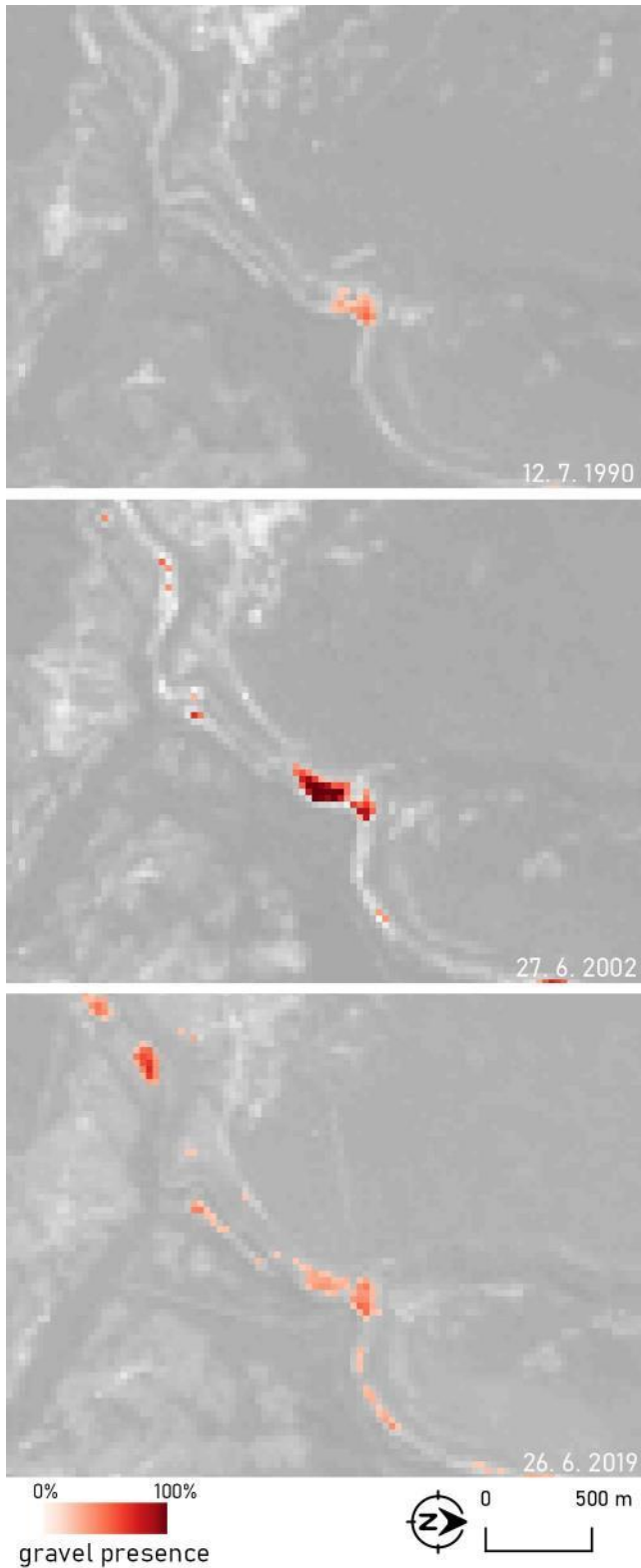
Figure A-5: Gravel presence on the Soča river on section 3 in three different timestamps based on Landsat images.

Slika A-5: Prisotnost proda na Soči na sekciji številka 3 v treh različnih časovnih obdobjih na podlagi posnetkov Landsat.

A-6

Stančič, L. 2022. Monitoring Changes of Fluvial Gravel Bars with Remote Sensing.
PhD Th. Ljubljana, UL FGG, Interdisciplinary doctoral study programme Environmental Protection.
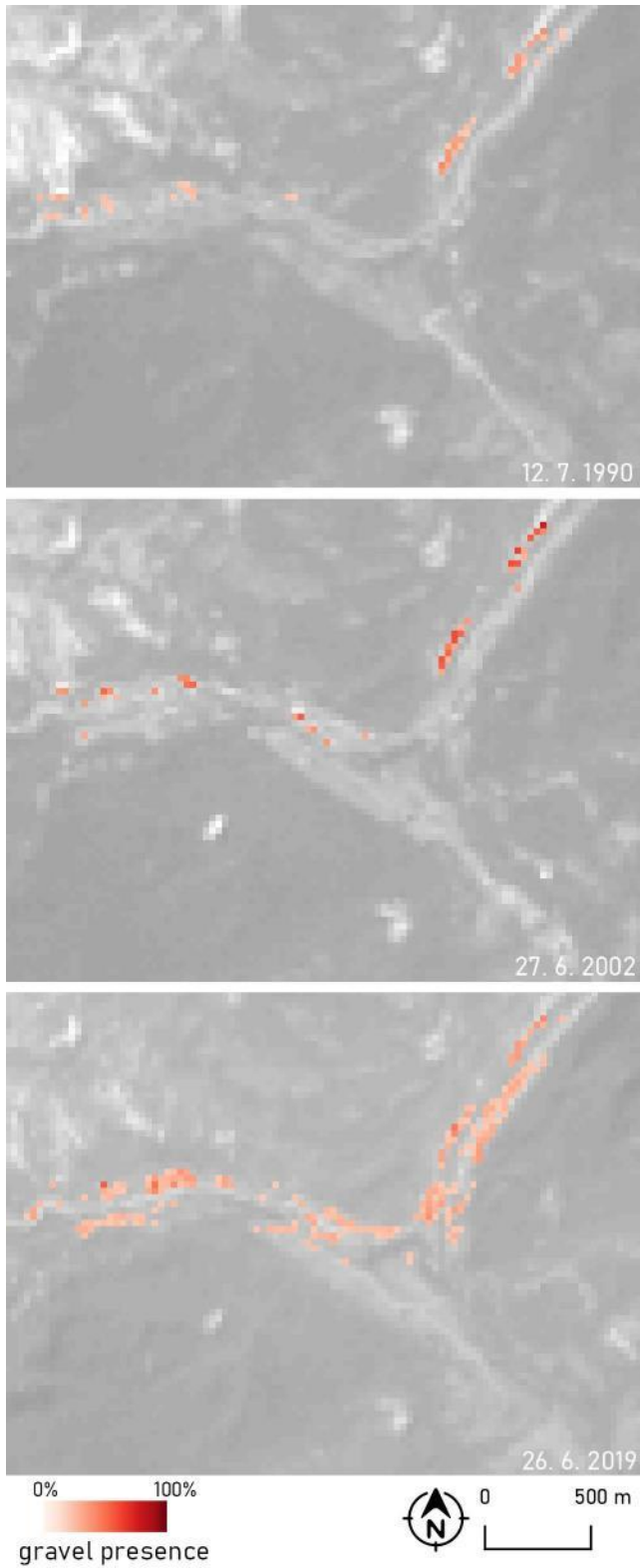
Figure A-6: Gravel presence on the Soča river on section 4 in three different timestamps based on Landsat images.

Slika A-6: Prisotnost proda na Soči na sekciji številka 4 v treh različnih časovnih obdobjih na podlagi posnetkov Landsat.

Stančič, L. 2022. Monitoring Changes of Fluvial Gravel Bars with Remote Sensing.

PhD Th. Ljubljana, UL FGG, Interdisciplinary doctoral study programme Environmental Protection.

A-7
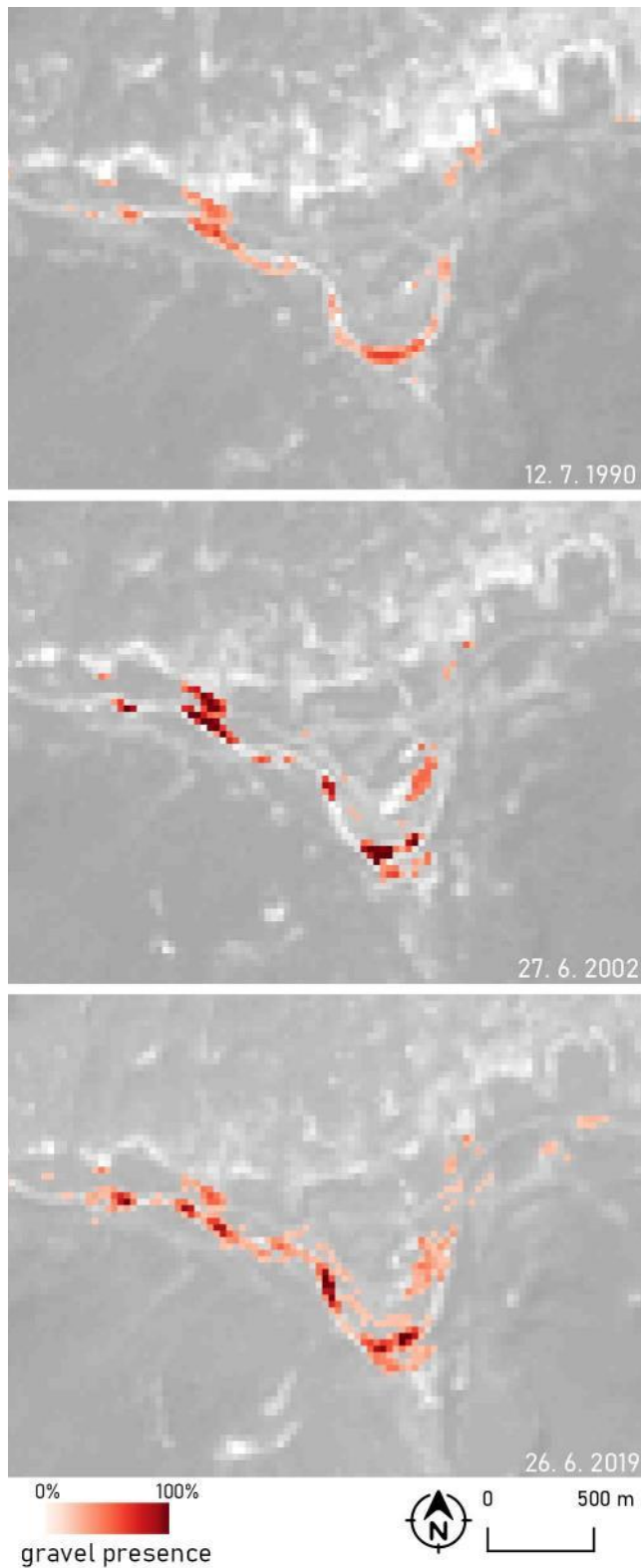
Figure A-7: Gravel presence on the Soča river on section 5 in three different timestamps based on Landsat images.

Slika A-7: Prisotnost proda na Soči na sekciji številka 5 v treh različnih časovnih obdobjih na podlagi posnetkov Landsat.
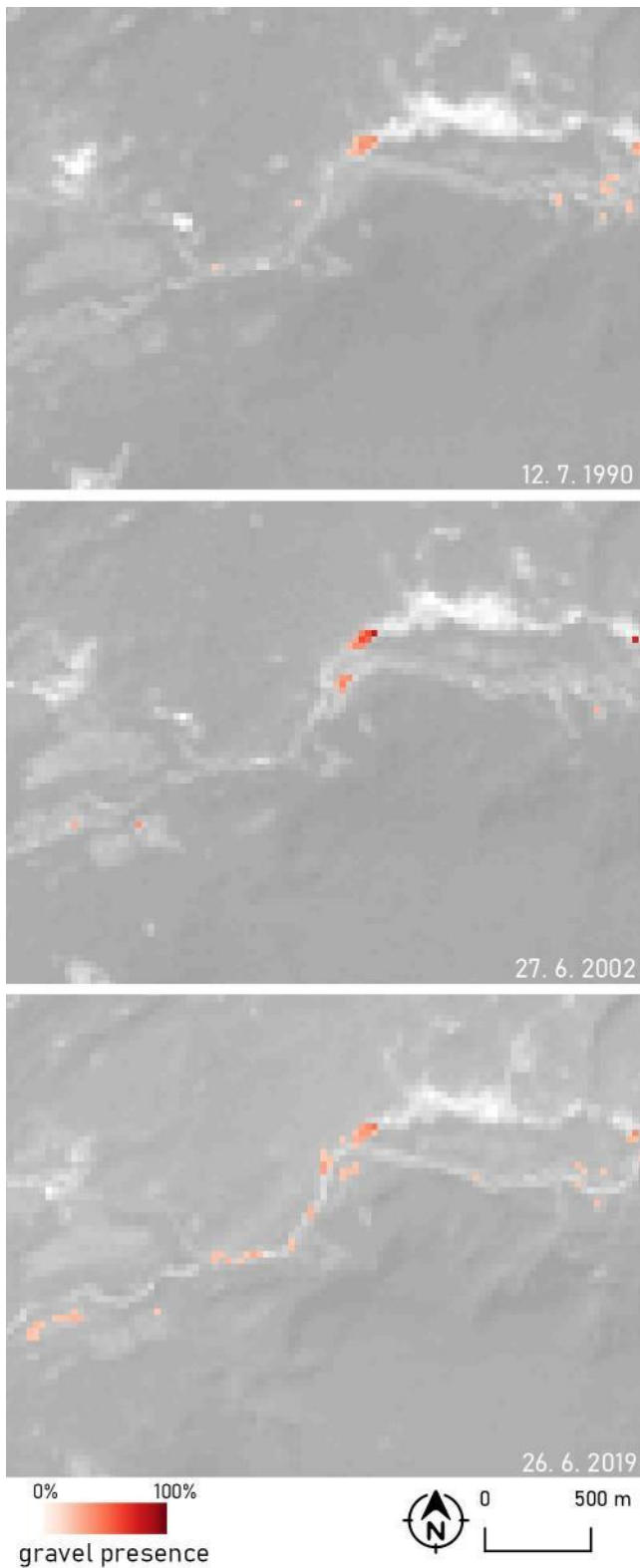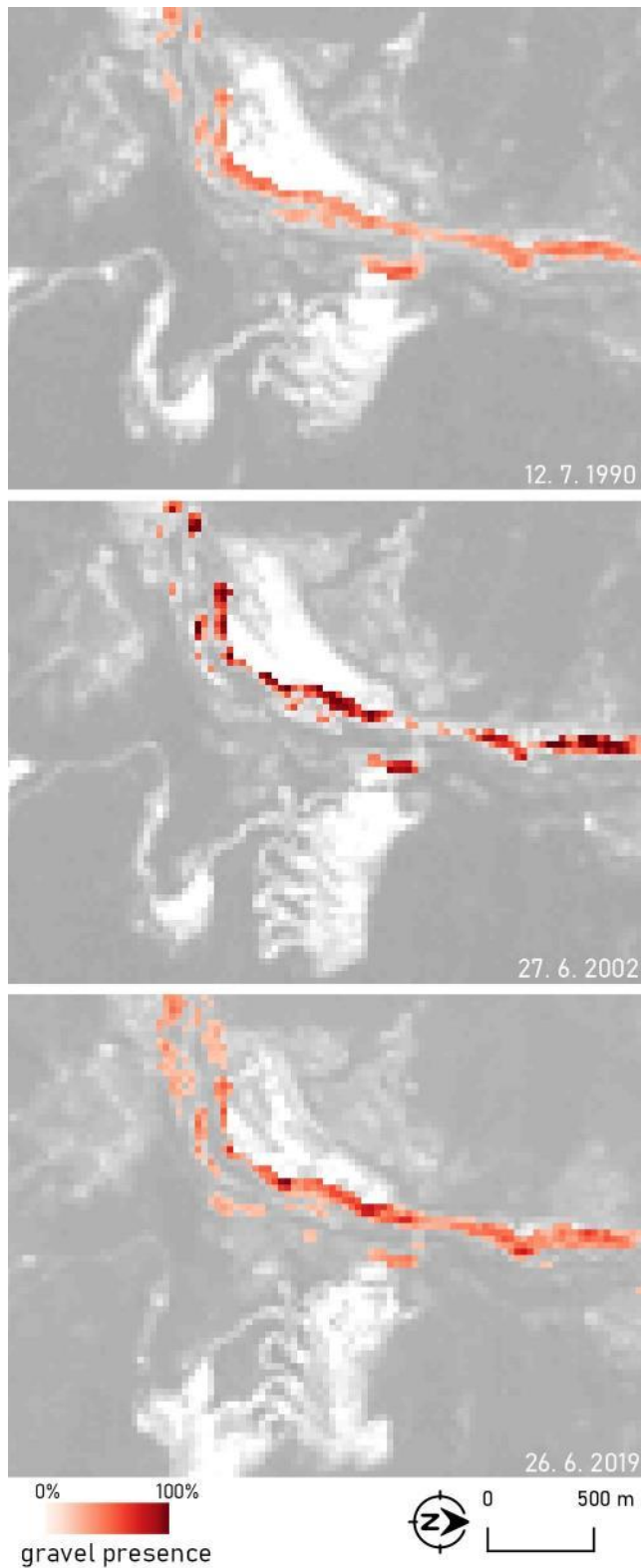
Figure A-8: Gravel presence on the Soča river on section 6 in three different timestamps based on Landsat images.

Slika A-8: Prisotnost proda na Soči na sekciji številka 6 v treh različnih časovnih obdobjih na podlagi posnetkov Landsat.
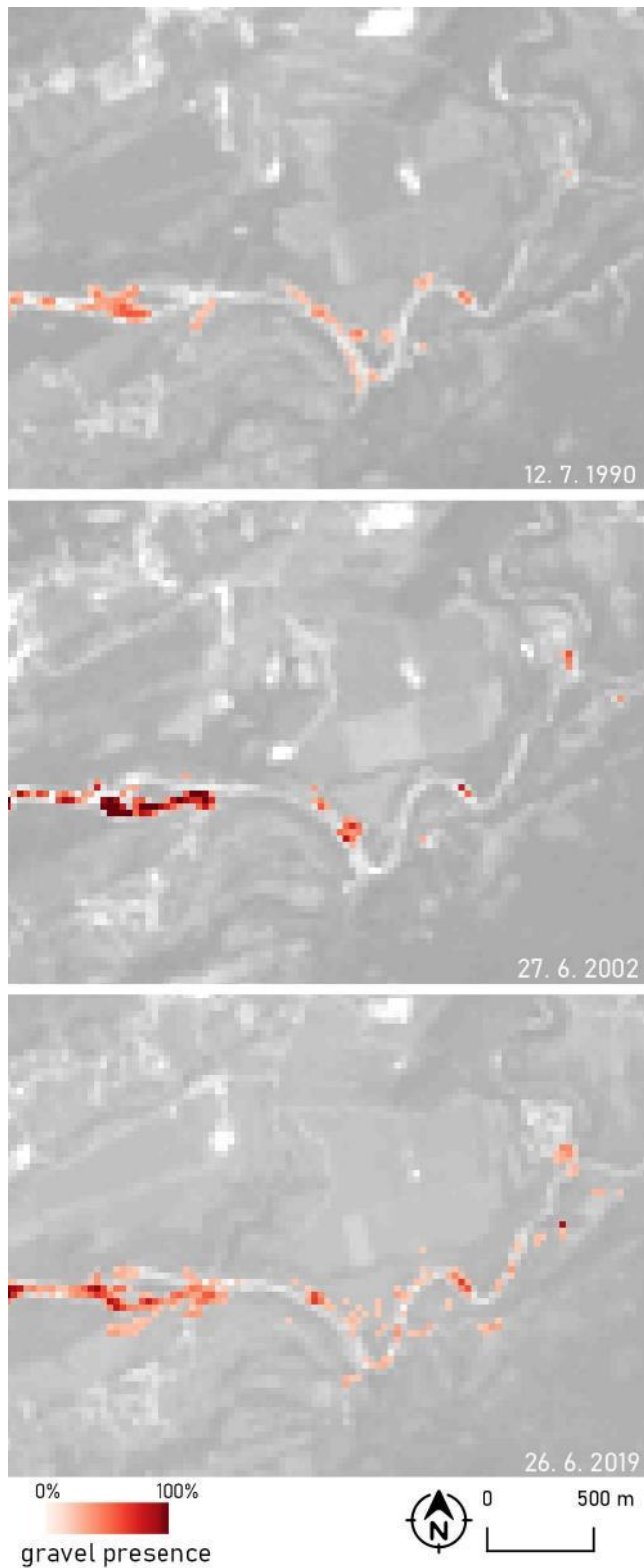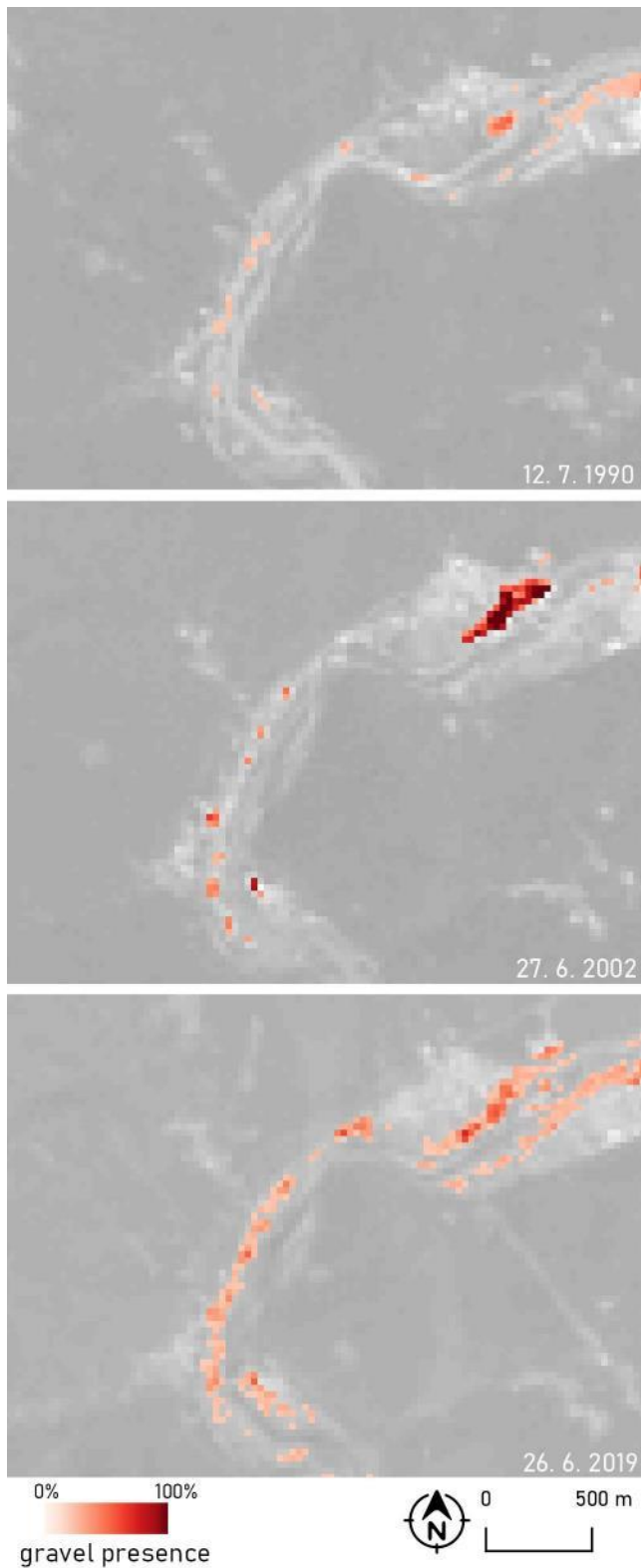
Figure A-9: Gravel presence on the Soča river on section 7 in three different timestamps based on Landsat images.

Slika A-9: Prisotnost proda na Soči na sekciji številka 7 v treh različnih časovnih obdobjih na podlagi posnetkov Landsat.
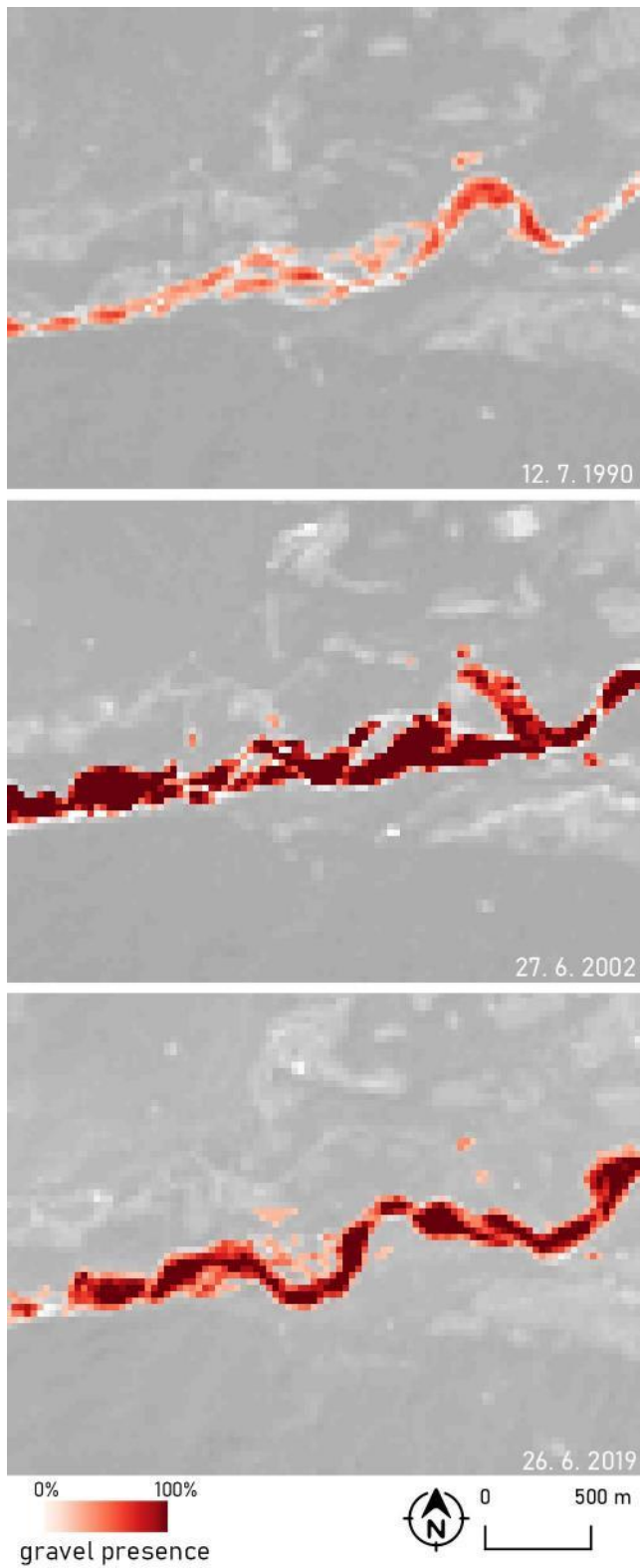
Figure A-10: Gravel presence on the Soča river on section 8 in three different timestamps based on Landsat images.

Slika A-10: Prisotnost proda na Soči na sekciji številka 8 v treh različnih časovnih obdobjih na podlagi posnetkov Landsat.

Stančič, L. 2022. Monitoring Changes of Fluvial Gravel Bars with Remote Sensing.

PhD Th. Ljubljana, UL FGG, Interdisciplinary doctoral study programme Environmental Protection.

A-11
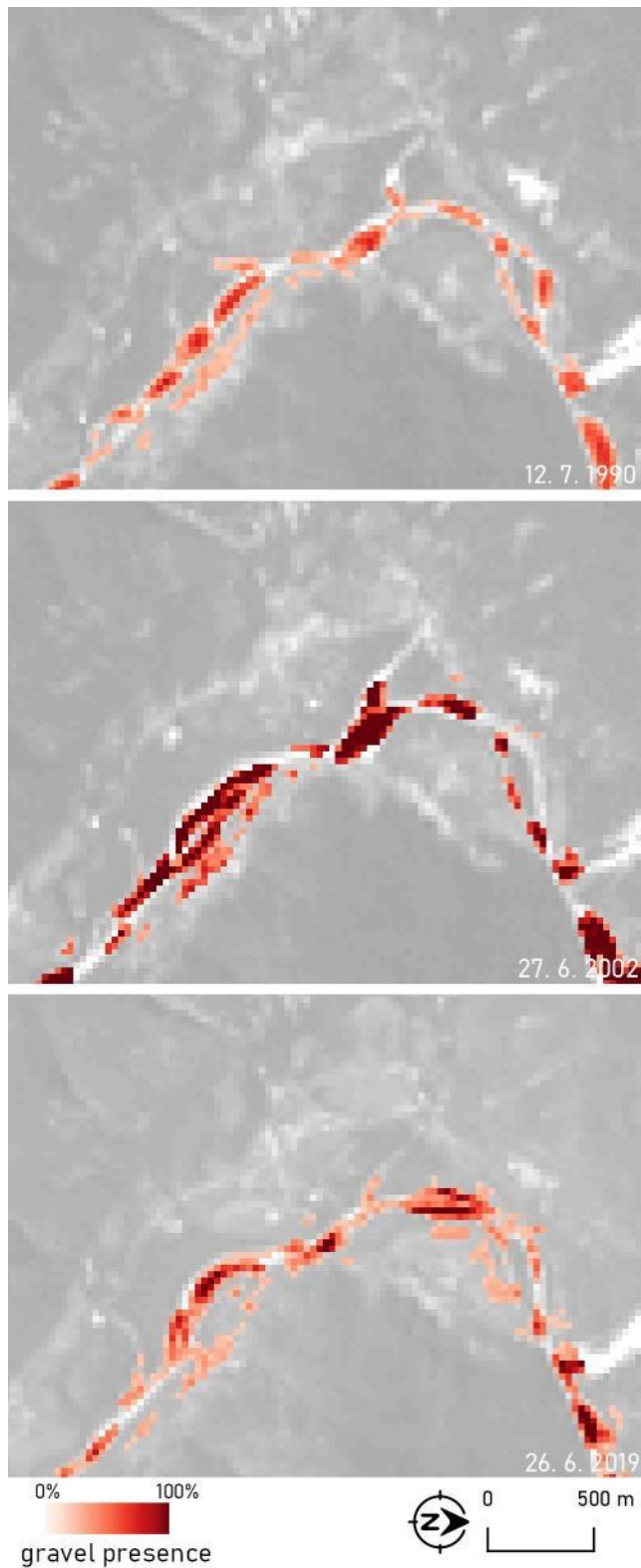
Figure A-11: Gravel presence on the Soča river on section 9 in three different timestamps based on Landsat images.

Slika A-11: Prisotnost proda na Soči na sekciji številka 9 v treh različnih časovnih obdobjih na podlagi posnetkov Landsat.
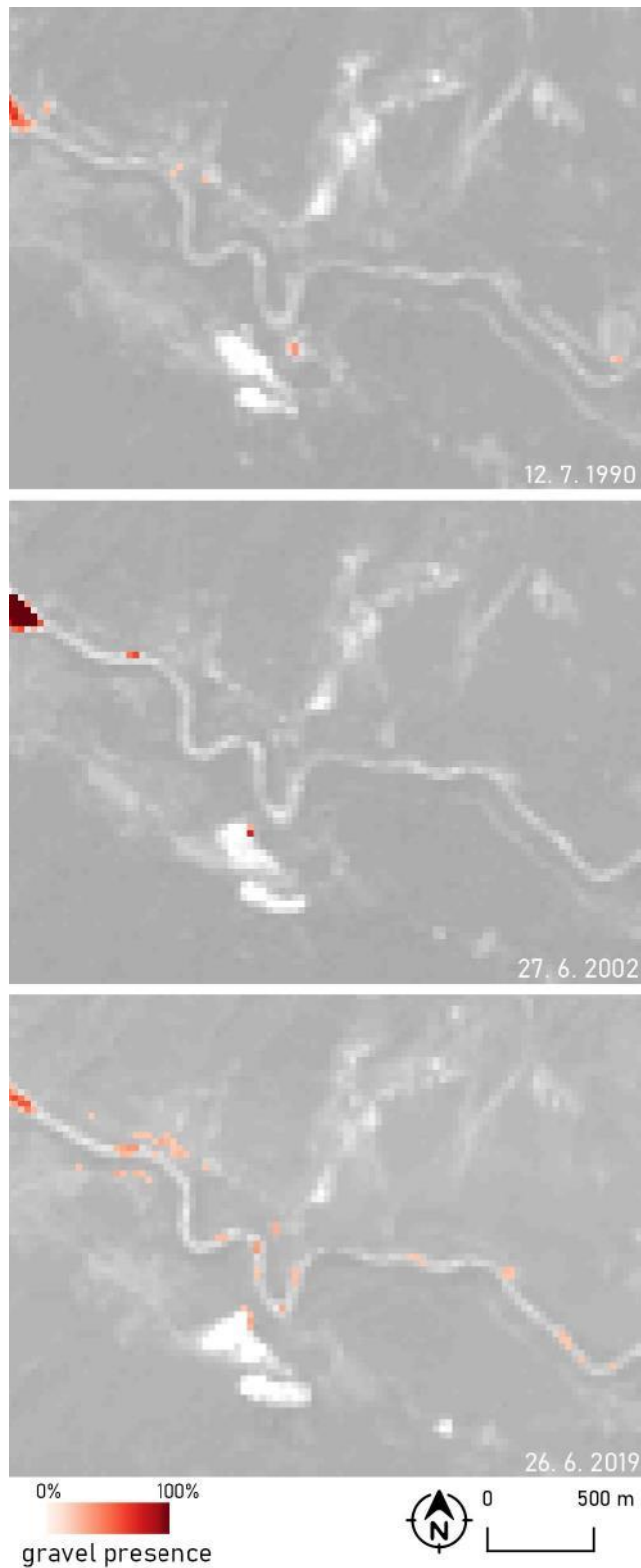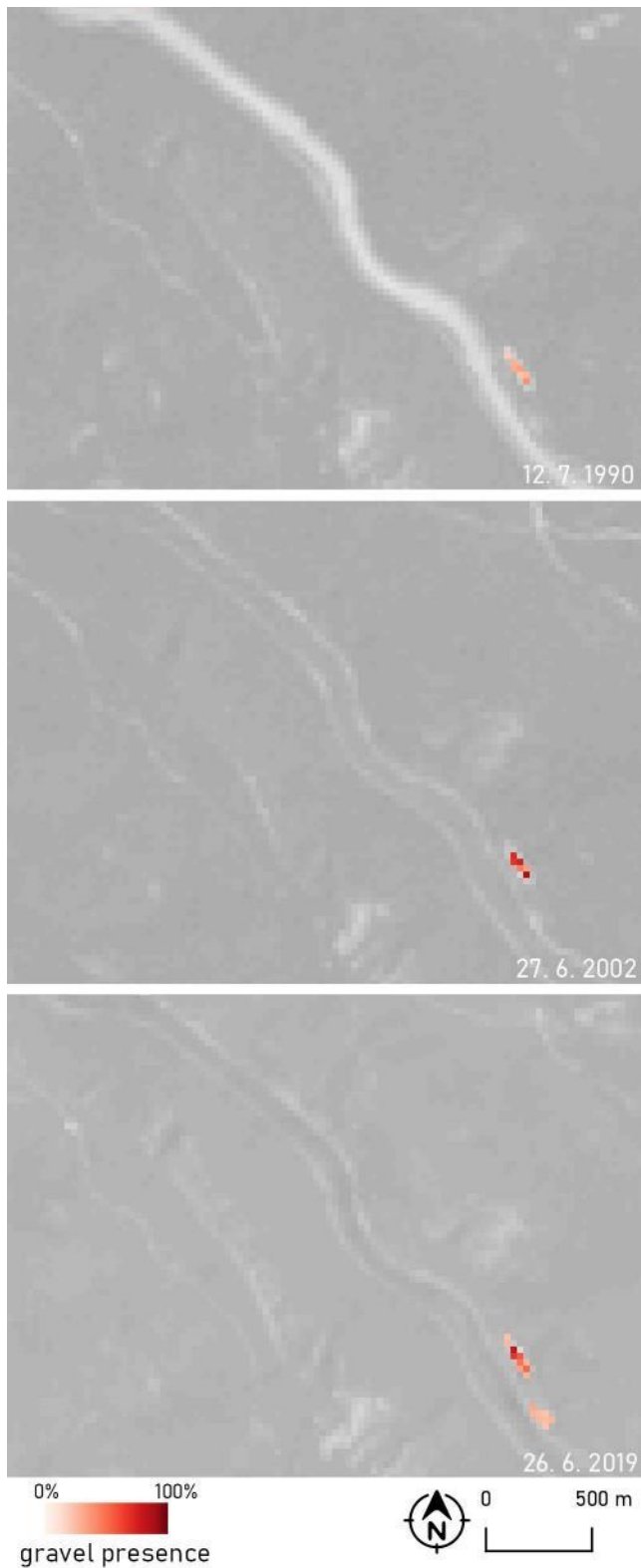
Figure A-12: Gravel presence on the Soča river on section 10 in three different timestamps based on Landsat images.

Slika A-12: Prisotnost proda na Soči na sekciji številka 10 v treh različnih časovnih obdobjih na podlagi posnetkov Landsat.
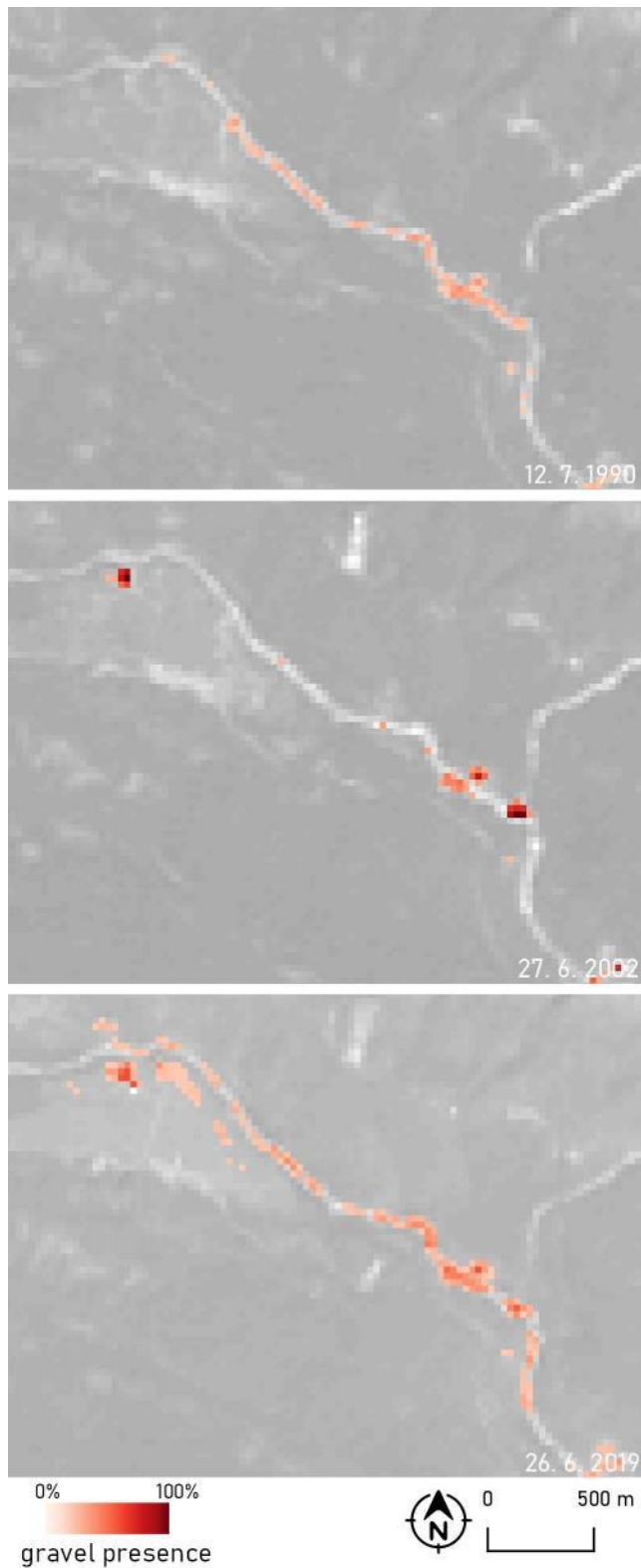
Figure A-13: Gravel presence on the Soča river on section 11 in three different timestamps based on Landsat images.

Slika A-13: Prisotnost proda na Soči na sekciji številka 11 v treh različnih časovnih obdobjih na podlagi posnetkov Landsat.
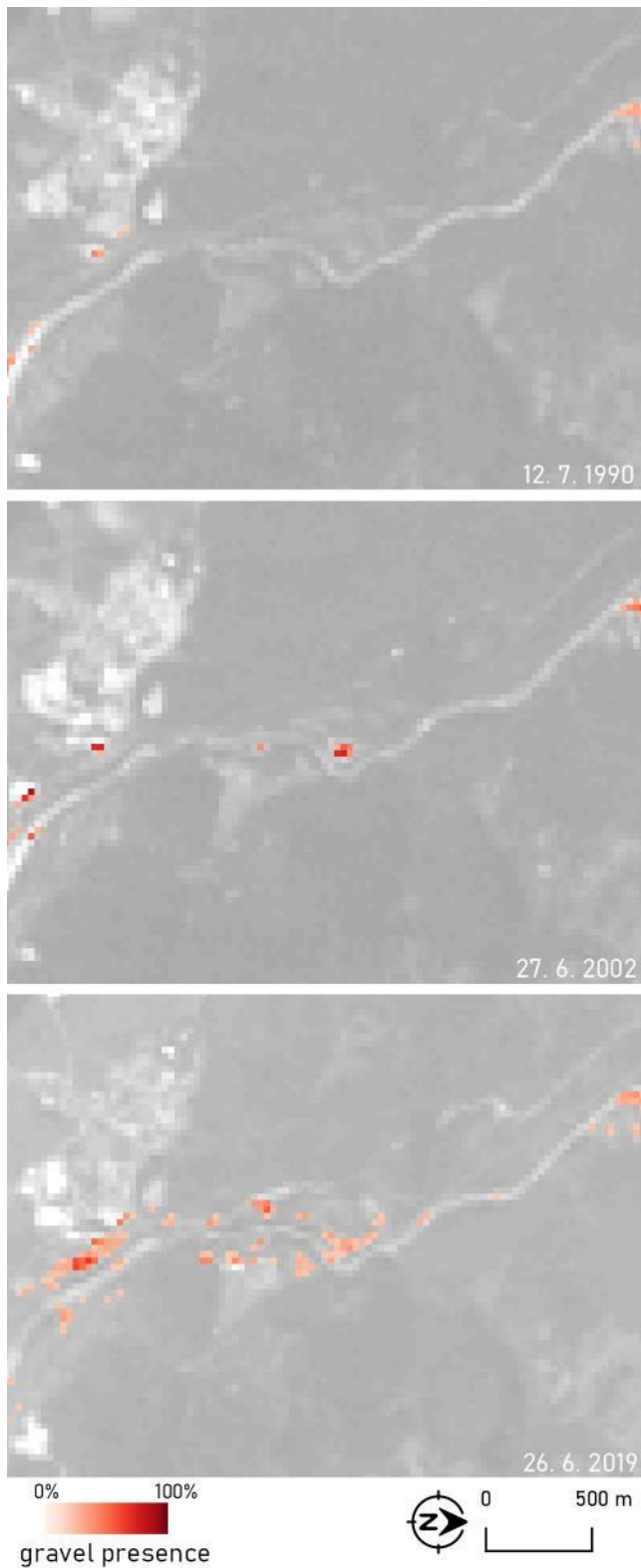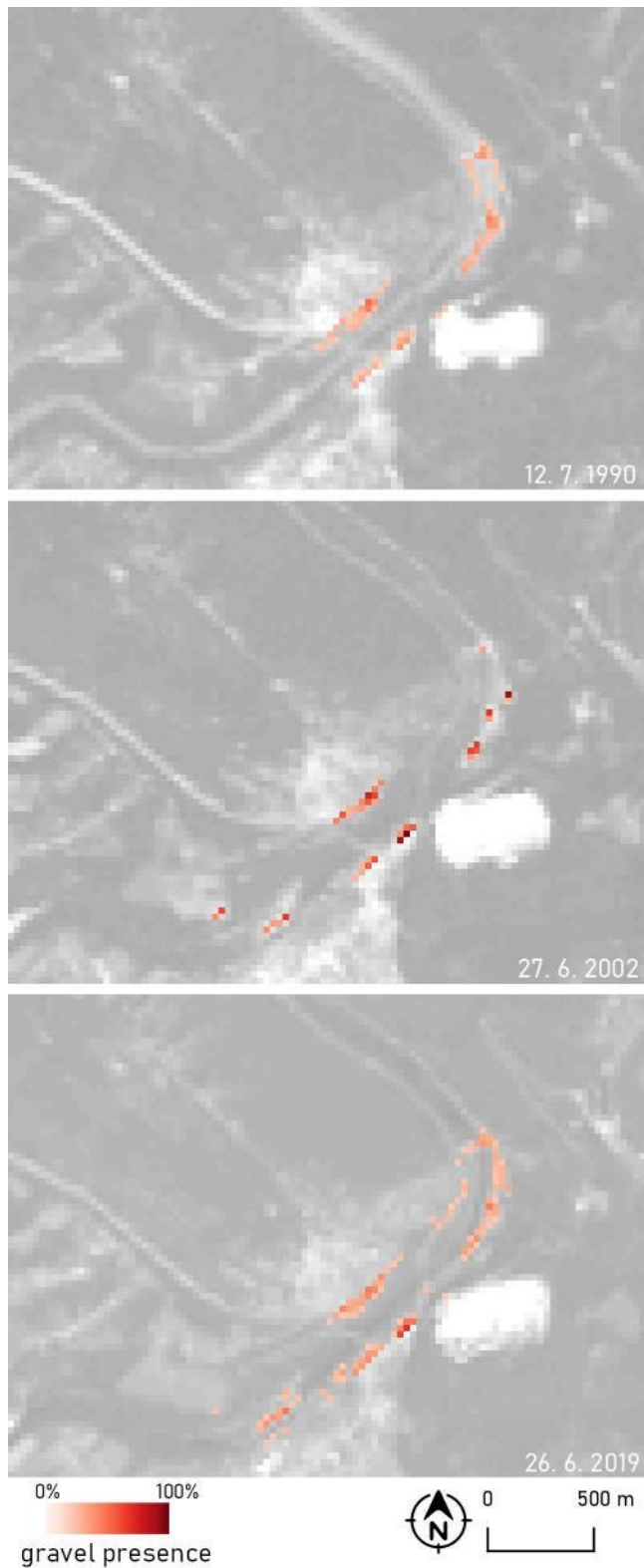
Figure A-14: Gravel presence on the Soča river on section 12 in three different timestamps based on Landsat images.

Slika A-14: Prisotnost proda na Soči na sekciji številka 12 v treh različnih časovnih obdobjih na podlagi posnetkov Landsat.
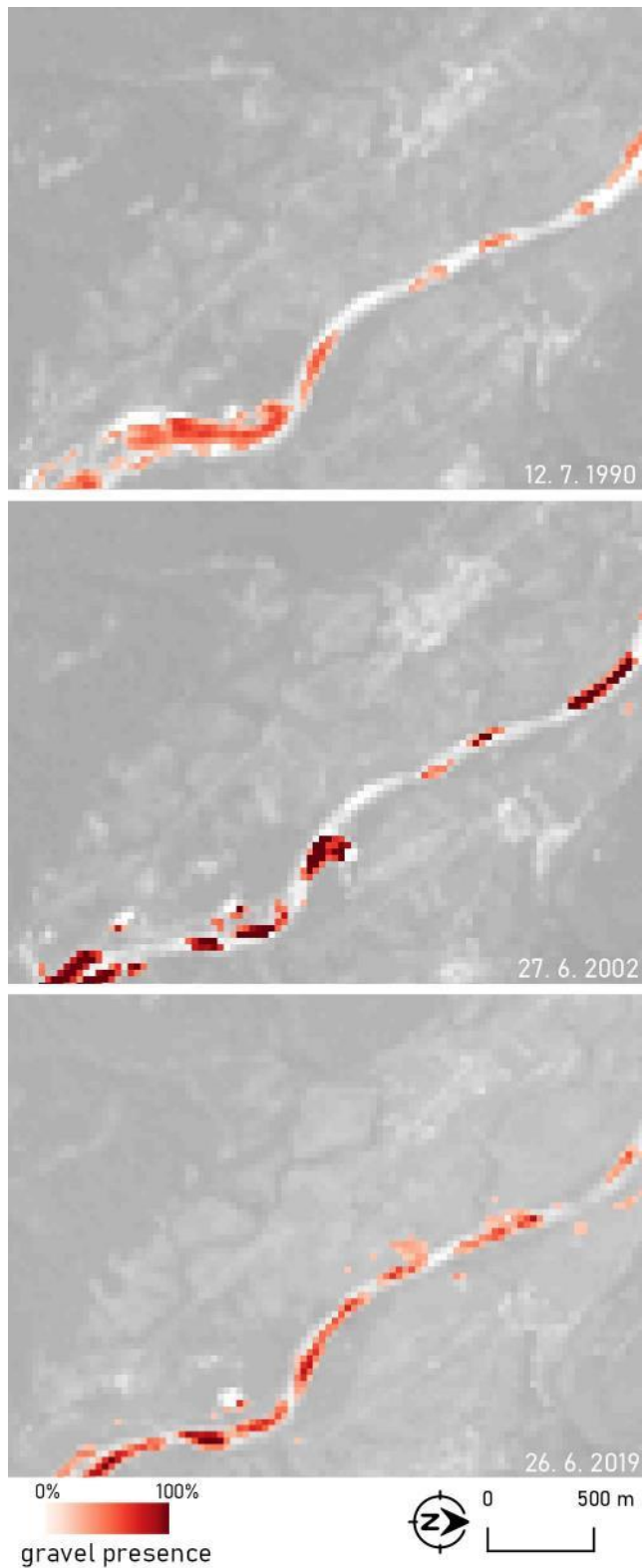
Figure A-15: Gravel presence on the Soča river on section 13 in three different timestamps based on Landsat images.

Slika A-15: Prisotnost proda na Soči na sekciji številka 13 v treh različnih časovnih obdobjih na podlagi posnetkov Landsat.
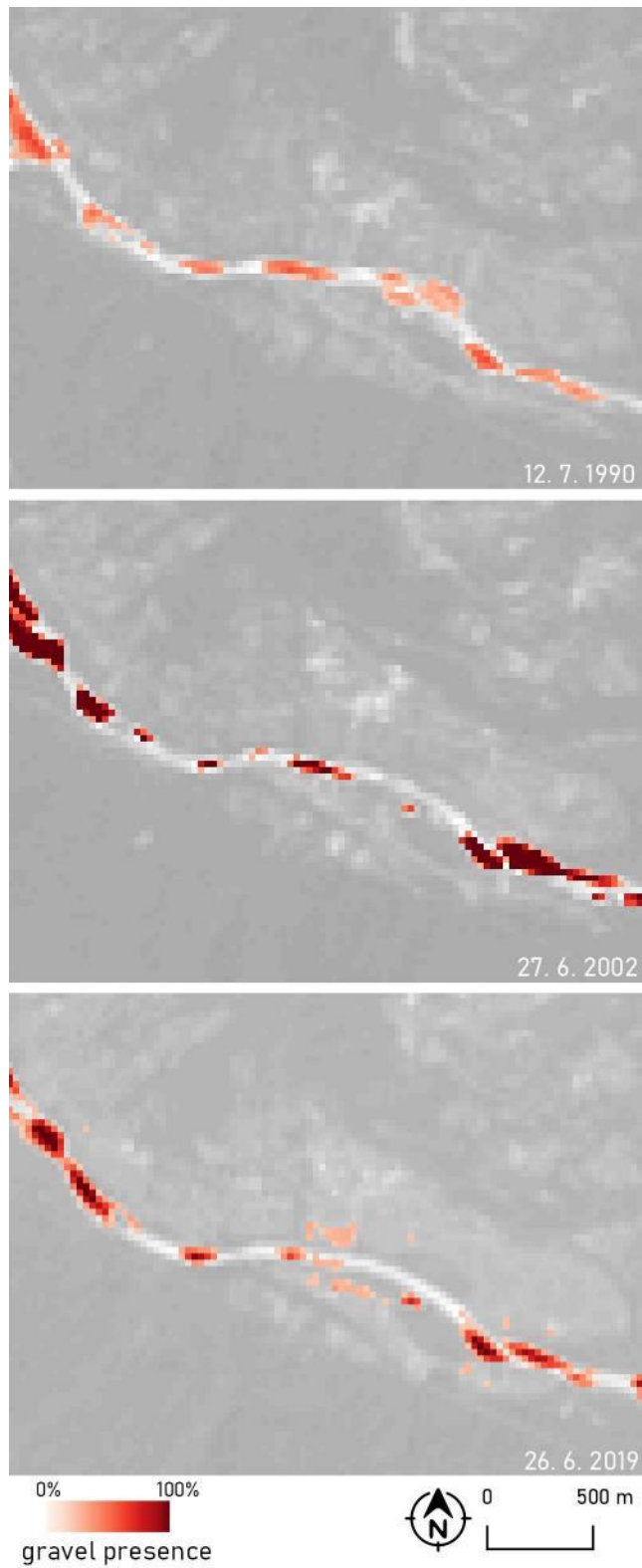
Figure A-16: Gravel presence on the Soča river on section 14 in three different timestamps based on Landsat images.

Slika A-16: Prisotnost proda na Soči na sekciji številka 14 v treh različnih časovnih obdobjih na podlagi posnetkov Landsat.

Stančič, L. 2022. Monitoring Changes of Fluvial Gravel Bars with Remote Sensing.
PhD Th. Ljubljana, UL FGG, Interdisciplinary doctoral study programme Environmental Protection.

A-17
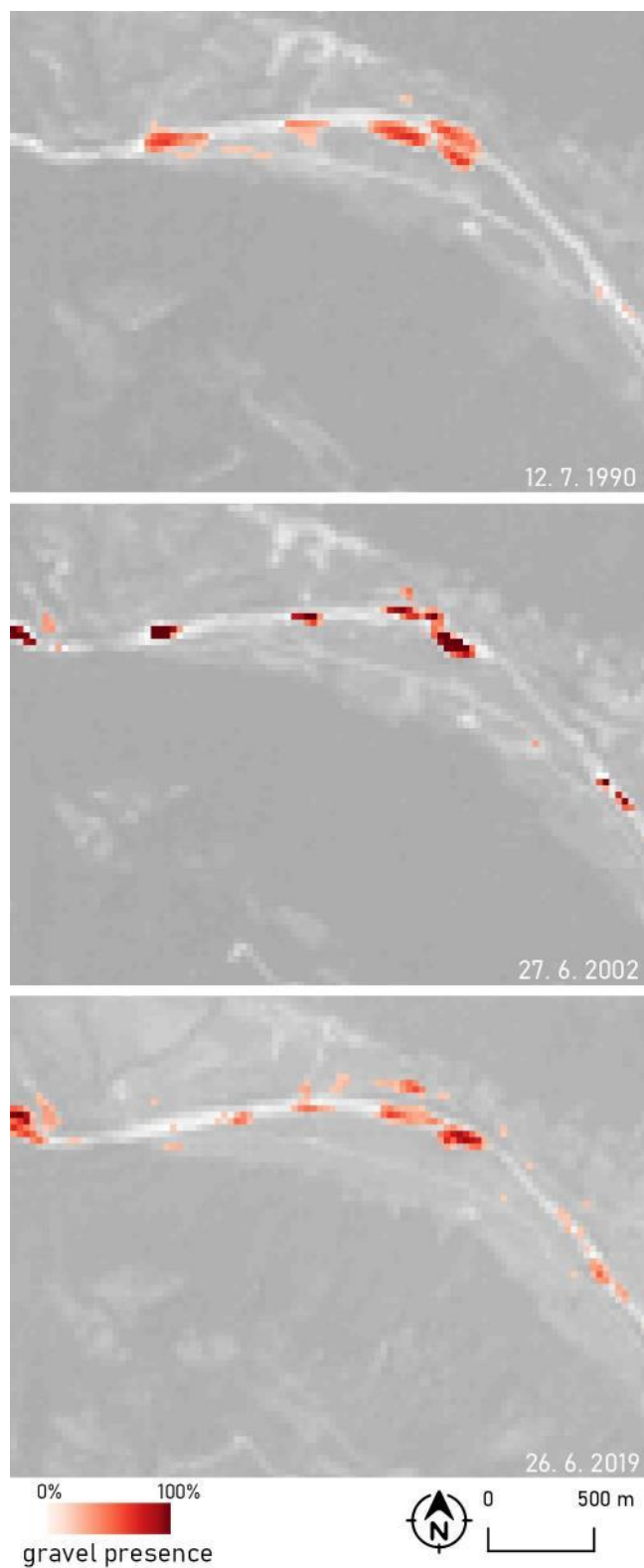
Figure A-17: Gravel presence on the Soča river on section 15 in three different timestamps based on Landsat images.

Slika A-17: Prisotnost proda na Soči na sekciji številka 15 v treh različnih časovnih obdobjih na podlagi posnetkov Landsat.
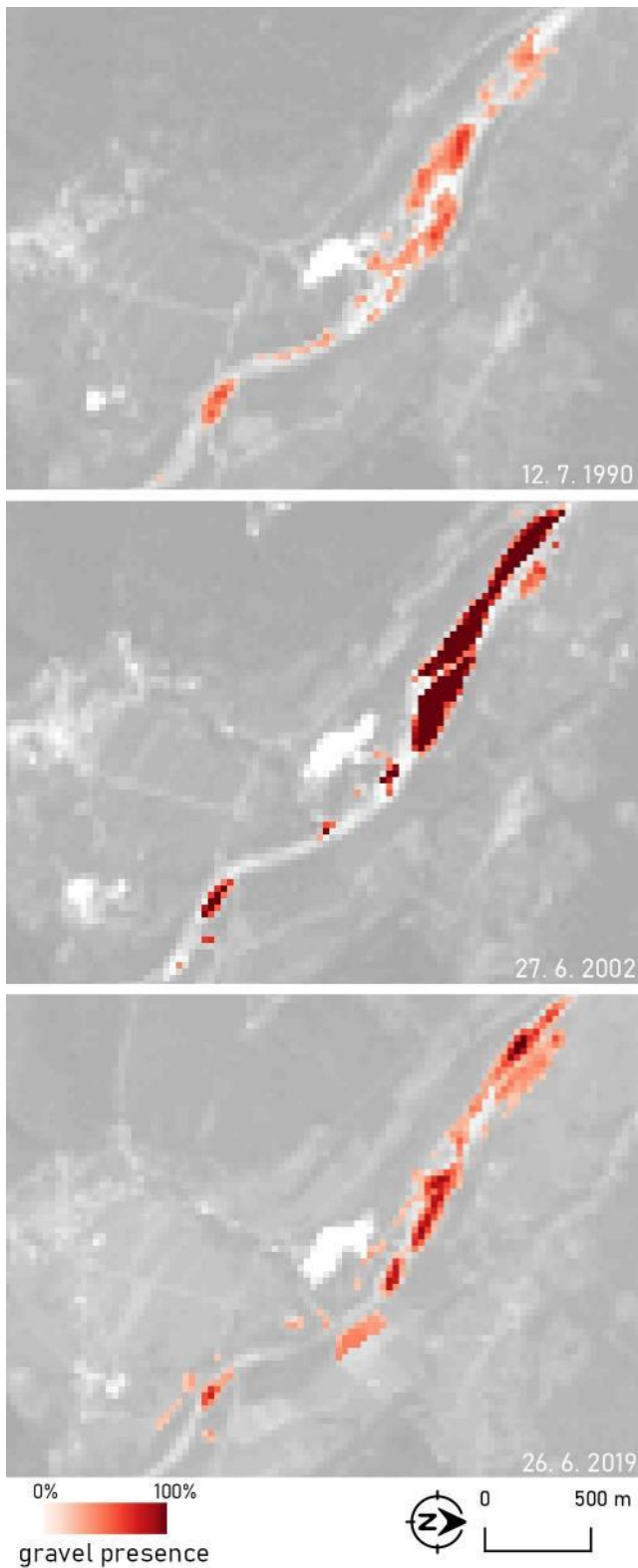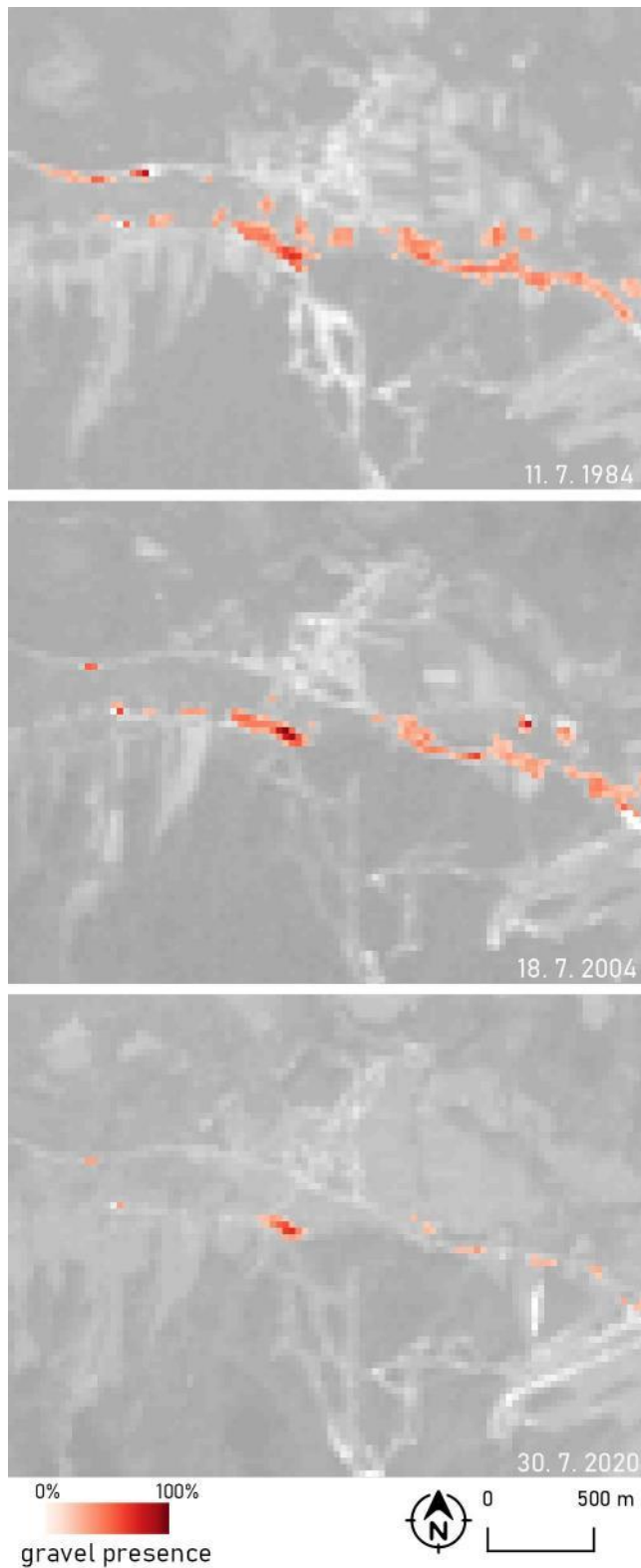
Figure A-18: Gravel presence on the Soča river on section 16 in three different timestamps based on Landsat images.

Slika A-18: Prisotnost proda na Soči na sekciji številka 16 v treh različnih časovnih obdobjih na podlagi posnetkov Landsat.
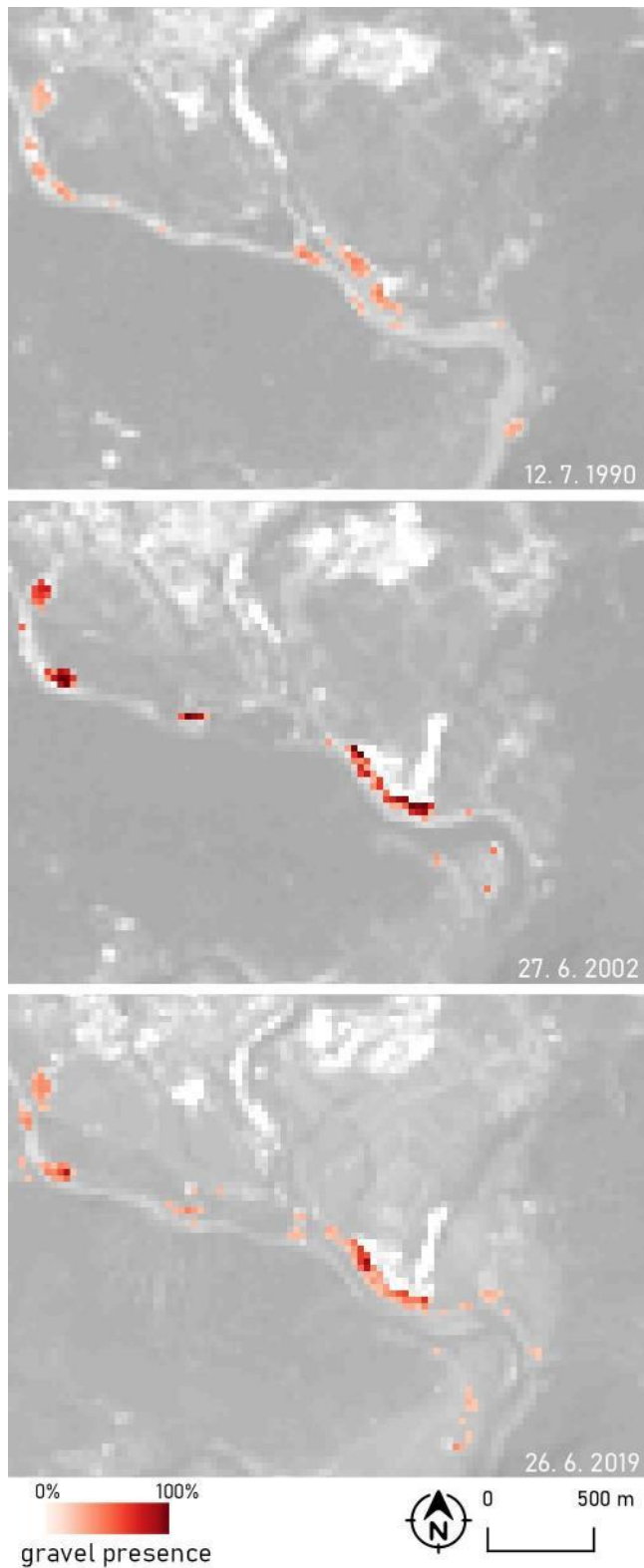
Figure A-19: Gravel presence on the Soča river on section 17 in three different timestamps based on Landsat images.

Slika A-19: Prisotnost proda na Soči na sekciji številka 17 v treh različnih časovnih obdobjih na podlagi posnetkov Landsat.
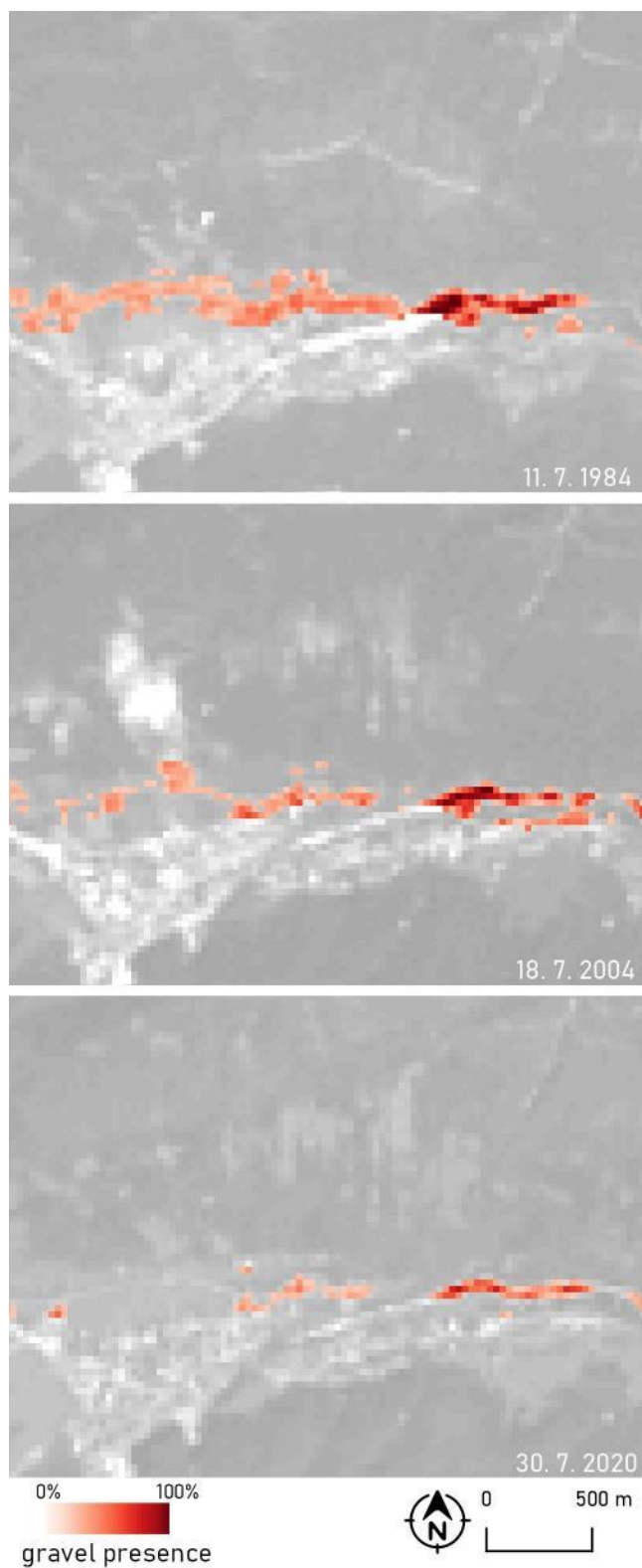
Figure A-20: Gravel presence on the Soča river on section 18 in three different timestamps based on Landsat images.

Slika A-20: Prisotnost proda na Soči na sekciji številka 18 v treh različnih časovnih obdobjih na podlagi posnetkov Landsat.

Stančič, L. 2022. Monitoring Changes of Fluvial Gravel Bars with Remote Sensing.

A-21

PhD Th. Ljubljana, UL FGG, Interdisciplinary doctoral study programme Environmental Protection.

Figure A-21: Gravel presence on the Soča river on section 19 in three different timestamps based on Landsat images.

Slika A-21: Prisotnost proda na Soči na sekciji številka 19 v treh različnih časovnih obdobjih na podlagi posnetkov Landsat.
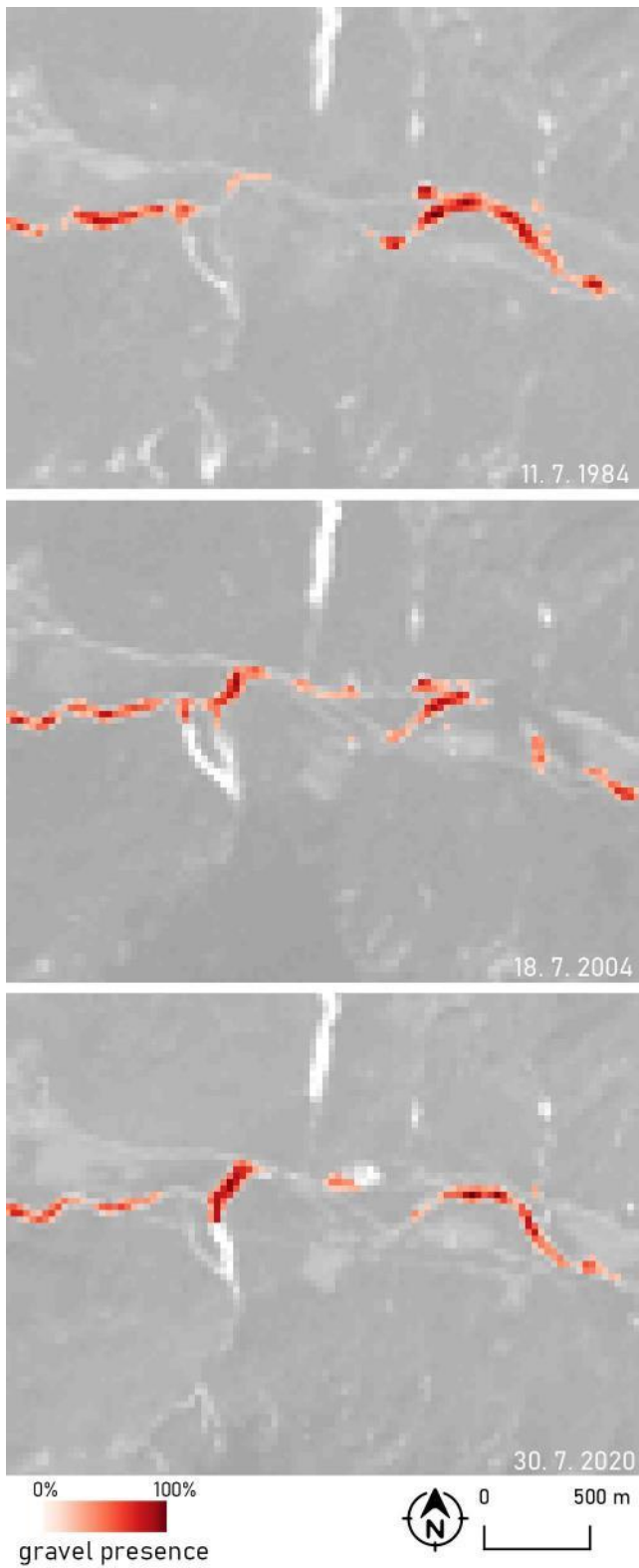
Figure A-22: Gravel presence on the Soča river on section 20 in three different timestamps based on Landsat images.

Slika A-22: Prisotnost proda na Soči na sekciji številka 20 v treh različnih časovnih obdobjih na podlagi posnetkov Landsat.
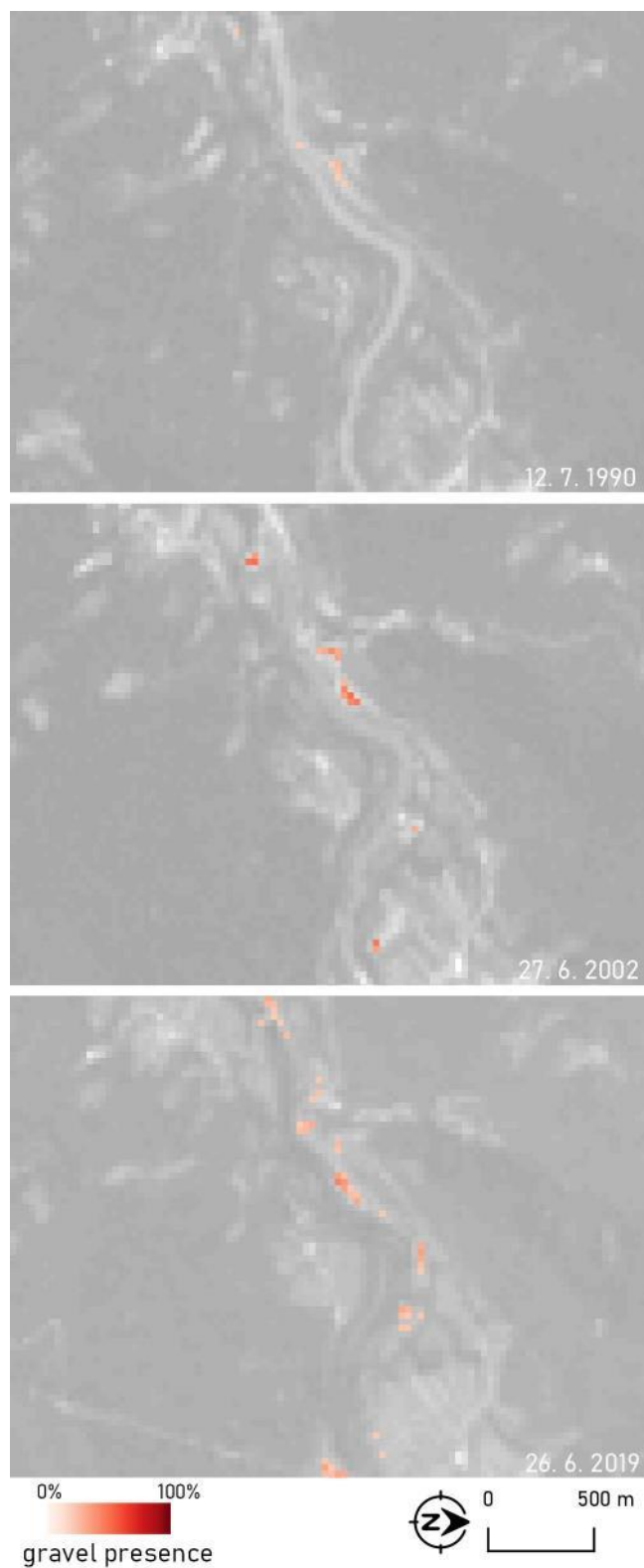
Figure A-23: Gravel presence on the Soča river on section 21 in three different timestamps based on Landsat images.

Slika A-23: Prisotnost proda na Soči na sekciji številka 21 v treh različnih časovnih obdobjih na podlagi posnetkov Landsat.
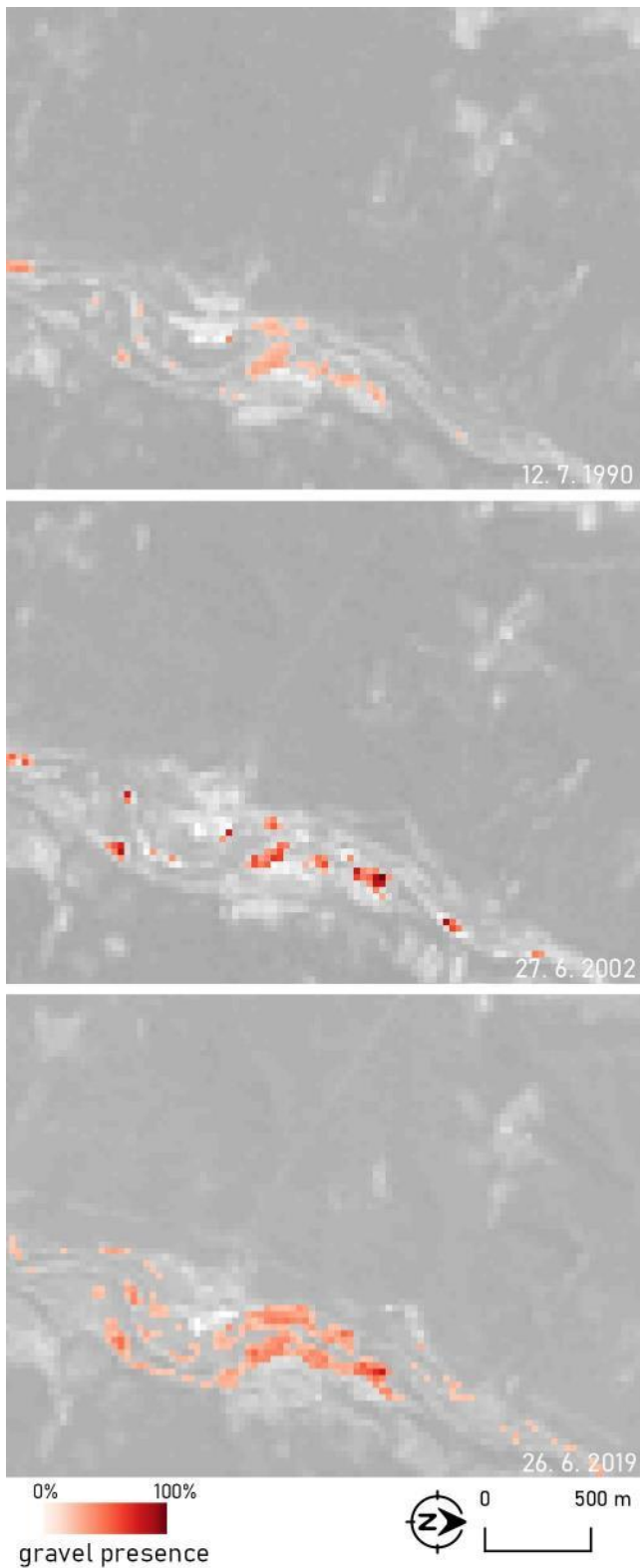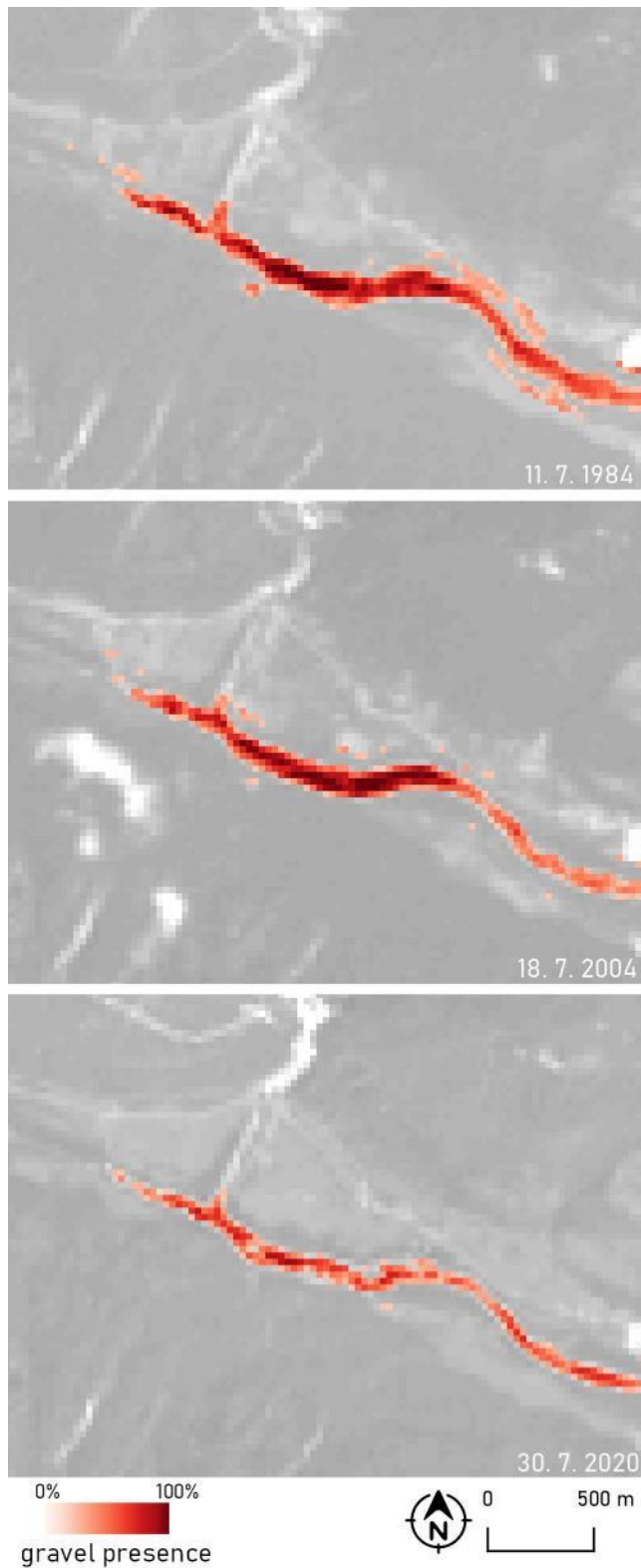
Figure A-24: Gravel presence on the Soča river on section 22 in three different timestamps based on Landsat images.

Slika A-24: Prisotnost proda na Soči na sekciji številka 22 v treh različnih časovnih obdobjih na podlagi posnetkov Landsat.
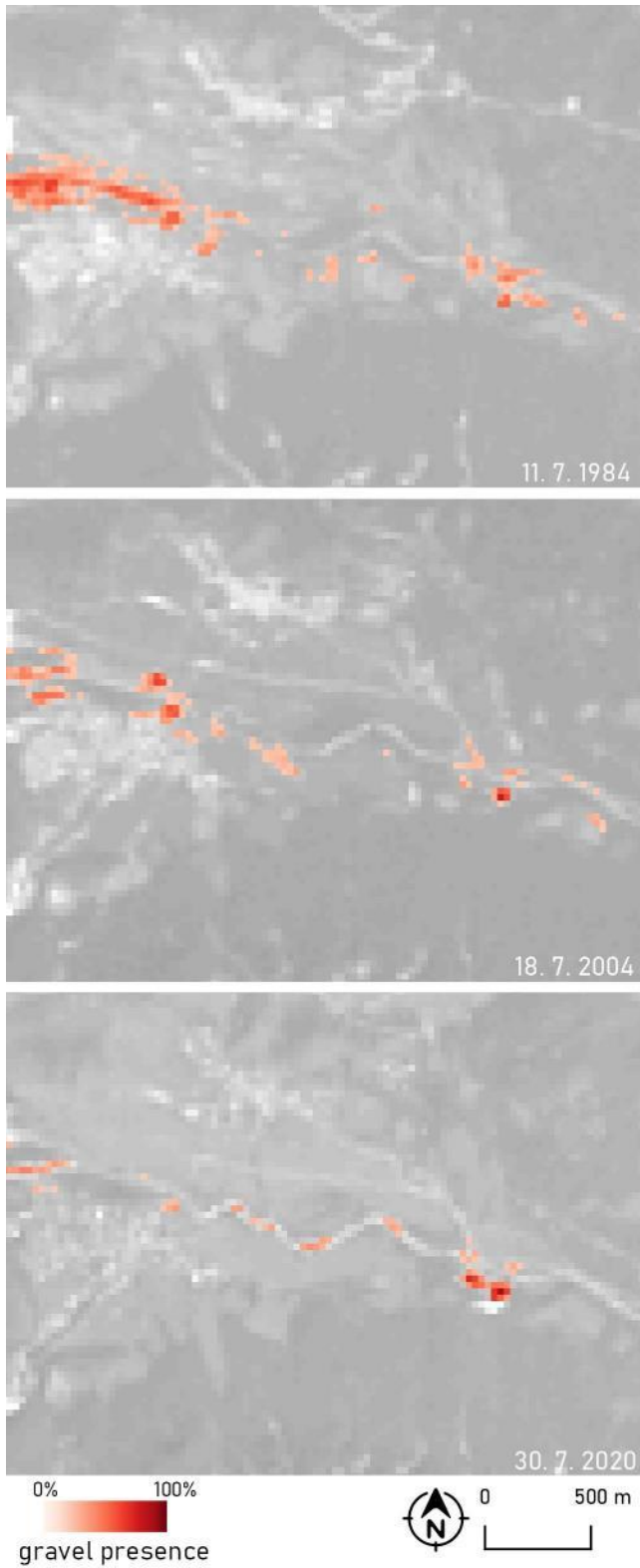
Figure A-25: Gravel presence on the Soča river on section 23 in three different timestamps based on Landsat images (basemap: Surveying and Mapping Authority of the Republic of Slovenia, 2021e).

Slika A-25: Prisotnost proda na Soči na sekciji številka 23 v treh različnih časovnih obdobjih na podlagi posnetkov Landsat (podlaga: GURS, 2021e).

Figure A-26: Gravel presence on the Soča river on section 24 in three different timestamps based on Landsat images.

Slika A-26: Prisotnost proda na Soči na sekciji številka 24 v treh različnih časovnih obdobjih na podlagi posnetkov Landsat.
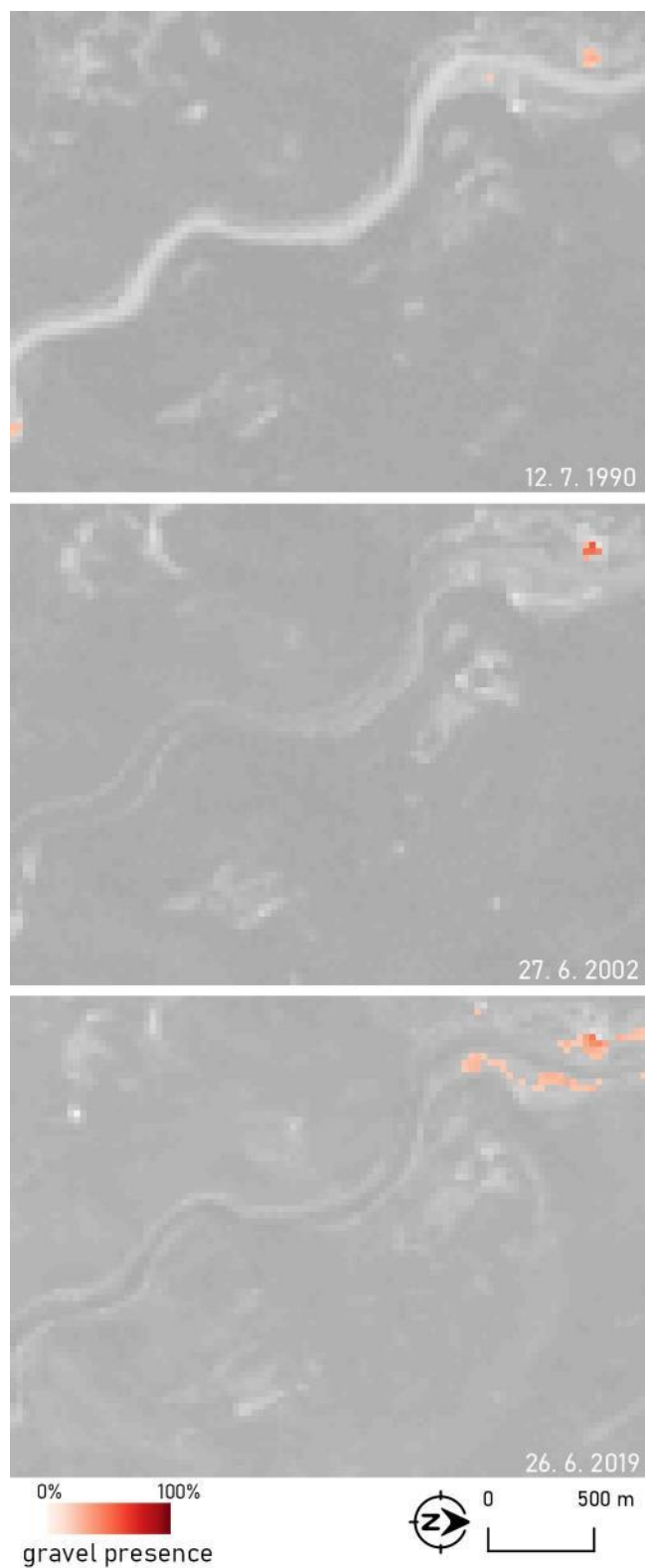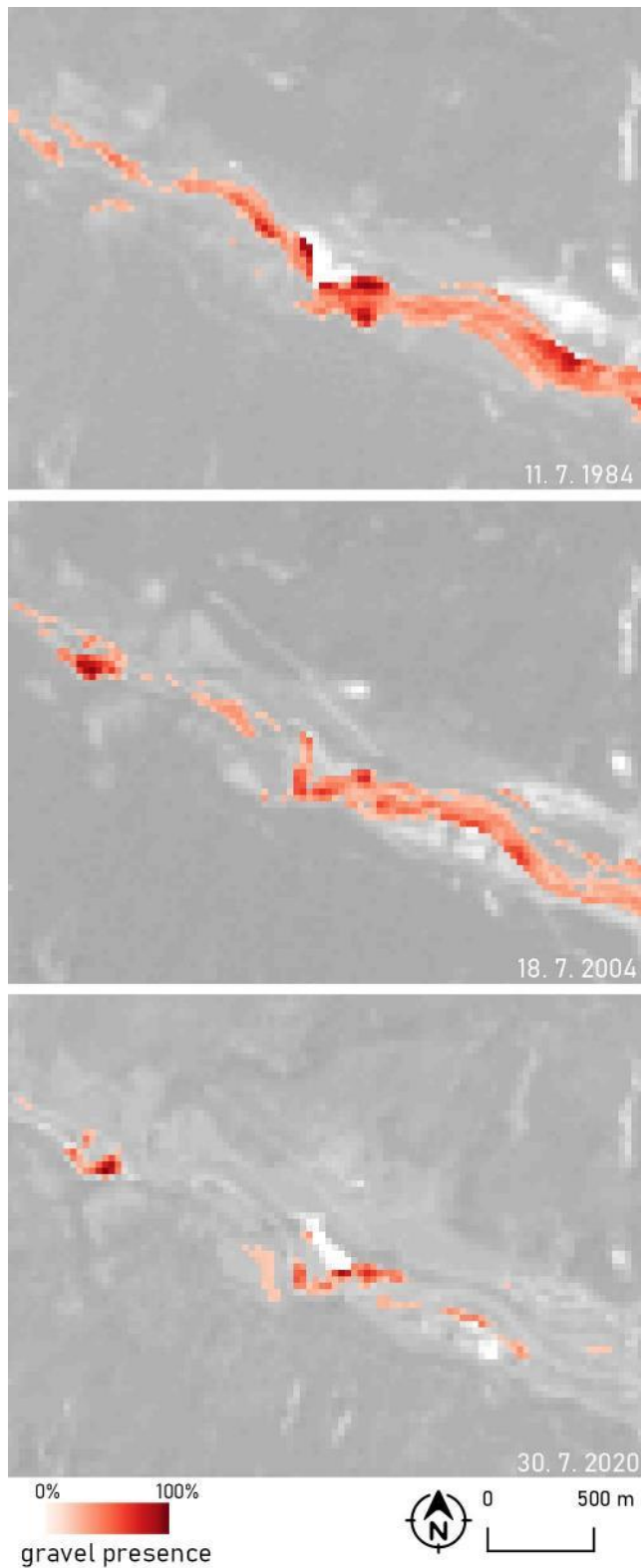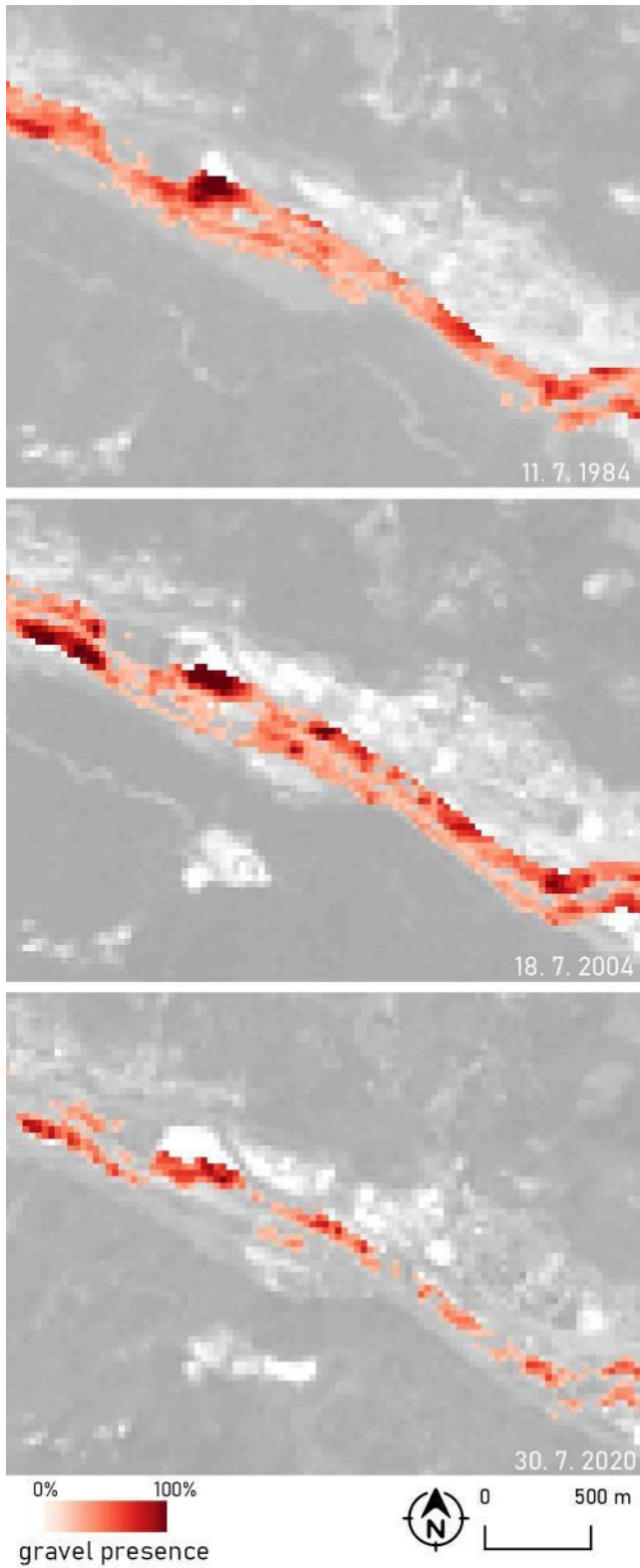
Figure A-27: Gravel presence on the Soča river on section 25 in three different timestamps based on Landsat images.

Slika A-27: Prisotnost proda na Soči na sekciji številka 25 v treh različnih časovnih obdobjih na podlagi posnetkov Landsat.

Figure A-28: Gravel presence on the Soča river on section 26 in three different timestamps based on Landsat images.

Slika A-28: Prisotnost proda na Soči na sekciji številka 26 v treh različnih časovnih obdobjih na podlagi posnetkov Landsat.
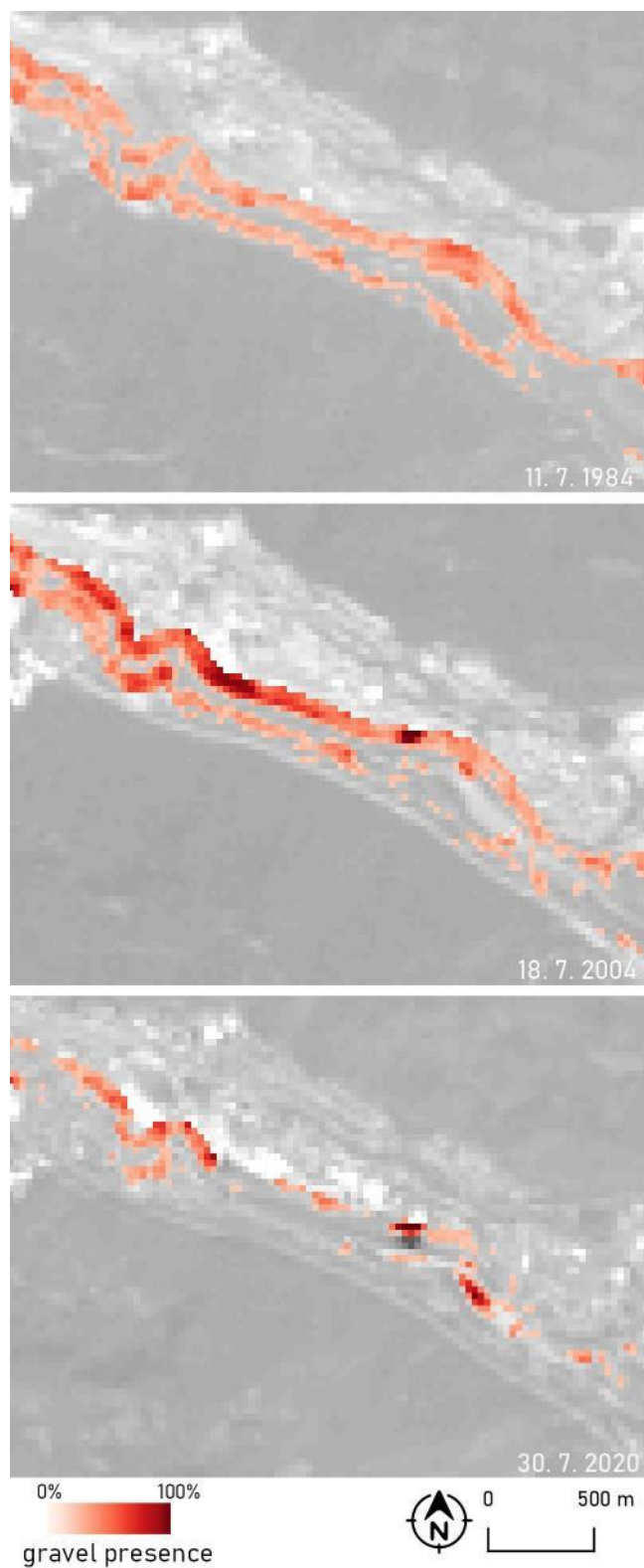
Figure A-29: Gravel presence on the Soča river on section 27 in three different timestamps based on Landsat images.

Slika A-29: Prisotnost proda na Soči na sekciji številka 27 v treh različnih časovnih obdobjih na podlagi posnetkov Landsat.

»This page is intentionally blank.«

Stančič, L. 2022. Monitoring Changes of Fluvial Gravel Bars with Remote Sensing.
PhD Th. Ljubljana, UL FGG, Interdisciplinary doctoral study programme Environmental Protection.

B-1

APPENDIX B : Gravel Fraction Maps of the Sava River
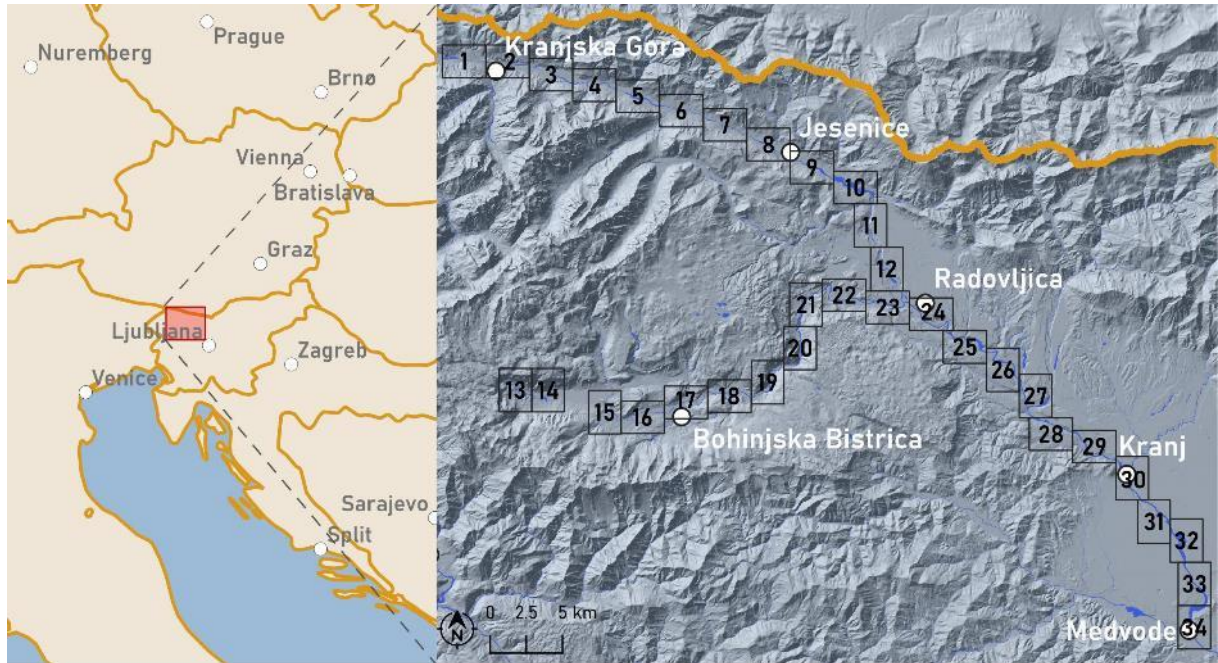
Figure B-1: Sections of the gravel presence maps on the upper Sava river between the spring and the Medvode settlement (data source: Natural Earth, 2020; Slovenian Water Agency, 2021b; Surveying and Mapping Authority of the Republic of Slovenia, 2016, 2021b).

Slika B-1: Sekcije kart prisotnosti proda na Zgornji Savi med izvirom in Medvodami (vir podatkov: Natural Earth, 2020; DRSV, 2021b; GURS, 2016, 2021b).
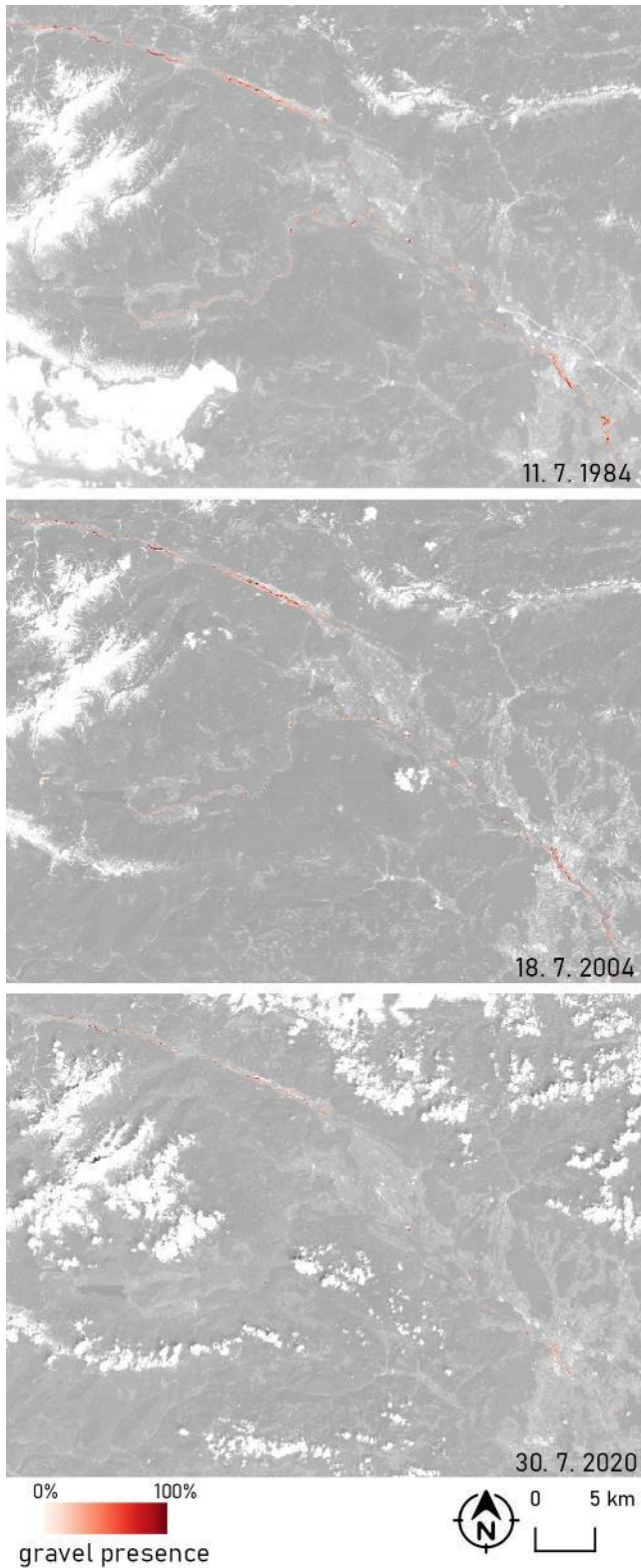
Figure B-2: Gravel presence on the upper Sava river between the spring and the Medvode settlement in three different timestamps based on Landsat images.

Slika B-2: Prisotnost proda na Zgornji Savi med izvirom in Medvodami v treh različnih časovnih obdobjih na podlagi posnetkov Landsat.
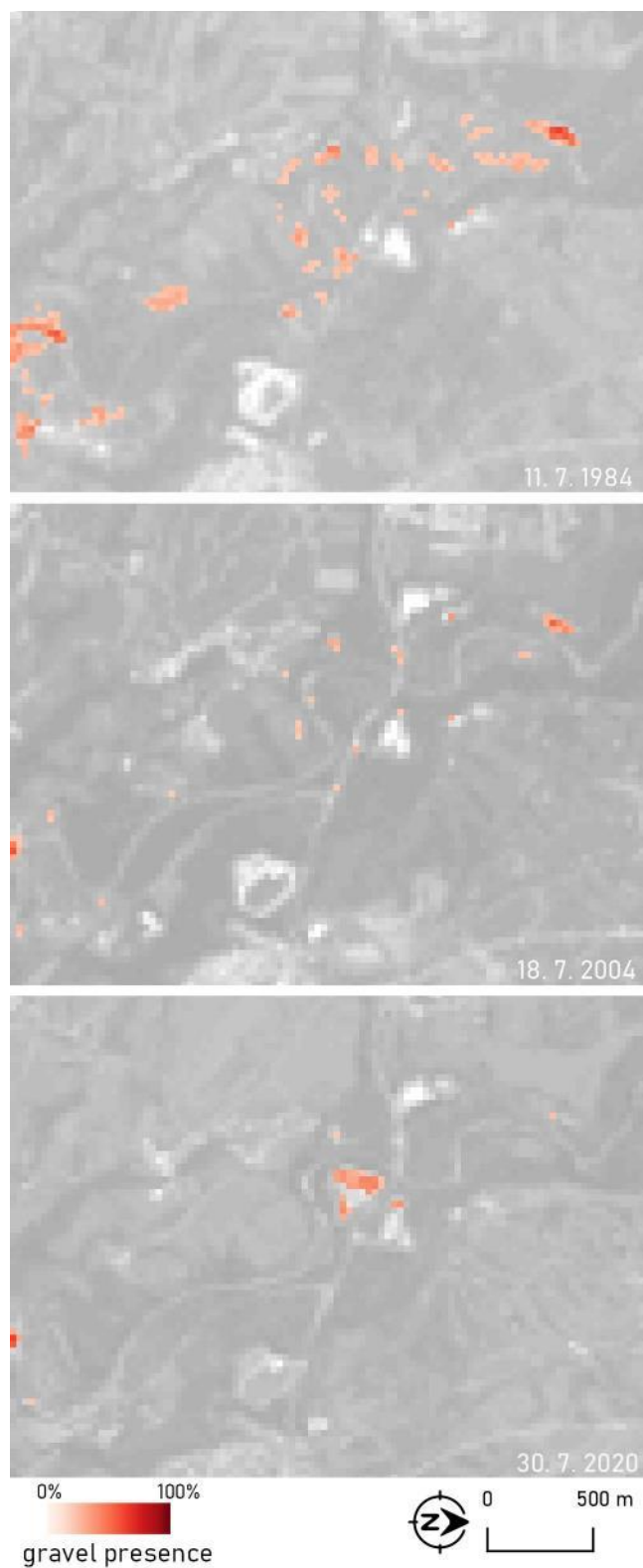
Figure B-3: Gravel presence on the Sava river on section 1 in three different timestamps based on Landsat images.

Slika B-3: Prisotnost proda na Savi na sekciji številka 1 v treh različnih časovnih obdobjih na podlagi posnetkov Landsat.
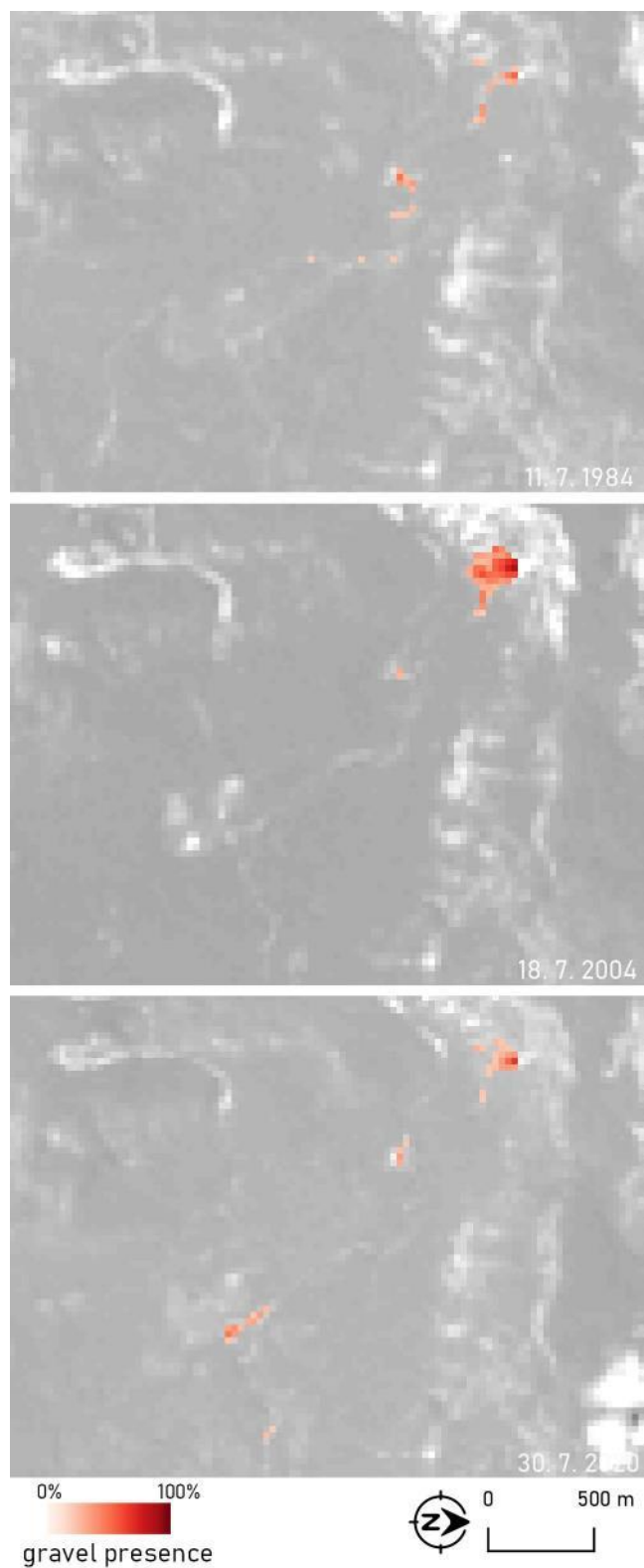
Figure B-4: Gravel presence on the Sava river on section 2 in three different timestamps based on Landsat images.

Slika B-4: Prisotnost proda na Savi na sekciji številka 2 v treh različnih časovnih obdobjih na podlagi posnetkov Landsat.
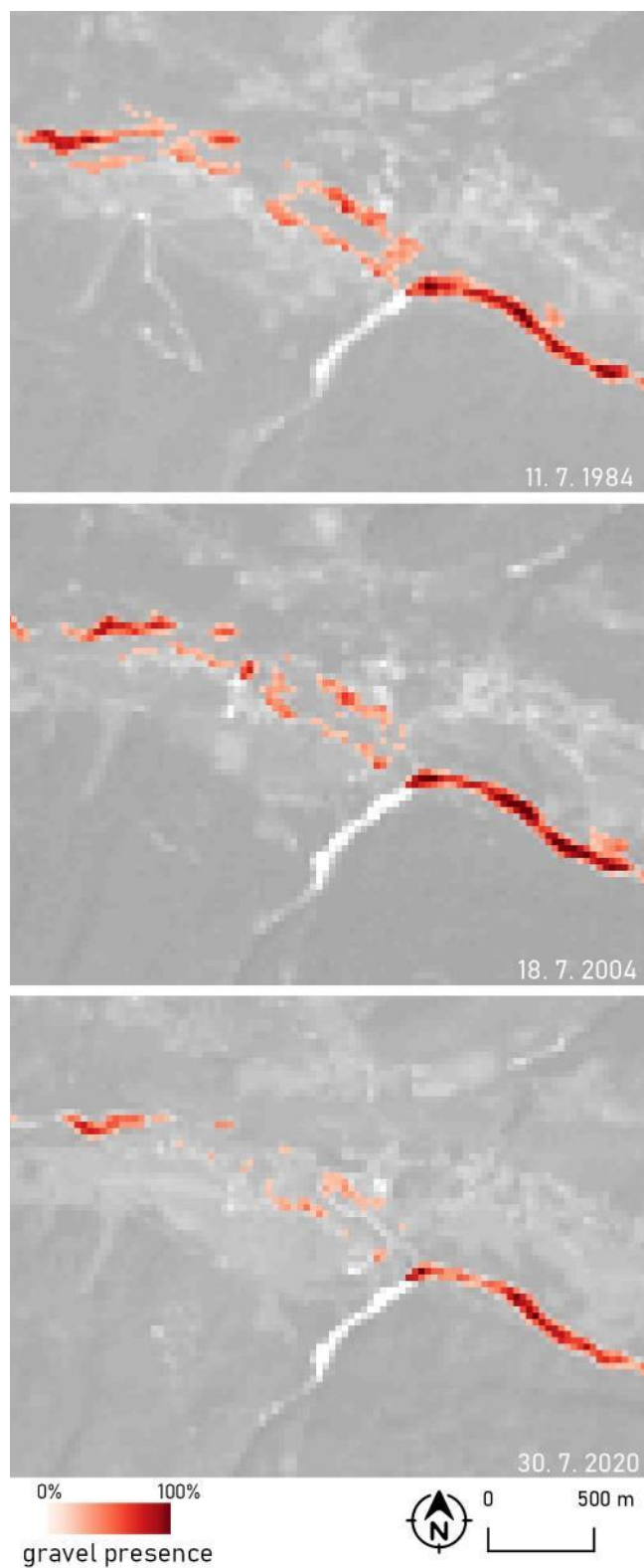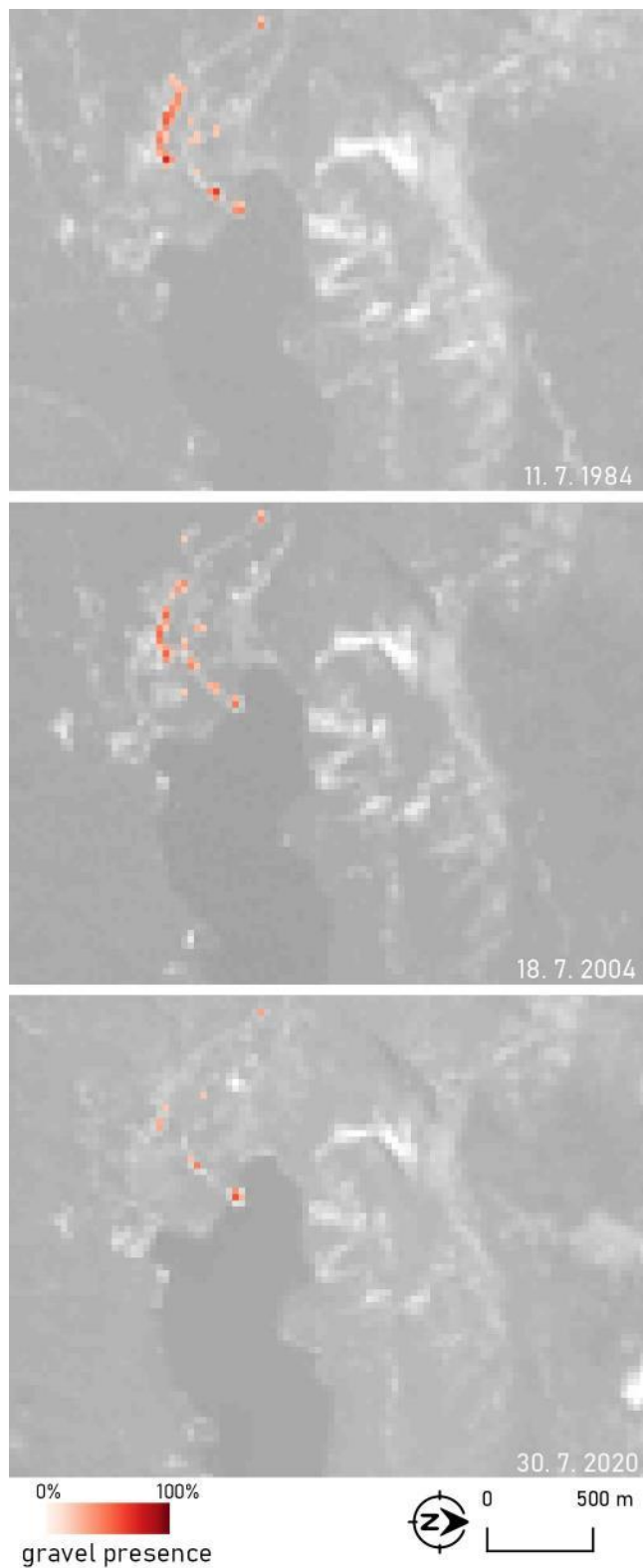
Figure B-5: Gravel presence on the Sava river on section 3 in three different timestamps based on Landsat images.

Slika B-5: Prisotnost proda na Savi na sekciji številka 3 v treh različnih časovnih obdobjih na podlagi posnetkov Landsat.
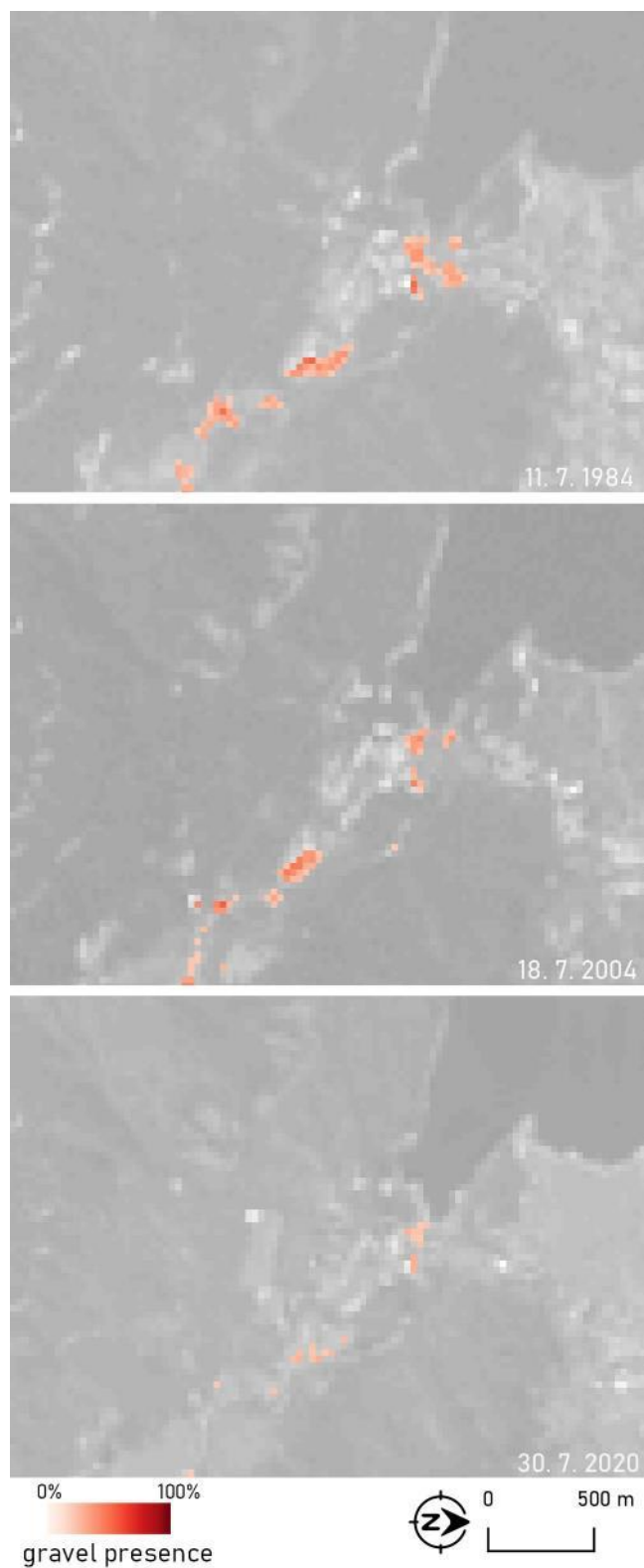
Figure B-6: Gravel presence on the Sava river on section 4 in three different timestamps based on Landsat images.

Slika B-6: Prisotnost proda na Savi na sekciji številka 4 v treh različnih časovnih obdobjih na podlagi posnetkov Landsat.

Figure B-7: Gravel presence on the Sava river on section 5 in three different timestamps based on Landsat images.

Slika B-7: Prisotnost proda na Savi na sekciji številka 5 v treh različnih časovnih obdobjih na podlagi posnetkov Landsat.

B-8   Stančič, L. 2022. Monitoring Changes of Fluvial Gravel Bars with Remote Sensing.

PhD Th. Ljubljana, UL FGG, Interdisciplinary doctoral study programme Environmental Protection.

Figure B-8: Gravel presence on the Sava river on section 6 in three different timestamps based on Landsat images.

Slika B-8: Prisotnost proda na Savi na sekciji številka 6 v treh različnih časovnih obdobjih na podlagi posnetkov Landsat.
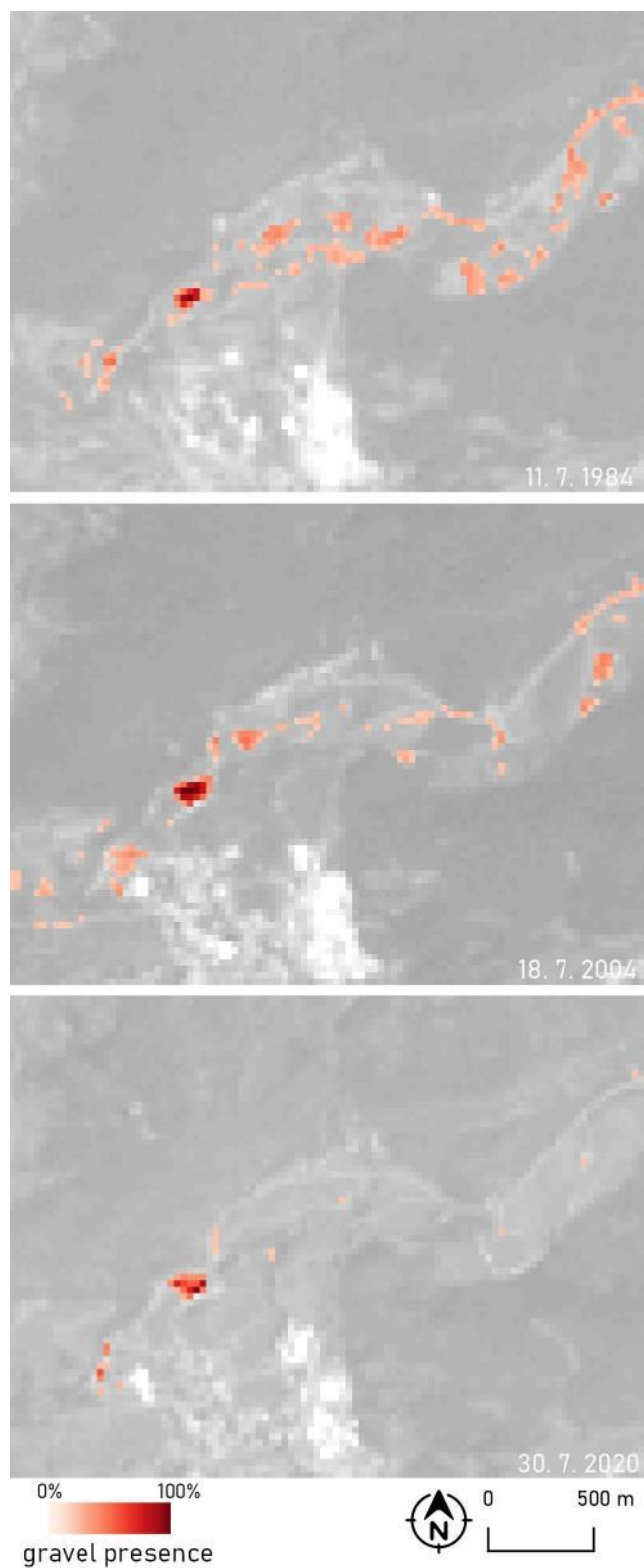
Figure B-9: Gravel presence on the Sava river on section 7 in three different timestamps based on Landsat images.

Slika B-9: Prisotnost proda na Savi na sekciji številka 7 v treh različnih časovnih obdobjih na podlagi posnetkov Landsat.
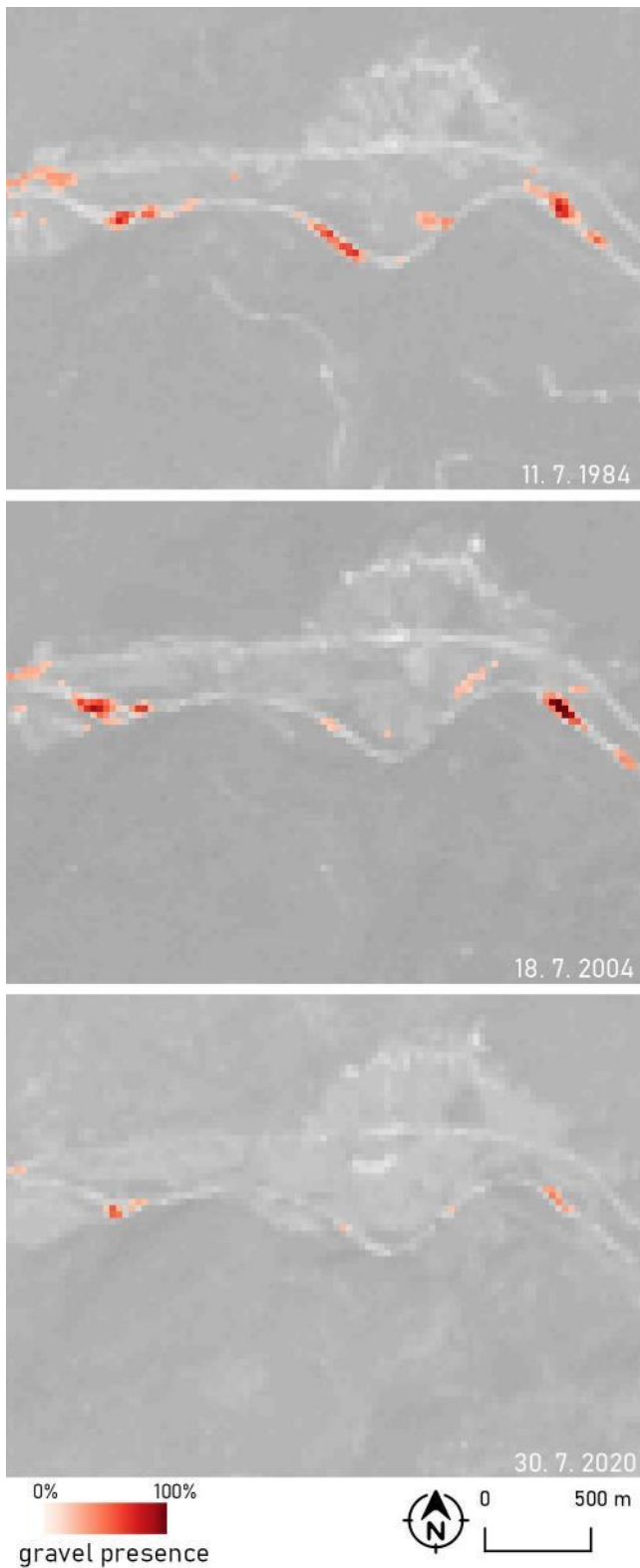
Figure B-10: Gravel presence on the Sava river on section 8 in three different timestamps based on Landsat images.

Slika B-10: Prisotnost proda na Savi na sekciji številka 8 v treh različnih časovnih obdobjih na podlagi posnetkov Landsat.
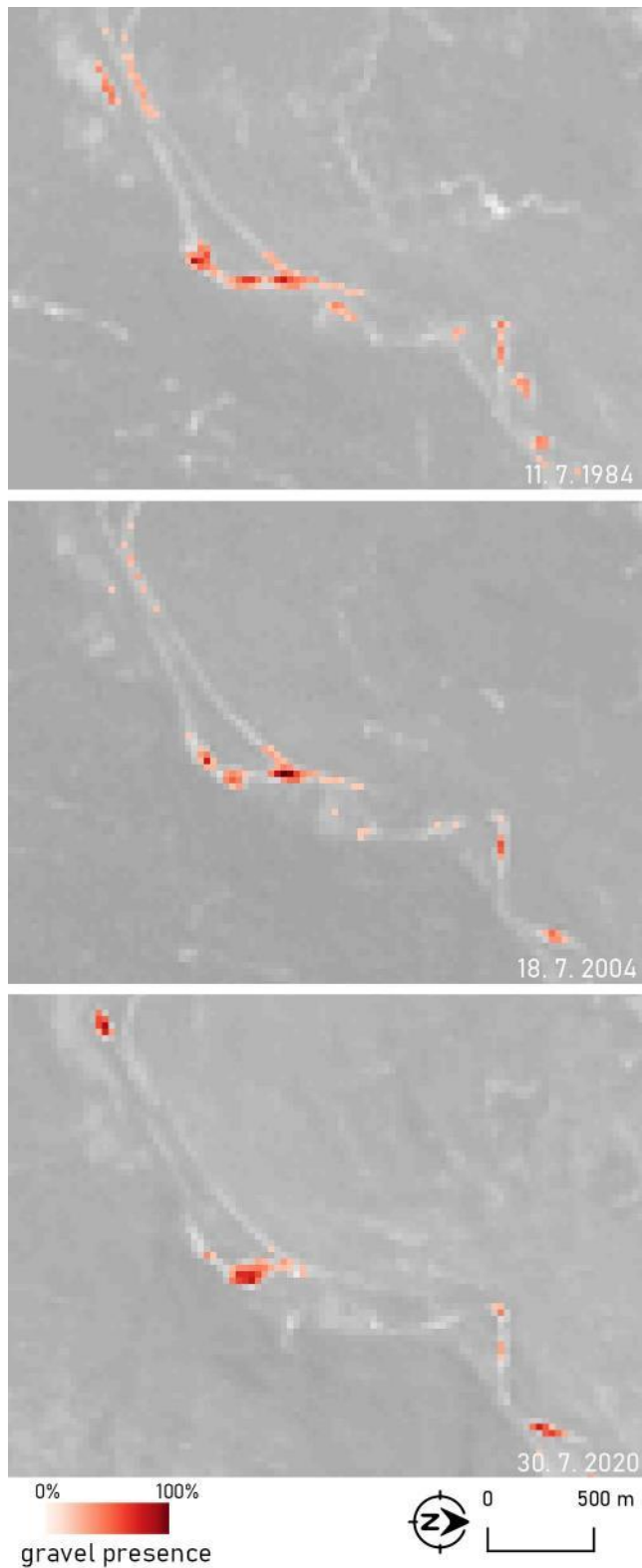
Figure B-11: Gravel presence on the Sava river on section 9 in three different timestamps based on Landsat images.

Slika B-11: Prisotnost proda na Savi na sekciji številka 9 v treh različnih časovnih obdobjih na podlagi posnetkov Landsat.
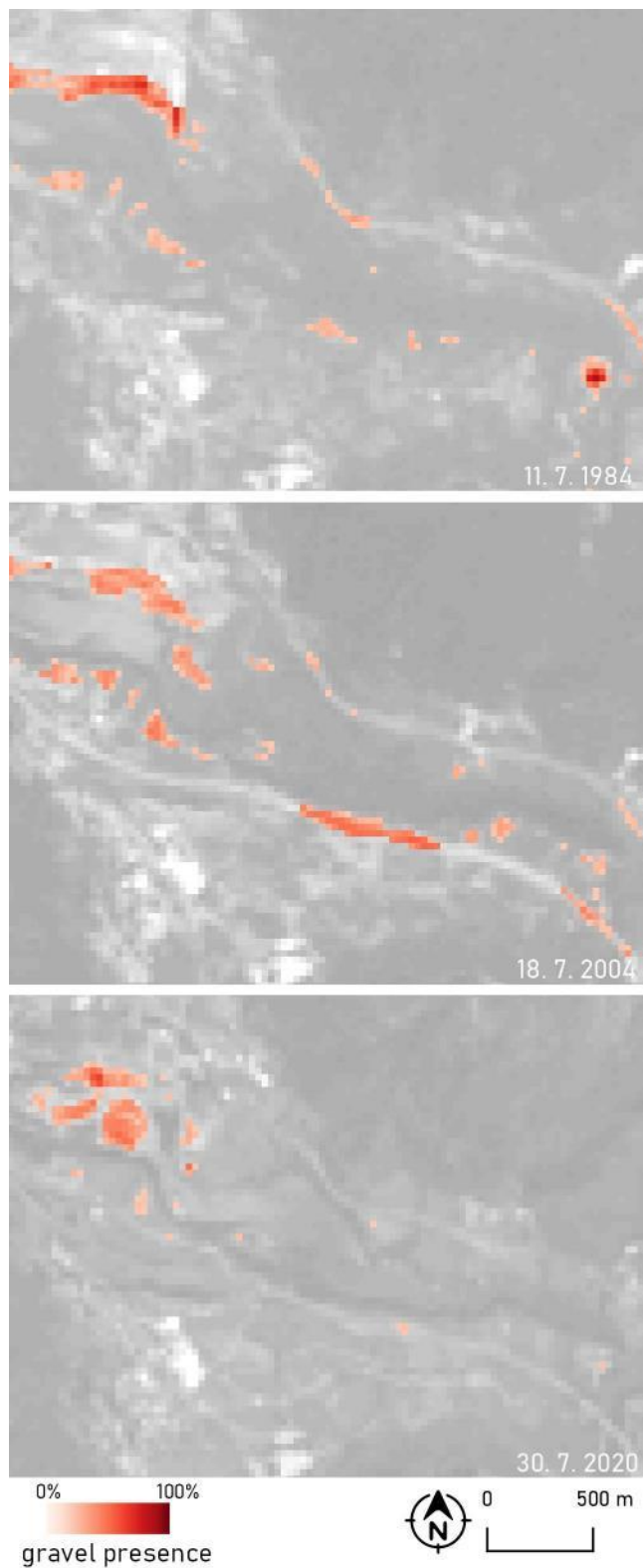
Figure B-12: Gravel presence on the Sava river on section 10 in three different timestamps based on Landsat images.

Slika B-12: Prisotnost proda na Savi na sekciji številka 10 v treh različnih časovnih obdobjih na podlagi posnetkov Landsat.
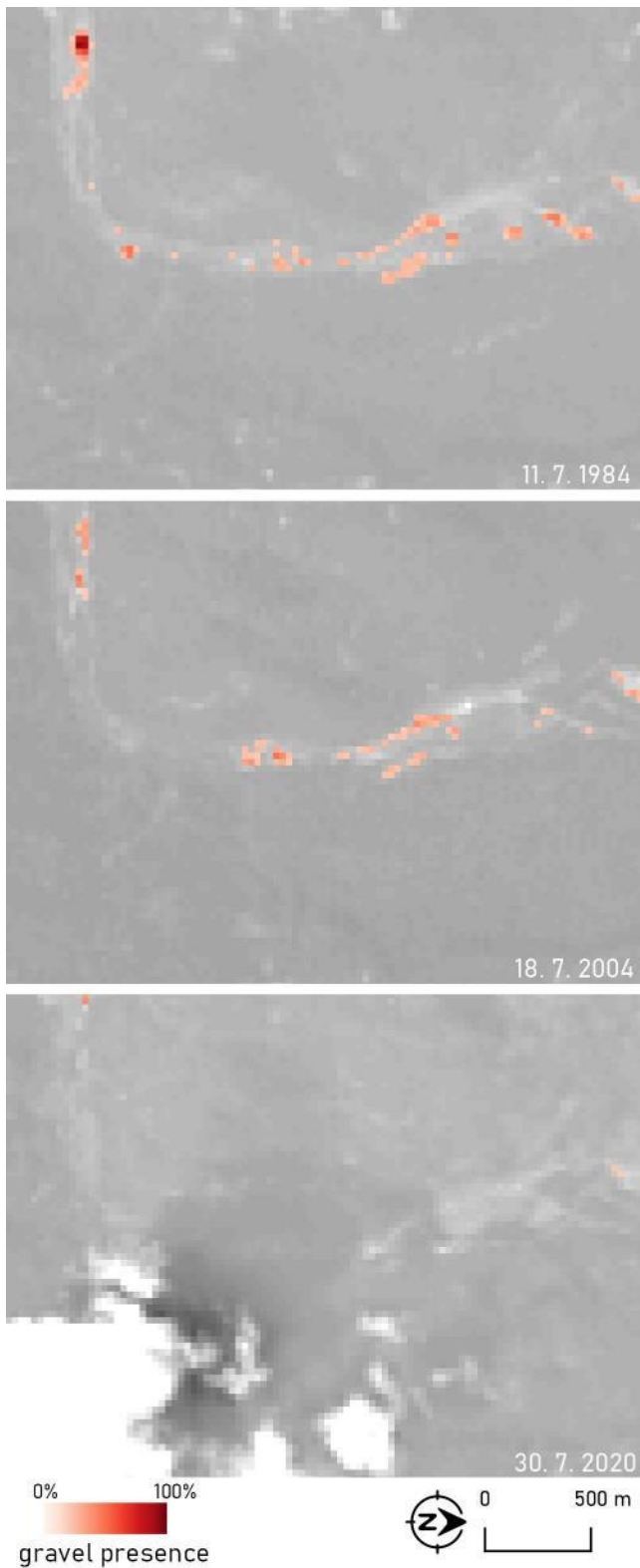
Figure B-13: Gravel presence on the Sava river on section 11 in three different timestamps based on Landsat images.

Slika B-13: Prisotnost proda na Savi na sekciji številka 11 v treh različnih časovnih obdobjih na podlagi posnetkov Landsat.
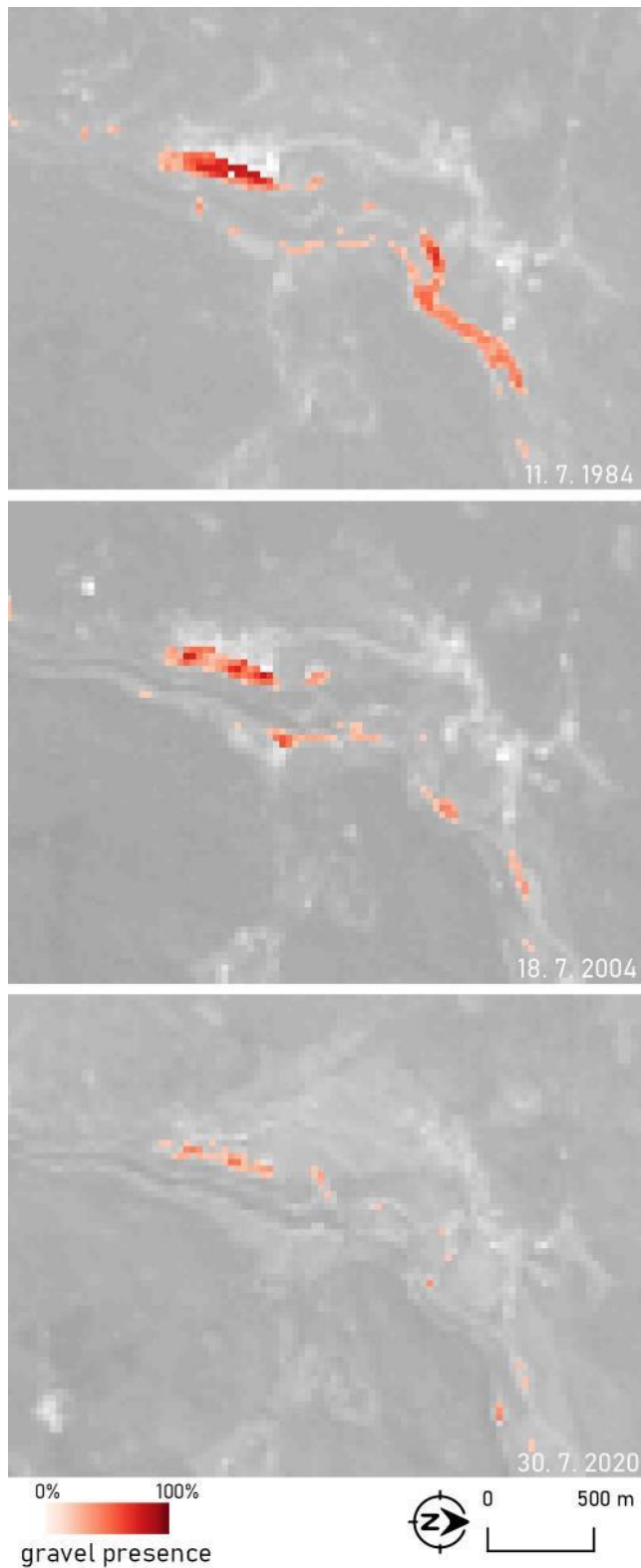
Figure B-14: Gravel presence on the Sava river on section 12 in three different timestamps based on Landsat images.

Slika B-14: Prisotnost proda na Savi na sekciji številka 12 v treh različnih časovnih obdobjih na podlagi posnetkov Landsat.

Stančič, L. 2022. Monitoring Changes of Fluvial Gravel Bars with Remote Sensing.

PhD Th. Ljubljana, UL FGG, Interdisciplinary doctoral study programme Environmental Protection.

B-15

Figure B-15: Gravel presence on the Sava river on section 13 in three different timestamps based on Landsat images.

Slika B-15: Prisotnost proda na Savi na sekciji številka 13 v treh različnih časovnih obdobjih na podlagi posnetkov Landsat.
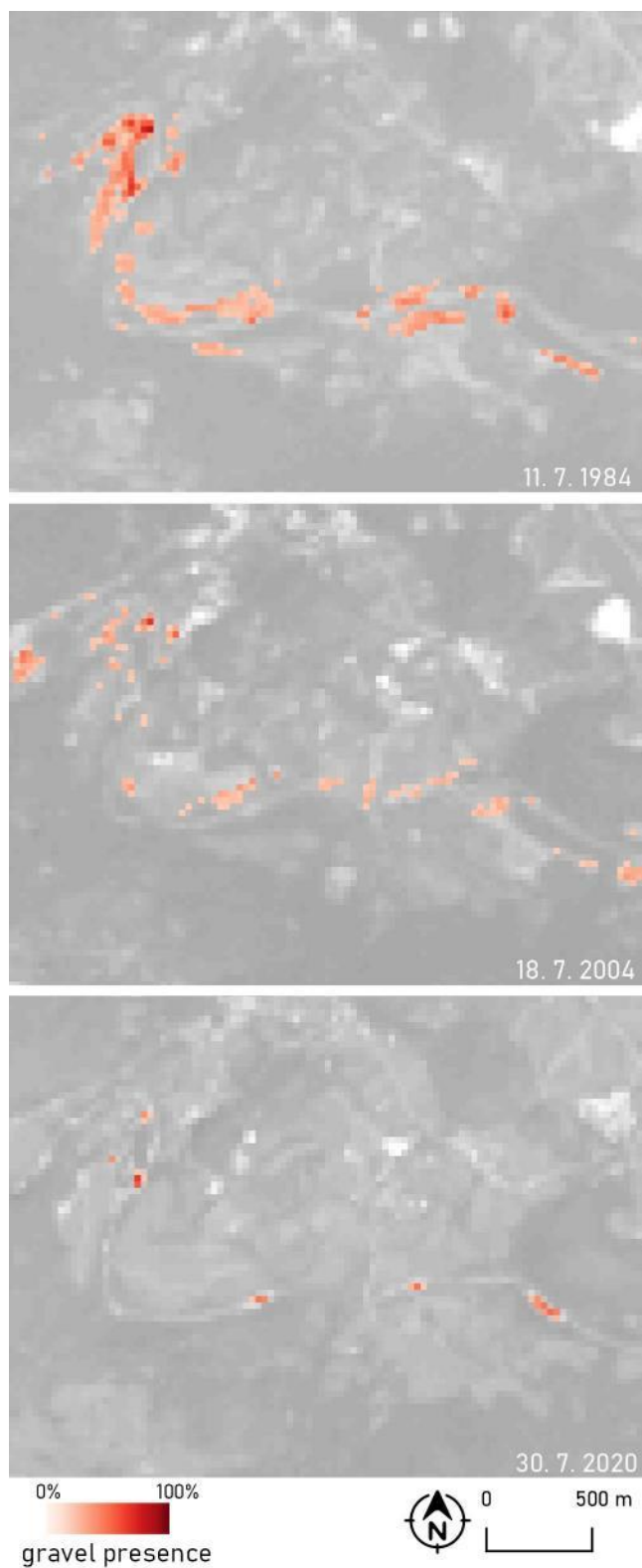
Figure B-16: Gravel presence on the Sava river on section 14 in three different timestamps based on Landsat images.

Slika B-16: Prisotnost proda na Savi na sekciji številka 14 v treh različnih časovnih obdobjih na podlagi posnetkov Landsat.
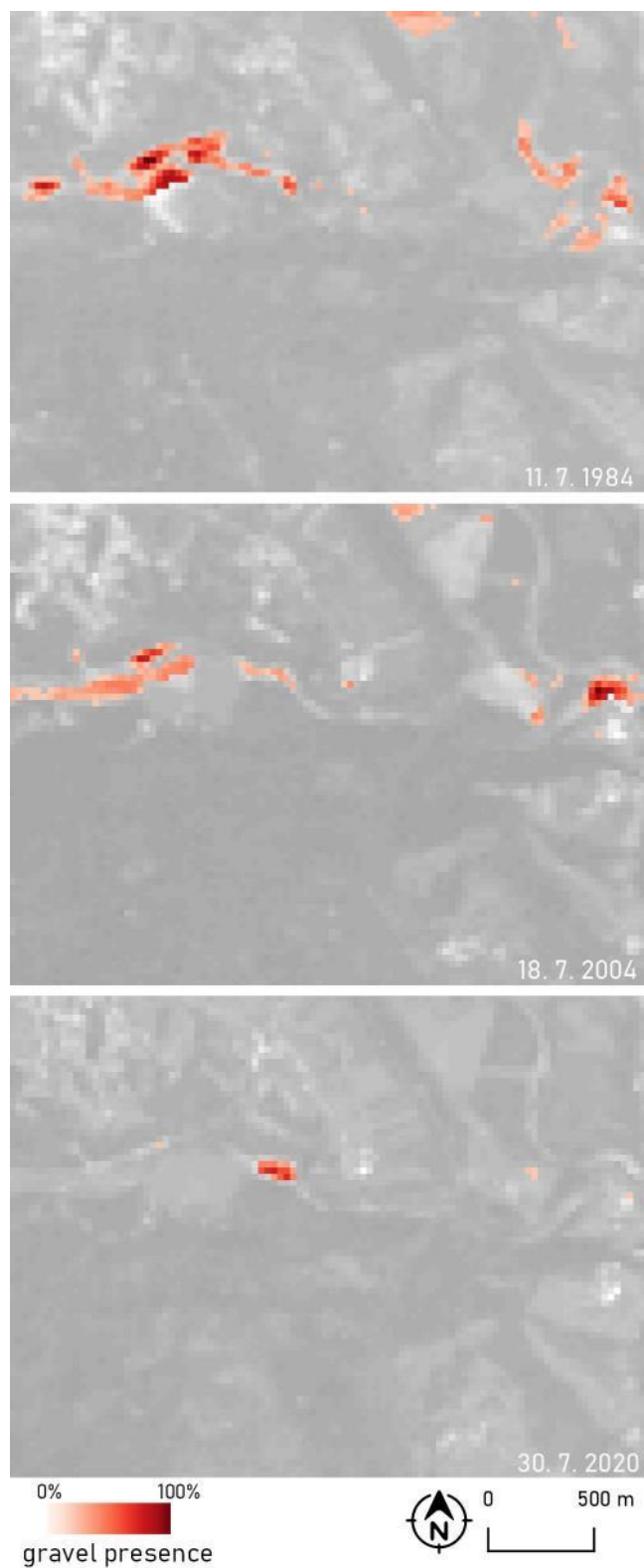
Figure B-17: Gravel presence on the Sava river on section 15 in three different timestamps based on Landsat images.

Slika B-17: Prisotnost proda na Savi na sekciji številka 15 v treh različnih časovnih obdobjih na podlagi posnetkov Landsat.
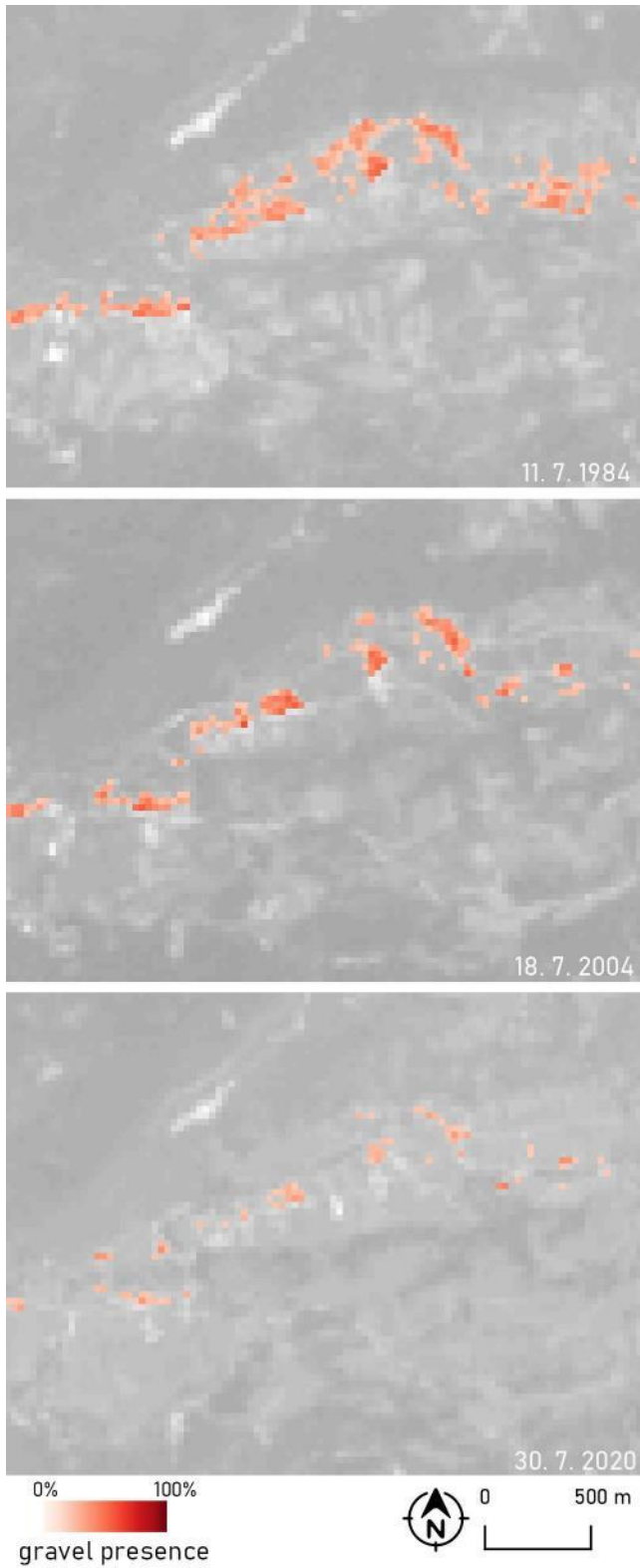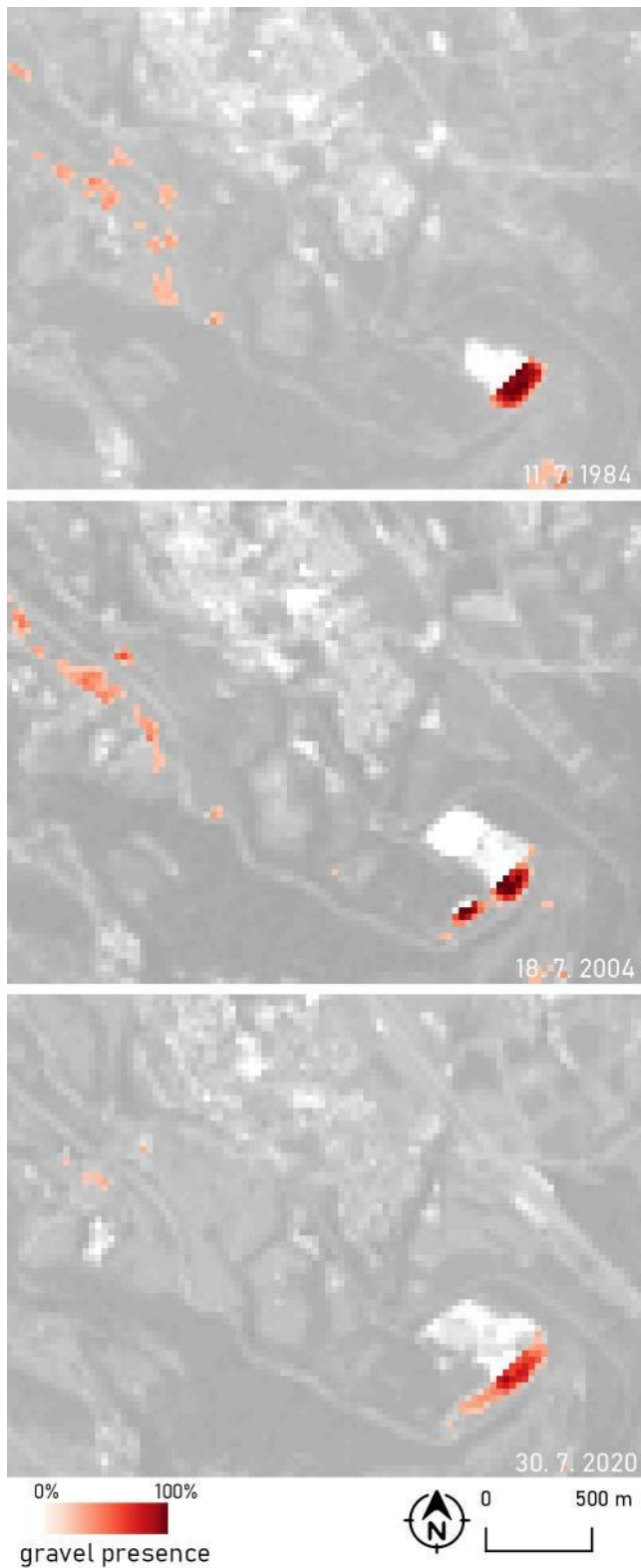
Figure B-18: Gravel presence on the Sava river on section 16 in three different timestamps based on Landsat images.

Slika B-18: Prisotnost proda na Savi na sekciji številka 16 v treh različnih časovnih obdobjih na podlagi posnetkov Landsat.

Figure B-19: Gravel presence on the Sava river on section 17 in three different timestamps based on Landsat images.

Slika B-19: Prisotnost proda na Savi na sekciji številka 17 v treh različnih časovnih obdobjih na podlagi posnetkov Landsat.

B-20

Stančič, L. 2022. Monitoring Changes of Fluvial Gravel Bars with Remote Sensing.
PhD Th. Ljubljana, UL FGG, Interdisciplinary doctoral study programme Environmental Protection.

Figure B-20: Gravel presence on the Sava river on section 18 in three different timestamps based on Landsat images.

Slika B-20: Prisotnost proda na Savi na sekciji številka 18 v treh različnih časovnih obdobjih na podlagi posnetkov Landsat.
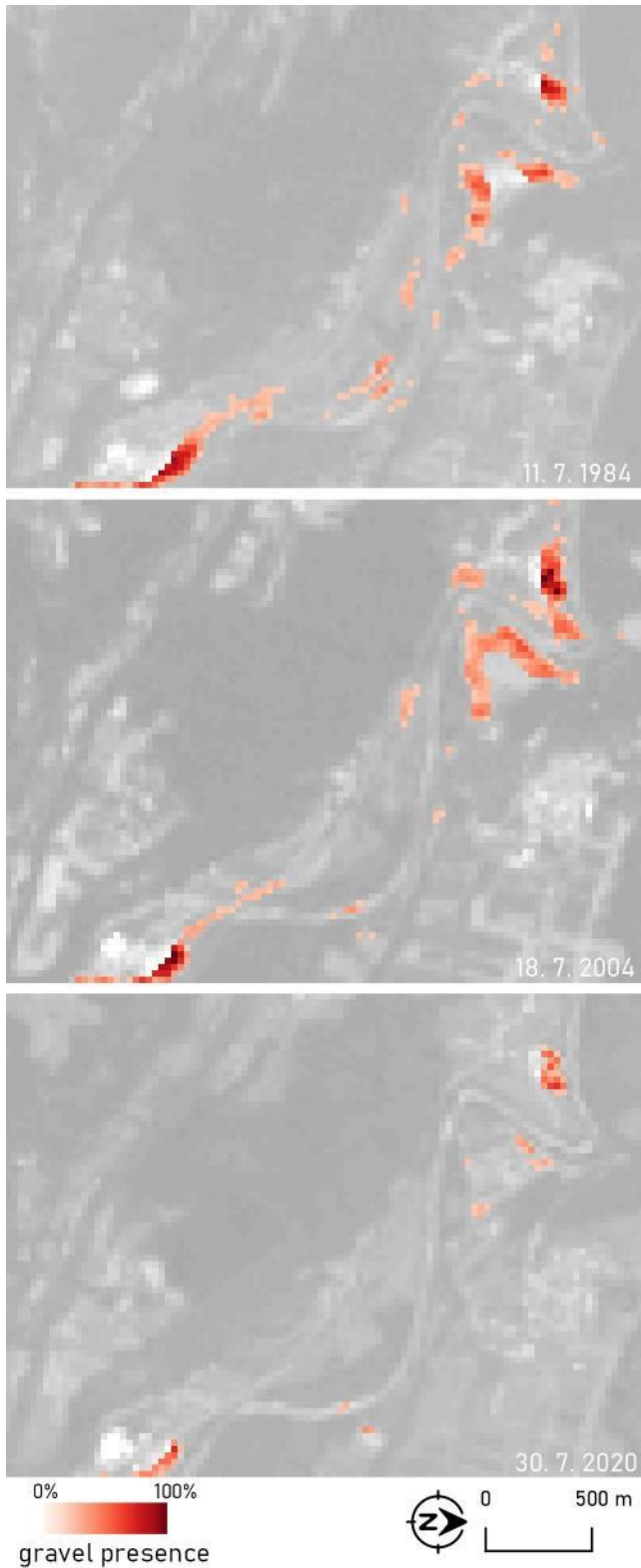
Figure B-21: Gravel presence on the Sava river on section 19 in three different timestamps based on Landsat images.

Slika B-21: Prisotnost proda na Savi na sekciji številka 19 v treh različnih časovnih obdobjih na podlagi posnetkov Landsat.

B-22

Stančič, L. 2022. Monitoring Changes of Fluvial Gravel Bars with Remote Sensing.
PhD Th. Ljubljana, UL FGG, Interdisciplinary doctoral study programme Environmental Protection.

Figure B-22: Gravel presence on the Sava river on section 20 in three different timestamps based on Landsat images.

Slika B-22: Prisotnost proda na Savi na sekciji številka 20 v treh različnih časovnih obdobjih na podlagi posnetkov Landsat.
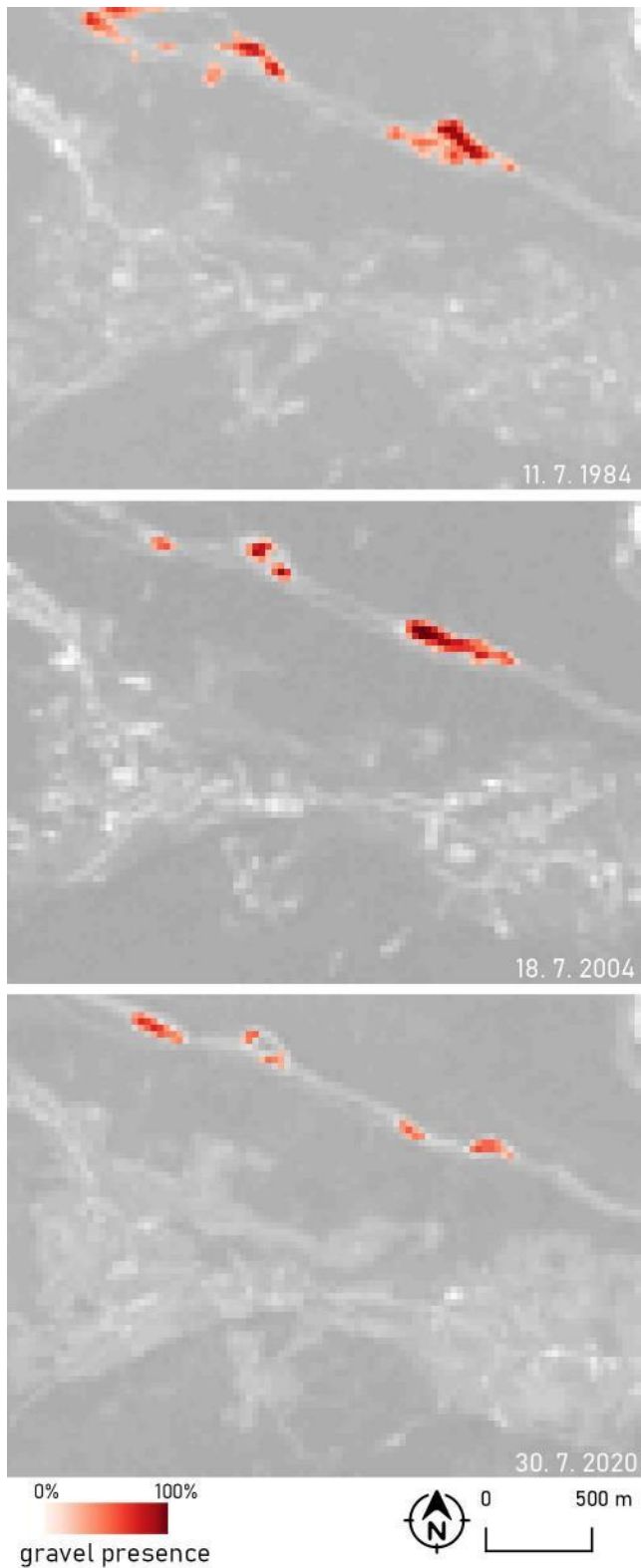
Figure B-23: Gravel presence on the Sava river on section 21 in three different timestamps based on Landsat images.

Slika B-23: Prisotnost proda na Savi na sekciji številka 21 v treh različnih časovnih obdobjih na podlagi posnetkov Landsat.
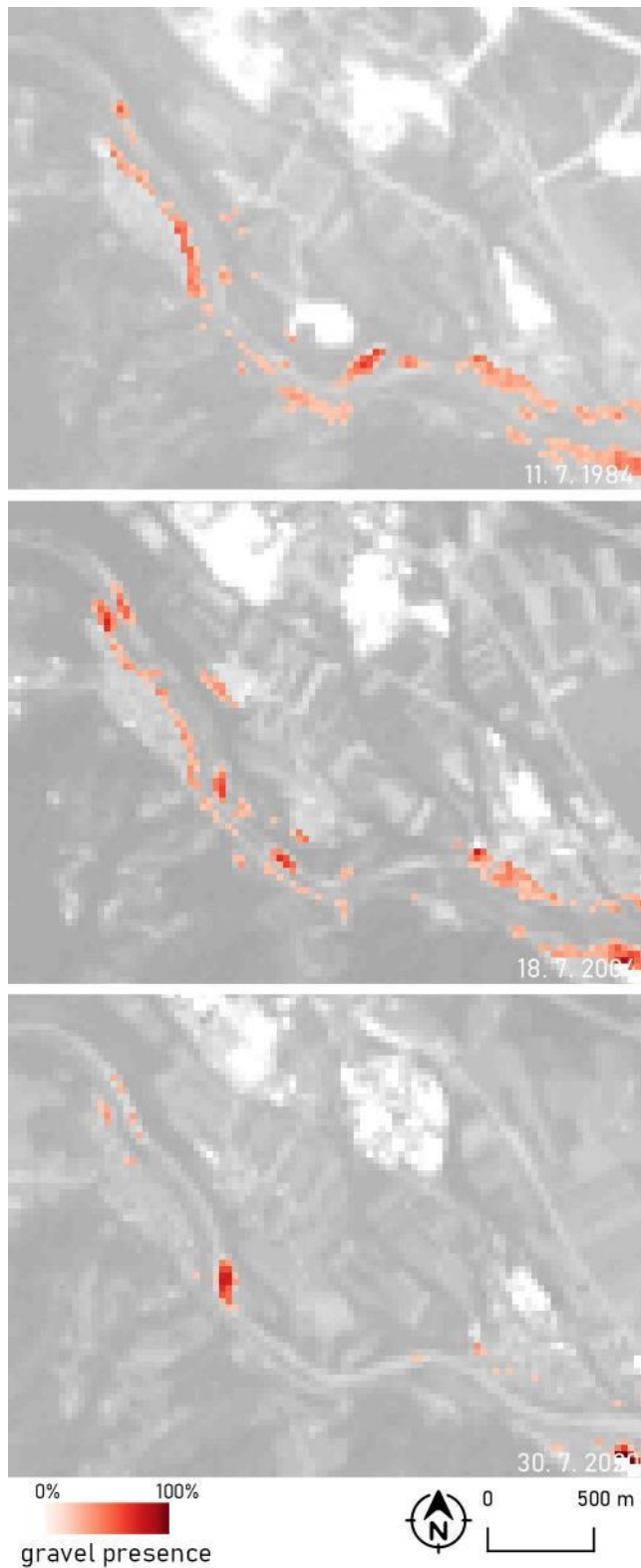
Figure B-24: Gravel presence on the Sava river on section 22 in three different timestamps based on Landsat images.

Slika B-24: Prisotnost proda na Savi na sekciji številka 22 v treh različnih časovnih obdobjih na podlagi posnetkov Landsat.

Stančič, L. 2022. Monitoring Changes of Fluvial Gravel Bars with Remote Sensing.
PhD Th. Ljubljana, UL FGG, Interdisciplinary doctoral study programme Environmental Protection.
B-25

Figure B-25: Gravel presence on the Sava river on section 23 in three different timestamps based on Landsat images.

Slika B-25: Prisotnost proda na Savi na sekciji številka 23 v treh različnih časovnih obdobjih na podlagi posnetkov Landsat.
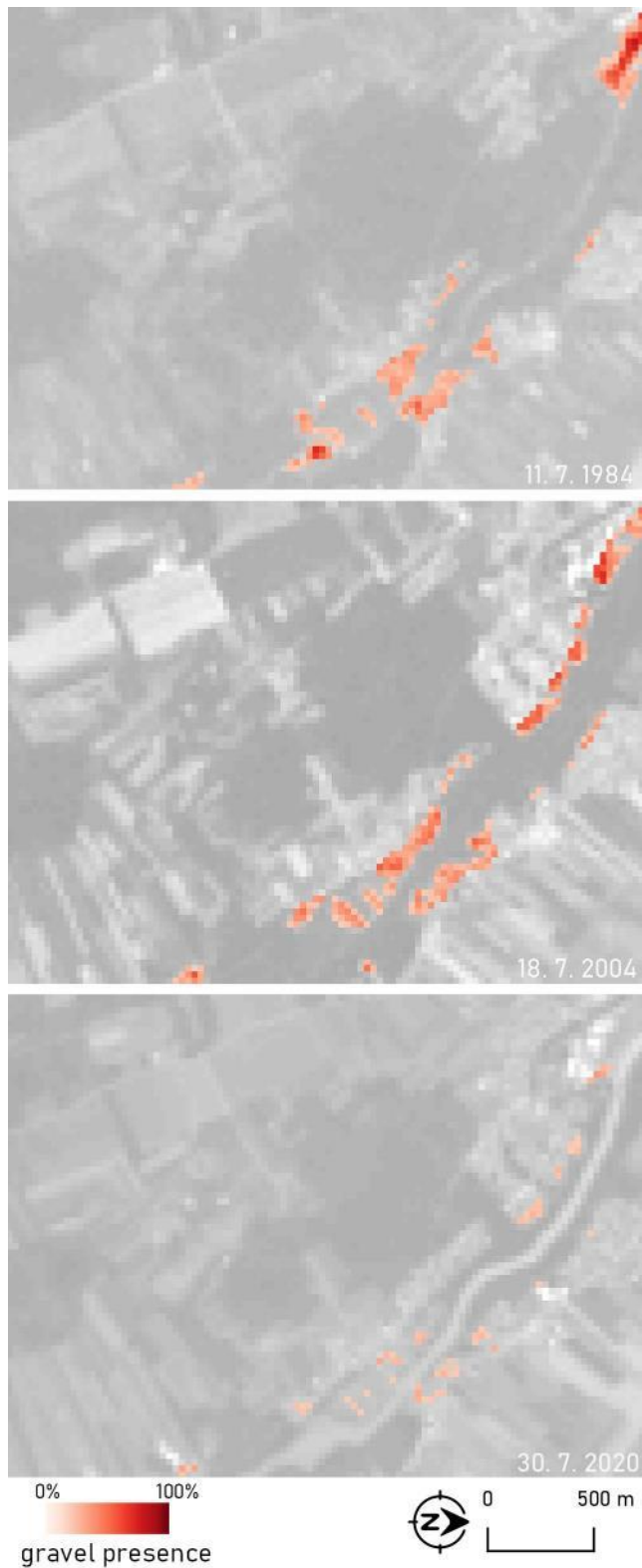
Figure B-26: Gravel presence on the Sava river on section 24 in three different timestamps based on Landsat images.

Slika B-26: Prisotnost proda na Savi na sekciji številka 24 v treh različnih časovnih obdobjih na podlagi posnetkov Landsat.
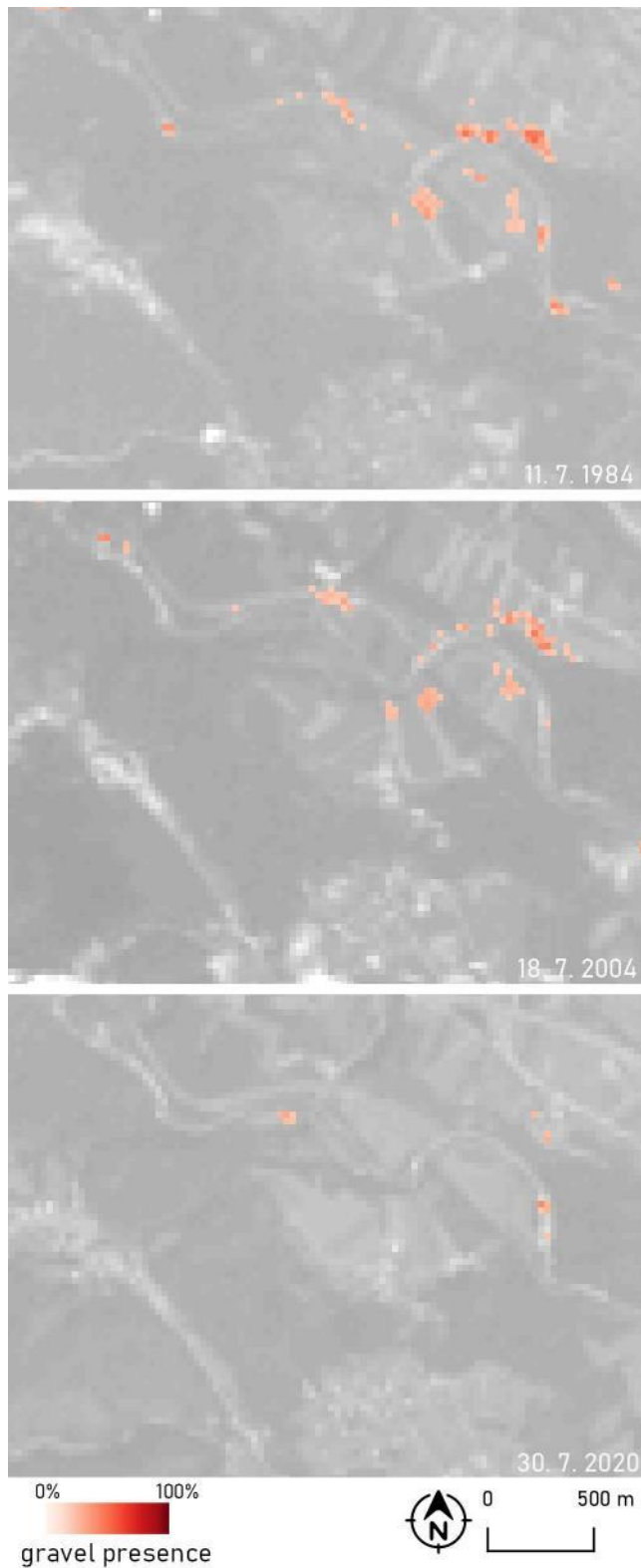
Figure B-27: Gravel presence on the Sava river on section 25 in three different timestamps based on Landsat images.

Slika B-27: Prisotnost proda na Savi na sekciji številka 25 v treh različnih časovnih obdobjih na podlagi posnetkov Landsat.

B-28

Stančič, L. 2022. Monitoring Changes of Fluvial Gravel Bars with Remote Sensing.
PhD Th. Ljubljana, UL FGG, Interdisciplinary doctoral study programme Environmental Protection.

Figure B-28: Gravel presence on the Sava river on section 26 in three different timestamps based on Landsat images.

Slika B-28: Prisotnost proda na Savi na sekciji številka 26 v treh različnih časovnih obdobjih na podlagi posnetkov Landsat.
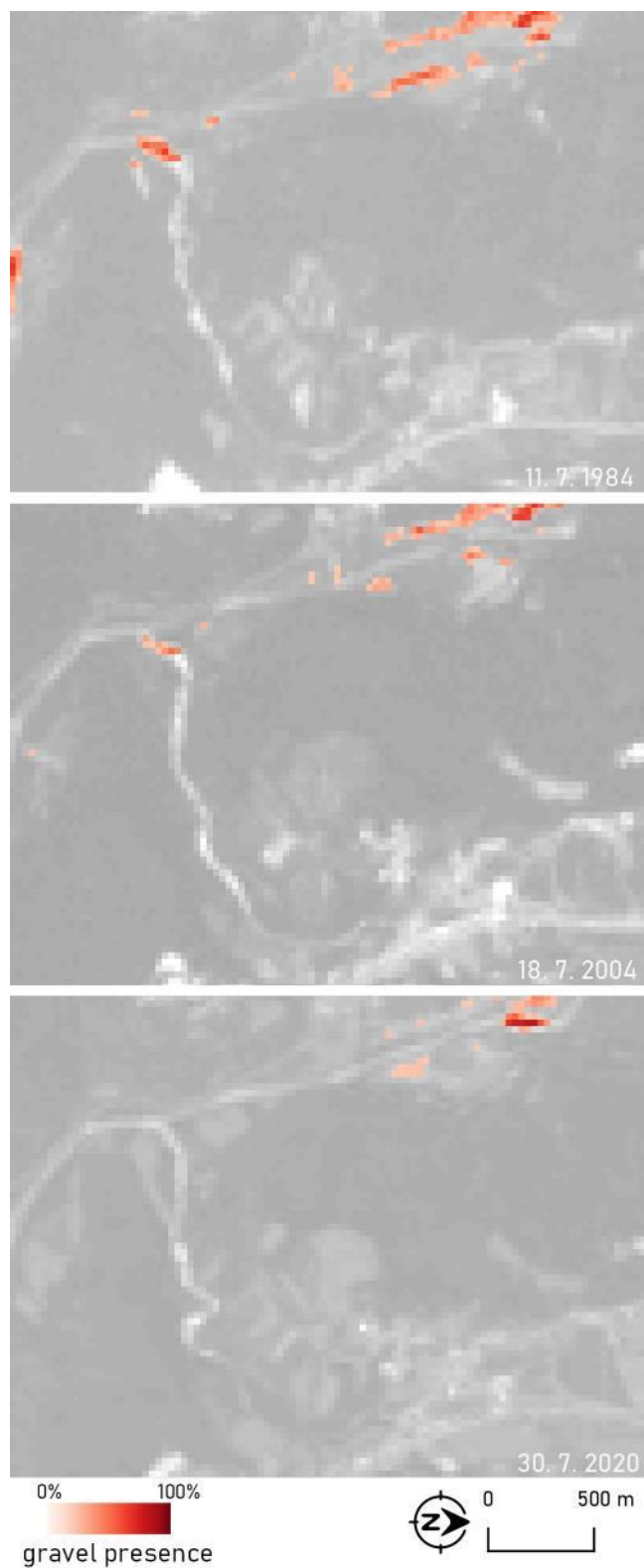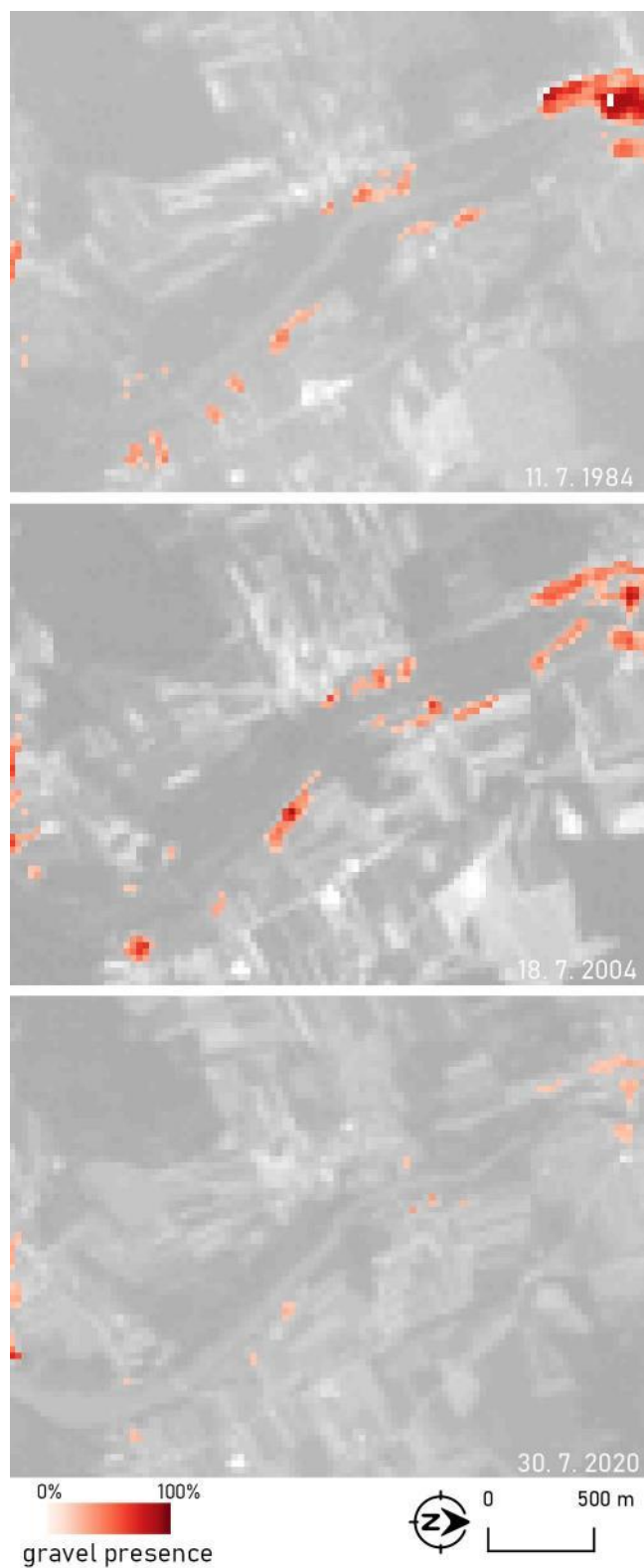
Figure B-29: Gravel presence on the Sava river on section 27 in three different timestamps based on Landsat images.

Slika B-29: Prisotnost proda na Savi na sekciji številka 27 v treh različnih časovnih obdobjih na podlagi posnetkov Landsat.
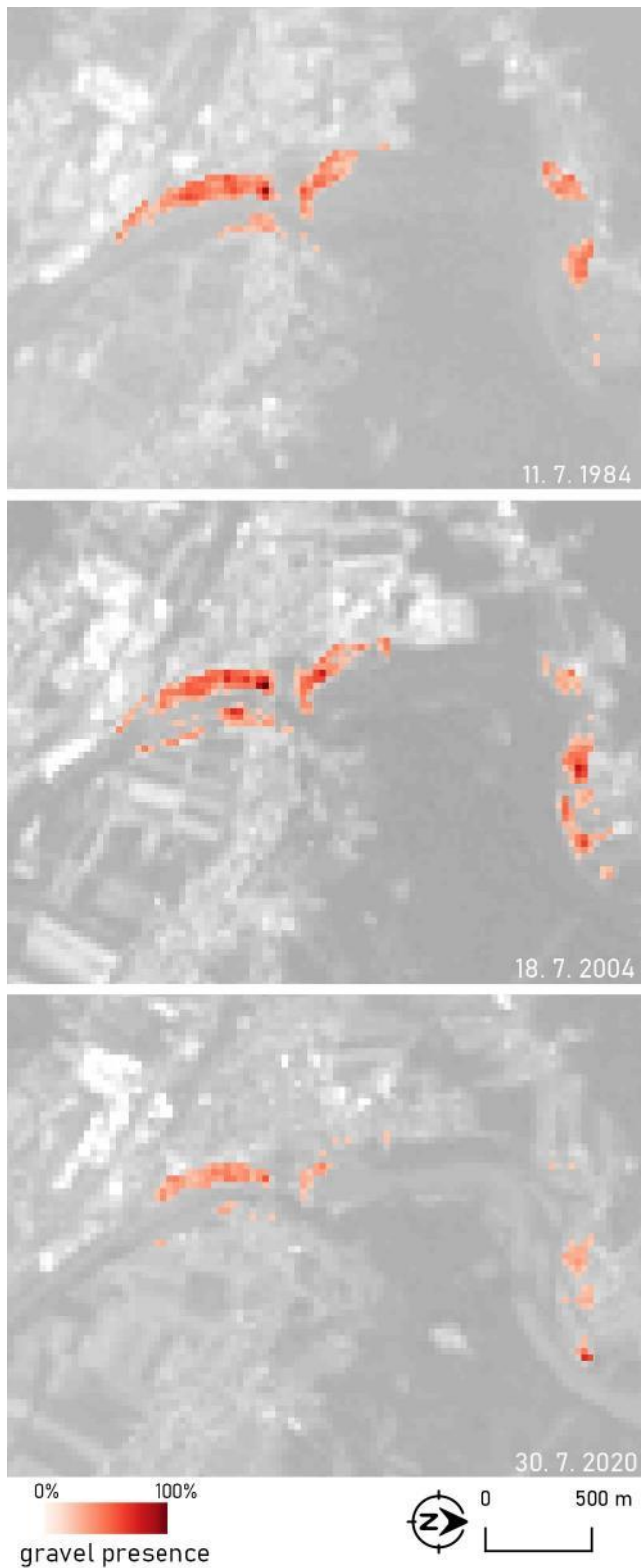
Figure B-30: Gravel presence on the Sava river on section 28 in three different timestamps based on Landsat images.

Slika B-30: Prisotnost proda na Savi na sekciji številka 28 v treh različnih časovnih obdobjih na podlagi posnetkov Landsat.

Figure B-31: Gravel presence on the Sava river on section 29 in three different timestamps based on Landsat images.

Slika B-31: Prisotnost proda na Savi na sekciji številka 29 v treh različnih časovnih obdobjih na podlagi posnetkov Landsat.
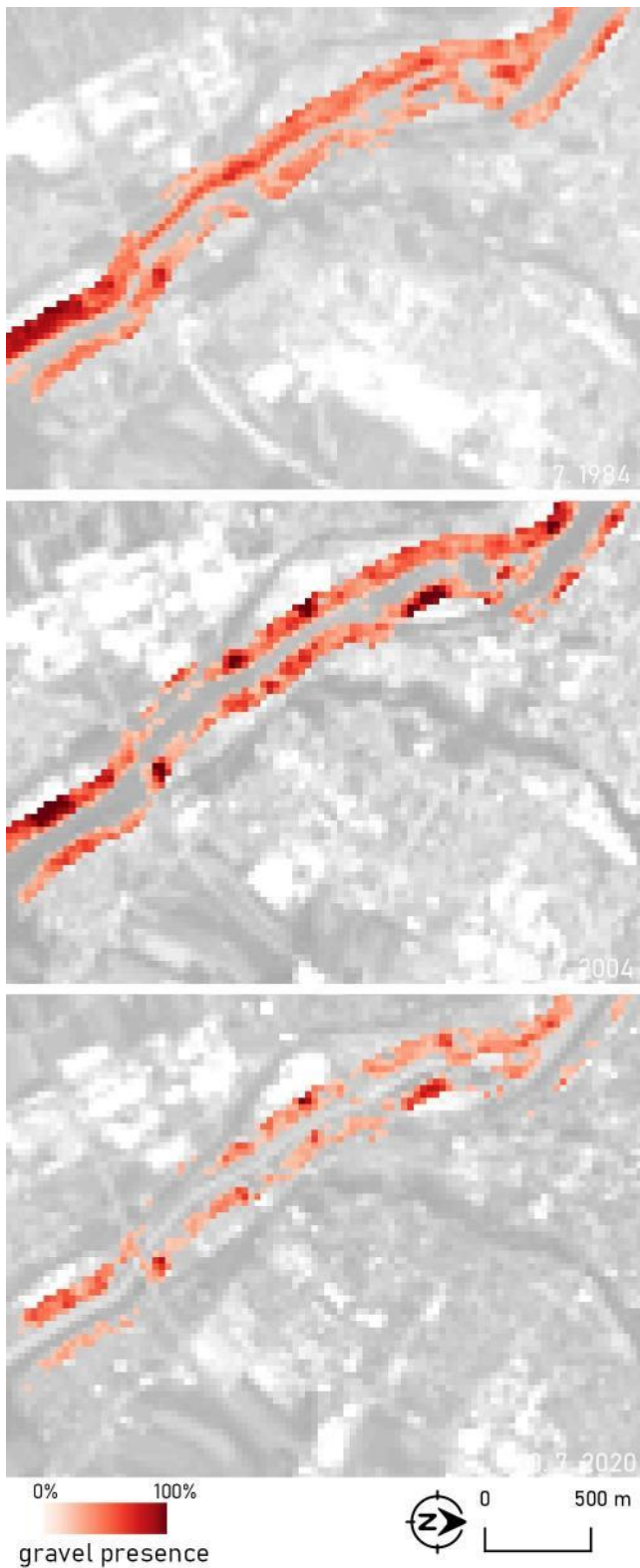
Figure B-32: Gravel presence on the Sava river on section 30 in three different timestamps based on Landsat images.

Slika B-32: Prisotnost proda na Savi na sekciji številka 30 v treh različnih časovnih obdobjih na podlagi posnetkov Landsat.

Figure B-33: Gravel presence on the Sava river on section 31 in three different timestamps based on Landsat images.

Slika B-33: Prisotnost proda na Savi na sekciji številka 31 v treh različnih časovnih obdobjih na podlagi posnetkov Landsat.
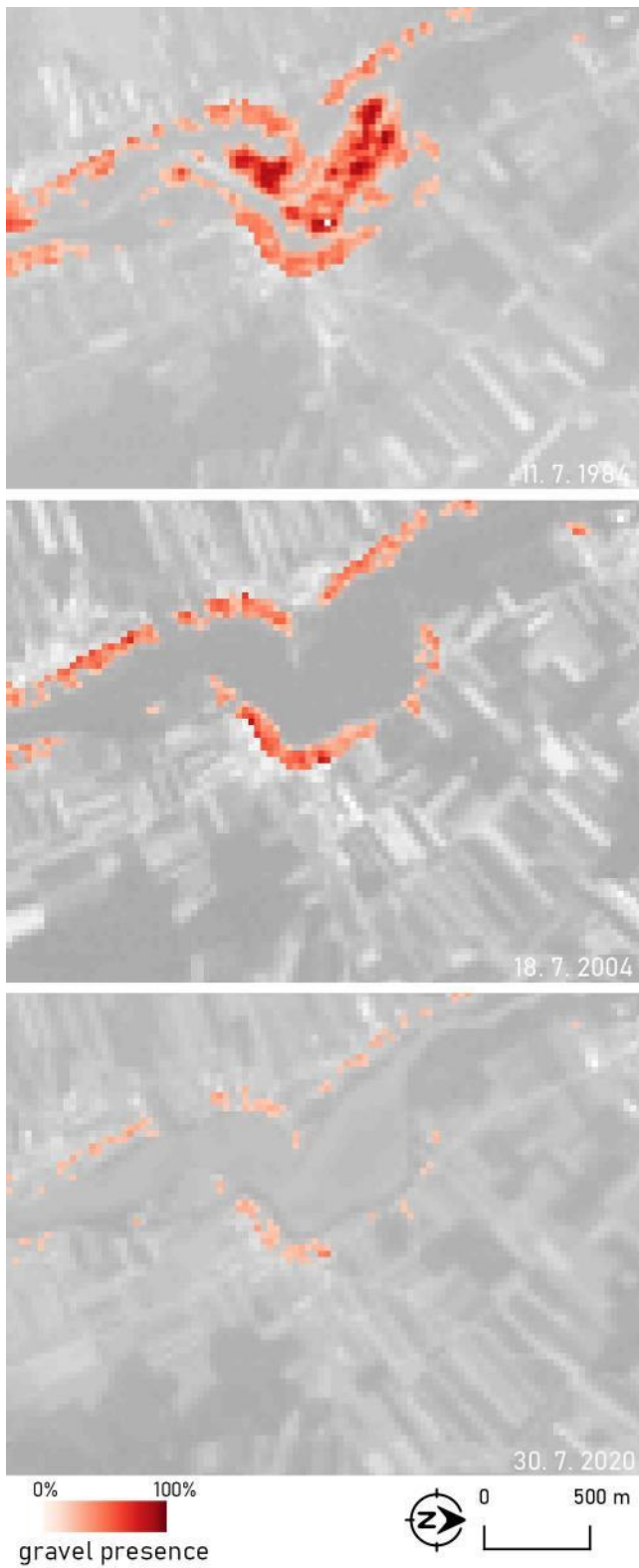
Figure B-34: Gravel presence on the Sava river on section 32 in three different timestamps based on Landsat images.

Slika B-34: Prisotnost proda na Savi na sekciji številka 32 v treh različnih časovnih obdobjih na podlagi posnetkov Landsat.
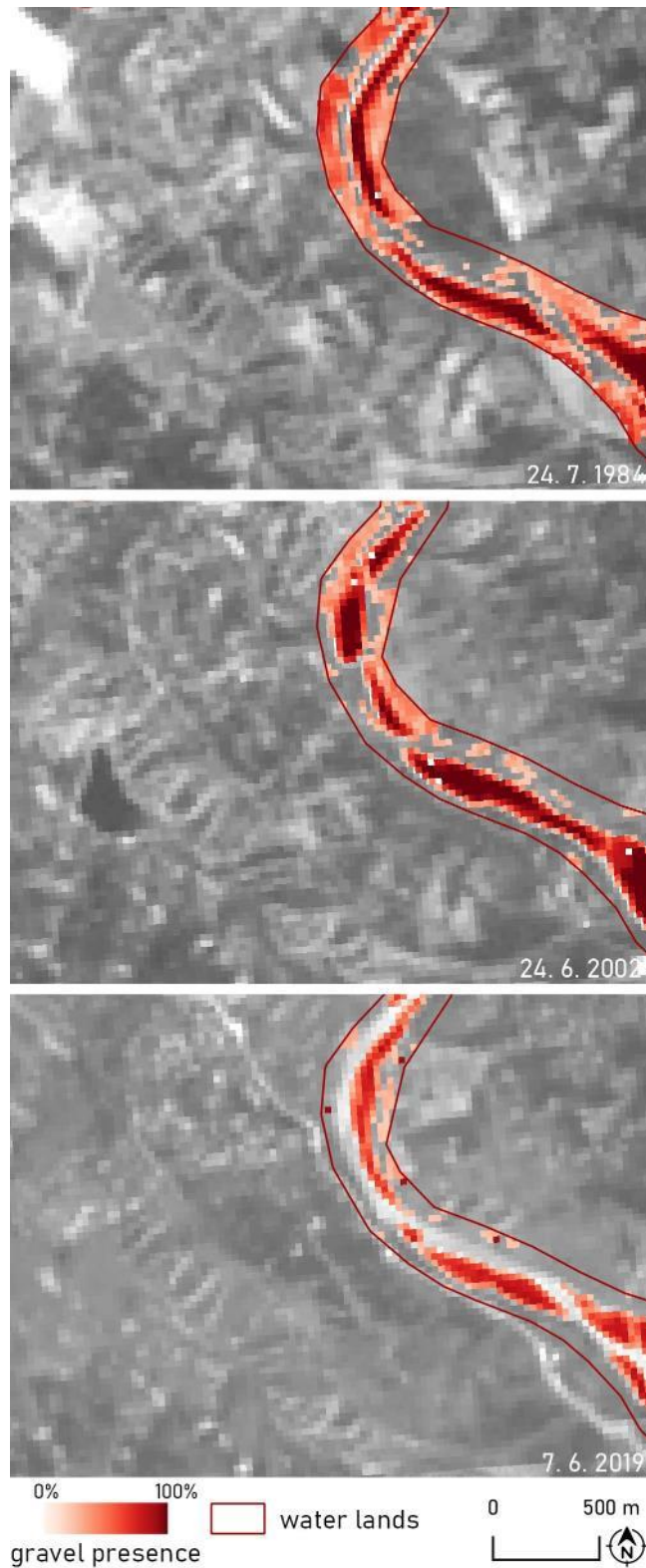
Figure B-35: Gravel presence on the Sava river on section 33 in three different timestamps based on Landsat images.

Slika B-35: Prisotnost proda na Savi na sekciji številka 33 v treh različnih časovnih obdobjih na podlagi posnetkov Landsat.

Figure B-36: Gravel presence on the Sava river on section 34 in three different timestamps based on Landsat images.

Slika B-36: Prisotnost proda na Savi na sekciji številka 34 v treh različnih časovnih obdobjih na podlagi posnetkov Landsat.

APPENDIX C : Gravel Fraction Maps of the Vjosa River
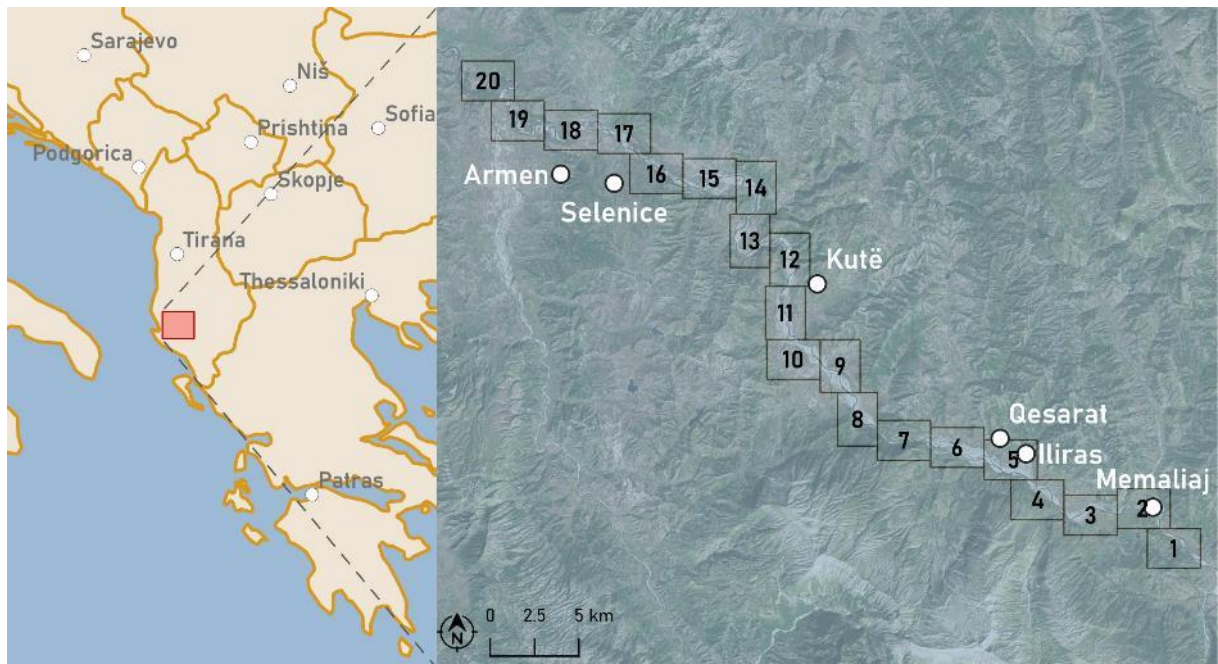
Figure C-1: Sections of the gravel presence maps on the Vjosa river between the Memaliaj settlement and the confluence with the Shushica river (data source: Natural Earth, 2020; Bing, 2021).

Slika C-1: Sekcije kart prisotnosti proda na reki Vjosi med naseljem Memaliaj in sotočjem z reko Šušico (vir podatkov: Natural Earth, 2020; Bing, 2021).
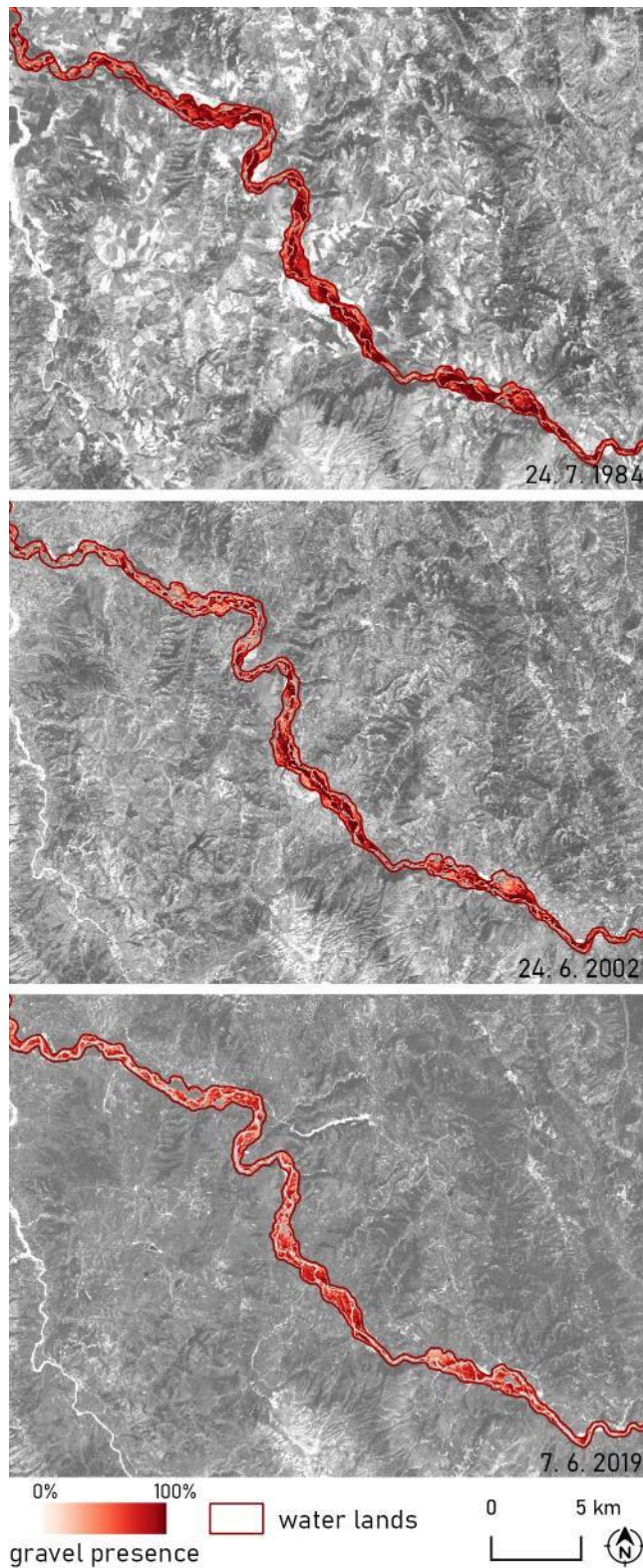
Figure C-2: Gravel presence on the Vjosa river between the Memaliaj settlement and the confluence with the Shushica river in three different timestamps based on Landsat images.

Slika C-2: Prisotnost proda na reki Vjosi med naseljem Memaliaj in sotočjem z reko Šušico v treh različnih časovnih obdobjih na podlagi posnetkov Landsat.

Figure C-3: Gravel presence on the Vjosa river on section 1 in three different timestamps based on Landsat images.

Slika C-3: Prisotnost proda na reki Vjosi na sekciji številka 1 v treh različnih časovnih obdobjih na podlagi posnetkov Landsat.
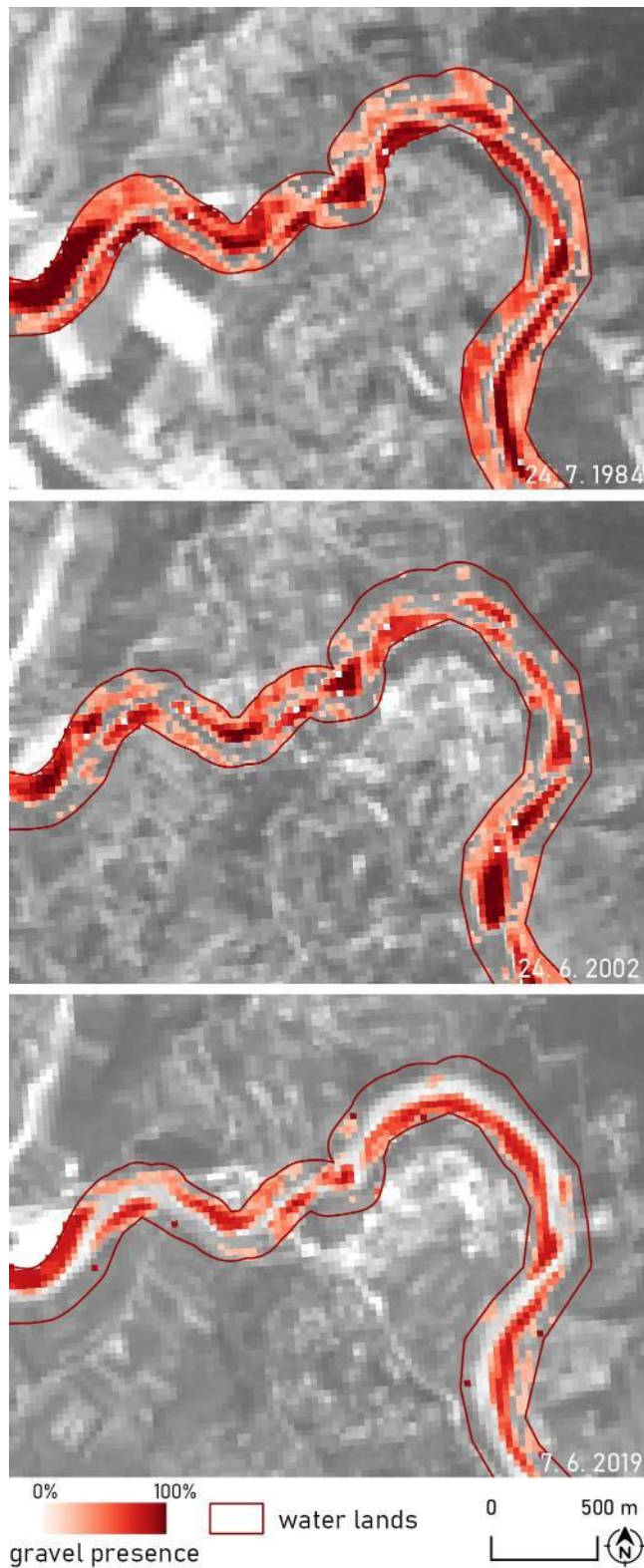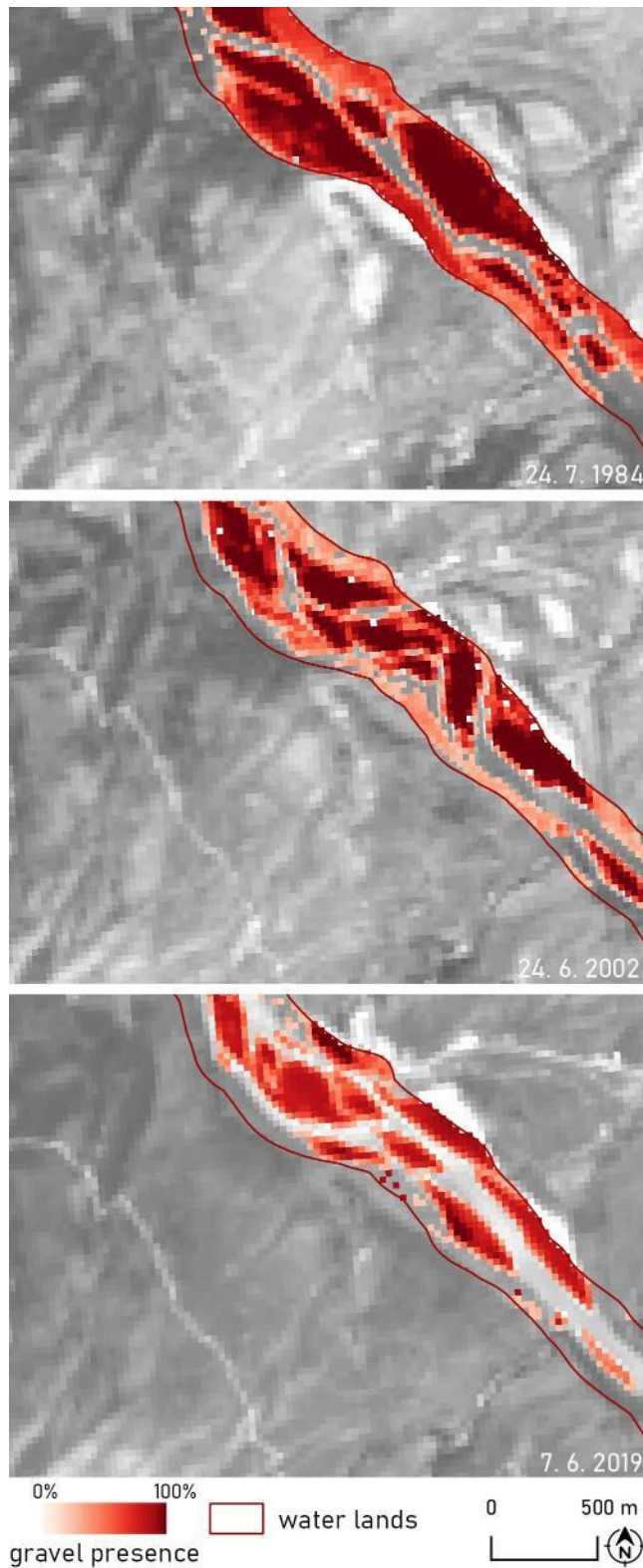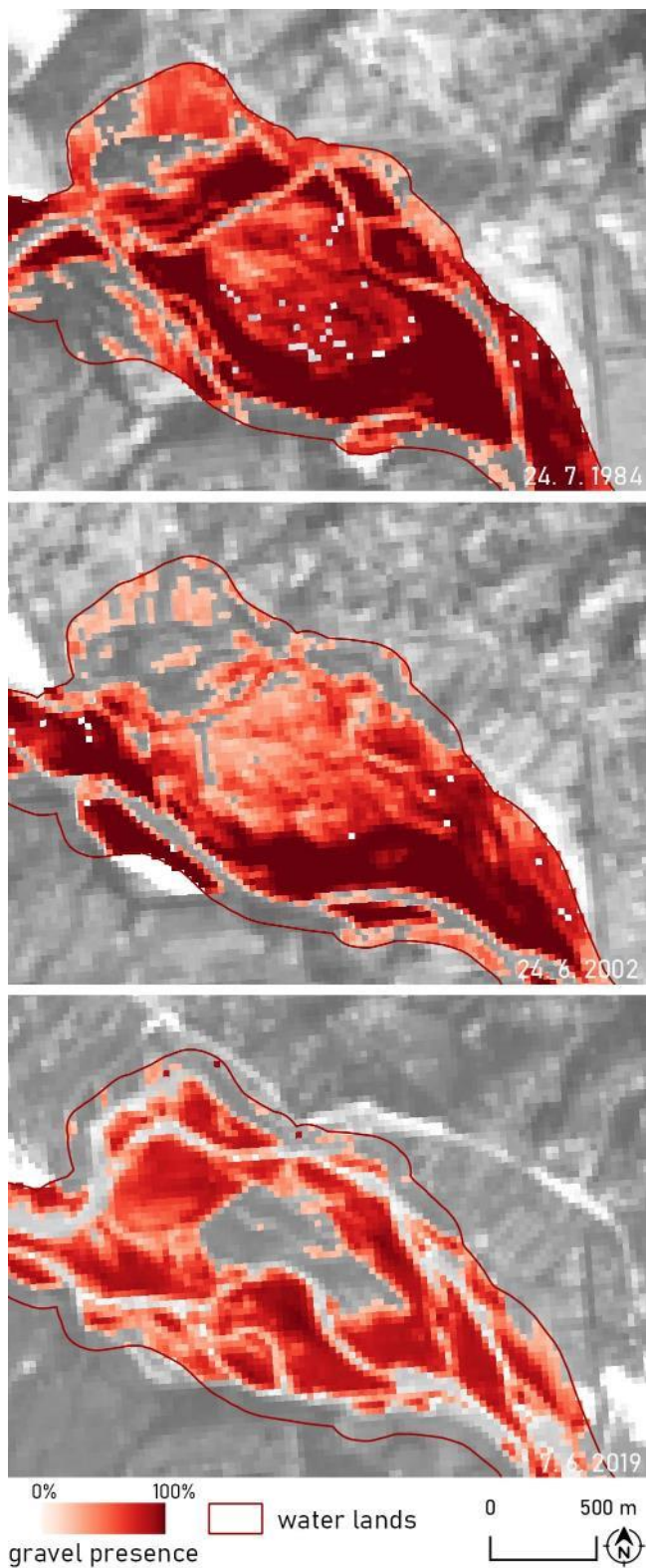
Figure C-4: Gravel presence on the Vjosa river on section 2 in three different timestamps based on Landsat images.

Slika C-4: Prisotnost proda na reki Vjosi na sekciji številka 2 v treh različnih časovnih obdobjih na podlagi posnetkov Landsat.
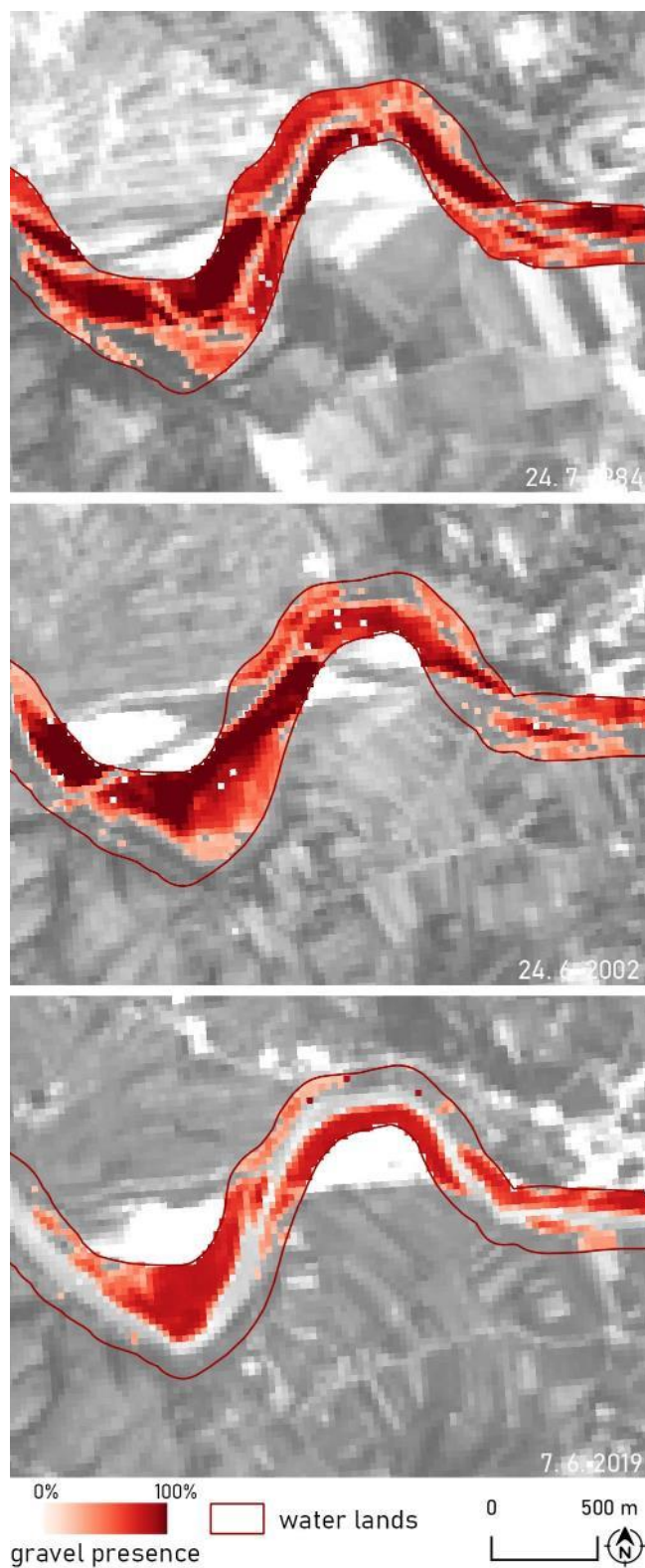
Figure C-5: Gravel presence on the Vjosa river on section 3 in three different timestamps based on Landsat images.

Slika C-5: Prisotnost proda na reki Vjosi na sekciji številka 3 v treh različnih časovnih obdobjih na podlagi posnetkov Landsat.
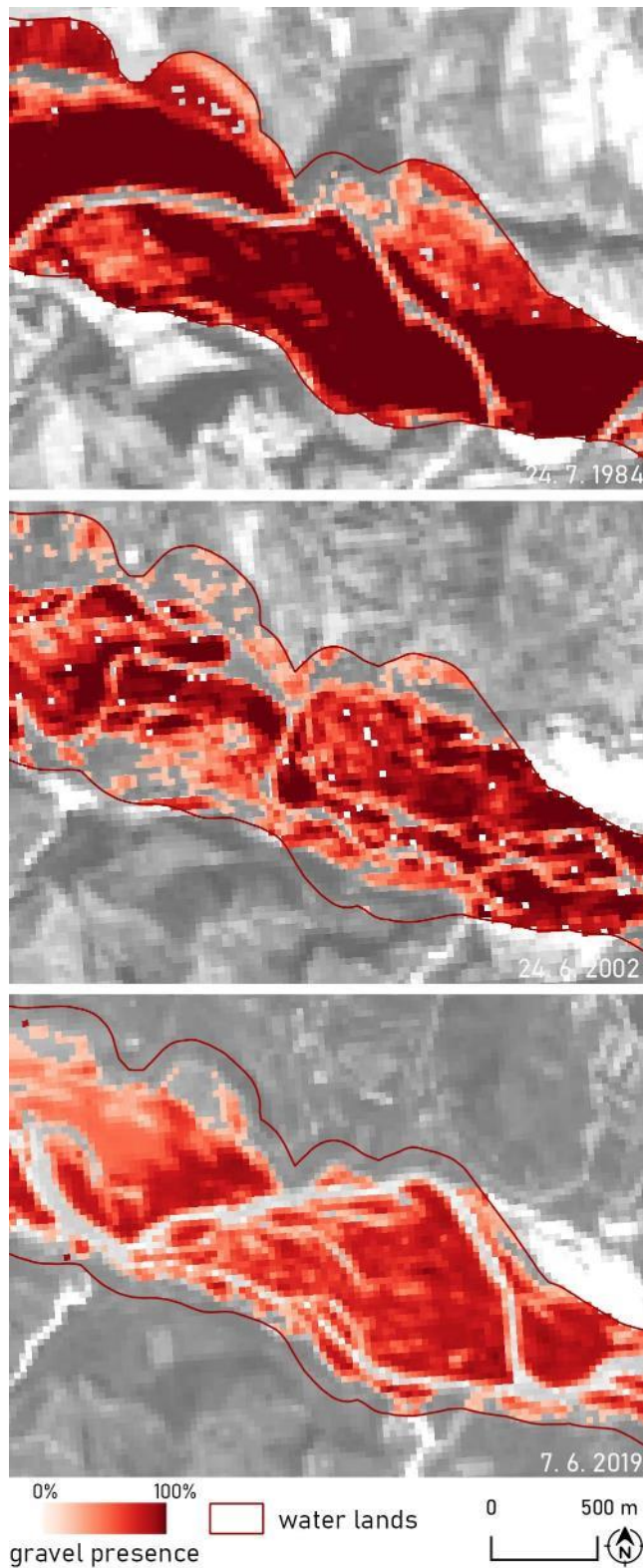
Figure C-6: Gravel presence on the Vjosa river on section 4 in three different timestamps based on Landsat images.

Slika C-6: Prisotnost proda na reki Vjosi na sekciji številka 4 v treh različnih časovnih obdobjih na podlagi posnetkov Landsat.
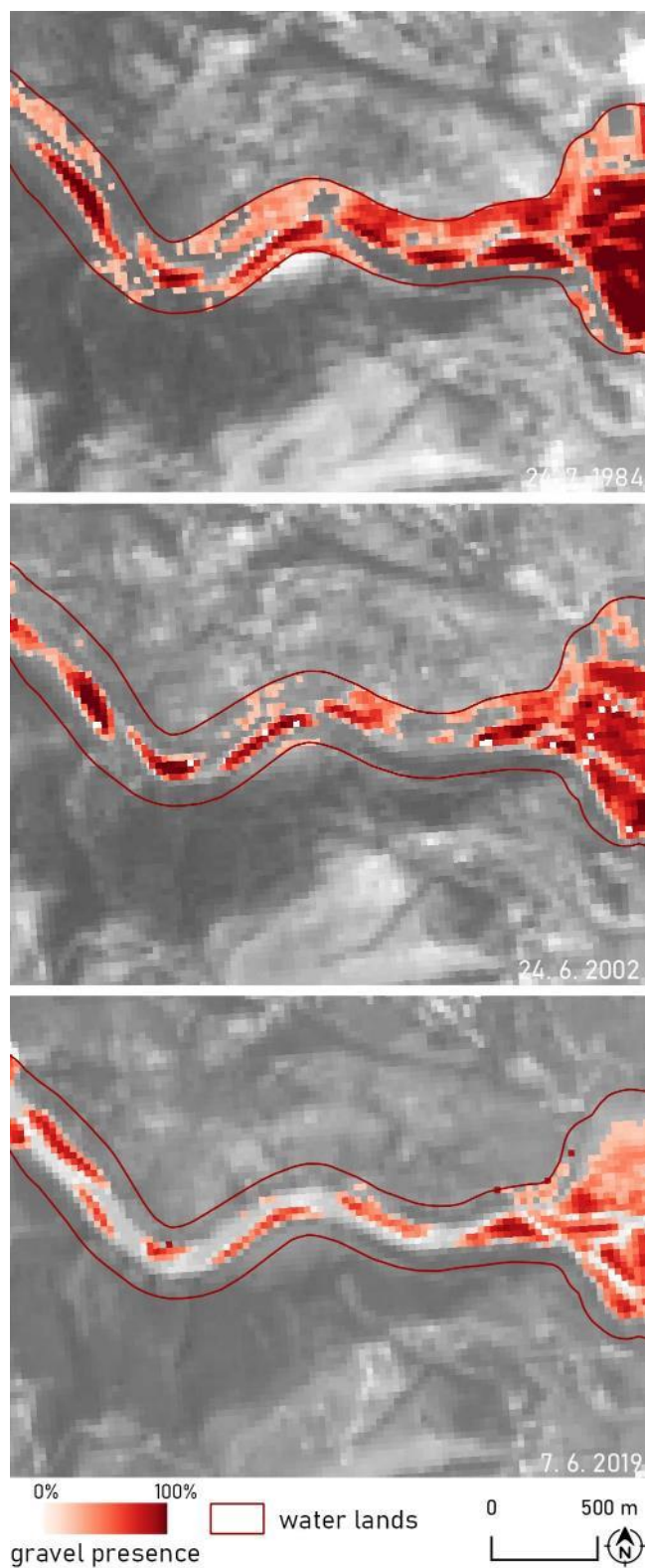
Figure C-7: Gravel presence on the Vjosa river on section 5 in three different timestamps based on Landsat images.

Slika C-7: Prisotnost proda na reki Vjosi na sekciji številka 5 v treh različnih časovnih obdobjih na podlagi posnetkov Landsat.

C-8

Stančič, L. 2022. Monitoring Changes of Fluvial Gravel Bars with Remote Sensing.
PhD Th. Ljubljana, UL FGG, Interdisciplinary doctoral study programme Environmental Protection.

Figure C-8: Gravel presence on the Vjosa river on section 6 in three different timestamps based on Landsat images.

Slika C-8: Prisotnost proda na reki Vjosi na sekciji številka 6 v treh različnih časovnih obdobjih na podlagi posnetkov Landsat.
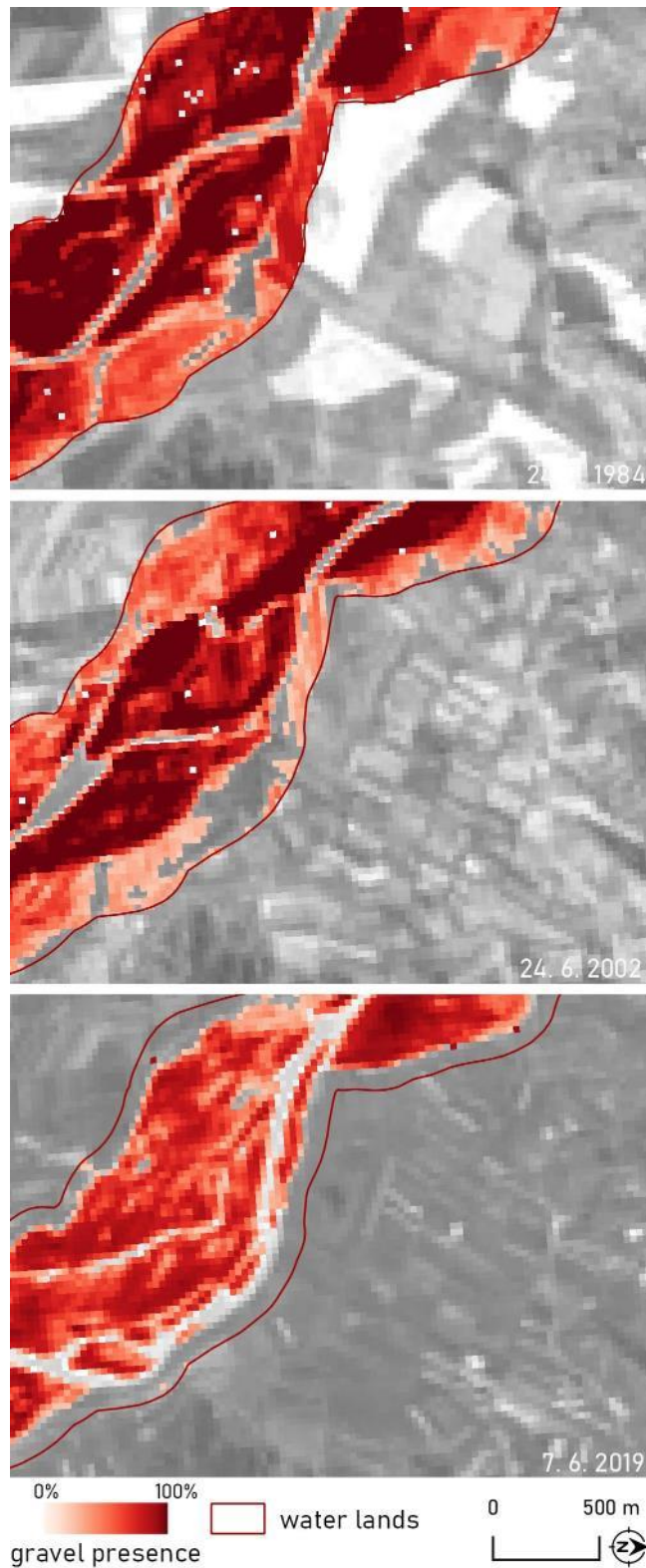
Stančič, L. 2022. Monitoring Changes of Fluvial Gravel Bars with Remote Sensing.   C-9

PhD Th. Ljubljana, UL FGG, Interdisciplinary doctoral study programme Environmental Protection.

Figure C-9: Gravel presence on the Vjosa river on section 7 in three different timestamps based on Landsat images.

Slika C-9: Prisotnost proda na reki Vjosi na sekciji številka 7 v treh različnih časovnih obdobjih na podlagi posnetkov Landsat.
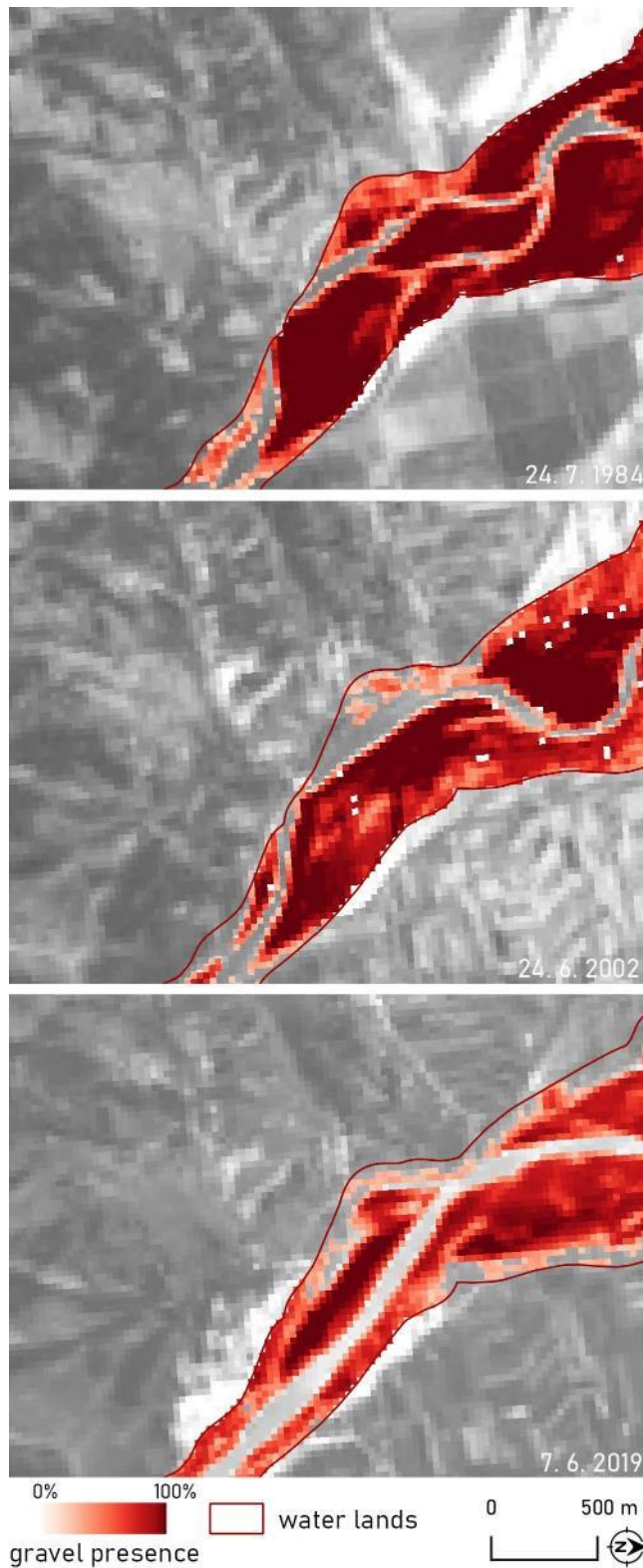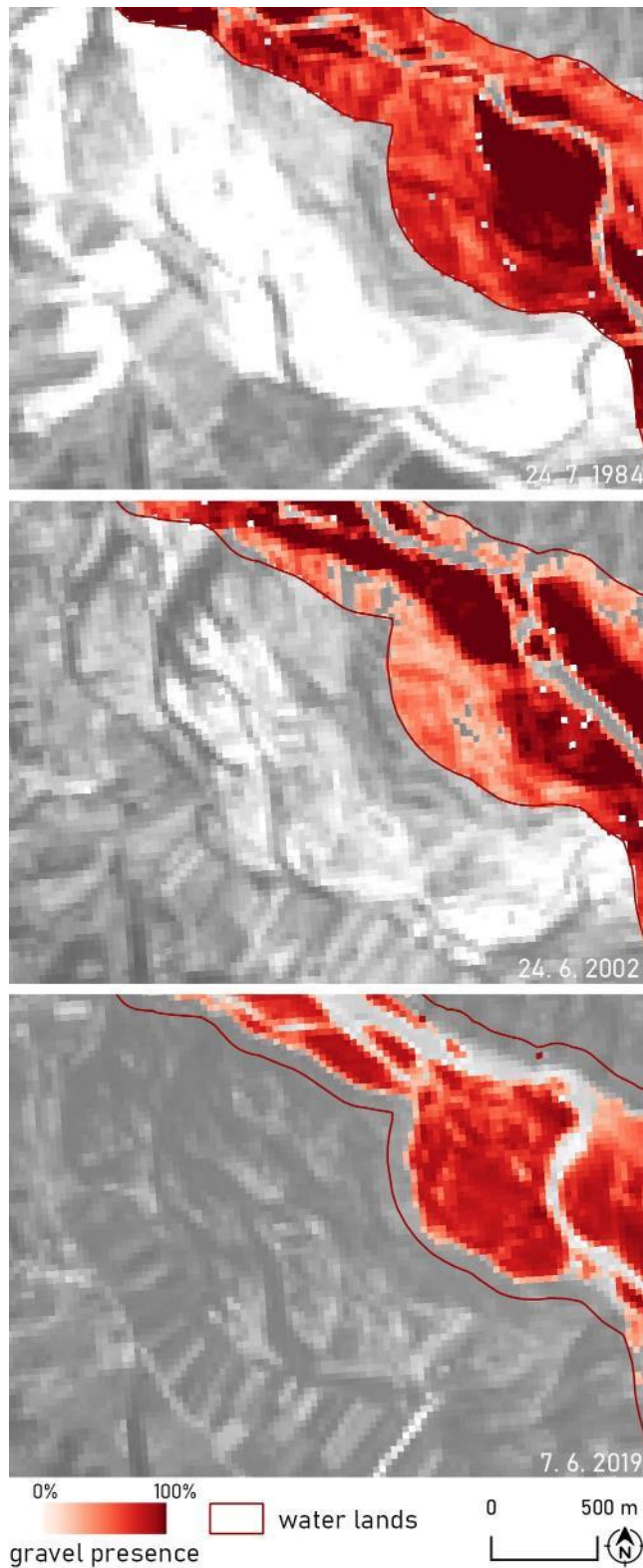
Figure C-10: Gravel presence on the Vjosa river on section 8 in three different timestamps based on Landsat images.

Slika C-10: Prisotnost proda na reki Vjosi na sekciji številka 8 v treh različnih časovnih obdobjih na podlagi posnetkov Landsat.

Stančič, L. 2022. Monitoring Changes of Fluvial Gravel Bars with Remote Sensing.
PhD Th. Ljubljana, UL FGG, Interdisciplinary doctoral study programme Environmental Protection.
C-11

Figure C-11: Gravel presence on the Vjosa river on section 9 in three different timestamps based on Landsat images.

Slika C-11: Prisotnost proda na reki Vjosi na sekciji številka 9 v treh različnih časovnih obdobjih na podlagi posnetkov Landsat.
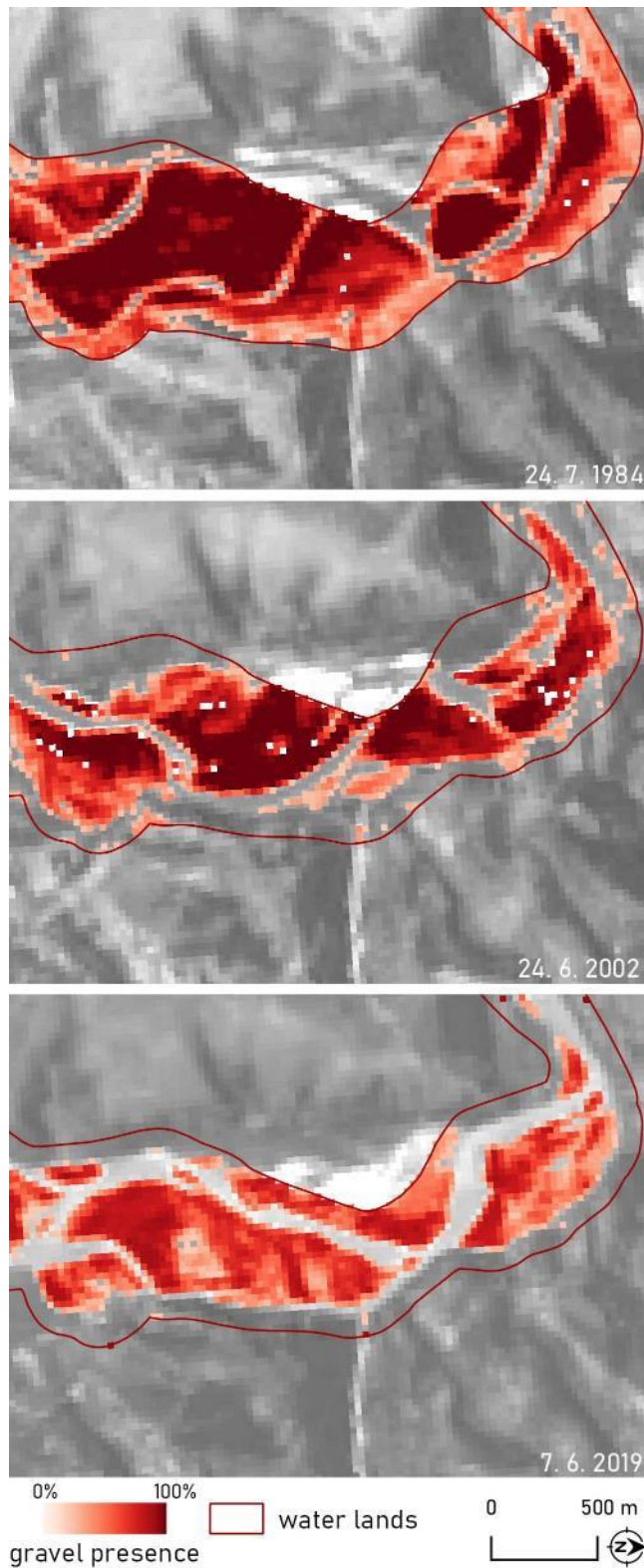
Figure C-12: Gravel presence on the Vjosa river on section 10 in three different timestamps based on Landsat images.

Slika C-12: Prisotnost proda na reki Vjosi na sekciji številka 10 v treh različnih časovnih obdobjih na podlagi posnetkov Landsat.
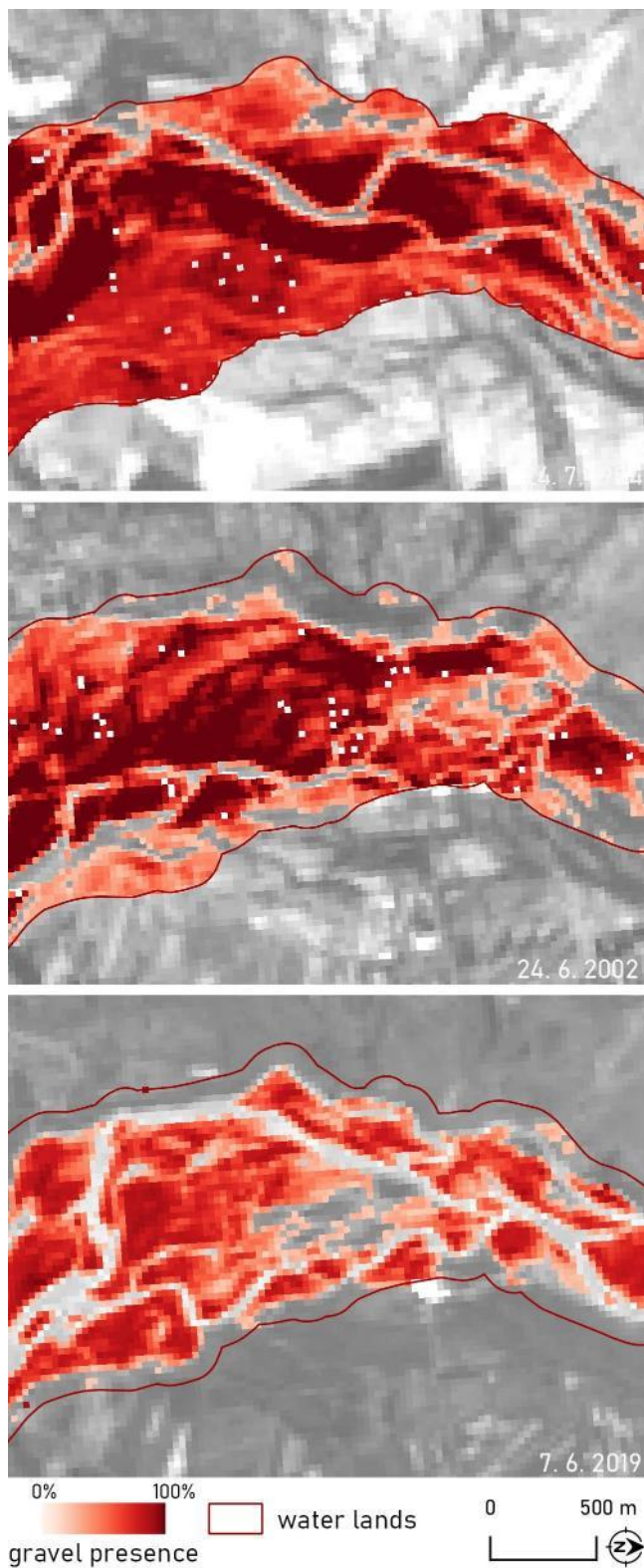
Figure C-13: Gravel presence on the Vjosa river on section 11 in three different timestamps based on Landsat images.

Slika C-13: Prisotnost proda na reki Vjosi na sekciji številka 11 v treh različnih časovnih obdobjih na podlagi posnetkov Landsat.

C-14
Stančič, L. 2022. Monitoring Changes of Fluvial Gravel Bars with Remote Sensing.
PhD Th. Ljubljana, UL FGG, Interdisciplinary doctoral study programme Environmental Protection.

Figure C-14: Gravel presence on the Vjosa river on section 12 in three different timestamps based on Landsat images.

Slika C-14: Prisotnost proda na reki Vjosi na sekciji številka 12 v treh različnih časovnih obdobjih na podlagi posnetkov Landsat.
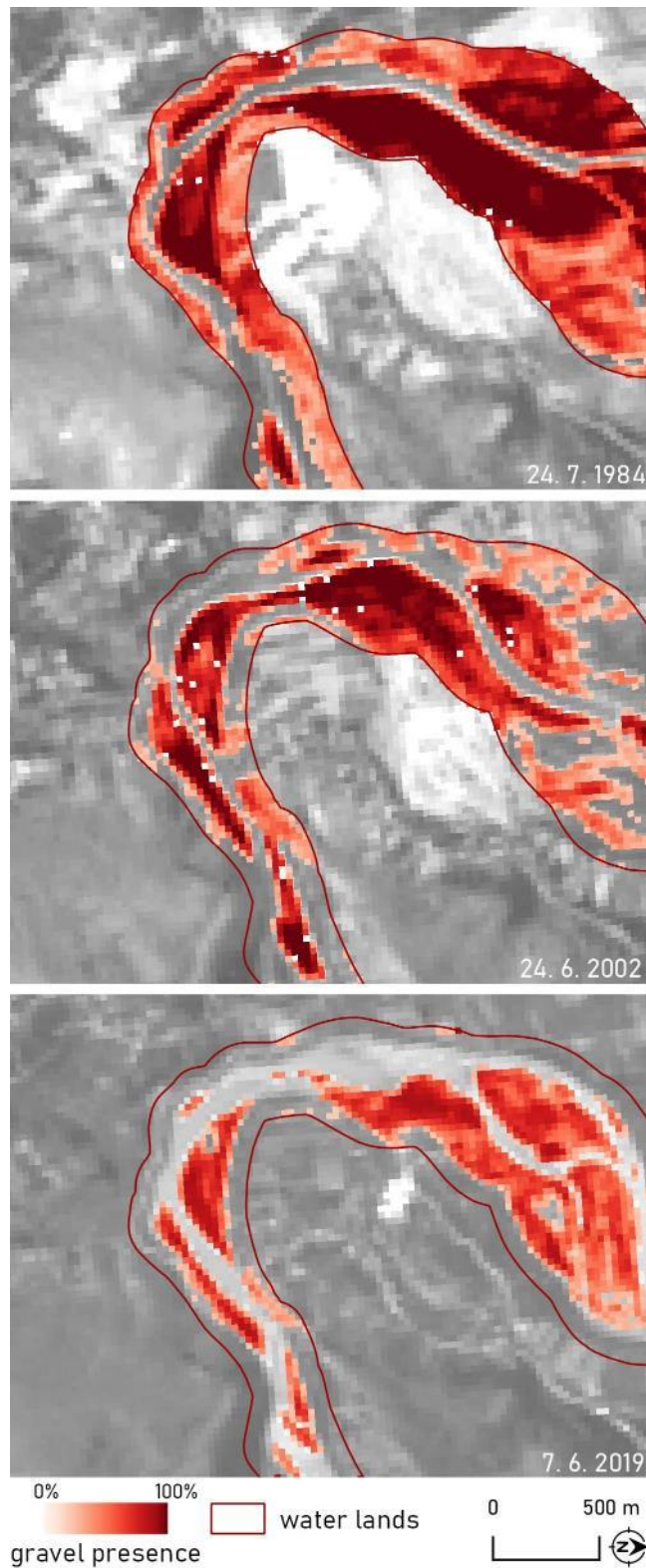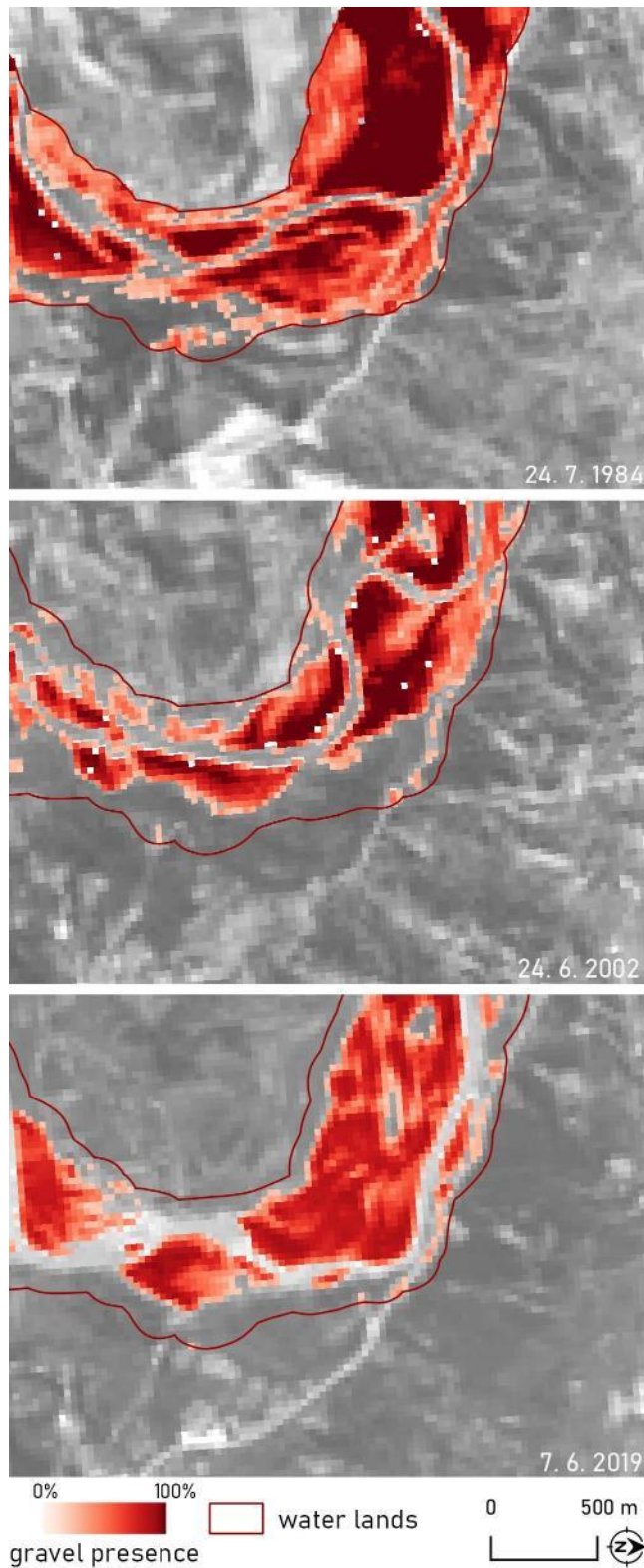
Figure C-15: Gravel presence on the Vjosa river on section 13 in three different timestamps based on Landsat images.

Slika C-15: Prisotnost proda na reki Vjosi na sekciji številka 13 v treh različnih časovnih obdobjih na podlagi posnetkov Landsat.
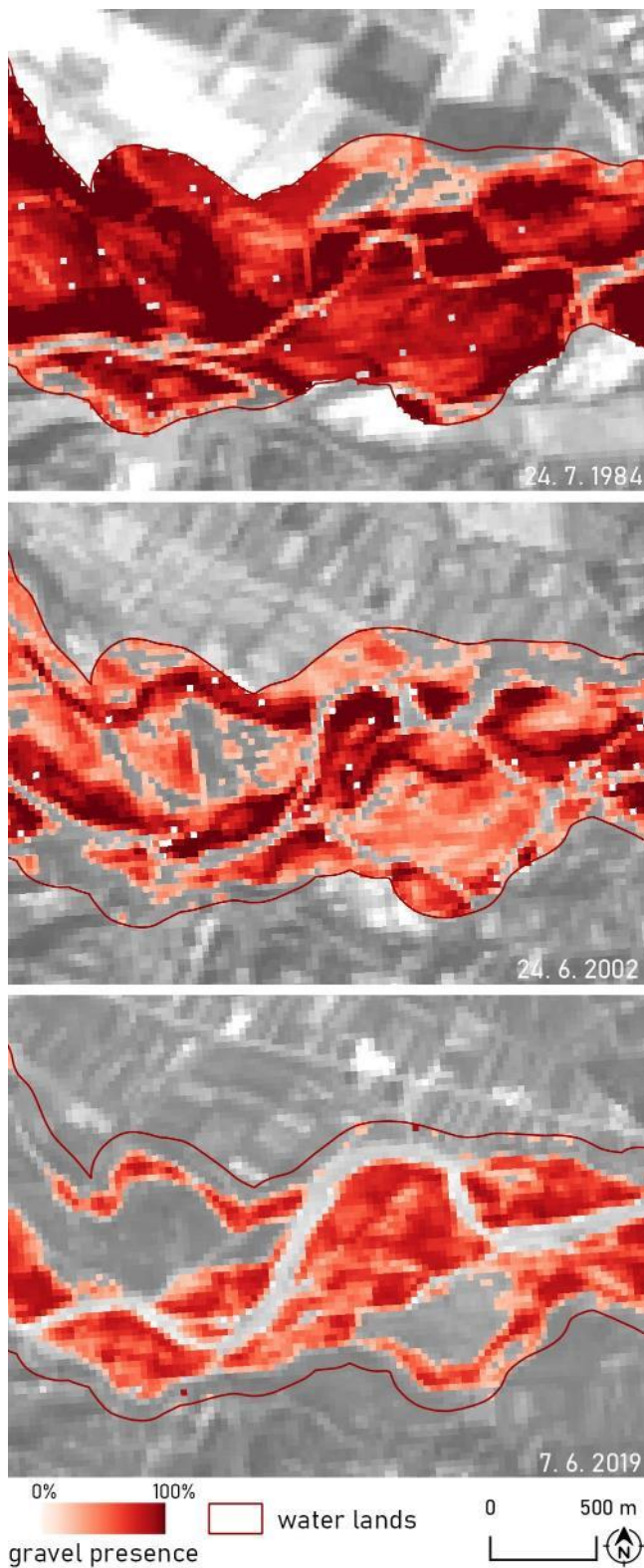
Figure C-16: Gravel presence on the Vjosa river on section 14 in three different timestamps based on Landsat images.

Slika C-16: Prisotnost proda na reki Vjosi na sekciji številka 14 v treh različnih časovnih obdobjih na podlagi posnetkov Landsat.
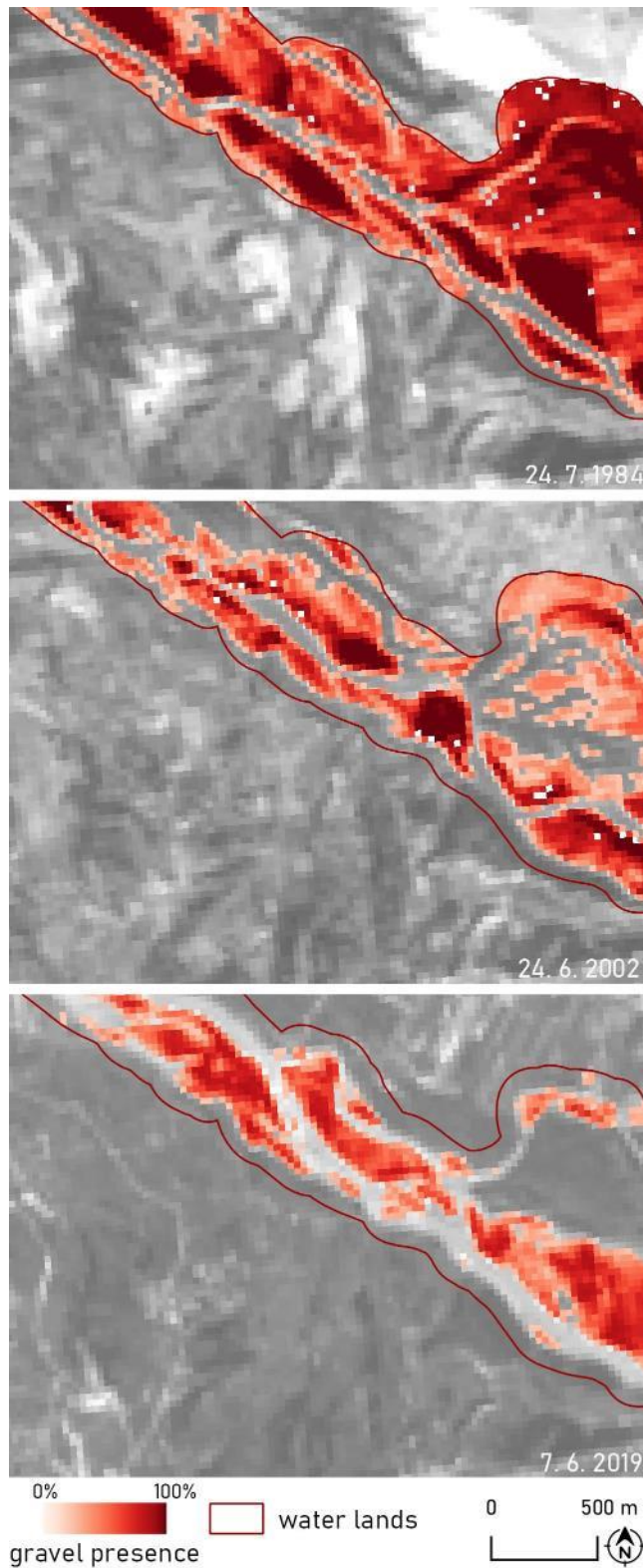
Figure C-17: Gravel presence on the Vjosa river on section 15 in three different timestamps based on Landsat images.

Slika C-17: Prisotnost proda na reki Vjosi na sekciji številka 15 v treh različnih časovnih obdobjih na podlagi posnetkov Landsat.

Figure C-18: Gravel presence on the Vjosa river on section 16 in three different timestamps based on Landsat images.

Slika C-18: Prisotnost proda na reki Vjosi na sekciji številka 16 v treh različnih časovnih obdobjih na podlagi posnetkov Landsat.
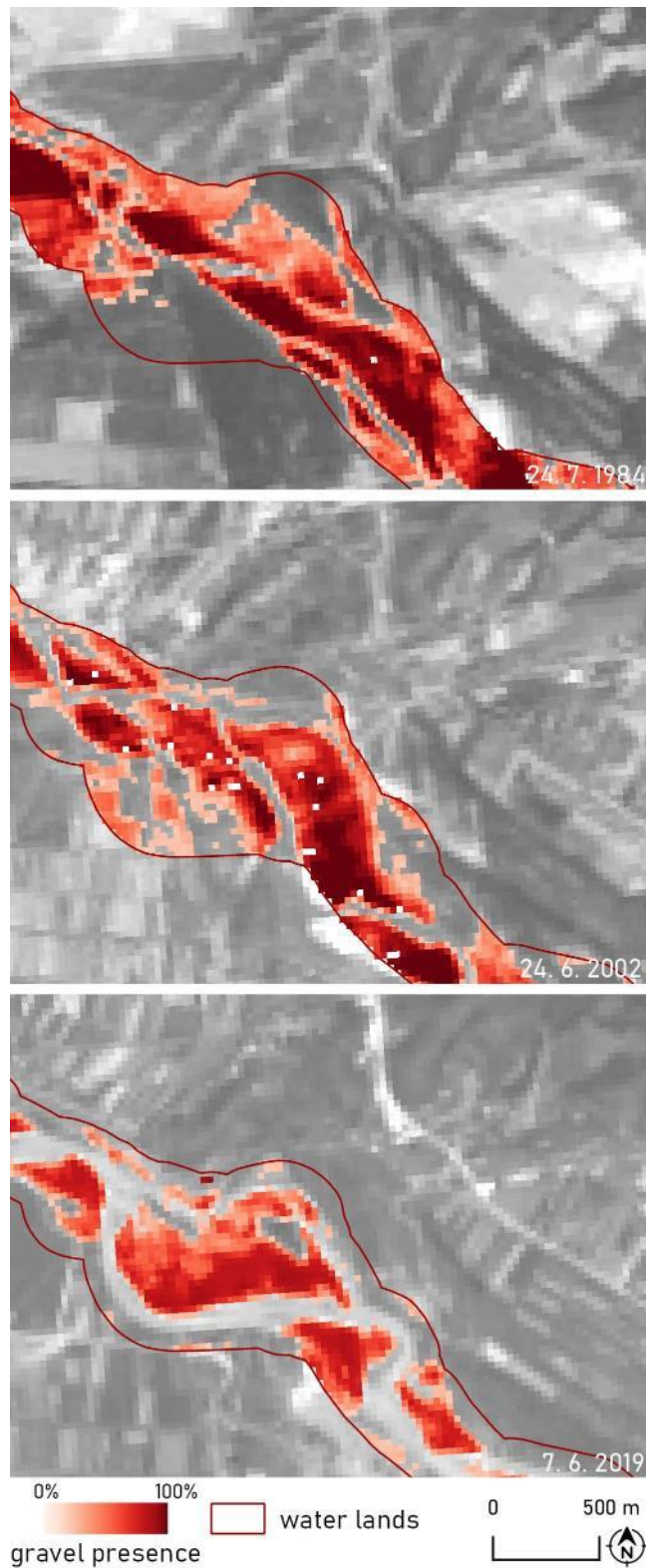
Figure C-19: Gravel presence on the Vjosa river on section 17 in three different timestamps based on Landsat images.

Slika C-19: Prisotnost proda na reki Vjosi na sekciji številka 17 v treh različnih časovnih obdobjih na podlagi posnetkov Landsat.
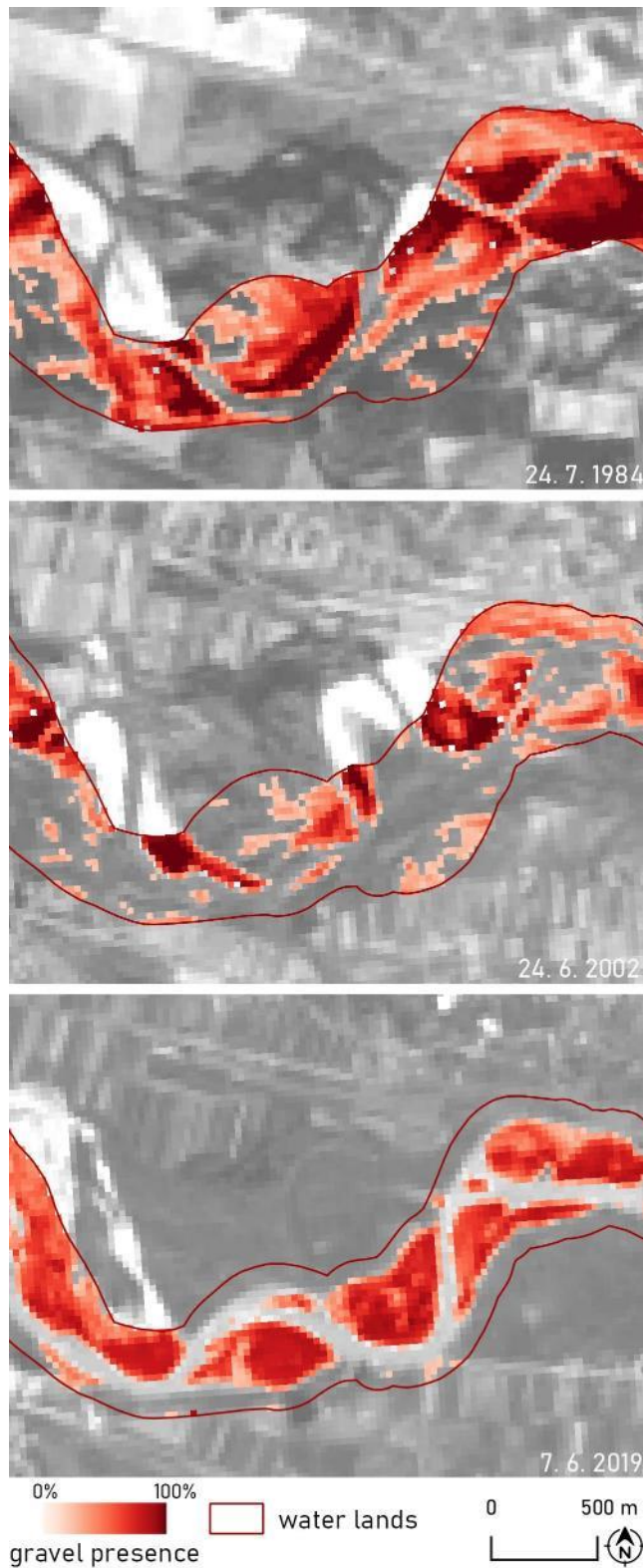
C-20

Stančič, L. 2022. Monitoring Changes of Fluvial Gravel Bars with Remote Sensing.

PhD Th. Ljubljana, UL FGG, Interdisciplinary doctoral study programme Environmental Protection.

Figure C-20: Gravel presence on the Vjosa river on section 18 in three different timestamps based on Landsat images.

Slika C-20: Prisotnost proda na reki Vjosi na sekciji številka 18 v treh različnih časovnih obdobjih na podlagi posnetkov Landsat.
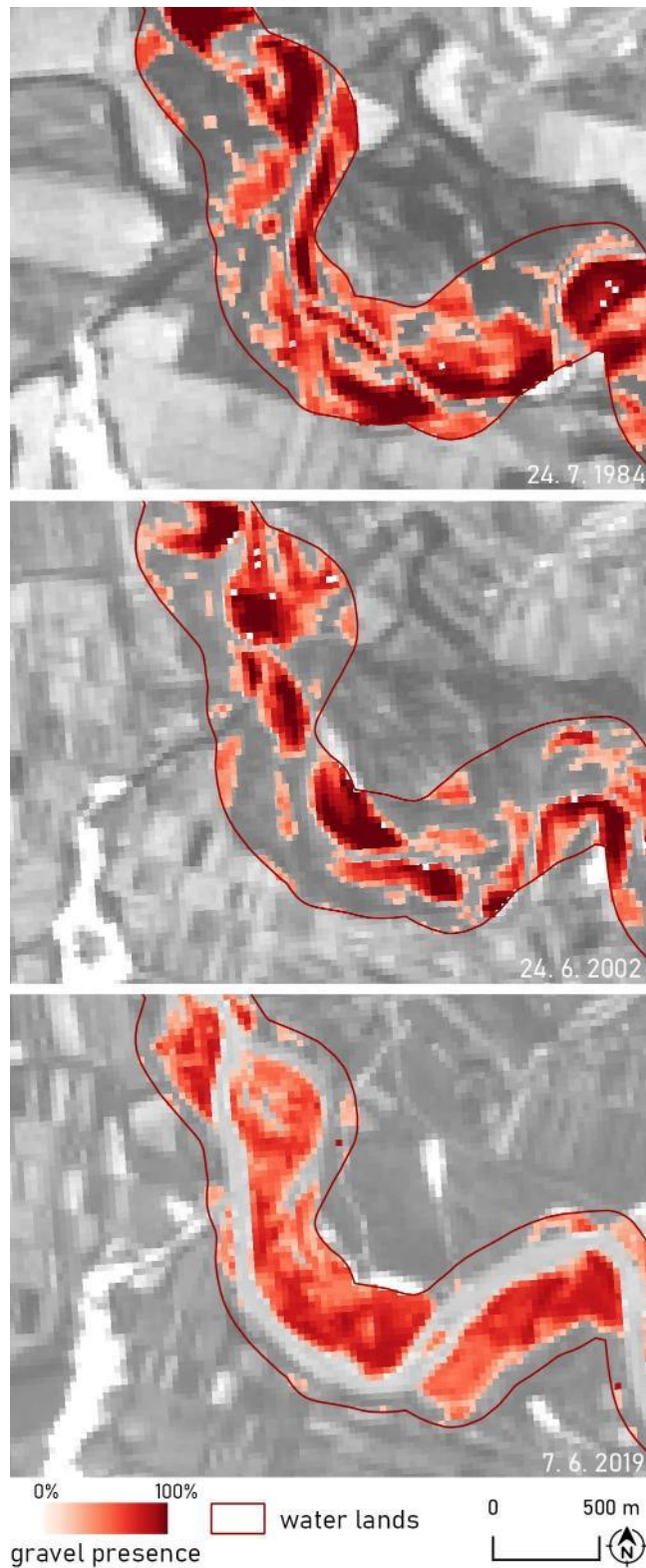
Figure C-21: Gravel presence on the Vjosa river on section 19 in three different timestamps based on Landsat images.

Slika C-21: Prisotnost proda na reki Vjosi na sekciji številka 19 v treh različnih časovnih obdobjih na podlagi posnetkov Landsat.
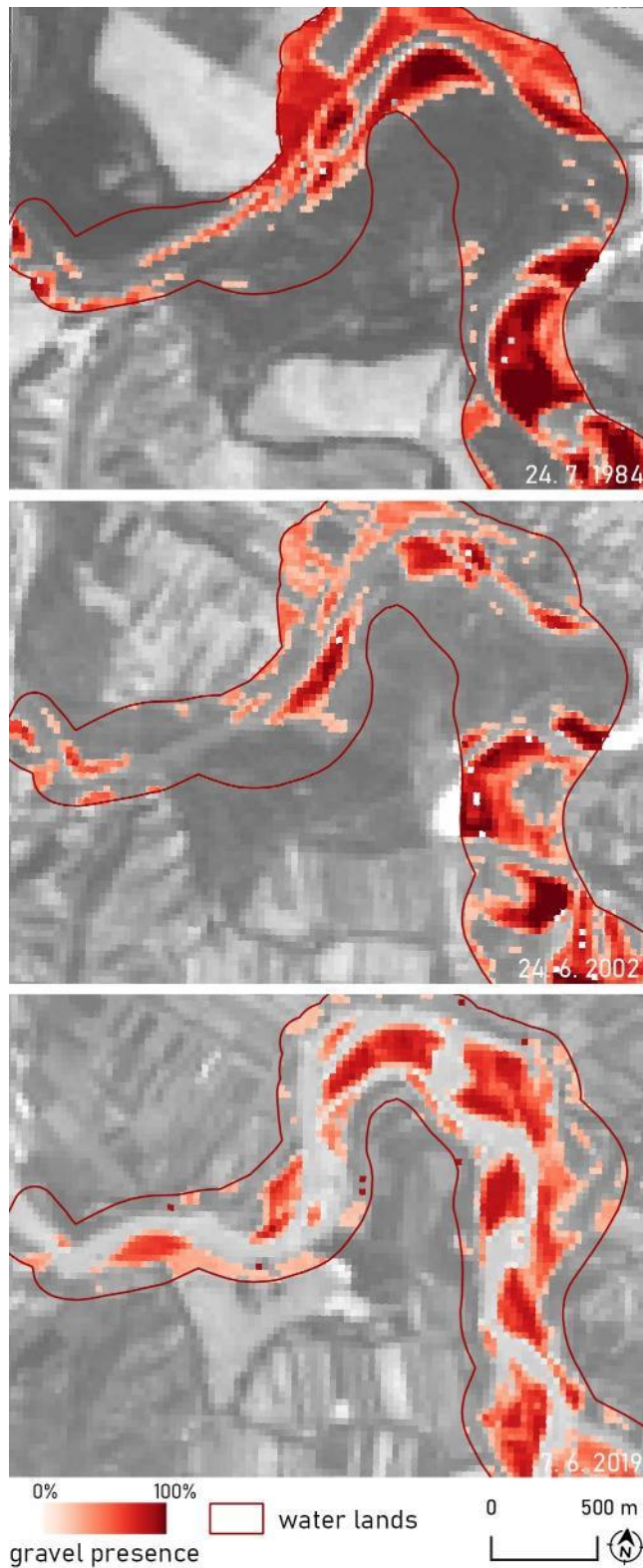
Figure C-22: Gravel presence on the Vjosa river on section 20 in three different timestamps based on Landsat images.

Slika C-22: Prisotnost proda na reki Vjosi na sekciji številka 20 v treh različnih časovnih obdobjih na podlagi posnetkov Landsat.